Theoretical examinations of optical tomography through scattering medium

by

FAN ZHANG, MSc

Thesis submitted to the University of Nottingham

for the degree of Doctor of Philosophy

FEBRUARY 2015

Abstract

Optical tomography is considered to be a non-invasive and non-ionising technique that can create a digital volumetric model of an object by reconstructing 3D images made from light transmitted and scattered through the object. It is becoming of increasing importance in the area of tissue engineering and biomedical diagnostics. The main limit of pure optical techniques is the heavy scattering of tissue, which causes a poor imaging resolution.

Ultrasound modulated optical tomography (USMOT) combines optical and ultrasonic techniques to produce optical contrast at ultrasound resolution. The modulation mechanism for incoherent USMOT is considered to be a secondary effect when coherent light is used. However, it is still valuable as it offers a chance to simulate the modulation of fluorescent light.

In this thesis, several models of fluorescence imaging systems are presented including incoherent USMOT, Fluorescence lifetime extraction system, full field illumination (FI) system and scanning input (SI) system.

A simple incoherent USMOT model is presented which allows varying of acoustic and optical parameters to provide an optimum setup to measure the incoherent USMOT effect. Afterwards, the combination of incoherent USMOT and fluorescence imaging is applied to provide an optimized SNR of modulated fluorescent light by changing the modulation frequency.

With the presence of ultrasound, a novel lifetime extraction technique is presented which provides more accurate lifetime measurements and further makes it possible to extract fluorescence lifetimes in a heavily scattering medium.

A broad range of excitation and emission optical parameters of NIR fluorescence imaging system have been investigated which aims to find out the optimized imaging pairs based on the SNR and spatial resolution detected. The scanning input system turns out to be better than the full field illumination system based on the spatial resolution detected, and longer wavelengths may lead to a higher SNR but degraded spatial resolution. The spatial resolution has been taken into account in fluorophore and imaging system selection over a broad range of excitation and emission

wavelength. Experimental results are shown as well as a supplement to the simulations.

Acknowledgement

This thesis could not be finished without the help and support of many people who are gratefully acknowledged here.

First and foremost, I'm honoured to express my deepest gratitude to my supervisors, Prof. Steve Morgan and Prof. John Crowe, under whose able guidance I have conducted this research. They are encouraging and motivating advisors, who have offered me valuable ideas, suggestions with their profound knowledge for this project. Their patience and understanding are greatly appreciated.

I'm also extremely grateful to Prof. Barrie Hayes-Gill for his valuable discussion on the theory, Dr. David Morris and Dr. Paul Rodmell for their discussion on the Monte Carlo modelling. I would also like to acknowledge Dr. Nam Trung Huynh and Dr. Diwei He for their help in the modelling and discussion throughout this project. I am also grateful to my colleagues and technicians for their help during my doctoral study.

At last but not least, I would like to thank my family for their support all the way from the very beginning of my PhD study. I am thankful to all my friends for their thoughtfulness and encouragement.

Contents

Abstract I

Acknowledgement III

Contents IV

Chapter 1 1

1 Introduction 1

1.1 Motivation 2

1.2 Optical properties of tissue 4

1.2.1 Scattering properties 4

1.2.2 Absorption properties 5

1.3 Imaging techniques for *in vivo* tissues 6

1.4 Thesis plan 7

Chapter 2 8

2 Review 8

2.1 Introduction 9

2.2 Ultrasound modulated optical tomography 9

2.2.1 Mechanisms 9

2.2.2 Simulations 11

2.2.3 Application of USMOT 16

2.3 Photoacoustic tomography 17

2.4 Fluorescence imaging 18

2.4.1 Fluorescence probes 18

2.4.2 Fluorescence lifetime imaging microscopy 20

2.4.3 Simulations 23
2.4.4 Application of fluorescence imaging 25
2.5 Combination of fluorescence and USMOT modelling 27
2.6 Summary 27
Chapter 3 29
3 Ultrasound modulated Monte Carlo model 29
3.1 Introduction 30
3.2 Model description 31
3.2.1 Photon initialization 31
3.2.2 Generating the step size 31
3.2.3 Moving the photon 32
3.2.4 Photon absorption 32
3.2.5 Photon scattering 34
3.2.6 Ultrasound focus 37
3.3 Ultrasound focus model design 38
3.3.1 Model setup and limitations 38
3.3.2 Results and discussion 41
3.4 Signal to noise ratio analysis 43
3.4.1 Ultrasound frequency variation 43
3.4.2 Pulsed and continuous wave simulation 45
3.4.3 Scattering coefficient variation 47
3.4.4 Detector size variation 51
3.4.5 Discussion 53

3.5 Ultrasound modulated fluorescence model 55
3.5.1 Model configuration 55
3.5.2 Results and discussion 56
3.6 Conclusion 60
Chapter 4 62
4 Lifetime based fluorescence optical diffusion model 62
4.1 Introduction 63
4.2 Fluorescence lifetime analysis 63
4.3 Phase shift in heavily scattering medium 65
4.4 Model description 69
4.5 Results 85
4.5.1 Non-USMOT analysis 86
4.5.2 USMOT analysis 90
4.5.3 Optical parameters variation 93
4.6 Discussion 93
4.7 Conclusion 100
Chapter 5 101
5 Optimising fluorescence imaging of deep tissue 101
5.1 Introduction 102
5.2 Optical windows within visible and infrared spectra 103
5.3 Monte Carlo simulation setup 106
5.3.1 Full field illumination (FI) system 106
5.3.2 Scanning input (SI) system 121

5.4 Diffusion model Setup 134
5.4.1 Model description 134
5.4.2 Full field illumination system 138
5.4.3 Scanning input system 147
5.5 Comparison of two imaging systems 155
5.6 Relationship between optical properties and wavelength 161
5.6.1 Fluorophore selection in full field illumination system 161
5.6.2 Auto-fluorescence (AF) in scanning input system 167
5.7 Conclusion 174
Chapter 6 176
6 Infrared fluorescent target imaging 176
6.1 Introduction 177
6.2 Experimental configuration 177
6.2.1 Sim. and Exp. results 178
6.2.2 Discussion 184
6.3 Revised experimental configuration 185
6.3.1 Sim. and Exp. results 185
6.3.2 Discussion 191
6.4 Conclusion 192
Chapter 7 193
7 Conclusion & Future work 193
7.1 Introduction 194
7.2 Summary of the thesis 194

7.3 Overall conclusion 195

7.4 Future works 196

7.4.1 Ultrasound techniques 196

7.4.2 NIR fluorescence techniques 197

7.4.3 Combining techniques 197

7.5 Closing remark 197

Appandix 198

References 202

Chapter 1

1 Introduction

1.1 Motivation

Biomedical imaging has drawn lots of interest and seen increasing development across a wide spectrum of applications from disease diagnostics to tissue monitoring. Among those applications, cancer detection in its early stage has received a great deal of attention in recent decades, as it is a worldwide medical problem. Optical imaging uses low energy non-ionizing radiation, photon energy is only about 2eV for 633nm wavelength laser radiation, which is much safer than X-ray imaging (50KeV photons) [1]. Magnetic resonance imaging (MRI) has no safety problem but is much more expensive compared to optical imaging. Ultrasound imaging is safe and inexpensive, which has been widely used in many applications such as foetal imaging [2, 3]. Ultrasound provides contrast to mechanical properties, but optics provides different functional information, such as oxygen saturation or using fluorescence other tissue properties such information about the environment of the fluorophore molecules as well as their location.

Optical tomography is a method that can create a digital volumetric model of an object by reconstructing images made from light transmitted and scattered through the object. It has drawn increasing interest recently as it offers high optical contrast and is considered to be a powerful method in dealing with biological matter especially for medical imaging. The light carries the spectroscopic information about the volume of tissue it has probed on its way to the detector, and no damage occurs during the process [4]. In other words, optical tomography is a non-invasive method for biomedical diagnostics [1-5].

The main factors that affect the design and performance of the any optical imaging systems are the absorption and scattering of light within the tissue, which limit the penetration depth. In addition, heavy scattering results in poor spatial resolution. In the non-scattering situation, as shown in Figure 1-1(a), a light beam passes through the medium directly as a straight line. A high resolution image can be obtained easily as it is fully dependent on the incident light profile. In a scattering medium, such as tissue, it is difficult to accurately know the region probed, as the light has been heavily scattered through

random paths (Figure 1-1(b)). If this problem can be overcome, it will be an important improvement for optical techniques in many applications.

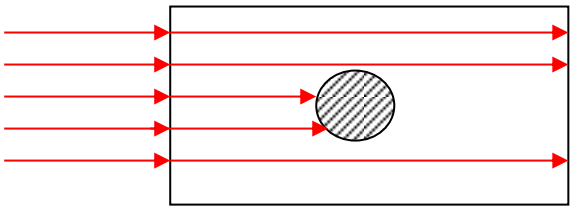

(a)

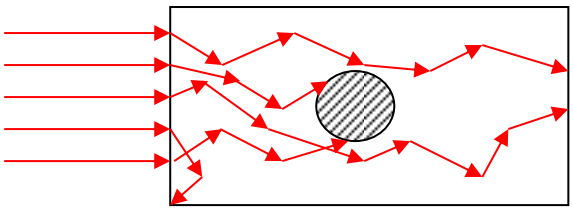

(b)

Figure 1-1 (a) High resolution image obtained under non-scattering conditions (b) Light propagation within scattering medium

Ultrasound modulated optical tomography (USMOT, also called acousto-optical tomography) is a technique that maintains the optical contrast advantage inherent in optical properties and greatly improves the spatial resolution due to the ultrasound. It aims to achieve high spatial resolution sensitivity due to the optical contrast, by modulating the refractive index and scatterer densities at the ultrasound focus region, which in turn changes the phase and exit position of photons that pass through this region. The combination of ultrasound and optics offers the chance to probe both mechanical and physiological parameters, which can be widely used in many applications such as tumour detection or assessment of osteoporosis [6]. This technique will be described and reviewed in detail in Chapter 2.

USMOT reduces the problem associated with spatial resolution, but the penetration depth is still the bottleneck of optical imaging techniques. For deep tissue imaging, fluorescence probes are applied as a contrast agent in optical imaging, especially in the infrared wavelength range as the scattering

and absorption coefficients are lower within that range compared to visible light.

Fluorescence imaging especially in the near-infrared (NIR) range is another technique that has advanced rapidly in the past two decades. The NIR region of the spectrum offers certain advantages for photon penetration due to its reduced scattering and absorption coefficients (μ_s and μ_a) and low autofluorescence effect. Development of both organic and inorganic fluorescence contrast agents is an important research direction. Meanwhile, the broad fluorescence emission spectrum makes it difficult to resolve two different fluorophores by their peak emission wavelength. In order to distinguish a particular fluorophore from other overlapping emission spectra, fluorescence lifetime imaging microscopy (FLIM) is necessarily applied.

The main aim of the research is to model USMOT and optical fluorescence imaging systems and evaluate the signal to noise ratio and spatial resolution obtained as the optical and imaging parameters vary.

1.2 Optical properties of tissue

The resolution of the image is highly dependent on the tissue properties. Therefore it is necessary to define parameters by which the tissue can be quantified. The parameters can be described in the following section [5].

1.2.1 Scattering properties

The scattering coefficient, μ_s (cm^{-1}), is defined in equation 1-1 as the mean number of scattering events that are encountered per unit distance. It provides the information how strong the scattering is quantitatively during the light propagation.

$$\mu_s = n\sigma_{scat} \qquad 1\text{-}1$$

where n is the number concentration of particles (cm^{-3}) and σ_{scat} is the scattering cross-section (cm^2).

Scattering cross-section, σ_{scat}, is a hypothetical area which describes the likelihood of a beam being scattered by a particle. Different from the geometrical cross-section, the scattering cross-section depends on the permittivity and wavelength of light in addition to the shape and size of the particle. Therefore, the value of μ_s is wavelength dependent. *In vivo* tissues, it is typically in the range from 50cm^{-1} to 500cm^{-1} [5].

The inverse of this value 1/ μ_s, indicates the mean distance between two scattering events, which is commonly named the mean free path (MFP).

Another parameter which has a great influence on light scattering is the anisotropy factor $g = \langle \cos\theta \rangle$, the mean cosine of the scattering angle θ. This parameter describes the tendency of the direction for light to scatter in when it hits a particle. $g = 0$ indicates isotropic scattering and $g = 1$ indicates direct forward scatter. For *in vivo* tissues, g is around 0.88 for visible and near infrared (NIR) wavelength [5].

A parameter named the reduced scattering coefficient μ_s' combines μ_s and g and is defined as,

$$\mu_s' = \mu_s(1 - g) \qquad 1\text{-}2$$

similarly, the reduced mean free path is defined as the reciprocal of μ_s'.

1.2.2 Absorption properties

When the light propagates in the medium, it will lose intensity each time it passes through a substance, either due to scattering or absorption. The absorption coefficient, μ_a (cm^{-1}), measures how quickly the light would lose intensity resulting from absorption only. The intensity of light transmitted through a medium is calculated from the Lambert-Beer law shown in equation 1-3.

$$I = I_0 \exp(-\mu_a d) \qquad 1\text{-}3$$

where I_0 is the intensity of incident light, I is the intensity of transmitted light and d is the optical path length in cm.

In the absence of scattering d is the geometrical thickness of the medium, however, in the presence of scattering the path length is a distribution known as the temporal point spread function (TPSF) which makes quantification of the tissue optical properties challenging. Similar to μ_s , the absorption coefficient is wavelength dependent. For *in vivo* tissues, it is typically in the order of $0.1cm^{-1}$ [5].

1.3 Imaging techniques for *in vivo* tissues

In general, the research on biomedical imaging techniques is focused on the advanced techniques and algorithms to provide higher imaging resolution, larger penetration depth and higher signal to noise ratio. As discussed in section 1.1, the main challenge for optical techniques in biomedical applications is optical scattering. For deep tissue imaging, the spatial resolution is degraded quickly because of the many scattering events that occur as the light propagates through the tissue. Researchers often attempt to find out the best balance between penetration and spatial resolution.

Diffuse optical tomography (DOT) [7,8] is a pure optical imaging technique used in optical properties measurement and image reconstruction with good imaging depth. The predominant factor of DOT is scatter, which limits the spatial resolution and reduces the image quality. Optical coherence tomography (OCT) [9,10] applies low-coherence interferometry to produce a two-dimensional image of optical properties. Excellent longitudinal resolution is obtained as it is only limited by the coherence length, but the coherence length limits the imaging depth to smaller than 2mm.

The combination of ultrasound with light greatly improves the resolution and maintains a reasonable imaging depth, which is around 3cm. Meanwhile, it leaves the possibility to further combine with fluorescence techniques, which offers a chance to probe some properties of the tissue, *e.g.* pH, oxygen at both excellent resolution and imaging depth.

1.4 Thesis plan

Chapter 2 reviews the USMOT associated techniques and fluorescence imaging techniques including fluorescent probes, fluorescence lifetime imaging microscopy (FLIM) and simulation models developed so far.

A simple USMOT Monte Carlo model is presented in Chapter 3 mainly based on the incoherent mechanism which has first been modeled by Mahan *et al.* [29] and has been described more concrete by Liu *et al.*[33]. The model is then applied under different conditions by varying the optical properties, ultrasound frequency, detector size and ultrasound operation mode. All the models will be evaluated with respect to signal to noise ratio (SNR).

Chapter 4 is associated with fluorescence lifetime extraction technique in the frequency-domain (FD). An ultrasound based novel algorithm is developed and modeled using the diffusion approximation and the extraction accuracy is evaluated and compared with traditional FD techniques.

The main purpose of Chapter 5 is to compare and evaluate the fluorescent probes within visible and near infrared (NIR) wavelengths on the SNR and spatial resolution. A Monte Carlo model is used to produce images using specific wavelengths by assigning appropriate scattering and absorption coefficients. A diffusion model is applied to cover a broad range of optical properties on both excitation and emission, with the aim being to find out the optimized imaging pairs. The spatial resolution has been considered in fluorophore and imaging system selections over a broad range of excitation and emission wavelength.

Chapter 6 demonstrates some simulation and experimental results of NIR fluorescent targets covered by agar gel containing polystyrene microspheres, giving support for the modelling work in Chapter 5.

Conclusion and suggestions for further work are made in Chapter 7.

Chapter 2

2 Review

2.1 Introduction

The aim of this chapter is to describe in more detail the problems associated with ultrasound modulated optical tomography and to review the development of fluorescent probes in the application of deep tissue imaging.

2.2 Ultrasound modulated optical tomography

Both the theoretical and experimental studies in the development of USMOT, mainly concerns the improvement of signal to noise ratio, spatial resolution and its biomedical applications. In this section, the basic principles of USMOT and techniques directly related to the work of this thesis are reviewed.

2.2.1 Mechanisms

Ultrasound modulated optical tomography (USMOT) is an imaging technique that combines acoustic and optical waves aiming to obtain the optical contrast of images at ultrasonic resolution [1, 6, 11]. Compared to photo-acoustic tomography (PAT) [12], it has similar configuration but with a different mechanism.

A typical USMOT configuration is shown in Figure 2-1,

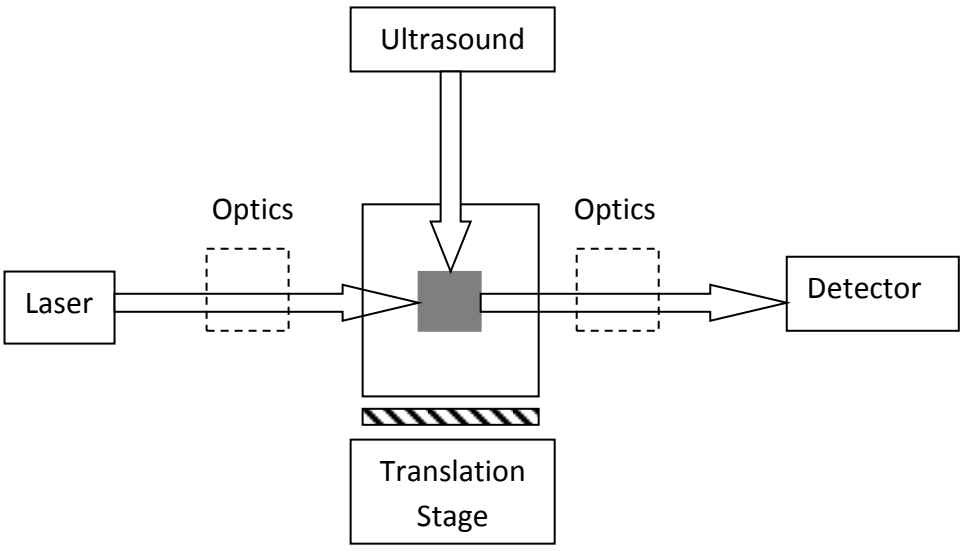

Figure 2-1 Typical USMOT configuration

The optical waves pass through the ultrasound focus region and are modulated after the interaction. The modulated light will then be detected by a photo detector. The amount of modulated photons predominantly carries the information about the optical properties of the ultrasound focus region.

Wang [13] proposed three possible mechanisms for modulation of light by ultrasound in a scattering medium.

The first mechanism is based on the ultrasound-induced variations of the optical properties of the media. The ultrasound pressure causes the medium to be compressed and rarified which changes the density of the medium, which further forms a high pressure region with higher absorption and scattering coefficients than that of rarefaction. Accordingly, the detected intensity of light varies with the ultrasonic wave. This mechanism is considered to be a secondary effect and hardly observed experimentally. This mechanism relies on the direct intensity modulation of light hence there is no particularly requirement of the light source.

The second mechanism is founded on variations of the optical phase in response to ultrasound-induced particles displacement. Assuming a photon successfully travelled through the medium, the total travel distance is the sum of path lengths between each scattering event. As discussed in the first mechanism, the displacement of scatterers and absorbers are varied due to ultrasound pressure, which results in the total path length or optical phase fluctuating with the ultrasonic wave.

The third mechanism relies on the variations of the optical phase in response to ultrasonic modulation of the refractive index. Optical path length in the scattering medium fluctuates as ultrasonic pressure generates a variation of refractive index. Both the second and third mechanisms require the use of coherent light and laser speckle detection.

Based on these theoretical possible mechanisms, the modeling of USMOT has been presented by several groups with the main focus on the second and third ones. Leutz and Maret [14] have developed a model based on the modulation of particle displacement but under a weakly scattering approximation. The

optical frequency shift has been demonstrated in simulation and further been implemented experimentally by applying a Fabry-Perot interferometer. Following the analysis of Leutz and Maret, Kempe *et al.* [15] extended the model considering a narrow beam of ultrasound and compared this model to experimental results. Wang and Zhao [16] experimentally demonstrated the imaging of an absorbing object with millimeter resolution inside a 5cm thick scattering medium with μ_a = 0.1cm^{-1} and μ_s' = 10cm^{-1} by applying 1MHz continuous ultrasound modulation.

2.2.2 Simulations

To describe the light propagation through scattering media various analytical and numerical models have been developed and mostly based on radiative transfer theory (RTT). The two most commonly used models will be introduced here, the diffusion approximation model and the Monte Carlo (MC) model. It should be noted that the diffusion approximation is an approximate analytical solution and the MC model is the numerical solution to the radiative transfer equation (RTE).

The RTT explains how the energy of the electromagnetic radiation transfers through a scattering medium. The propagation is affected by absorption and scattering. This process is described by the RTE is as follows,

$$\begin{aligned}\frac{1}{c_n}\frac{\partial I(r,\hat{s},t)}{\partial t} + \hat{s}\cdot\nabla I(r,\hat{s},t) \\ = -(\mu_s+\mu_a)I(r,\hat{s},t) \\ + \frac{\mu_s}{4\pi c_n}\int_{4\pi} I(r,\hat{s},t)p(\hat{s},\hat{s}')d\omega' + \varepsilon(r,\hat{s},t)\end{aligned} \qquad 2\text{-}1$$

$I(r,\hat{s},t)$ is the radiance in Wm^{-2}s^{-1}r^{-1}, which describes the energy through a spatial point r along the direction of a unit vector $\hat{s}$ per unit normal area per unit solid angle per unit time. c_n is the speed of light in the tissue, as determined by the relative refractive index n. $p(\hat{s},\hat{s}')$ is the phase function, which represents the probability of light being scattered in a particular direction. The scattering anisotropy g satisfies,

$$g = \int_{4\pi} (\hat{s} \cdot \hat{s}')p(\hat{s} \cdot \hat{s}')d\omega \qquad 2\text{-}2$$

and the last term $\varepsilon(r, \hat{s}, t)$ is the light source.

In the RTE, six independent variables (three variables from Cartesian coordinates *x*, *y*, *z*, polar angle θ, azimuthal angle ϕ and time *t*) define the radiance at any spatial and temporal point. It is an optimal mathematical model but too complicated to be analytically solved in practical geometries. Therefore, some assumptions are made to simplify the equation so that it can be solved analytically. The diffusion approximation [7, 17] of RTE is considered to be one of the best known and widely used analytical models that describes light propagation through a heavily scattering medium.

2.2.2.1 Analytical model with diffusion approximation

Two assumptions are made there to permit the application of diffusion theory [18]. First of all, after numerous scattering events, the propagation of light becomes isotropic. Secondly, the time for substantial light density change is much longer than the time to traverse one transport mean free path. Both assumptions require a primary scattering medium for light propagation ($\mu_s \gg \mu_a$).

Under the first assumption, the radiance $I(r, \hat{s}, t)$ can be expressed as,

$$I(r, \hat{s}, t) = \frac{1}{4\pi}\Phi(r, t) + \frac{3}{4\pi}j(r, t) \cdot \hat{s} \qquad 2\text{-}3$$

where $\Phi(r, t)$ is the isotropic photon density and $j(r, t)$ is the flux at direction $\hat{s}$.

And under the second assumption, by applying Fick's law,

$$j(r, t) = -D\nabla\Phi(r, t) \qquad 2\text{-}4$$

with D the diffusion coefficient,

$$D = \frac{1}{3(\mu_a + \mu_s^{'})} \qquad 2\text{-}5$$

Substituting equation 2-3 and 2-4 into 2-1 and integrating over the complete 4π solid angle, the RTE can be rewritten as follows,

$$\frac{1}{c_n}\frac{\partial \Phi(r,t)}{\partial t} + \mu_a \Phi(r,t) + D\nabla^2 \Phi(r,t) = \varepsilon(r,\hat{s},t) \qquad 2\text{-}6$$

For a short pulse from an isotropic point source, the analytical solution of equation 2-6 is then presented by applying the Green's function,

$$\Phi(r,t) = c_n(4\pi c_n\, t)^{-3/2}\exp\left(-\frac{\mathrm{r}^2}{4\mathrm{D}c_n\mathrm{t}} - \mu_a c_n t\right) \qquad 2\text{-}7$$

2.2.2.2 Monte Carlo model

The Monte Carlo technique is based around the numerical solution of equation 2-1. It is first proposed by Metropolis and Ulam to simulate physical processes using a stochastic model [19]. Monte Carlo programs with great sophistication have been developed since then [20, 21]. In all applications of the Monte Carlo method, a stochastic model is constructed in which the value expected is determined from a certain random variable or of a combination of several variables. This expected value is then estimated by the average of multiple independent samples.

A basic Monte Carlo model of photon propagation usually includes four steps.

1. Launching a photon packet: the initial position, direction and weight (weight is unity if ignoring initial specular reflectance) of photon packet is been set.
2. Photon packet movement with step size selection: the step size is the distance the photon packet travels between each interaction sites. The step size is randomly selected following certain probability density function. Once selected, the position of photon packet is updated accordingly.

3. Absorption and scattering: A portion of the photon weight is absorbed at each interaction site and the rest is scattered. The scattering direction is determined often using the Henyey-Greenstein phase function.
4. Photon termination: When the weight left in the photon packet is of little consequence, a roulette technique is often employed to kill the photon and keep total energy constant.

The details of Monte Carlo model applied in this thesis will be discussed in chapter 3.

Monte Carlo simulations of photon propagation offer a flexible but rigorous approach toward photon transport in a turbid medium such as tissue. It has been firstly reported by Prahl *et al.* [22]. The method describes the basic rules of photon propagation, so the modelled geometry can be easily modified. It simulates the light transport inside medium on a photon by photon basis in terms of each photon-particle interactions, which is treated as a stochastic process following certain principles of statistics. It is assumed that a photon travels in straight path, and based on the probability distributions which describe the step size of photon movement between each two sites of photon-particle interaction, and the angles of deflection in a photon's trajectory when a scattering event occurs. The deflection angle can be derived by applying either Henyey-Greenstein [23-24] or Mie theory [25]. This simulation can record multiple physical quantities simultaneously. However, the method is statistical in nature and relies on calculating the propagation of a large number of photons by the computer. As a result, this method requires a large amount of computation time.

2.2.2.3 Application of Diffusion and MC simulations

Based on both of the mechanisms for the ultrasonic modulation of coherent light in scattering media, Wang [26] presented an analytical model which shows that the contribution from the modulation of refractive index is comparable with that from modulation of displacement when the factor $k_a l$ is small and becomes dominant as $k_a l$ increases, where k_a is the acoustic wave number and l is the optical scattering mean free path. Through further research,

Wang's model was extended to the case of anisotropically scattering media [27] by calculating the temporal autocorrelation function and further taking the correlation in the interaction between successive scattering sites into account [28].

Several numerical models were developed to describe the interaction of ultrasound with light in scattering media. Before Wang identified the three possible mechanisms, Mahan *et al.* [29] derived an expression for the intensity of the modulated signal, as well as the noise spectrum and thus predicted the detection efficiency of modulated light which does not require a coherent light source. The first coherent USMOT Monte Carlo model is developed by Wang [13], who jointly modeled the two coherent mechanisms of interaction to support his analytical model. On the basis of Wang's model, it has been extended to fulfill different applications. The model is applied to calculate the interaction of diffuse photons with ultrasound by Nieva and Dimarzio [30]. Sakadzic and Wang extended the model to provide a spatial distribution of the optical power spectrum in scattering media and heterogeneous distributions of optically scattering and absorbing objects to the case of continuous wave ultrasound [31] and pulsed ultrasound [32] respectively by developing a temporal correlation transfer equation. Liu *et al.* [33] presented a Monte Carlo model which takes the incoherent effect into consideration. They demonstrated that the modulation depth due to the photon exit location is the dominant incoherent effect, but it is still two to three orders of magnitude lower than that due to coherent phase variation.

Leung and Powell [34] have ported an USMOT Monte Carlo model onto a graphics processing unit (GPU Nvidia GeForce 9800) which is theoretically 125 times faster than traditional CPU (Intel Core Quad). They demonstrated that the time this took to run their USMOT model is 6 times less than that spent on CPU, which addressed the main challenge of Monte Carlo. They further developed a USMOT Monte Carlo model relying on the two coherent mechanisms on the GPU platform [35] and compare the same configuration on a CPU platform.

Published research on USMOT modeling is mainly focused on the two coherent mechanisms as they are considered to be the dominant factors of acousto-optic interaction. However, the incoherent effect cannot be ignored. Liu *et al.* [33] has presented an incoherent model but in a weakly scattering medium. The incoherent USMOT model of biological media is still a gap, which further offers an opportunity to combine with fluorescence detection or bioluminescence.

2.2.3 Application of USMOT

USMOT has first been studied experimentally by Marks *et al.* [36]. They investigated the interaction of pulsed ultrasound and laser light and detected a modulated signal in a homogeneous turbid medium. Kempe *et al.* then applied USMOT in tissue phantoms to image absorbing objects [37]. The modulated signals were detected by a single detector, *e.g.*, a photomultiplier tube (PMT) or a photodiode. The detection method has developed rapidly since then. Li *et al.* proposed a method of optical filtering to leave only the light in the acoustic sideband by applying a cryogenically cooled spectral-hole burning crystal [38].

As *ex vivo* imaging is considered to be the preliminary stage of clinical research, many groups have put their efforts into *ex vivo* tissue such as chicken or turkey breast [37, 39]. Parallel speckle detection was developed by Leveque *et al.* [40, 41], in which a CCD camera was employed and a source-synchronized lock-in detection was applied. It is reported as the first time that acoustic-optic method is applied in deep tissue (35mm) imaging with millimetre resolution. Yao *et al.* [42] subsequently extended this approach to obtain 2D images of multiple objects buried in biological tissues. Kothapalli and Wang [43] developed ultrasound-modulated optical microscopy based on a Fabry-Perot interferometer, which is used for real-time detection of scattered light modulated by high frequency (30-75MHz). They successfully imaged blood vasculature in heavily scattering samples from a rat *ex vivo* for the first time.

The USMOT technique was first applied *in vivo* by Lev and Sfez [44]. They compared the ultrasound modulated light signals in dynamic phantoms and

living tissues and further analyzed the corresponding effect of speckle fluctuations. Two years later, Lev *et al.* have extended their research to the clinical experiment [45]. They have measured the scattering coefficient of bone tissues by USMOT and compared them with the bone density obtained using dual X-ray absorption. The two results were close as reported, which makes USMOT a technique potentially for the assessment of osteoporosis. Gross *et al.* [46] measured *in vivo* the spectrum of the modulated light scattered through the breast of a female volunteer based on the digital heterodyne holography detection technique. They demonstrated that this technique achieved a high SNR compared to the system with single detector.

2.3 Photoacoustic tomography

Photoacoustic tomography (PAT) is another technique that combines ultrasound and optics and is considered as the main competitor to USMOT. This was first introduced by Bell in 1880 [47]. This technique requires high power, diffuse, short pulses *e.g.* a visible laser pulse, to illuminate tissue samples. A fraction of the incident energy is absorbed and converted into heat, which raises the temperature and leads to thermoelastic expansion. This detected ultrasonic variation is considered as the PAT signal. It was first applied to biomedical imaging by Hoelen *et al.* [48]. They used PAT to image blood vessels in heavily scattering samples. The imaging depth presented is about 1cm and the lateral resolution is around 200μm.

Combining the advantages of ultrasound and optics, USMOT and PAT have the potential to serve as a non-invasive and non-ionising biomedical imaging technique. Both of them are able to achieve scalable ultrasound resolution and penetration depth by varying ultrasonic frequency without optical speckle artefacts [1, 49]. To date, PAT is superior to USMOT for its higher imaging resolution *in vivo*, but it cannot be used to directly image fluorescence (just indirectly via absorption) and also cannot be used for bioluminescence [50].

2.4 Fluorescence imaging

Imaging of fluorescence *in vivo* has become one of the most commonly used tools in all pre-clinical experiments. In the last decade, fluorescence imaging systems and the development of fluorescent probes has emerged with a wide range of utilities and niche application areas. The development of fluorescent probes, especially the ones in near infrared (NIR) range is described in this section. The imaging techniques and related models which are close to the research described in this thesis are reviewed as well.

2.4.1 Fluorescence probes

The non-invasive quantization and visualization of molecular processes is an important research direction in molecular imaging as they occur *in vivo* [51]. Driven by the deep penetration depth compared to traditional optical imaging approaches, near infrared (NIR) fluorescent agents have played a major role in this field and increasing interest has been put into the development of NIR particles and their application for imaging thick tissue [52]. The effectiveness of a probe is invariably defined by the ability to provide a high target to background ratio (TBR) with strong emission enabling clear visualization of the intended molecular target [53]. Exciting at longer wavelengths reduces the autofluorescence (AF) effect which means the TBR is higher.

The fluorescent probes, by their emission range, can be generally classified into two groups, visible and NIR, but the range of probes in this region of the electromagnetic spectrum continues to expand. There has been much recent research focusing on the probes of which peak emission beyond the 630 nm wavelength, because the absorption of light sharply decreases *in vivo*, which leads to a deeper penetration depth than that in the visible range. The main absorber within the visual spectrum in tissues is hemoglobin, but wavelengths longer than 1100nm are absorbed by water. Therefore the favorable optical window for visualization in living tissues is approximately between 630 and 1100nm [54, 55].

Tung *et al.* first developed a NIR small molecule targeted probe which consisted of a NIR fluorophore and folic acid applied for both *in vitro* and *in*

vivo imaging [56]. Johnson *et al.* has then reported a squaraine dye which can be readily converted into extremely bright and highly stable NIR fluorescent probes for *in vitro* and *in vivo* optical imaging of live and fixed cells [57]. In the last decade, several fluorescent proteins have been developed such as HcRed [58], mPlum [59] and AQ143 [60], whose maximum emission spectra are around 650nm. But these proteins are limited by the low quantum yield (QY) (<10%) which leads to a low brightness (<4100$M^{-1}cm^{-1}$, the product of molar extinction coefficient and QY). Shcherbo *et al.* then reported a far-red fluorescent protein named Katushka [61], which has superiority for whole-body imaging by direct comparison with other red and far-red fluorescent proteins including pH-stability, QY (34%) and brightness (22100$M^{-1}cm^{-1}$). Two years later, new fluorescent proteins mKate2 and tdKatushka2 have been reported by Shcherbo *et al.* [62] for their far-red emission spectrum, excellent pH resistance, higher QY (40%) and brightness (25000$M^{-1}cm^{-1}$), photostability and low toxicity.

If classified by their constitution, current near infrared (NIR) probes generally include two categories [51]: inorganic and organic molecules. The fluorescent proteins described above belong to the organic molecules. Inorganic NIR contrast molecules are mainly associated with quantum dots (QDs) [63, 64, 65] and other nanoparticles (NPs) [66, 67, 68].

The detailed description of QDs properties was first described by Alivisatos [69]. Quantum dots are single crystals and typically have a core-shell structure of a few nanometers in diameter whose size and shape can be precisely controlled by the duration, temperature and ligand molecules used in their synthesis, which yields QDs with size-dependent absorption and fluorescence emission [70]. The QDs with several different wavelengths can be excited with a single wavelength, and thus are suitable for multiplex detection within a single experiment. The unique optical properties of QDs for *in vivo* optical imaging include high quantum yield (QY), narrow emission bands, large Stokes shifts, high absorbency and high resistance to photobleaching [53]. These novel electronic, optical, magnetic and structural properties make them

quite different from those of bulk materials [71]. So they can be utilized as contrast agents for optical imaging, particularly for deep tissue imaging.

Single QDs can be monitored and tracked over an extended period of time with confocal microscopy [72], total internal reflection microscopy [73], or basic wide-field epi-fluorescence microscopy [74, 75]. It has been tested in most biotechnological applications that use fluorescence over the past few years especially in the field of *in vivo* imaging [70, 76, 77]. Larson *et al.* [78] have demonstrated the application of two photon excitation confocal microscopy to image blood vessels in live mice. They imaged QDs (～1μM) and fluorescein isothiocyanate (FITC) (～40μM) at the same depth (～100μm the deep). The comparison shows that the organic dyes need five times as much input power and show considerably less detail.

To illustrate the potential of NIR and far-red fluorescent proteins for whole-body imaging techniques, polyurethane mouse phantoms have been used [79, 80, 81].

The developments of fluorescent dyes reported are mostly characterized by the improvement in brightness and imaging depth, where NIR probes have a clear advantage. However, little literature has evaluated the NIR and visible dyes regarding the spatial resolution they provide.

2.4.2 Fluorescence lifetime imaging microscopy

Fluorescence lifetime, the average decay time of a fluorescence molecule's excited state is a quantitative signature which can be used to probe structure and dynamics at micro- and nano- scales [82].

The temporal decay of fluorescence probes can be expressed as an exponential decay probability function [83],

$$P_{Decay}(t) = e^{-t/\tau}, \quad t > 0 \qquad 2\text{-}8$$

where t is time and τ is the excited state lifetime.

More complex fluorophores can be described by using a multiple exponential probability density function,

$$P_{Multi-Decay}(t) = \sum_{i=1}^{N} \alpha_i P_{\tau_i}(t) \ , \ \ t > 0 \qquad 2\text{-}9$$

where *t* is time, τ_i is the lifetime of each component and α_i is the relative contribution of each component.

Fluorescence spectroscopy is emerging as a powerful biological diagnostic and imaging probe for highly scattering media, which is applied in detecting and localizing heterogeneities like hematomas and tumours in tissue [53]. However, due to the overlapped fluorescence emission spectra, fluorescence intensity and many intrinsic and extrinsic variables, it has potential difficulties in data acquisition and analysis within *in vivo* research. To overcome these problems, advanced optical algorithms and experimental systems have been developed [53]. Fluorescence lifetime imaging microscopy (FLIM) is considered to be a complementary method to fluorescence emission *in vivo* studies. Similar to fluorescence emission, the lifetime is an important reflection of a species' constitution and surroundings, and typically occurs within 1-100ns [84]. It is sensitive to tissue environment, independent of excitation light and less affected by photobleaching [85], excitation intensity [86] and light scattering [87].

The studies of fluorescence lifetime (FLT) reconstruction have a long history. The first presence of multiple fluorescence emissions was made by Dushinsky [88] in 1933, and the determination of FLT by phase shift techniques goes back to Bailey and Rollefson [89] in 1953. The excitation and fluorescent signals were detected by two photomultiplier tubes and fed into two similar phase shifting networks which consisted of two cathode followers and one calibrated circuit. Breuvich *et al.* [90] then reported an experimental model of lifetime extraction by phase shift. Several years later, an instrument designed for the measurement of fluorescence decay times was reported by Birks and Dyson [91]. The instrument includes a modulated hydrogen discharge lamp, photomultiplier tube and a phase sensitive detector circuit. Spencer and Weber

[92] demonstrated a fluorometer based on a pulse method to measure sub-nanosecond lifetime.

The theoretical basis of those fluoremeters is the relationship between phase shift and lifetime in frequency-domain (FD). Besides, several algorithms of deconvolving fluorescence decay curves have been developed. Grinvald and Steinberg [93] applied the least squares algorithm to find out the best fit of decay rate, and this method has been experimentally validated by Easter *et al.* [94]. Another method relied on the moments of the decay curve was first formulated by Bay [95] in 1950. Based on this algorithm, Brody [96] developed an instrument to measure the single exponential decay lifetime. O'Connor *et al.* [97] presented and compared six possible methods of deconvolving fluorescence decay curves. All methods are tested with real data for which the decay times were known. They draw a conclusion that least-squares technique is recommended as the technique of preference for the analysis of simple decay laws, as it can be used with no loss in accuracy, to fit any chosen section of the decay curve. But this method is not applicable in multi-exponential decay deconvolution.

The instruments stated above are mainly based on the analogue circuits which are simple and robust [83]. Fluorometers and frequency domain techniques were not commonly applied until the early 1980s. The first useful frequency domain phase fluorometer was described by Gratton and Limkeman [98], which is based on the cross-correlation technique and can operate over the frequency range 1-160 MHz. It is considered as the basis of commercially available instruments. Thereafter, Lakowicz and Maliwal [99] presented another fluoremeter, which is similar but extended the range of phase and modulation measurements from 1 to 200 MHz. Mature algorithms of FLT extraction has been presented by Lakowicz [82] in both time-domain (TD) and frequency-domain. The specific principle is described in detail in Chapter 4.

The FLIT was first developed in frequency domain by Theodorus *et al.* [100]. They demonstrated the fluorescence lifetime image obtained by applying a fluorescence microscope along with a charge-coupled devices (CCD) camera. Hassan *et al.* has presented a fluorescence lifetime imaging system consisting

of one single source fiber and several detection fibers, which aimed to localize tumors and monitor their progression by using specific fluorescent probes (Alexa Fluor 750) [101]. The combination of this lifetime imaging system with known analytic solutions for lifetime intensity distributions will make it possible to perform time-resolved lifetime imaging *in vivo* for deeply embedded targets in heavily scattering media. However, the accuracy of lifetime extraction in tissue like media is still a problem due to the scattering effect. Current algorithms [102, 103] are only applicable for non-scattering or weakly scattering conditions. A novel technique for lifetime extraction in heavily scattering medium developed based on the mechanism of ultrasound modulated fluorescence will be discussed in Chapter 4.

2.4.3 Simulations

Simple analytical models were developed to extract the fluorophore concentrations from fluorescence measurements of tissue in the early 1990s [104, 105, 106], but most were designed to calculate the emitted fluorescence under assumptions, *e.g.*, the fluorophore is homogeneously distributed in the tissue. Models cannot provide accurate predictions when the assumptions are not fulfilled.

Another, more general approach to extract the fluorescence information is to measure the optical properties of the tissue itself and correct the emission results accordingly by using a theoretical model for light transport in tissue. Such models are reported in the literature [107, 108]. However, they are all derived for restricted geometries, *e.g.*, a homogeneous semi-infinite medium.

The Monte Carlo method is therefore considered to be the favorable approach in modeling fluorescence imaging for its ability to handle complex geometries without restrictions in optical properties, which is not possible for analytical models.

The Monte Carlo fluorescence imaging model was firstly reported by Welch *et al.* [109 , 110]. They presented a model with uniformly distributed fluorescence in a semi-infinite medium and assumed that when an excitation photon is absorbed it gets a chance to regenerate a photon at the emission

wavelength. The probability depends on the QY of the fluorophore. The fluorescence photon propagates until absorbed or escaped from the medium. At the point of creation, the start direction is assumed to be isotropic.

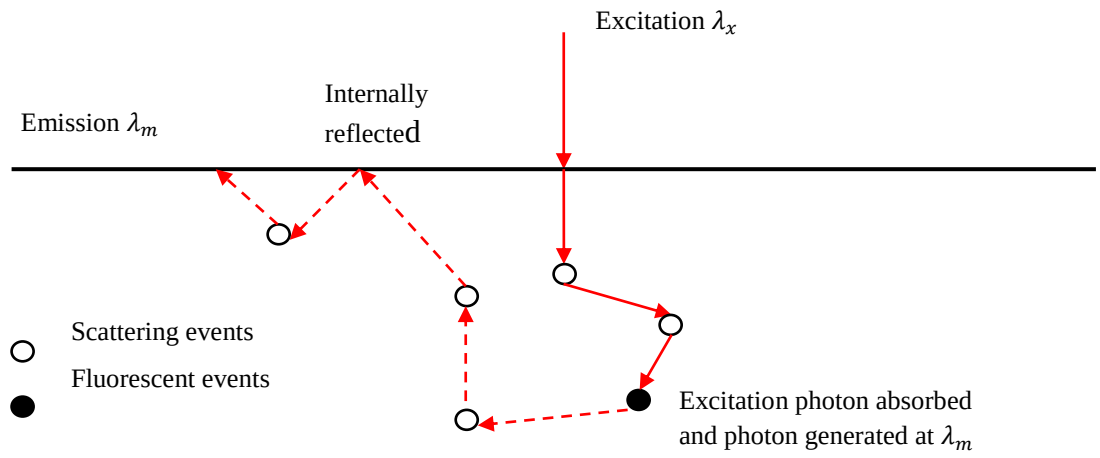

Figure 2-2 Random walk of Monte Carlo simulation for fluorescence. The solid line represents a path of an excitation photon and the dotted line is a path of emission photon

Following the concepts outlined by Welch, Swartling *et al.* [111] developed two more efficient models and compared these with the standard model in terms of accuracy, signal-to-noise statistics, and simulation time. One of them, based on the symmetry properties and reverse-emission simulation approach, sets a source at the surface of the medium and records the spatial and temporal distributions of the absorbed photons, instead of launching the fluorescence photons at different positions within the medium and recording the photon fluence detected at the surface. The reverse-simulation approach avoids repeat running for each fluorescence photon position and better utilizes the photons simulated with the Monte Carlo technique. In this technique it is assumed that excitation and emission have the same μ_s and μ_a, and only applies to uniform fluorophore distribution.

The second one relies on the white Monte Carlo method [112, 113]. The idea of this approach is to run the simulation with the absorption coefficient set to zero ($\mu_a = 0$). The attenuations due to absorption are analytically scaled afterward based on the total path length, which is easily repeatable for a list of

absorption coefficients. This approach is motivated by the fact that the photon path length and scattering directions are essentially determined by the scattering coefficient and anisotropy (μ_s and g) only, while the μ_a generally determines the survival probability of each photon travelling step. This approach can be applied in every Monte Carlo simulation associated with the transportation of light within scattering medium, and is especially useful in simulating different emission wavelengths, fluorophore concentrations, and background absorptions. Similarly, the same μ_s for excitation and emission is assumed in this approach.

S. Jacques [114] presented another model with uniformly distributed fluorescence. To make the model more efficient, the excitation and emission stage can run separately. The medium has been divided into lots of bins, and at the excitation stage, photons absorbed by each bin are recorded. At the emission stage, each bin has an opportunity to become an isotropic fluorescent source, and the intensity depends on the amount of excitation photons absorbed. This model is efficient in the simulation of uniformly distributed fluorescence as the excitation and emission stages can run in parallel, but it is not applicable for localized fluorophores with finite size.

2.4.4 Application of fluorescence imaging

The development of fluorescence imaging from nano- scale to whole-body makes it widely used in pre-clinical studies of disease progression and pathology [52]. The most common application and experiment reported is brain tumors imaging in mice [115-117]. Magnetic resonance imaging (MRI) and co-registered fluorescence tomography (FT) were applied to trace and quantify cathepsin B activity in tumors [115, 116], and Gibbs-Strauss *et al.* reported the detection has been improved by using PpIX fluorophore compared to standard MRI [117].

Fluorescence imaging also plays a significant role in the diagnosis of cardiovascular disease. One of the most essential pathogenic processes in cardiovascular disease is atherosclerosis, which causes vasculature plaque formation, and can lead to tissue infarction and even death if severe enough. *In*

vivo fluorescence imaging offers the opportunity to probe the atherosclerosis state [118].

At the gastrointestinal level, fluorescence whole-body imaging has focused mostly on the better ways to image. The vascular volume fraction (VVF) has been quantified by Montet *et al.* [119] with FT in an orthotopic colon cancer model and an ectopic tumor model. Von Burstin *et al.* presented a fluorescence system with high sensitivity to detect pancreatic cancer at an early stage using protease-activatable NIR fluorescent probes [120].

Another application is disease diagnosis of the respiratory system especially on the lung tumor imaging and airway inflammation. Koenig *et al.* has presented a tomography system model to image a mouse lung tumor [121] in which fluorescent probes were reliably used to assess disease progression.

The applications of fluorescence imaging in musculoskeletal processes are encouraging as well. In one study, Kozloff *et al.* reported that a far-red fluorescent probe binding mineral may function as a suitable local biomarker to image active bone formation and bone resorption as well as quiescent bone [122]. A similar study has been demonstrated by Zaheer et al. [123] that FT was used to image the complete growing skeleton and corresponding osteoblastic activity with a bisphosphonate-conjugated NIR fluorescent probe.

To summarize, the emphasis of fluorescent imaging research today is on the development of advanced imaging probes and *in vivo* imaging system design. The research on fluorescence lifetime imaging systems has a bright future but it is still limited by its high cost. Some fluorescent light transportation models have been published [109, 114], but mostly focus on the uniform fluorophore distribution which is more like auto-fluorescence than an artificial probe. The modeling of fluorescent imaging system especially the scanning imaging system is still a gap.

2.5 Combination of fluorescence and USMOT modelling

The combination of USMOT and fluorescence imaging is a new subject and needs to be explored in depth. The possibility of this combination has been first proposed and demonstrated by Kobayashi *et al.* [124, 125]. By scanning the ultrasonic beam and measuring the modulated fluorescence signal, a map of fluorophore concentration in the turbid medium can be acquired even within heavily scattering medium. Based on their experimental results, two underlying mechanisms of fluorescence modulation have then been proposed by Yuan *et al.* [126].

They suggested that the density of fluorophore concentration is oscillated following the ultrasound pressure, which is founded on the fact that the modulation strength is highly related to the local fluorophore concentration. With the condition that the concentrations of fluorophore are high or quenchers are adopted, the second mechanism is suggested that the quenching efficiency is modulated due to the oscillation of the microsphere volume caused by the ultrasonic field.

As the ultrasound modulated fluorescence signal is too weak to observe, microbubbles are applied by Yuan *et al.* [127] as enhancement agents. They demonstrated that the modulation efficiency is significantly improved by using microbubbles(ten times better compared to the case without microbubble). A fluorescent tube (～1mm) embedded in a turbid medium with a depth of 2 cm can be clearly observed with an ultrasonic spatial resolution.

2.6 Summary

The development of ultrasound modulated optical tomography (USMOT) and fluorescence imaging especially the research on NIR probes are reviewed in this chapter.

USMOT is an imaging technique which combines the optical contrast and ultrasonic resolution. The modelling of USMOT presented in literature are mainly based on the coherent mechanisms proposed by Wang [13], and

incoherent model reported [33] is with a weakly scattering condition. The Monte Carlo model of incoherent USMOT mechanism in heavily scattering medium is still a gap. An incoherent USMOT model along with a preliminary ultrasound modulated fluorescence model are presented and discussed in Chapter 3.

Fluorescence lifetime imaging technique is an advanced technique applied to distinguish multiple fluorophores which have overlapped emission spectra. Lifetime extraction algorithms reported [102, 103] are mainly within non-scattering or weakly scattering medium, and the lifetime decay introduced by scattering is not taken into account. A novel lifetime extraction technique applied in heavily scattering medium has been investigated in Chapter 4 based on the ultrasound modulated technique.

Driven by the deep penetration, low autofluorescence and reduced scattering and absorption, the development of NIR probes and corresponding imaging systems draw many interests. It is considered as a superior imaging technique due to the high SNR, but the evaluation on spatial resolution has not been covered. Chapter 5 aims to find out the optimized imaging pairs for excitation and emission on the SNR and spatial resolution obtained.

Chapter 3

3 Ultrasound modulated Monte Carlo model

3.1 Introduction

The aim of this chapter is to present an simplified ultrasound modulated optical Monte Carlo model and investigate the effect of ultrasound on incoherent light in terms of the SNR by varying optical properties and simulation configurations. The possibility of combining this with a fluorescent imaging model is also discussed.

As stated in chapter 2, the Monte Carlo method is a numerical solution to the radiative transfer equation (RTE), which offers an accurate, but computationally intensive model of light propagation in a scattering medium. The geometry of the model is easily adapted to various applications. The Monte Carlo model of light propagation in a scattering medium is described in detail in section 3.2.

A simple and ideal model based on the equations presented by Liu *et al.* [33], is presented in section 3.3, followed by an SNR analysis in section 3.4. This model considers the variation of scattering coefficient μ_s and absorption coefficient μ_a which are the most significant factors in an incoherent USMOT model. Although simple, the approach provides an indication of the level of performance that might be expected from ultrasound modulated optical tomography in terms of spatial resolution and signal to noise ratio. This work was carried out early in the PhD studies and helped to guide research in the remainder of this thesis.

Fluorescence is an important method for providing functional imaging of tissue but is limited in its spatial resolution. USMOT is a technique that has the potential to improve spatial resolution and so there is considerable merit in combining these techniques.

An ultrasound modulated fluorescence model is presented in section 3.5 along with discussion of effects of varying the size of the fluorescent target varies. Finally conclusions follow in section 3.6.

3.2 Model description

3.2.1 Photon initialization

The Monte Carlo method begins by launching a photon into the tissue slab. Each photon is assigned a weight W, which equals unity initially and represents the photon's energy. It is injected orthogonally at a point into the tissue, which corresponds to a collimated narrow beam of photons. All the photons follow the same direction yet different path lengths up to the first scattering event.

After the photon is launched, some specular reflectance will occur during the first step if there is a mismatched boundary. The reflectance R is specified as [128][129]:

$$R = \frac{(n_1 - n_2)^2}{(n_1 + n_2)^2} \qquad 3\text{-}1$$

where n_1 and n_2 are the refractive index of outside the medium and tissue respectively.

In this simulation, an index matched boundary is assumed.

3.2.2 Generating the step size

The step size of the photon Δs is defined as the distance between scattering events, which is calculated based on a sampling of the probability distribution for a photon's mean free path, where $\Delta s \in (0\ ,\ +\infty]$.

A random variable ξ is easily obtained by applying ***ran3()***, a generator issued on the numerical recipes in the Visual C environment, which generates a random number that is uniformly distributed between 0 and 1. The period of the ***ran3()*** is 2^{55}-1 which has an overwhelming advantage over the built in random number generator ***rand()*** (2^{29}). Then, a non-decreasing function $f(\xi)$ is applied to produce a one-to-one mapping on ξ. As discussed by Prahl *et al.* [130], the step size can be generated using the probability density function;

$$\Delta s = -\ln(\xi) * MFP \qquad 3\text{-}2$$

where $-\ln(\xi)$ is the probability function, and MFP indicates the mean free path length of the step size.

The MFP is usually defined as the reciprocal of the sum of scattering coefficient μ_s and absorption coefficient μ_a [21].

$$MFP = \frac{1}{\mu_s + \mu_a} \qquad 3\text{-}3$$

However, in the situation where μ_s dominates ($\mu_s \gg \mu_a$) or a nonabsorbing medium, the MFP length can be expressed as the reciprocal of μ_s alone.

3.2.3 Moving the photon

After the step size has been specified, the photon is ready to be moved to a new position. The new coordinate position x', y', z' is updated by applying equation 3-4.

$$\begin{aligned} x' &= x + u * \Delta s \\ y' &= y + v * \Delta s \\ z' &= z + w * \Delta s \end{aligned} \qquad 3\text{-}4$$

It is convenient to describe the photon's spatial position with three Cartesian coordinates and the direction of travel with three direction cosines. *x, y, z* represents the three spatial coordinates. And *u, v, w* are the direction cosines specified by taking the cosine of the angle that the photon's direction makes with each axis.

3.2.4 Photon absorption

There are three methods to add absorption during Monte Carlo simulation. The first, and most common, was introduced by Prahl [130]. He assumed that the weight of the photon will split into two parts during each step as a photon

moves. A fraction is absorbed and the rest will continue propagating. The total attenuation coefficient μ_t is defined as, $\mu_t = \mu_s + \mu_a$.

The ratio of the attenuation depends on the absorption and attenuation coefficients:

$$\text{Fraction Absorbed} = \frac{\mu_a}{\mu_t} \tag{3-5}$$

In this case, the weight of photon will get smaller and smaller but is never fully absorbed. Therefore, if the photon weight has been sufficiently decremented after many steps such that it falls below a threshold value, a technique named roulette is applied to terminate the photon. The roulette technique gives the photon a probability m% (e.g. m = 10) of surviving with a weight of m*W. If the photon packet does not survive the roulette, the photon weight is reduced to zero and the photon is terminated.

$$W = \begin{cases} m * W & \xi \leq 1/m \\ 0 & \xi > 1/m \end{cases} \tag{3-6}$$

The second method is closer to the real situation in that no splitting of photon energy is required. The photon will either be fully absorbed within an absorption event or scatter to another place without losing any weight. During each step, the probability of an absorption event depends on the ratio of μ_a and μ_t. This method is more practical but less efficient, as a large number of simulated photons are required to produce a convincing statistical result.

The third method is the white Monte Carlo approach, which is widely applied in homogeneous media [131]. The medium is assumed to be nonabsorbing and the weight of the photon will not be decreased until the photon exits the scattering medium. Instead, the total path length within the medium and corresponding time of flight is recorded [113]. Attenuation is then added based on the Lambert-Beer's Law shown in equation 3-7.

$$I = I_o exp(-\mu_a d) \tag{3-7}$$

where I_o and I are the original and final intensity respectively, d is the photon total path length. A threshold value is defined according to the value of μ_a. If the total path length d goes beyond that threshold value, the photon is terminated. The advantage of this approach is that a range of absorption values can be applied for a single MC simulation which avoids repeated operation and makes the simulation more efficient.

The first and classic method is the one applied in this chapter. It is considered inefficient compared to the white Monte Carlo method but it can be applied in a more complex geometric configuration, which is a useful property in the modelling of an ultrasound focus.

3.2.5 Photon scattering

The scattering direction depends on the deflection angle, $\theta \in [0, \pi)$ and an azimuthal angle, $\Psi \in [0,2\pi)$. The probability distribution for the cosine of the deflection angle $cos\,\theta$ shown in equation 3-8 has been described by the scattering function that Henyey and Greenstein originally proposed for galactic scattering [132],

$$p(\cos\theta) = \frac{1-g^2}{2(1+g^2-2g\cos\theta)^{3/2}} \qquad 3\text{-}8$$

where g represents the anisotropy, $(-1 < g < 1)$. A value of 0 indicates isotropic scattering and a value of 1 indicates totally forward directed scattering. The generating function for the Henyey-Greenstein phase function is [132],

$$\cos\theta = \begin{cases} \frac{1}{2g}\left\{1+g^2-\left[\frac{1-g^2}{1+g^2-2g\xi}\right]^2\right\} & g > 0 \\ 2\xi - 1 & g = 0 \end{cases} \qquad 3\text{-}9$$

If a photon is scattered at an angle (θ, Ψ) from the direction (u, v, w) in which it is travelling, then the new direction (u', v', w') is specified by [132],

$$\begin{cases} u' = \dfrac{\sin\theta}{\sqrt{1-w^2}}(uw\cos\Psi - v\sin\Psi) + u\cos\theta \\ v' = \dfrac{\sin\theta}{\sqrt{1-w^2}}(vw\cos\Psi - u\sin\Psi) + v\cos\theta \\ w' = -\sin\theta\cos\Psi\sqrt{1-w^2} + w\cos\theta \end{cases} \quad 3\text{-}10$$

If the angle of the photon packet is too close to normal of the tissue surfaces (e.g., |w| > 0.99999), then the following formulas should be used to obtain the new direction [132].

$$\begin{cases} u' = \sin\theta\cos\Psi \\ v' = \sin\theta\sin\Psi \\ w' = \dfrac{\mathrm{w}}{|\mathrm{w}|}\cos\Psi \end{cases} \quad 3\text{-}11$$

Figure 3-1 is a flow chart of Monte Carlo program. Once launched, the photon is moved a distance Δs where it may be scattered, absorbed, propagated undisturbed or transmitted out of the tissue. The photon is repeatedly moved until it either escapes from or is absorbed by the tissue. If a photon is absorbed, the position of the absorption is recorded. This process is repeated until the desired number of photons has been propagated. Once a photon hits a boundary of the tissue, a shortened step size Δs_1 is calculated,

$$\Delta s_1 = \begin{cases} (z - z_0)/w \\ (z - z_1)/w \end{cases} \quad 3\text{-}12$$

where z_0 and z_1 are the coordinates applied in reflection and transmission respectively. The shortened step size Δs_1 is the distance between the current photon location and the boundary in the direction of the photon propagation. As a matched boundary is assumed, the photon travelling terminates at the boundary, and the remaining weight is calculated based on the distance it travelled according to the Lambert-Beer's law.

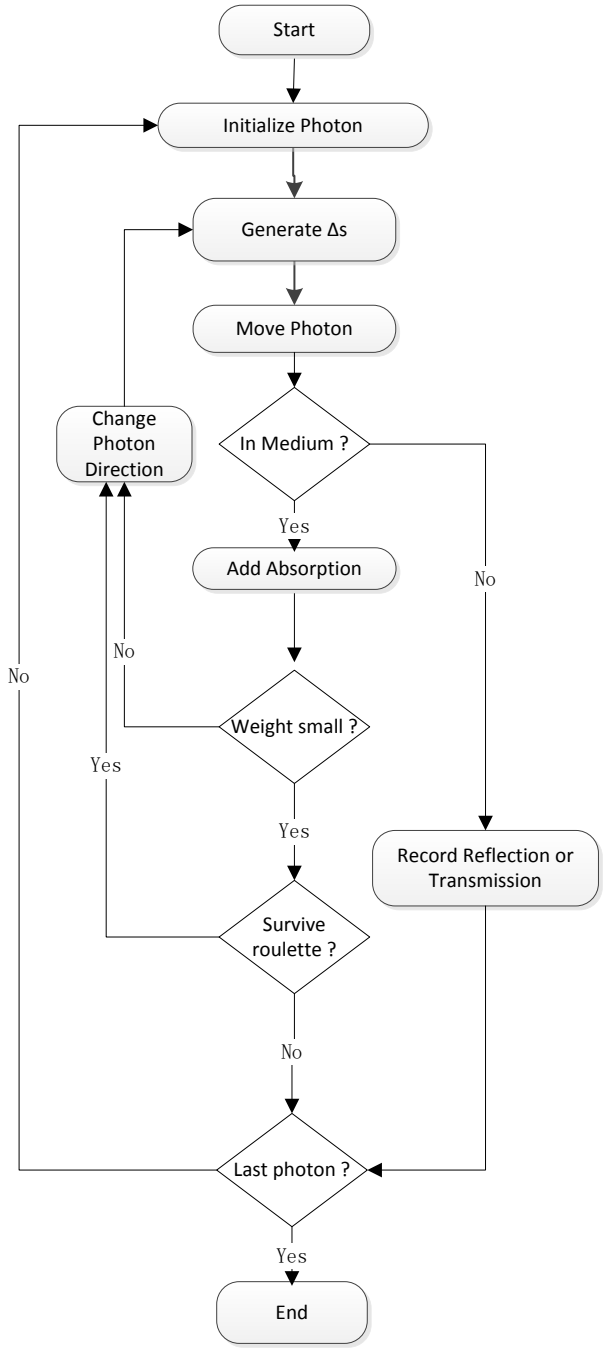

Figure 3-1 Flowchart for the Monte Carlo simulation

3.2.6 Ultrasound focus

Liu *et al.* [33] have presented an USMOT Monte Carlo model for the modulation depth and photon exit location due to the particles displacement and refractive index mismatch in which the incoherent effect has been considered. Based on the Liu's equations, a simplified version of the incoherent model is presented here. The variation in the optical properties results from the density variations of the medium caused by the ultrasound is modelled and the matched refractive index is assumed.

To model the ultrasound focus, the simplest case assumes that the ultrasound focus is a grating, which represents the heavily and weakly scattering and absorbing regions.

Further developments of the USMOT model combine it with an incoherent fluorescent model. Based on the possible mechanisms proposed by Wang [13], the incoherent effect is introduced by the compressed and rarified medium.

The grating model is simple and ideal but at an early stage in the PhD study provided a framework to better understand the potential of USMOT.

3.3 Ultrasound focus model design

3.3.1 Model setup and limitations

Practically, as stated by Wang [13], as an ultrasonic wave propagates in a scattering medium, the medium is compressed and rarified following the ultrasound amplitude, which changes the scattering coefficient μ_s, absorption coefficient μ_a and index of refraction *n* of the medium.

A MC model is presented here that improves the simulation of the ultrasound focus. As seen from Figure 3-2, the red and blue blocks represent the heavily and weakly scattering and absorbing regions. Each one indicates half ultrasound wavelength, and 10 periods is applied in the model of continuous ultrasound waves. The photons transmitted will be collected by a single detector with 5mm radius.

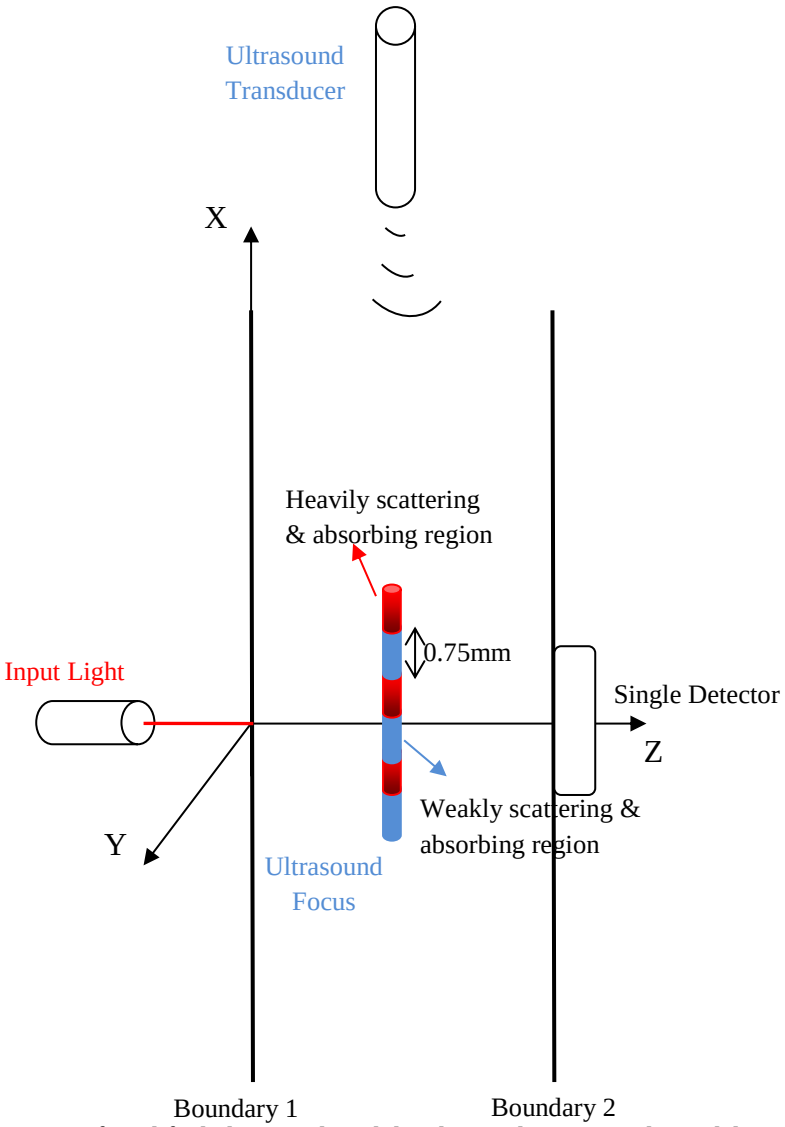

Figure 3-2 Setup of modified ultrasound modulated optical Monte Carlo model. Red and Blue blocks indicate heavily and weakly scattering and absorbing regions respectively.

To make the model more physical and comparable to the experimental set up, the next step is to evaluate the effect that ultrasound has on the scatterers and absorbers. According to the formula stated by Liu *et al.*[33]:

$$\Delta\mu_s(t) = \mu_s(1 + 0.37\eta)k_a A \sin\left(\overrightarrow{k_a} \cdot \vec{r_j} - \omega_a t\right)$$

$$\Delta\mu_a(t) = \mu_a k_a A \sin\left(\overrightarrow{k_a} \cdot \vec{r_j} - \omega_a t\right) \quad \text{3-13}$$

where μ_s and μ_a are the scattering and absorption coefficient respectively, η is a constant related to the adiabatic piezo-optical coefficient of material, $\partial n/\partial p$, density ρ, and the acoustic velocity v_a.

$$\eta = (\partial n/\partial p)\rho v_a^2 \qquad 3\text{-}14$$

and k_a is the corresponding scalar of ultrasonic wave vector $\overrightarrow{k_a}$, A is the acoustic amplitude that refers to the amplitude of the displacement of the medium in which ultrasound propagates. It is assumed here that $k_a A \ll 1$.

Through calculation, for the case $\partial n/\partial p = 1.466 * 10^{-10}\, m^2/N$, $\rho = 1000\ kg/m^3$, $v_a = 1480\ m/s$, A = 0.1 nm, $\Delta\mu_s$ theoretically equals 11% of the background scattering coefficient and $\Delta\mu_a$= 9% μ_a. If $\mu_s = 100\ cm^{-1}$ and $\mu_a = 0.6\ cm^{-1}$

Heavily Scattering: $\mu_{s1} = \mu_s + \Delta\mu_s = 111\ cm^{-1}$

$$\mu_{a1} = \mu_a + \Delta\mu_a = 0.654\ cm^{-1}$$

Weakly Scattering: $\mu_{s2} = \mu_s - \Delta\mu_s = 89\ cm^{-1}$

$$\mu_{a2} = \mu_a - \Delta\mu_a = 0.546\ cm^{-1}$$

The ultrasound wavelength is 1.5mm and the velocity of ultrasound is 1480 ms^{-1} hence the frequency of the ultrasound will be

$$f = \frac{v}{\lambda} = \frac{1480 ms^{-1}}{0.15 cm} \approx 1 MHz$$

The model presented is derived based on the work presented by Liu *et al.* [33] but a more simplified one which considers the variation of scattering and absorption coefficients in a binary manner. To make the model more accurate, the μ_s and μ_a should change sinusoidally, and a mismatched boundary condition should be applied. The assumptions made here are ideal and far from real ultrasound modulation but provided insight into the basics of the approach and guided later research.

3.3.2 Results and discussion

Several Monte Carlo simulations are performed with increasing photon numbers *N* to find out when the standard deviation (SD) of photon fluence detected per photon input converges i.e. when sufficient photons have been simulated.

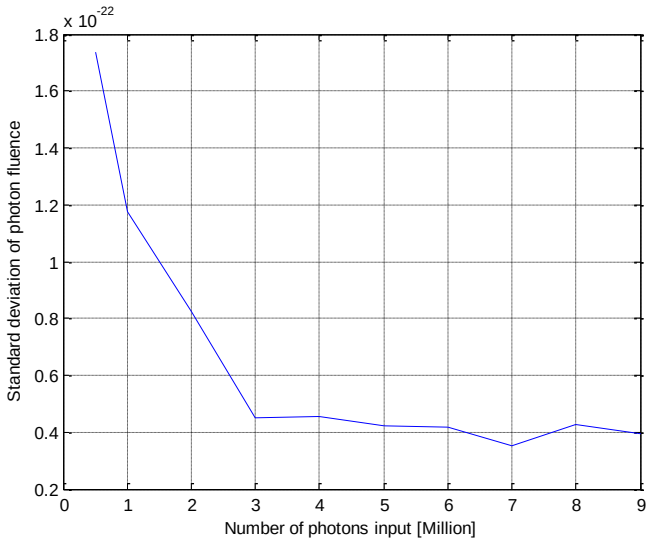

Figure 3-3 Standard deviation via number of photons input (Grating USMOT model)

Figure 3-3 shows SD of photon fluence detected against N (averaged 10 times) with 1cm slab thickness, μ_s = 100cm^{-1} and μ_a = 0.6cm^{-1}. As shown in the figure, the curve converges when the number of photons is above 3M.

The spatial light distribution obtained at boundary 2 (Figure 3-2) at different grating positions is shown in Figure 3-4. Both source and detector are fixed while the grating position is moves along the X axis from x = -0.75mm to x = 0.75mm at a step of 0.25mm which causes a series of overlapping spatial distributions. It can be further noticed from Figure 3-4 that the variation of the peak value of the distribution follows the variation of the scattering coefficient with grating position i.e. when the lowest region of lowest scattering coefficient is co-axial with the source-detector, the spatial distribution is a maximum.

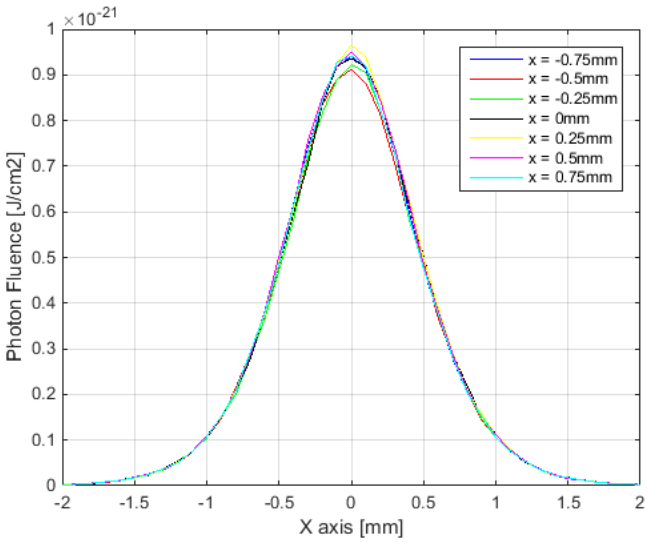

Figure 3-4 Spatial light distribution with different grating positions

Based on the results shown in Figure 3-4, the grating positions are extended to 21 points within one period, allowing the effect of a time varying grating to be simulated. The peak value of the individual spatial distribution at different grating positions is shown in Figure 3-5.

Figure 3-5 shows a sinusoidal like signal (10 times average). The X axis shows the grating position, while the Y axis indicates the photon fluence per photon input detected at each grating position.

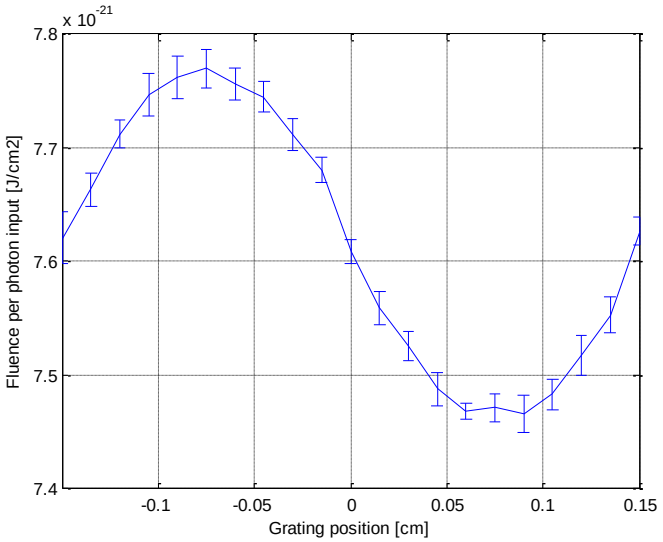

Figure 3-5 Modulated Signal obtained from moving grating model

3.4 Signal to noise ratio analysis

By applying the grating ultrasound focus model described in section 3.3, the signal detected is sinusoidal like as shown in Figure 3-5. The peak to peak value is defined as the modulated AC signal while the square root of the average DC level is treated as the shot noise. Hence, the Signal to Noise Ratio (SNR) is defined as

$$SNR_{dB} = 20 \log \frac{AC}{\sqrt{DC}} \qquad 3\text{-}15$$

Different configurations are applied and compared in terms of the SNR in the following sections.

3.4.1 Ultrasound frequency variation

As discussed previously, the light from the interaction region between the light and pulsed ultrasound will be modulated at the ultrasound frequency. It is a challenge to detect this modulated incoherent light component because of diffused light propagation and uncorrelated phases among individual speckles. Several schemes to obtain resolution along the ultrasonic axis have been explored, including an ultrasound frequency sweep [133], computer tomography [134], and tracking of ultrasound pulses [135] or short bursts [136]. The following simulation aims to investigate the effect that the ultrasound frequency has on the signal to noise ratio.

Table 3-1 SNR analysis for different ultrasound frequency(10 times average)

		Peak fluence (10^{-23}J/cm^2)	Trough fluence (10^{-23}J/cm^2)	AC fluence (10^{-23}J/cm^2)	DC fluence (10^{-23}J/cm^2)	SNR(dB)
500kHz	**Mean**	788.20	735.17	54.11	761.61	5.85
	StdDev	1.23	1.13	1.19	1.38	
1MHz	**Mean**	776.97	746.62	31.93	761.60	1.27
	StdDev	1.73	1.64	1.51	1.45	

2MHz	**Mean**	766.67	756.02	12.05	761.60	-7.20
	StdDev	1.40	1.19	1.11	1.36	

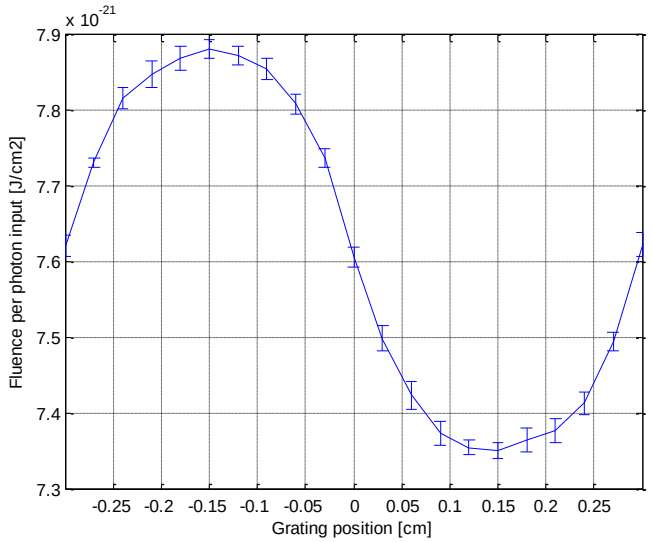

(a) AC signal at 500Hz ultrasound

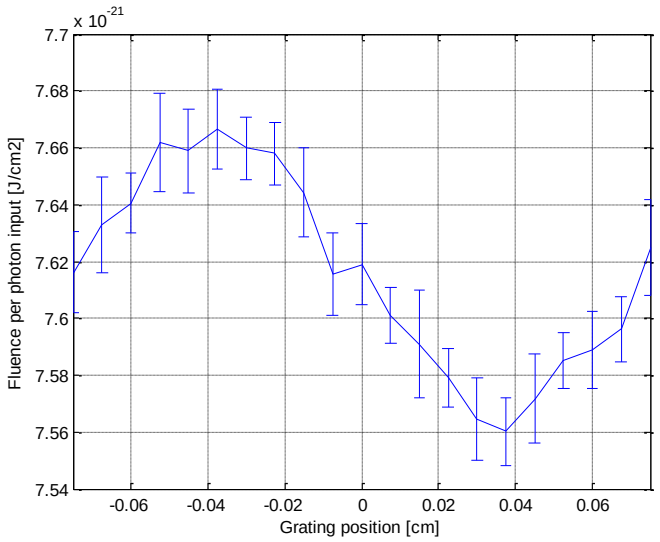

(b) AC signal at 2MHz ultrasound

Figure 3-6 AC signal detected with different ultrasound frequencies (10 times average)

Figure 3-6 shows the AC signal detected at (a) 500 kHz and (b) 2 MHz respectively, with three million photons input, μ_s = 100cm^{-1}, μ_a = 0.6cm^{-1} and the slab thickness is 1cm. At first glance, the signal is much smoother and

more stable at lower frequency, and noise has been introduced while the frequency increases due to the reduced grating period.

3.4.2 Pulsed and continuous wave simulation

The configurations applied here are comparable to the simulation in section 3.4.1 except the operation mode of ultrasound. Comparing the use of continuous and pulsed ultrasound, Wang *et al.* has presented experimental results for continuous-wave ultrasonic modulation [137]. He mentioned that the major advantage of applying continuous-wave ultrasound will be the significant increase of SNR, while pulsed ultrasound offers a better optical contrast [136]. Figure 3-7 shows in the continuous wave case in which 10 grating periods are used whereas in the pulsed wave case 3 grating periods are used.

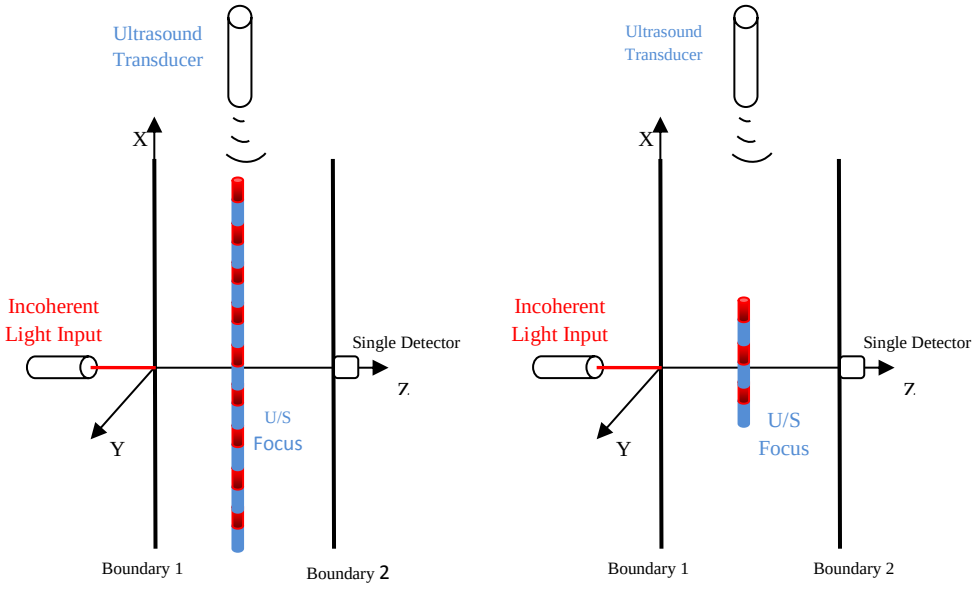

Figure 3-7 Model configuration of (a) continuous and (b) pulsed U/S

Table 3-2 shows the signal detected with a 5mm radius detector. Three million photons are input for each of the continuous and pulsed ultrasonic wave cases at μ_s = 100cm^{-1}, μ_a = 0.6cm^{-1} and the slab thickness is 1cm.

Table 3-2 SNR analysis for continuous and pulsed ultrasound wave simulation (10 times average)

		Peak fluence (10^{-23}J/cm^2)	Trough fluence (10^{-23}J/cm^2)	AC fluence (10^{-23}J/cm^2)	DC fluence (10^{-23}J/cm^2)	SNR(dB)
Continuous	**Mean**	776.97	746.62	31.93	761.60	1.27
	StdDev	1.73	1.64	1.51	1.45	
Pulsed	**Mean**	776.24	746.71	31.13	761.65	1.05
	StdDev	1.26	0.88	0.62	1.33	

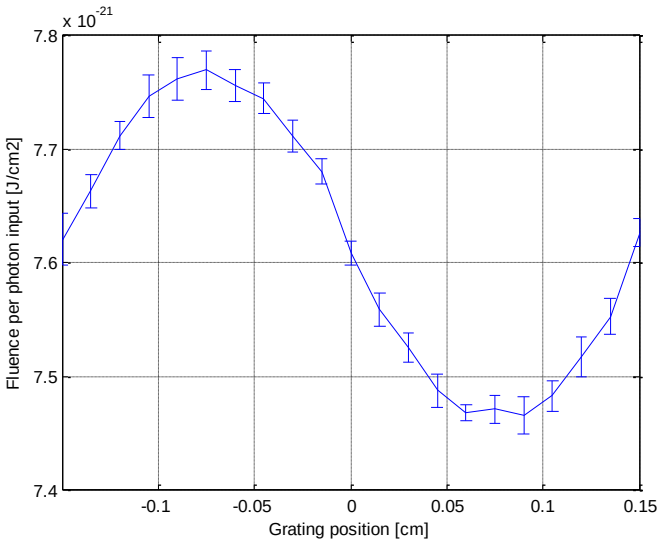

(a) AC signal with continuous ultrasound

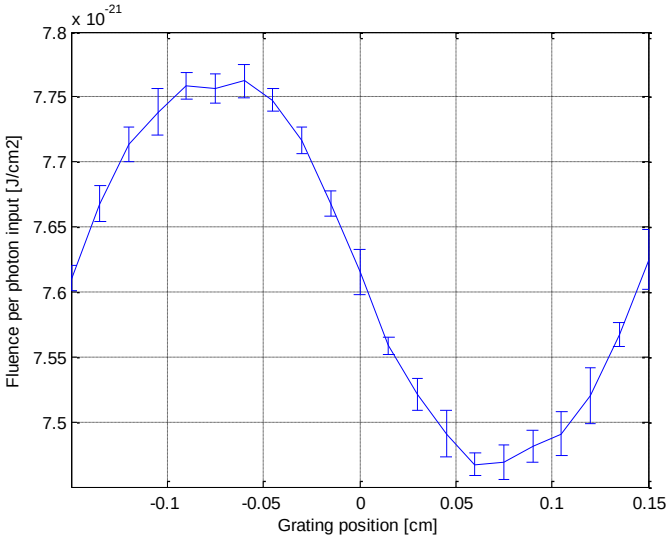

(b) AC signal with pulsed ultrasound

Figure 3-8 AC signal detected with continuous and pulsed ultrasound wave (10 times average)

Seen from the table above, while the ultrasound changes from continuous-wave to pulsed, fewer photons get modulated. The AC detected fluence slightly decreases from $31.93*10^{-23}$J to $31.13*10^{-23}$J, and the standard deviation level goes the opposite way. This leads to a 0.22dB tiny drop in SNR.

3.4.3 Scattering coefficient variation

Table 3-3 shows the SNR under different scattering coefficients with a 1MHz pulsed ultrasound modulation configuration. The μ_s of the background was changed from 60cm^{-1} to 180cm^{-1} in the simulation which is listed in the first column below (typical μ_s values of *in vivo* tissues [5]), with the μ_s within the ultrasound focus region having a 10 percent difference from it, while the μ_a was fixed at 0.2cm^{-1}.

Table 3-3 SNR analysis for different scattering coefficient (10 times average)

		Peak fluence (10^{-23}J/cm^2)	Trough fluence (10^{-23}J/cm^2)	AC fluence (10^{-23}J/cm^2)	DC fluence (10^{-23}J/cm^2)	SNR(dB)
μ_s = 180cm^{-1}	Mean	301.48	292.73	9.66	297.01	-5.03
	StdDev	0.64	0.33	0.83	0.70	
μ_s = 140cm^{-1}	Mean	466.57	450.46	17.09	458.29	-1.96
	StdDev	1.55	0.80	1.23	1.04	
μ_s = 100cm^{-1}	Mean	776.97	746.62	31.93	761.60	1.27
	StdDev	1.73	1.64	1.51	1.45	
μ_s = 60cm^{-1}	Mean	1479.35	1403.15	78.35	1441.83	6.29
	StdDev	1.86	2.09	2.31	2.41	

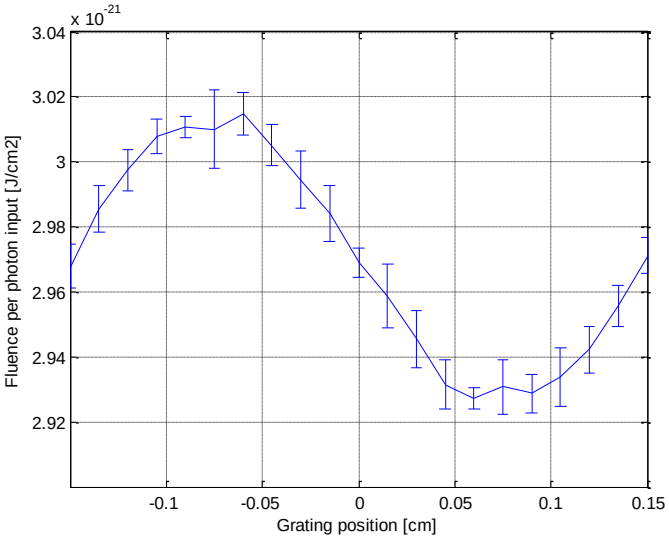

(a) μ_s = 180cm^{-1}

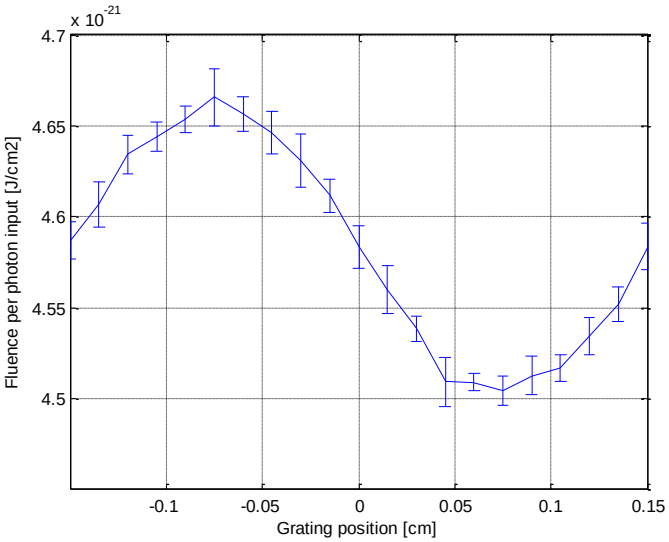

(b) μ_s = 140cm^{-1}

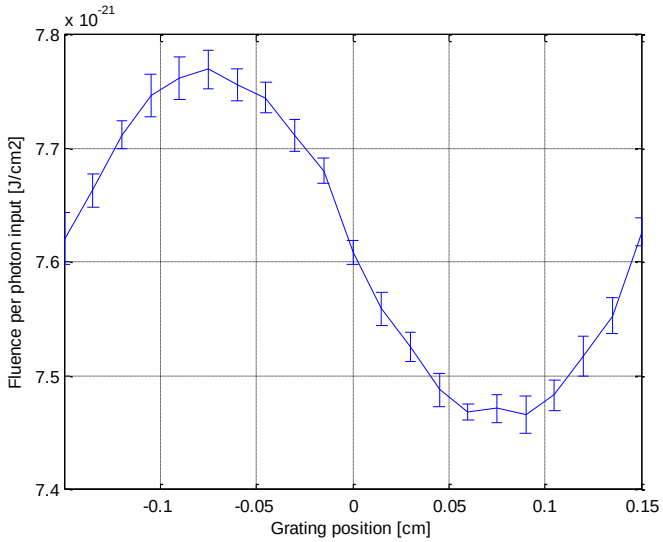

(c) μ_s= 100cm^{-1}

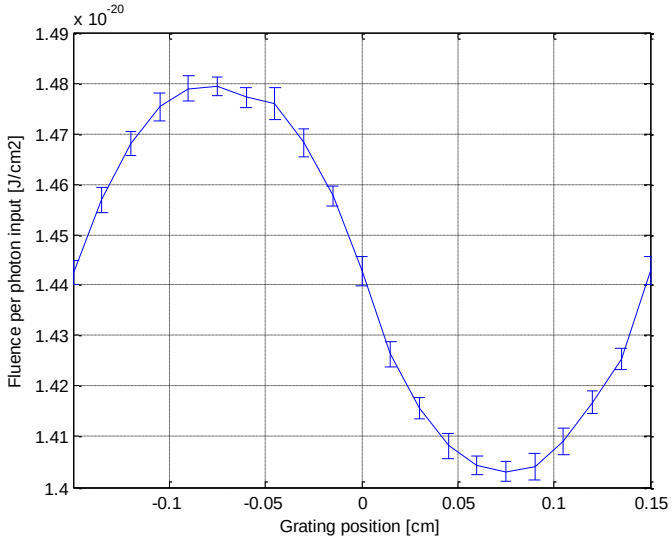

(d) μ_s = 60cm^{-1}

Figure 3-9 AC signal detected with different background scattering coefficients (10 times average)

The ratio of number of scatterers in the heavily and weakly scattered region follows the change of scattering coefficient which affects both AC and DC signals, but it has a more significant impact on the DC fluence (proportional to the shot noise level) as seen in Table 3-3. The SNR increases from -5.03dB to 6.29dB, when the μ_s drops from 140cm^{-1} to 60cm^{-1}.

3.4.4 Detector size variation

Table 3-4 SNR analysis for different detector size (10 times average)

		Peak fluence (10^{-23}J/cm^2)	Trough fluence (10^{-23}J/cm^2)	AC fluence (10^{-23}J/cm^2)	DC fluence (10^{-23}J/cm^2)	SNR(dB)
Radius = 3mm	**Mean**	361.04	345.53	16.89	353.06	-0.92
	StdDev	1.18	1.35	1.32	1.24	
Radius = 5mm	**Mean**	776.97	746.62	31.93	761.60	1.27
	StdDev	1.73	1.64	1.51	1.45	
Radius = 7mm	**Mean**	1119.97	1079.62	42.19	1099.60	2.09
	StdDev	1.01	1.41	1.19	1.56	
Radius = 10mm	**Mean**	1418.95	1370.95	50.06	1394.81	2.55
	StdDev	1.50	1.39	1.69	1.69	

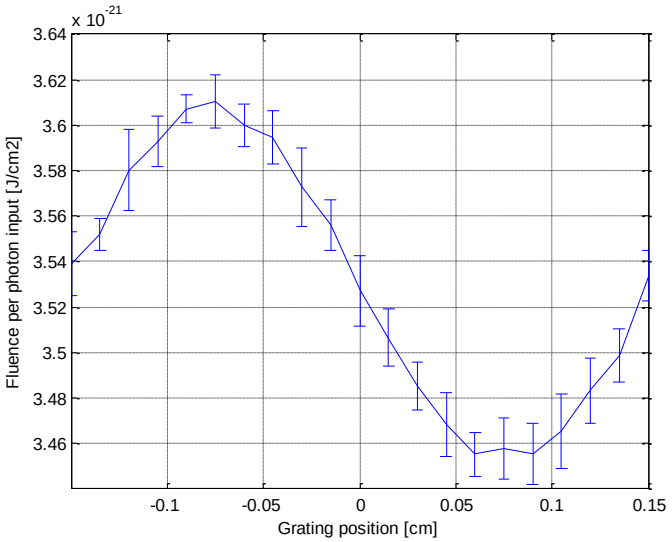

(a) Radius = 3mm

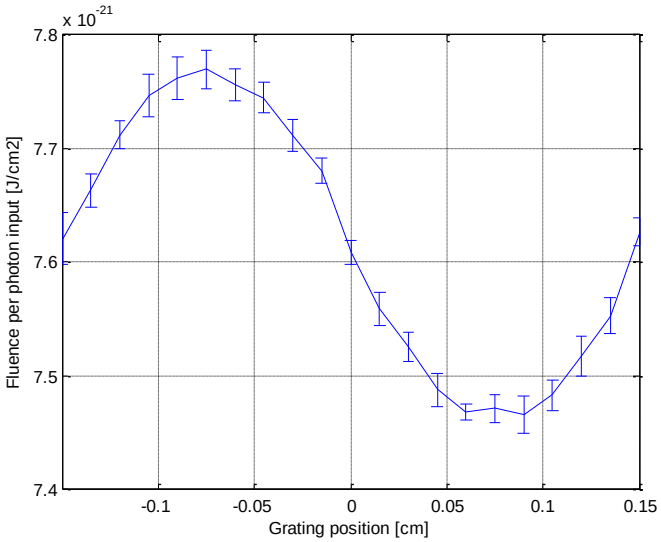

(b) Radius = 5mm

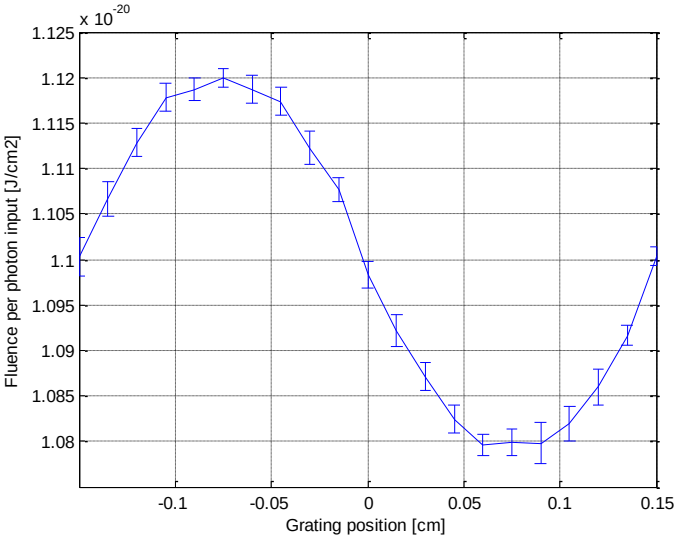

(c) Radius = 7mm

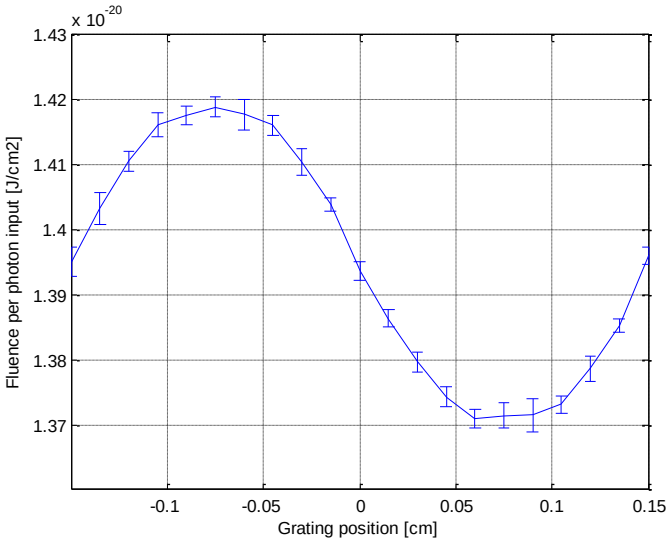

(d) Radius = 10mm

Figure 3-10 AC signal detected with different detector size (10 times average)

Table 3-4 shows the SNR using different detector sizes. When the detector size increases from 3mm to 7mm, similar results are obtained in that both AC and DC signal increase, but with the AC dominant which leads to an increase of SNR. As the detector size increases to 10mm, The SNR still goes up but with a slower rate. This can be understood as most of the transmitted photons are detected within 7 mm area, and so increasing detector size further offers no SNR improvement.

3.4.5 Discussion

Comparing Figure 3-6 (a) and (b), the increasing ultrasound frequency makes the SNR drop quickly from 5.85dB to -7.2dB. This is because the grating period becomes smaller at higher frequencies. A photon is more likely to propagate across both heavily and weakly scattering regions, which averages out the effect of the variation in optical coefficients induced by US and makes the result much noisier.

It can be seen from Table 3-2 that the SNR is slightly higher with continuous ultrasound wave. Practically, continuous-wave ultrasound forms a narrow band in the frequency domain so less noise is integrated within that range and narrow band detection like a lock-in approach can be applied to achieve a high

SNR. Because the ultrasound in the model only affects the displacement of the scatterers, the total amount of scatterers within the medium will not change. Continuous wave constructs a larger focal volume, hence there is more opportunity for a photon to become modulated. This result agrees with the conclusions of Wang *et al.* [137], but the improvement of SNR is not that prominent as only the incoherent modulation effect is considered here. The use of pulsed ultrasound wave has an advantage in terms of optical image contrast. Consider the case where an object is placed in front of the focal volume. If there is a small focal volume then it is more likely that a higher proportion of modulated light will be blocked by the object which will increase contrast.

The effect of varying optical properties within the medium is quite straightforward. Although both AC and DC signals increase with decreasing μ_s, the SNR changes approximately linearly in the opposite direction to the μ_s trend. On a macroscopic scale, it can be understood that the light spatial distribution changes more rapidly when the μ_s increases from 54cm^{-1} to 66cm^{-1} than that from 160cm^{-1} to 200cm^{-1}, as the ratio of μ_s between two ultrasound optical interaction regions and background is fixed at 11%.

The feature of varying detector size can be understood with reference to the explanation given above. A large detector collects higher AC and DC signals at the same time, but under shot noise limited condition, the more photons detected, the higher the SNR achieved.

3.5 Ultrasound modulated fluorescence model

3.5.1 Model configuration

The model is constructed based on the ultrasound modulated optical configuration. A spherical fluorescent target with variable size is introduced based on the previous model. The simulation here aims to investigate the influence on SNR of modulated fluorescent light with different radius spherical fluorescent targets. The fluorescent target is placed in the middle of the tissue slab with radius *R* and will be excited by the input normally from boundary 1 (Figure 3-11). 10 grating periods are used and the frequency of the ultrasound is 1MHz. The fluorescent light is collected with a single detector (5mm in radius) on boundary 2 of the slab, with μ_s = 60cm^{-1}, μ_a = 0.3cm^{-1} and 1cm slab thickness.

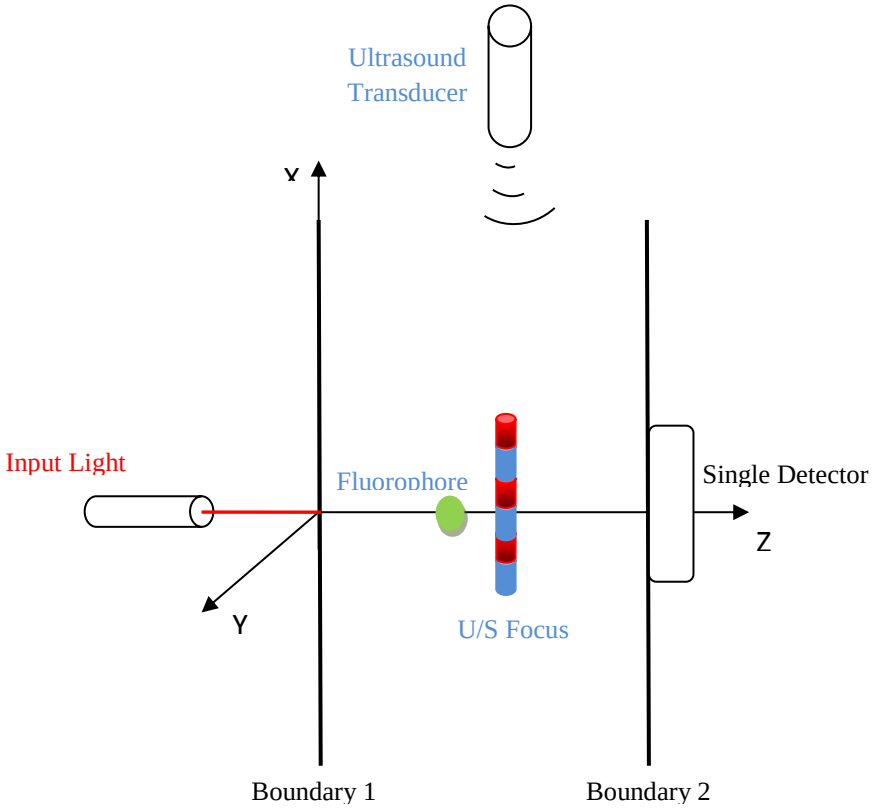

Figure 3-11 Ultrasound modulated fluorescence model setup

3.5.2 Results and discussion

To establish the required number of photons to use in the simulation, the standard deviation versus number of input photons is calculated as shown in Figure 3-12. The size of the fluorescent target is 0.5mm in radius.

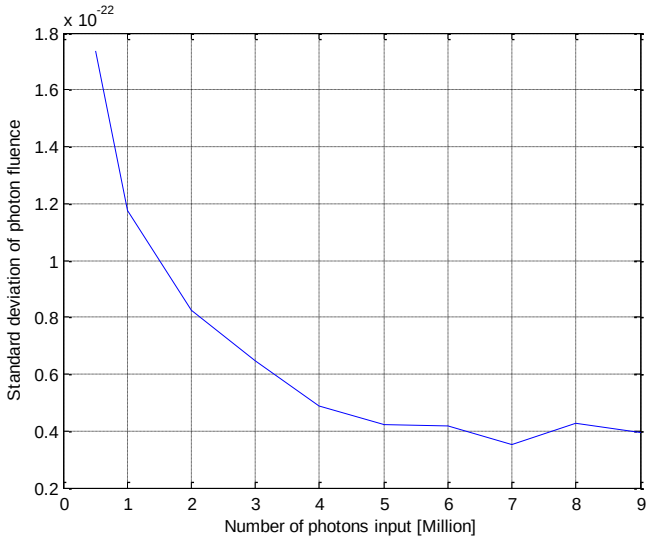

Figure 3-12 Standard deviation via number of photons input (Fluorescence model)

Five million photons are injected into the medium. The results are listed in Table 3-5 for different fluorescent target radii.

Table 3-5 SNR analysis for different fluorescent targets size (10 times average)

		Peak fluence (10^{-22}J/cm^2)	**Trough fluence** (10^{-22}J/cm^2)	**AC fluence** (10^{-22}J/cm^2)	**DC fluence** (10^{-22}J/cm^2)	**SNR(dB)**
Radius = 0.5mm	**Mean**	429.35	421.75	7.96	425.56	1.73
	StdDev	0.49	0.28	0.44	0.38	
Radius = 0.75mm	**Mean**	427.81	421.63	6.63	424.83	0.15
	StdDev	0.30	0.34	0.25	0.37	
Radius = 1.5mm	**Mean**	421.05	420.58	1.60	420.79	-12.15
	StdDev	0.47	0.52	0.30	0.40	

Radius = 2.25mm	**Mean**	415.02	413.01	2.59	414.07	-7.91
	StdDev	0.43	0.27	0.22	0.35	

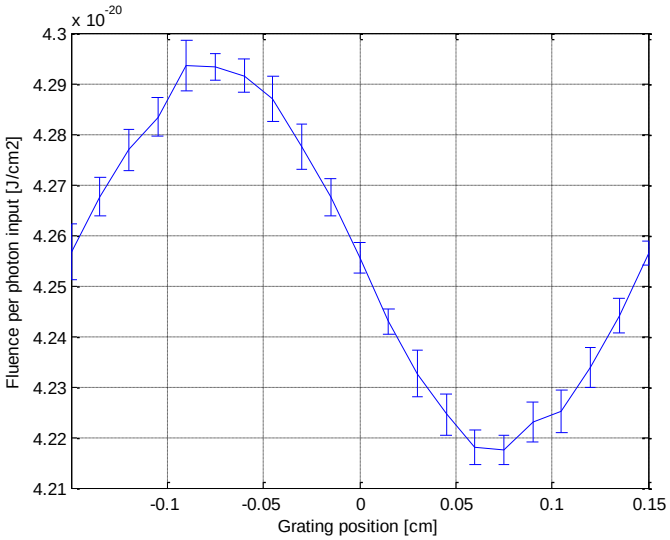

(a) Radius = 0.5mm

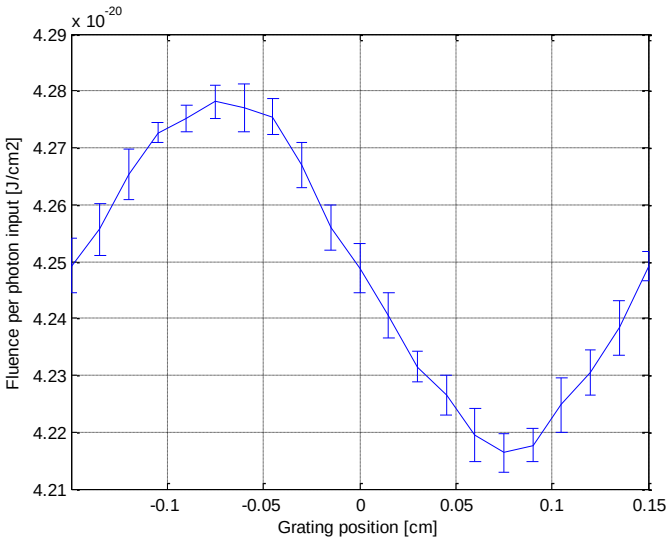

(b) Radius = 0.75mm

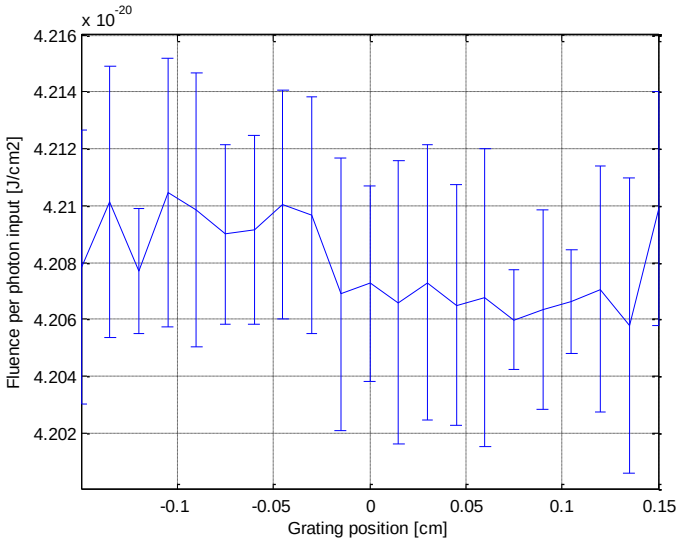

(c) Radius = 1.5mm

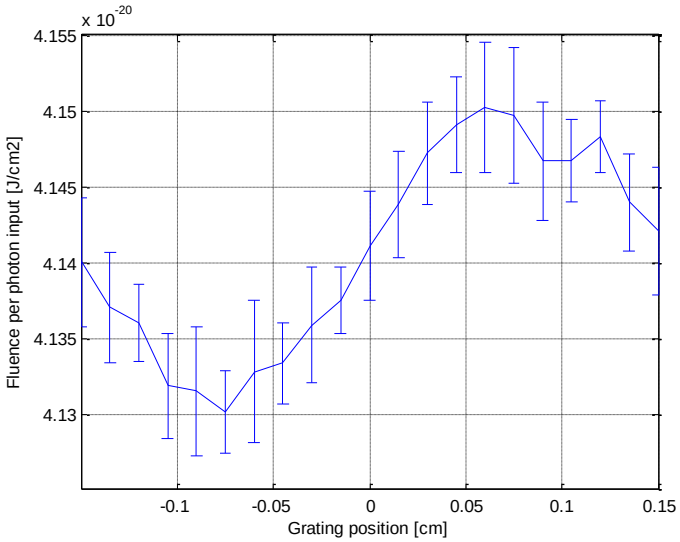

(d) Radius = 2.25mm

Figure 3-13 AC signal detected with different fluorescent target size (10 times average)

The simulation starts from the simplest case, when the light illuminates a small target embedded inside the tissue slab. The modulated fluorescent light detected has a relatively high SNR (1.73dB). As the size of the fluorescent target is increased, when the diameter equals half the ultrasound period, the SNR is lower than the previous case, but it is still easily observed from Figure 3-13(b). As the size further increases, the signal is dominated by the noise, the SNR has a worst case of -12.15dB when the fluorescent target diameter equals the ultrasound period. This is because the effects of the heavily and weakly region cancel out, no matter how the grating moves, the average signal stays

relatively constant. When the diameter of the fluorescent is further increased to 2.25mm, then the SNR increases to -7.91dB. These results show that the SNR detected for different target diameters d, can be optimised by changing the ultrasound frequency to make $f \approx c/2d$, where c is the speed of the light in the medium. This conclusion is similar to the one reached experimentally by Huynh *et al.* [138].

3.6 Conclusion

The primary aim of this chapter has been to demonstrate the Monte Carlo model and to investigate the effect on signal to noise ratio of varying the ultrasonic and optical configurations. A model which investigates the ultrasound modulated signal obtained from fluorescent targets of different radii has also been presented and some preliminary results demonstrated. Even though the models have their limitations due to many assumptions described previously some conclusion about the overall trends can be drawn.

The SNR drops rapidly down to -7.2dB when the ultrasound frequency increases from 500KHz to 2MHz (Table 3-1), it could be concluded that the incoherent effect may be difficult to observe in high frequency ultrasound-optical interactions. There is only 0.22dB difference in SNR between applying pulsed and continuous ultrasound (Table 3-2).

The scattering coefficients within the medium also have a significant effect on SNR. The high scatterer concentration dominates resulting in a low SNR, as the μ_s of the background increased from 60cm^{-1} to 180cm^{-1}, the SNR changed from 6.29dB to-5.03dB accordingly (Table 3-3). An appropriate detector size also helps to obtain a high SNR. It is clear that, the larger the detector size, the more photons that are detected. But the SNR is not proportional to the photon fluence. Seen from Table 3-4, the best SNR obtained when the detector radius is 7mm.

As a fluorescent target is added into the model, the modulated emission light excited by the laser input is detected in transmission. With fixed fluorescence concentration and increasing fluorescent target size, the SNR does not increase monotonically. The best SNR is obtained when the size of fluorescent target is equivalent to half ultrasound period, while the worst case is when the size of the target equals the ultrasound period.

In summary, the optimum system to measure incoherent effect of USMOT should include the following factors:

- Red or NIR laser with high power, which provides sufficient input energy and long wavelength needed to minimize the scattering and absorption.
- Low frequency ($\leq$ 2MHz) ultrasound transducer, scatterers follow the ultrasound oscillations and form the weakly and heavily scattering regions better in low frequency condition.
- Appropriate detector size, which optimises the SNR.

Further simulation results while combining fluorescence and ultrasound will be shown in chapter 4 with an analytical model.

Chapter 4

4 Lifetime based fluorescence optical diffusion model

4.1 Introduction

Fluorescence lifetime imaging (FLI) is a technique that provides a map of fluorescence lifetimes within tissue rather than one of the intensity of the emission light. It has been considered as an advanced technique as it overcomes problems associated with fluorophores having overlapping emission spectra. One difficulty is how to extract lifetimes with high accuracy. Current lifetime extraction algorithms [139-145] work well when the lifetime decay rate can be obtained, which is difficult in tissue due to the effects of light scattering which will be discussed in section 4.3. In Chapter 3, a basic ultrasound modulated fluorescence Monte Carlo model was presented and evaluated via its SNR. An analytical model is demonstrated in this chapter to investigate whether it is possible to extract the fluorescence lifetime in a heavily scattering medium by using ultrasound to modulate the both the fluorescence excitation and emission light and making a relative temporal measurement between the detected modulated signals. This is compared to the case where no US is applied. The possibility of this technique has been proposed by Yuan *et al.* [126] but to date this has not been investigated further.

The theoretical basis applied to extract single fluorescence lifetime is described in sections 4.2 and 4.3. Section 4.4 presents the model description and simulation results are shown in section 4.5, with discussions following in section 4.6.

4.2 Fluorescence lifetime analysis

Fluorescence lifetime analysis can be performed either in the time domain using a pulsed laser and measuring the fluorescence emission pulse using a fast detector [93], or in the frequency domain using a modulated light source at a single frequency and measuring the phase of the modulated emitted light [139]. Frequency domain fluorometry is the original approach to perform lifetime analysis, because at the time ultrashort pulsed light sources were too expensive to adopt in many laboratories. In recent years, as the price of pulsed light sources and fast detectors has reduced, time domain fluorometry has become the mainstream approach. However, at the time of conducting this

research, the Applied Optics Group at the University of Nottingham were investigating frequency domain ultrasound modulated optical tomography using CW US [50, 140]. As there was the possibility of comparing with experimental data, it was decided to model a frequency domain system. It should be noted that both approaches are equally valid for obtaining the fluorescence lifetime and are simply related by the Fourier Transform.

In frequency domain fluorometry, the sample is excited with intensity modulated light at a frequency which is comparable to the reciprocal of the lifetime [83]. Hence, the emission will be intensity modulated at the same frequency but the emission exhibits a time delay and amplitude change that are determined by the intensity decay law of the sample. The time delay is measured as a phase angle shift between the excitation and emission, as shown in Figure 4-1. The peak-to-peak amplitude of the modulated emission is decreased relative to the amplitude of the modulated excitation, which provides another independent measure of the lifetime [83].

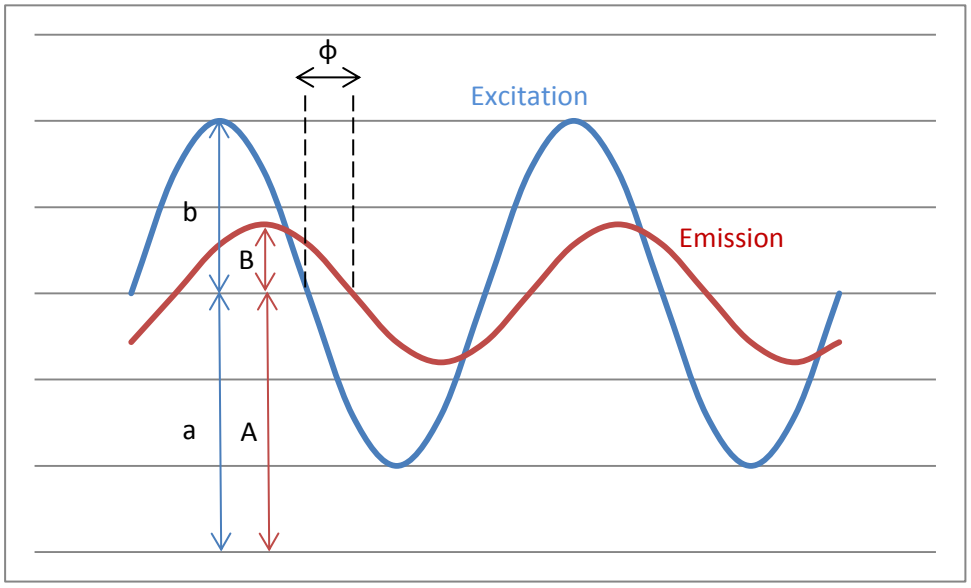

Figure 4-1 Definition of phase angle and modulation

The modulation depth *m* is defined as [82],

$$m = \frac{B/A}{b/a} \qquad 4\text{-}1$$

For a single-exponential decay, the phase and modulation are related to the decay time τ by [82]

$$m_\omega = (1 + \omega^2\tau^2)^{-1/2} \quad 4\text{-}2$$

and

$$\tan \phi_\omega = \omega\tau \quad 4\text{-}3$$

where ω is the modulation frequency of input signal.

The origin of the phase shift and demodulation can be understood by considering the time-dependent excitation intensity and the time of intensity decay of the fluorescence target.

4.3 Measuring lifetime in a heavily scattering medium

In the presence of scattering a phase shift can also be caused by the distribution of path lengths that occurs when light takes many random paths through the sample. As shown in Figure 4-2, the more scattering the medium is, the further the results deviate from the actual lifetime. The curves shown in Figure 4-2 are obtained using the model described in section 4.4 for an infinite slab geometry. In a heavily scattering medium such as human tissue, the scattering coefficient varies from 60cm^{-1} to 200cm^{-1} [5]. The measurement of fluorescence lifetime becomes difficult as the phase shift and demodulation due to the scattering is comparable to that resulting from the fluorescence decay (Figure 4-2). It is therefore important to develop techniques that can overcome or at least take into account the effects of light scattering.

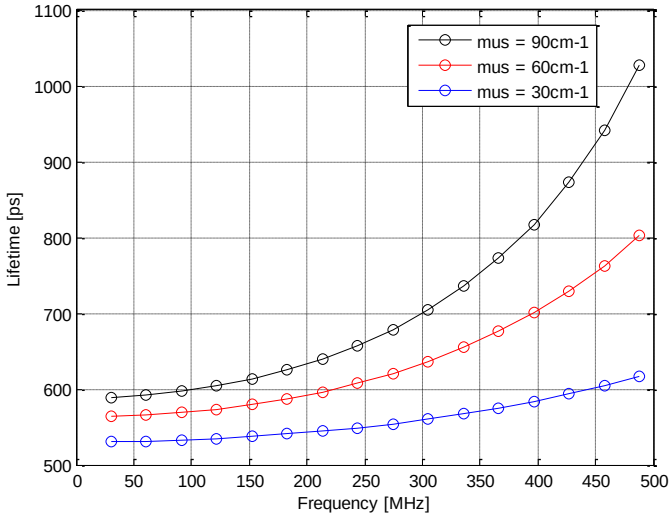

Figure 4-2 Measured lifetime at a detector for a fluorophore with a 500ps lifetime embedded at the mid-plane of a 1cm scattering infinite slab with different scattering coefficient, $\mu_{ax} =$ 0.6cm^{-1} and $\mu_{am} = 0.5$cm^{-1}

Several techniques have been introduced to measure the fluorescence lifetime in the presence of scattering. For example, Hutchinson *et al.* reported measurements of nanosecond and sub-nanosecond fluorescence lifetime in the frequency domain [102, 103], assuming that the excitation and emission light have the same optical properties. In these papers the phase shift φ_s of the transmitted light due to scattering alone are defined as the phase. In the presence of a fluorophore, the emission light detected has a phase shift φ_t caused by both lifetime and scattering. Therefore, the phase shift φ_f introduced by lifetime individually can be simply represented as,

$$\varphi_f = \varphi_t - \varphi_s \qquad 4\text{-}4$$

The scattering coefficient varies from 5cm^{-1} to 20cm^{-1}. It was reported that the reference phase cannot be measured accurately as it is impossible to remove the fluorescent target to obtain a homogenous environment.

Mayer *et al.* presented a method [139] which applied dual-wavelength photon-migration measurements to develop fluorescence properties. No reference output was given but an intensity modulated source at the emission wavelength is applied to estimate the optical parameters of the medium

containing the uniform fluorophore, as well as the fluorescence properties. However, the experiments were carried out with the scattering coefficient varying from 7.9cm^{-1} to 9.2cm^{-1} to measure a lifetime around 1ns. It is suggested that this method could be useful in estimating the fluorescence lifetime in a weakly scattering medium.

In this chapter, the method shown in Figure 4-3 is used as the standard for comparison with the ultrasound modulated approach (known as the Standard model throughout this chapter to distinguish it from the US modulated method) [102]. A modulated light source illuminates the sample and both excitation and emission wavelengths are detected. Assuming that the embedded fluorophore will not introduce significant change to the overall optical properties of the medium, the phase shift of the excitation light can be used as the reference phase, φ_r.

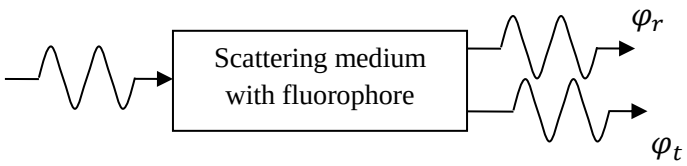

Figure 4-3 Schematic of standard lifetime extraction approach in frequency domain

Equation 4-4 can be rewritten as

$$\varphi_f = \varphi_t - \varphi_r \qquad 4\text{-}5$$

The use of ultrasound offers the opportunity to minimize the phase shift caused by scattering. This technique provides an opportunity to extract lifetime with higher accuracy than the standard approach within a heavily scattering medium. A schematic is shown in Figure 4-4. Unmodulated CW excitation light illuminates the sample. An ultrasound wave is generated along the vertical direction and, through the mechanism described by Yuan *et al.* [126], both the excitation and emission wavelengths become modulated at the frequency of the US. Recording the US modulated excitation and emission allows Equation 4-5 to be applied. There are two advantages of this approach; firstly, modulating the light within the medium rather than at the source shorten the distance between the modulated light source and the detector

which reduces the scattering effect; secondly better spatial resolution can be obtained using ultrasound modulation when compared with diffuse optical imaging.

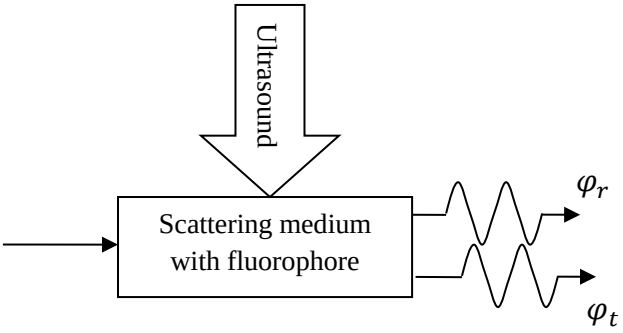

Figure 4-4 Schematic of ultrasound associated lifetime extraction approach in frequency domain. Unmodulated light illuminates the sample and modulation is provided by the US within the medium.

As described in the next section, the standard and ultrasound modulated cases can be simulated by simply placing the modulated light source at the boundary (standard) or at the position of the fluorescent target within the medium (ultrasound modulated).

4.4 Model description

As discussed in section 4.2, the time domain and frequency domain methods are simply related by a Fourier transform relationship but that due to experimental constraints it was of interest to investigate the frequency domain case. According to the superposition principle, for all linear systems, the response at a given place and time caused by two or more stimuli is the sum of the responses which caused each stimulus individually [141].

$$F(x_1 + x_2 + \cdots) = F(x_1) + F(x_2) + \cdots \quad \text{4-6}$$

Therefore, a pulsed light input is applied in the model described in this chapter which represents the superposition of an infinite number of sinusoids. Due to the superposition principle, each of these sinusoids can be analysed separately and the response to a range of modulation frequencies can be computed.

The propagation of light in a heavily scattering medium is most accurately described by the radiative transfer equation. However analytical solutions only exist for simple geometries and Monte Carlo simulations (Chapter 3) are usually applied to provide a numerical solution. A widely used approximation to the radiative transfer equation is the diffusion approximation.

The specific intensity of the radiance can be assumed to be isotropic and can be approximated with the first two orders of the Taylor's expansion as discussed in the Appendix.

$$L(\vec{r}, \hat{s}, t) = \frac{1}{4\pi}\Phi(\vec{r}, t) + \frac{3}{4\pi}\vec{J}(\vec{r}, t) \cdot \hat{s} \quad \text{4-7}$$

where $L(\vec{r}, \hat{s}, t)$ is the radiance which can be defined as energy flow per unit normal area per unit solid angle per unit time, $\Phi(\vec{r}, t)$ is the fluence rate and $\vec{J}(\vec{r}, t)$ is the fluence flux vector.

The basis of the model is illustrated in Figure 4-5 which has been previously demonstrated by Wilson *et al.* [142]. A collimated pulsed light beam illuminates normally into a homogeneous infinite tissue slab. The illumination can be approximated by an isotropic point source that is situated a distance of

one transport mean free path $(1/\mu_s')$ away from the boundary within the medium. A negative image source is placed outside the medium at an equal distance to the original source to satisfy a boundary condition $\Phi = 0$ as discussed by Wilson *et al.* [142]. To satisfy this boundary condition at both boundaries, an infinite series of dipole photon sources needs to be added.

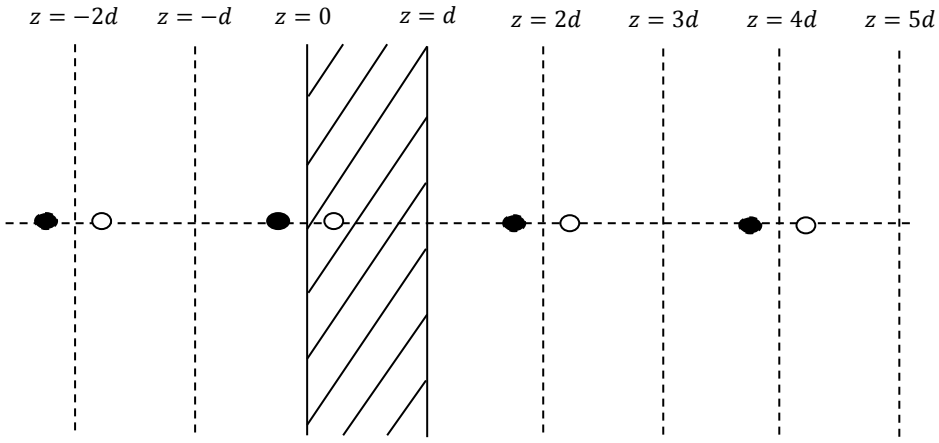

Figure 4-5 Geometry for a homogeneous slab. Boundary conditions can be met by adding an infinite series of dipole photon sources. Four of them are shown in the figure.

As the fluence rate at the boundary tends to zero, the radiance at the boundary will be estimated by the fluence flux. The number of photons transmitted per unit area per unit time can be calculated from Fick's law,

$$J(\rho, d, t) = -D\nabla\Phi(\rho, z, t)|_{z=d} \qquad 4\text{-}8$$

The fluence rate per incident photon at any position within the medium can be calculated based on the Green's function [143].

$$\Phi(\rho, z, t) = c(4\pi Dct)^{-3/2} exp\left(-\mu_a ct - \frac{\rho^2}{4Dct}\right)\left\{\sum_{m=-\infty}^{m=+\infty} exp\left[-\frac{(z - 2md - z_0)^2}{4Dct}\right] - \sum_{m=-\infty}^{m=+\infty} exp\left[-\frac{(z - 2md + z_0)^2}{4Dct}\right]\right\} \qquad 4\text{-}9$$

where c is the speed of the light in the tissue, t is time, z_0 is the position of point isotropic light source, z and ρ represents the distance from the point of interest to the incident point in the radial and depth directions respectively and D is the diffusion coefficient,

$$D = \frac{1}{\mu_a + (1-g)\mu_s} \tag{4-10}$$

μ_a is the absorption coefficient, μ_s is the scattering coefficient and g is the anisotropy factor.

The photon intensity transmitted at the boundary can be calculated from the flux;

$$T(\rho, d, t) = (DC)^{-3/2}(4\pi t)^{-5/2} exp\left(-\mu_a ct - \frac{\rho^2}{4Dct}\right)\left\{\sum_{m=-\infty}^{m=+\infty} exp\left[-\frac{(d-2md-z_0)^2}{4Dct}\right] - \sum_{m=-\infty}^{m=+\infty} exp\left[-\frac{(d-2md+z_0)^2}{4Dct}\right]\right\} \tag{4-11}$$

In the simulations, the number of dipoles needs to be truncated. Several values of m have been tested to work out the convergence of Transmittance. The results turn up to be no difference between 7 dipoles and 21 dipoles. For the scattering medium properties typically used in this chapter, m is set to 3, which means 7 dipoles will be added.

4.4.1 Standard configuration fluorescence lifetime model

In the Standard configuration (Figure 4-3) modulated light illuminates the sample and both excitation and emission light are measured at the detector plane. It is assumed that a fluorescent target lies on an intermediate plane within the sample.

To calculate the excitation light intensity arriving at the detector plane simply involves applying the Green's function for the Transmittance (Equation 4-11) which propagates the light from the source to the detector plane. Figure 4-6 (a) shows the geometry for calculating the transmitted light in the Standard configuration (2 dipoles shown).

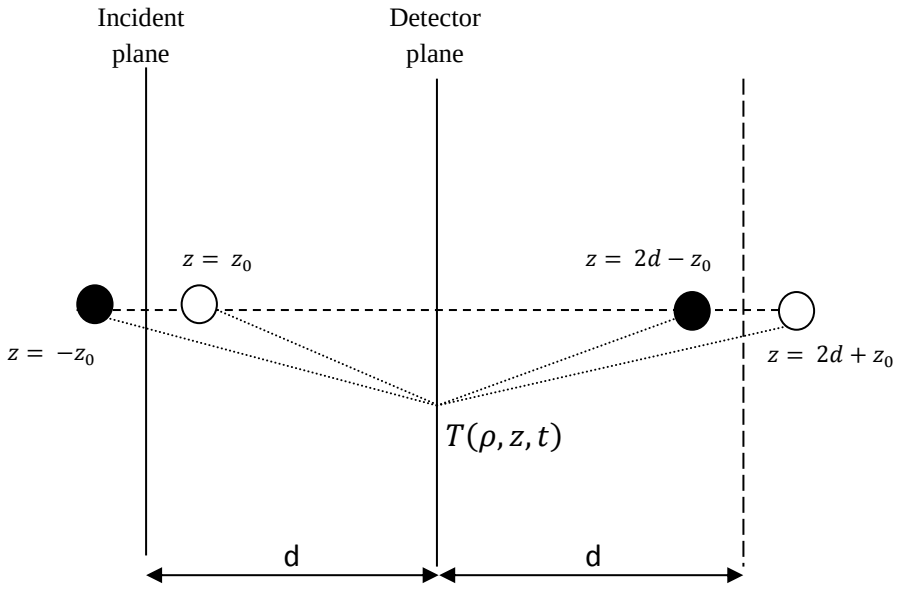

(a)

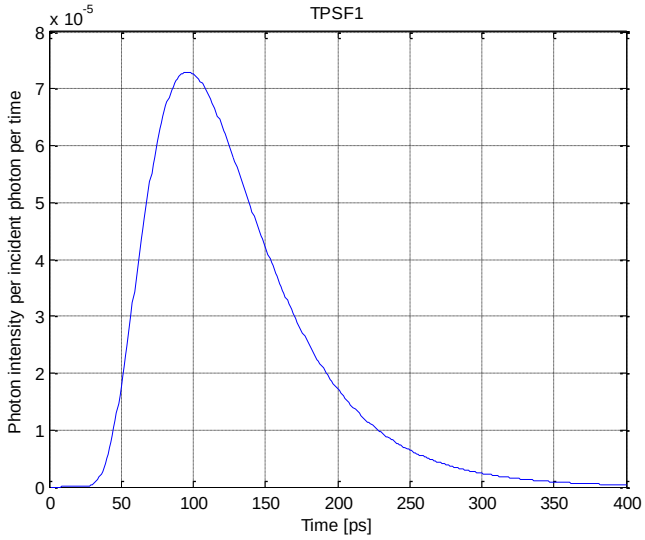

(b)

Figure 4-6 (a) Diffusion model geometry of excitation in the standard configuration seven dipole sources are applied, two of them are shown in the figure; (b) TPSF of Standard model excitation (TPSF1)

The flux detected per unit incident photon per unit time of each point at the detector plane can be plotted as a temporal point spread function (TPSF). An example is shown in Figure 4-6 (b) for position ($\rho = 0.4$) at the detector plane.

To calculate the fluorescence emission in the Standard configuration involves propagating the incident excitation light from the source to an intermediate plane where the fluorescent target lies and then propagating the fluorescence emission light from the fluorescent target plane to the detector plane.

For a fluorescent target situated at z = d/2, the excitation light entering the target plane can be obtained from the fluence rate Equation 4-9;

$$\Phi_{Ex}(\rho, d/2, t) = c(4\pi Dct)^{-3/2} exp\left(-\mu_a ct - \frac{\rho^2}{4Dct}\right)\left\{\sum_{m=-\infty}^{m=+\infty} exp\left[-\frac{(d/2 - 2md - z_0)^2}{4Dct}\right] - \sum_{m=-\infty}^{m=+\infty} exp\left[-\frac{(d/2 - 2md + z_0)^2}{4Dct}\right]\right\} \quad 4\text{-}12$$

Figure 4-7 (a) shows an example where the fluorescent target is situated at z = d/2. Figure 4-7 (b) shows the TPSF of excitation light entering the fluorescence target plane. The quantum efficiency (QE) of the fluorescence target equals 40% which is a typical value among well-known fluorophores [144].

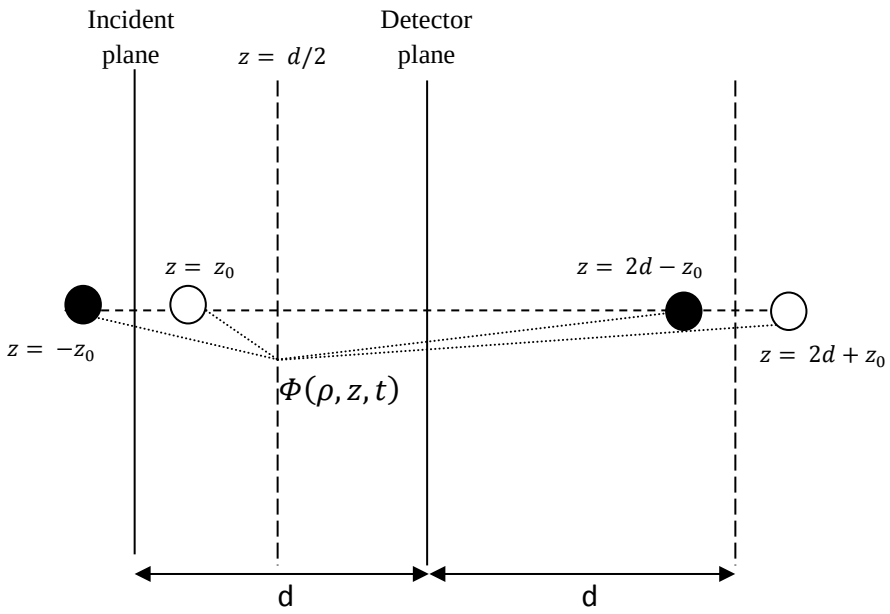

(a)

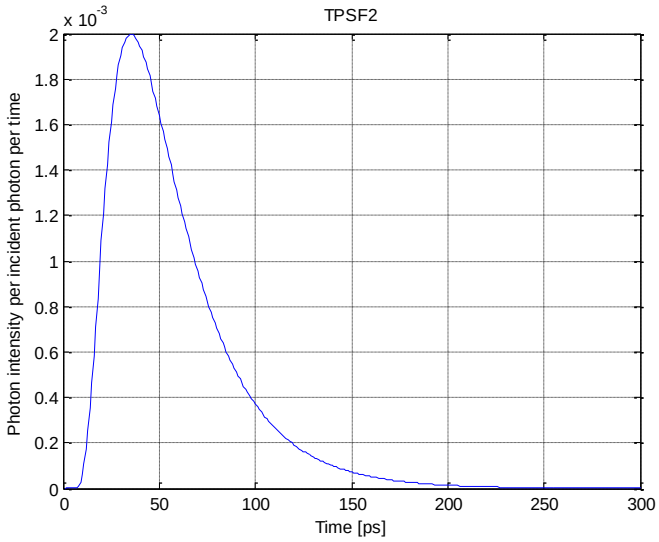

(b)

Figure 4-7 (a) Diffusion model geometry of excitation light entering the fluorescence target intermediate plane, seven dipole sources applied, two of them are shown in the figure; (b) TPSF of excitation light entering the fluorescence target (TPSF2)

For calculating the fluorescence emission light at the detector plane, it is necessary to use the Transmittance Equation Equation 4-11, which takes into account the $\Phi = 0$ boundary condition. For the fluorescence source position at the midplane of the slab, $z_0 = d/2$;

$$T_{Em}(\rho,d,t) = (4\pi D_m C)^{-3/2} t^{-5/2} exp\left(-\mu_a ct - \frac{\rho^2}{4Dct}\right)\left\{\sum_{m=-\infty}^{m=+\infty} exp\left[-\frac{(d/2-2md)^2}{4Dct}\right] - \sum_{m=-\infty}^{m=+\infty} exp\left[-\frac{(3d/2-2md)^2}{4Dct}\right]\right\} \quad 4\text{-}13$$

Figure 4-8 (a) shows the geometry for calculation of emission light transmitted. The light emitted from the fluorescence target that reaches the detector plane is presented in Figure 4-8 (b).

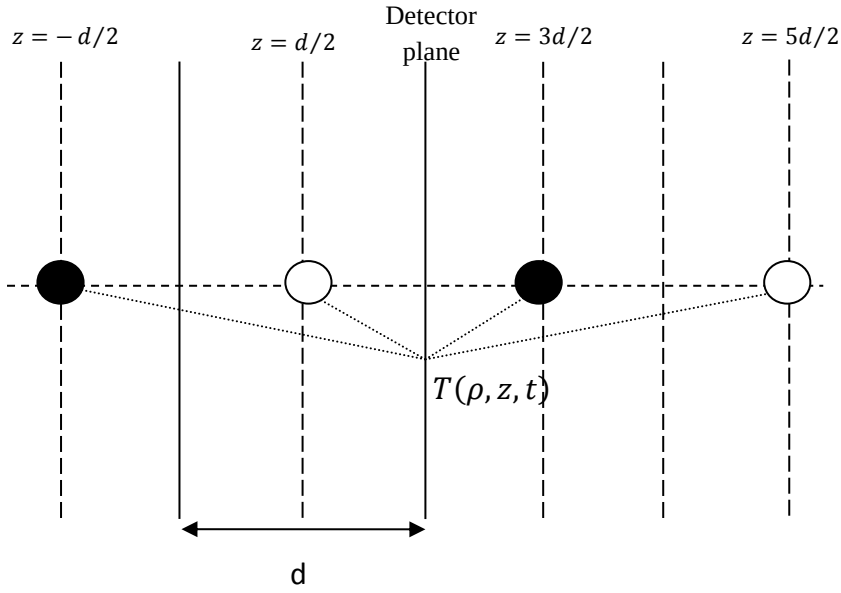

(a)

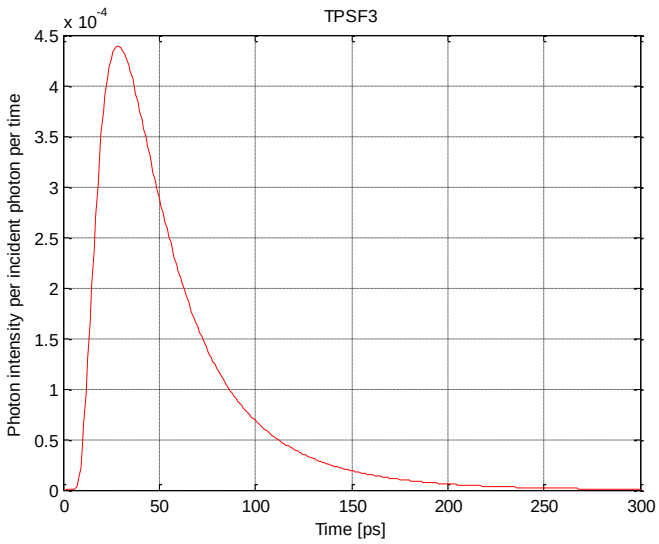

(b)

Figure 4-8 (a) Diffusion model for the Standard configuration for propagating fluorescence emission light from the intermediate fluorescence plane to the detector, seven dipole sources applied, two of them are shown in the figure; (b) TPSF of emission light detected (TPSF3)

The TPSFs shown in Figure 4-7 (b) and Figure 4-8 (b) (TPSF2 and TPSF3) respectively need to be combined in order to produce the final fluorescence emission signal. If the fluorescence emission is considered as a linear system, TPSF3 is the impulse response and TPSF2 is the input of the system. Lifetime is a time dependent function to describe the transformation from excitation to emission light. The TPSF of the fluorescence emission light in the Standard configuration can be obtained through the convolution of TPSF2, TPSF3 and the fluorescence lifetime decay. A similiar model is applied by Ma *et. al* [143], where this process is represented as:

$$F(\rho,d,t) = S(t)\otimes E_x(\rho,z,t)\otimes\left[\sum\frac{A_i}{\tau_i}exp\left(-\frac{t}{\tau_i}\right)\right]\otimes E_m(\rho,d,t) \qquad 4\text{-}14$$

where the $\otimes$ sign represents the convolution integral, $S(t)$ is the system impulse response function, $E_x(\rho,z,t)$ is the light propagated from the excitation source to the fluorophore, $E_m(\rho,d,t)$ is the fluorescent light propagated from the fluorophore to the detector, and $F(\rho,d,t)$ is the fluorescent signal detected at the boundary. The terms in square brackets

represent fluorescent decay, where A_i and τ_i are the amplitude and lifetime of the i_{th} fluorophore component. A_i is usually related to the concentration, extinction coefficient, and quantum yield of the fluorophore.

In this Chapter, the aim is to develop accurate measurements of fluorescence lifetime τ in heavily scattering media, which is described by the last three terms of equation 4-14. As the concentration, extinction coefficient, and quantum yield of the fluorophore only affect the signal intensity detected, it is assumed that there is adequate SNR at the detector plane so that one can set:

$$S(t) = \delta(t),\ A_i = 1 \text{ and } i = 1$$

As discussed above, the light at the plane of the fluorescent target is given by the fluence rate but the transmittance is the appropriate term to use at the boundary as $\Phi = 0$. The TPSF of the fluorescence emission light in the Standard configuration can be represented as:

$$F(\rho, d, t) = \Phi_{Ex}(\rho, d/2, t) \otimes \left[\frac{1}{\tau} exp\left(-\frac{t}{\tau}\right)\right] \otimes T_{Em}(\rho, d, t) \qquad 4\text{-}15$$

where $\Phi_{Ex}(\rho, d/2, t)$ is the light propagated from the excitation source to the fluorescent target plane (TPSF2), $T_{Em}(\rho, d, t)$ is the transmittance of fluorescent light propagated from the fluorescence target plane to the detector (TPSF3). The terms in square brackets represent the temporal properties of the fluorescent decay. The convolution of TSF2, TPSF3 and the fluorescence lifetime is labelled TPSF5.

The general practice of estimating lifetime is to fit a mono-exponential to the detected fluorescence TPSF [145], but the frequency domain analysis is still applied nowadays as an alternative approach [146]. As discussed in section 4.2, operating in the frequency domain was of interest due to experiment constraints in the Applied Optics Laboratory.

The frequency domain response can be obtained by taking the Fourier transform of the key equations that have been obtained in the time domain.

Convolution is reduced to a multiplication in the frequency domain.

By taking the Fourier transform (FT) of Equation 4-12,

$$\begin{aligned}\Phi_{Ex}(\rho, d/2, \omega) &= \sum_{m=0}^{+\infty}\left[\left(2md+\frac{d}{2}-z_0\right)\right. \\ &\times \frac{exp(-\Pi_{1x})\left(1+{\Pi_{+x}}^2+2\Pi_{1x}\right)^{1/2}}{2\pi(\rho^2+{z_0}^2)^{3/2}} \\ &\times\left\{\cos\left[\Pi_{2x}-\tan^{-1}\left(\frac{\Pi_{2x}}{1+\Pi_{1x}}\right)\right]\right. \\ &\left.\left.+\,i\sin\left[\Pi_{2x}-\tan^{-1}\left(\frac{\Pi_{2x}}{1+\Pi_{1x}}\right)\right]\right\}\right] \\ &-\sum_{m=0}^{+\infty}\left[\left(2md+\frac{d}{2}+z_0\right)\right. \\ &\times \frac{exp(-\Pi_{3x})\left(1+{\Pi_{-x}}^2+2\Pi_{3x}\right)^{1/2}}{2\pi(\rho^2+{z_0}^2)^{3/2}} \\ &\times\left\{\cos\left[\Pi_{4x}-\tan^{-1}\left(\frac{\Pi_{4x}}{1+\Pi_{3x}}\right)\right]\right. \\ &\left.\left.+\,i\sin\left[\Pi_{4x}-\tan^{-1}\left(\frac{\Pi_{4x}}{1+\Pi_{3x}}\right)\right]\right\}\right]\end{aligned} \quad 4\text{-}16$$

where

$$\Pi_{+x}=\left\{\frac{\left[\rho^2+\left(2md+\frac{d}{2}-z_0\right)^2\right]\sqrt{(\mu_{ax}c)^2+\omega^2}}{D_x c}\right\}^{1/2} \quad 4\text{-}17$$

$$\Pi_{1x}=\Pi_{+x}\cos\left[\frac{1}{2}\tan^{-1}\left(\frac{\omega}{\mu_{ax}c}\right)\right] \quad 4\text{-}18$$

$$\Pi_{2x}=-\Pi_{+x}\sin\left[\frac{1}{2}\tan^{-1}\left(\frac{\omega}{\mu_{ax}c}\right)\right] \quad 4\text{-}19$$

$$\Pi_{-x}=\left\{\frac{\left[\rho^2+\left(2md+\frac{d}{2}+z_0\right)^2\right]\sqrt{(\mu_{ax}c)^2+\omega^2}}{D_x c}\right\}^{1/2} \quad 4\text{-}20$$

$$\Pi_{3x}=\Pi_{-x}\cos\left[\frac{1}{2}\tan^{-1}\left(\frac{\omega}{\mu_{ax}c}\right)\right] \quad 4\text{-}21$$

$$\Pi_{4x} = -\Pi_{-x} \sin\left[\frac{1}{2}\tan^{-1}\left(\frac{\omega}{\mu_{ax}c}\right)\right] \tag{4-22}$$

And similarly taking the Fourier transform of Equation 4-13, we have,

$$\begin{aligned} T_{Em}(\rho, d, \omega) = \sum_{m=0}^{+\infty} \Bigg[& \left(2md + \frac{d}{2}\right) \\ & \times \frac{exp(-\Pi_{1m})\left(1 + \Pi_{+m}{}^2 + 2\Pi_{1m}\right)^{1/2}}{2\pi(\rho^2 + {z_0}^2)^{3/2}} \\ & \times \left\{\cos\left[\Pi_{2m} - \tan^{-1}\left(\frac{\Pi_{2m}}{1 + \Pi_{1m}}\right)\right]\right. \\ & \left. + i \sin\left[\Pi_{2m} - \tan^{-1}\left(\frac{\Pi_{2m}}{1 + \Pi_{1m}}\right)\right]\right\}\Bigg] \\ - \sum_{m=0}^{+\infty} \Bigg[& \left(2md + \frac{3d}{2}\right) \\ & \times \frac{exp(-\Pi_{3m})\left(1 + \Pi_{-m}{}^2 + 2\Pi_{3m}\right)^{1/2}}{2\pi(\rho^2 + {z_0}^2)^{3/2}} \\ & \times \left\{\cos\left[\Pi_{4m} - \tan^{-1}\left(\frac{\Pi_{4m}}{1 + \Pi_{3m}}\right)\right]\right. \\ & \left. + i \sin\left[\Pi_{4m} - \tan^{-1}\left(\frac{\Pi_{4m}}{1 + \Pi_{3m}}\right)\right]\right\}\Bigg] \end{aligned} \tag{4-23}$$

with

$$\Pi_{+m} = \left\{\frac{\left[\rho^2 + \left(2md + \frac{d}{2}\right)^2\right]\sqrt{(\mu_{am}c)^2 + \omega^2}}{D_m c}\right\}^{1/2} \tag{4-24}$$

$$\Pi_{1m} = \Pi_{+m} \cos\left[\frac{1}{2}\tan^{-1}\left(\frac{\omega}{\mu_{am}c}\right)\right] \tag{4-25}$$

$$\Pi_{2m} = -\Pi_{+m} \sin\left[\frac{1}{2}\tan^{-1}\left(\frac{\omega}{\mu_{am}c}\right)\right] \tag{4-26}$$

$$\Pi_{-m} = \left\{\frac{\left[\rho^2 + \left(2md + \frac{3d}{2}\right)^2\right]\sqrt{(\mu_{am}c)^2 + \omega^2}}{D_m c}\right\}^{1/2} \tag{4-27}$$

$$\Pi_{3m} = \Pi_{-m} \cos\left[\frac{1}{2}\tan^{-1}\left(\frac{\omega}{\mu_{am}c}\right)\right] \quad 4\text{-}28$$

$$\Pi_{4m} = -\Pi_{-m} \sin\left[\frac{1}{2}\tan^{-1}\left(\frac{\omega}{\mu_{am}c}\right)\right] \quad 4\text{-}29$$

Therefore, the Transmittance of fluorescence signal in the frequency domain can be written as,

$$F(\rho, d, \omega) = E_x(\rho, d/2, \omega) \times E_m(\rho, d, \omega) \times \left[\frac{1 - i\omega\tau}{1 + (\omega\tau)^2}\right] \quad 4\text{-}30$$

The phase shifts of excitation and emission light at the detector can be similarly obtained from the real and imaginary parts of the Fourier transform;

$$\begin{aligned} \sigma_r &= \tan^{-1}\frac{Im[T_x(\rho, d, \omega)]}{Re[T_x(\rho, d, \omega)]} = Phi_{TPSF1}(\omega) \\ \sigma_\omega &= \tan^{-1}\frac{Im[F(\rho, d, \omega)]}{Re[F(\rho, d, \omega)]} = Phi_{TPSF5}(\omega) \end{aligned} \quad 4\text{-}31$$

where σ_r and σ_ω are the phase shifts of excitation and emission light.

Figure 4-9 summarises the calculations of the excitation and emission responses in the Standard configuration. TPSF1 represents the excitation light propagation from the source to detector (Equation 4-11) which through the Fourier Transform can be used to obtain the phase response.

TPSF2 represents propagation of excitation light from the source to the fluorescence target plane. TPSF3 represents propagation of emission light from the fluorescence target plane to the detector. Convolving TPSF2, TPSF3 and the fluorescence lifetime decay provides the TPSF of the emission light at the detector (TPSF5) (Equation 4-15). Taking the Fourier Transform provides the magnitude and phase response of the fluorescence at the detector.

The difference between the excitation and emission phases (Equation 4-5) can then be used to calculate the fluorescence lifetime.

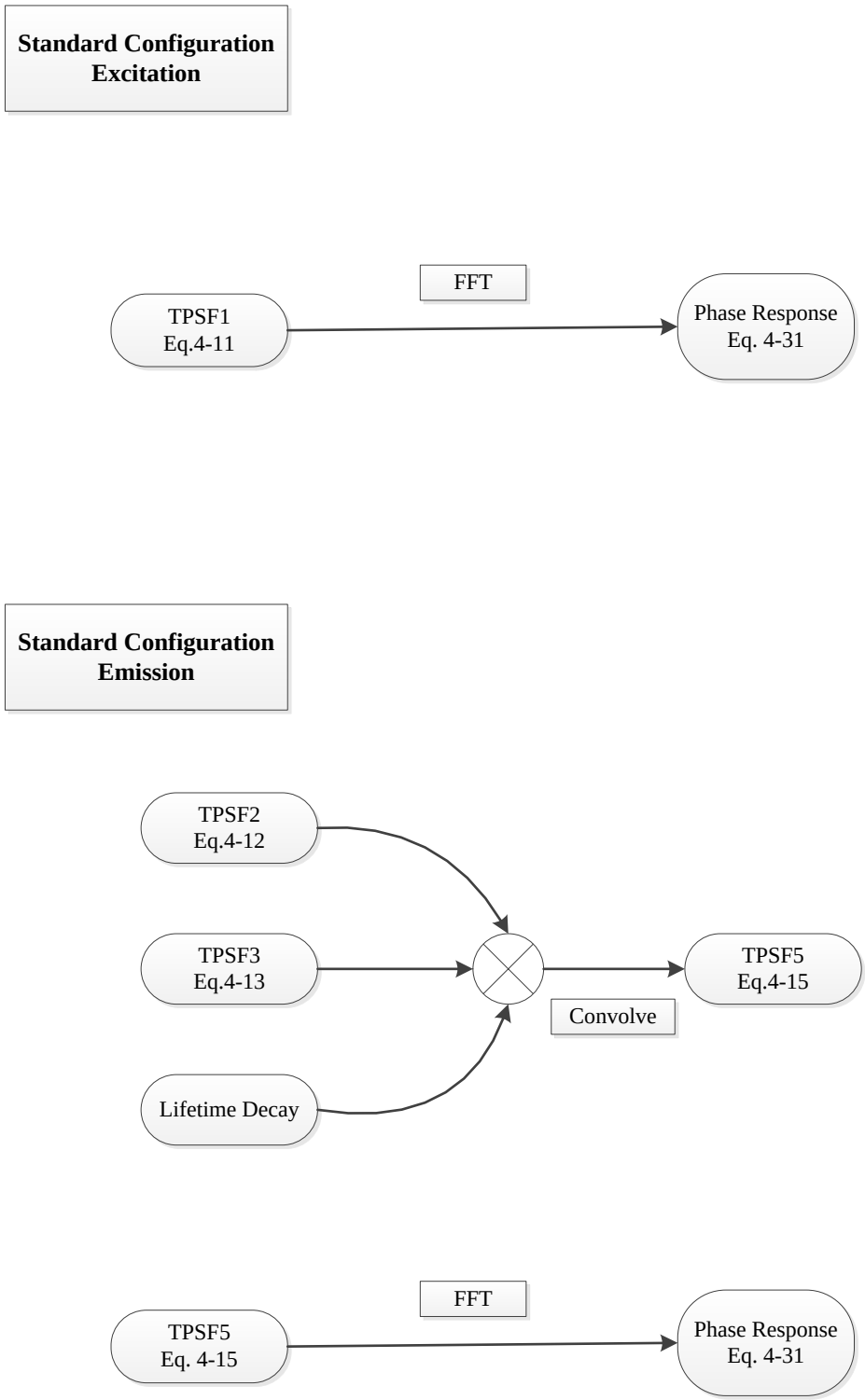

Figure 4-9 Flowchart to demonstrate calculation of the emission and excitation light using the Standard configuration

4.4.2 Ultrasound modulated fluorescence lifetime model

As discussed in section 4.3, in this case unmodulated CW excitation light illuminates the sample (Figure 4-4). An ultrasound wave is generated along the vertical direction and, through the mechanisms described by Yuan et al. [126], both the excitation and emission wavelengths become modulated at the frequency of the US. Recording the US modulated excitation and emission allows Equation 4-5 to be applied and this offers the potential for more accurate measurement of fluorescence lifetime.

To compare with intensity modulated light input (Standard configuration), it is assumed the excitation light produces a stable and time independent illumination on the fluorescence target, so the ultrasonic-optical interaction can be modelled simply as an intensity modulated light source inside the medium. The ultrasound propagation direction is parallel to the tissue slab boundary. Figure 4-10 shows the geometry of the ultrasound associated model, which is the same as Figure 4-8(a), but assumes that both excitation and emission light is modulated by the ultrasound within the medium. Thus the modulated excitation light and emission light can be described by Figure 4-11. The only difference is due to the different optical properties at the emission and excitation wavelengths.

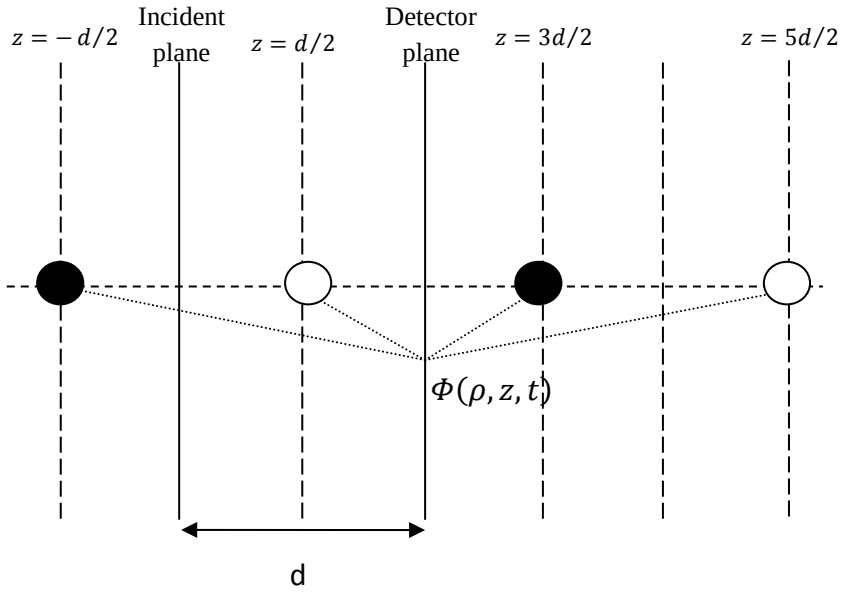

Figure 4-10 Diffusion model geometry of ultrasound modulated light detected, seven dipole sources applied, two of them are shown in the figure.

Figure 4-11 (a) shows the TPSF obtained with the configuration shown in Figure 4-10 but at the excitation wavelength. The TPSF at the emission wavelength is shown in Figure 4-11 (b).

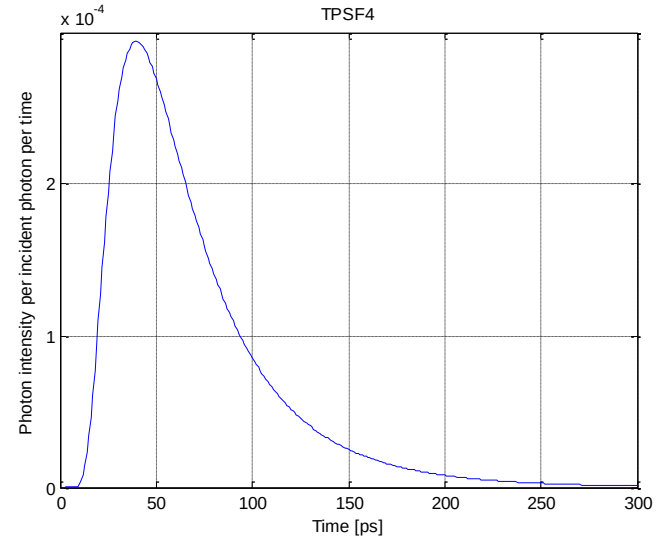

(a)

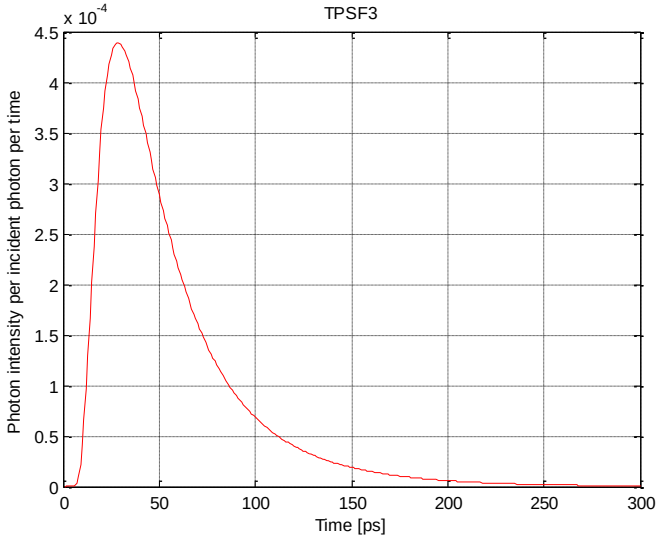

(b)

Figure 4-11 (a) TPSF of ultrasound modulated excitation light detected (TPSF4); (b) TPSF of ultrasound modulated emission light detected (TPSF3).

The flow chart describing light interaction with ultrasound is shown in Figure 4-12. With ultrasound, the localized fluorophore is assumed to be a modulated

source embedded within the medium. TPSF6 is defined as the convolution of TPSF3 and the lifetime decay.

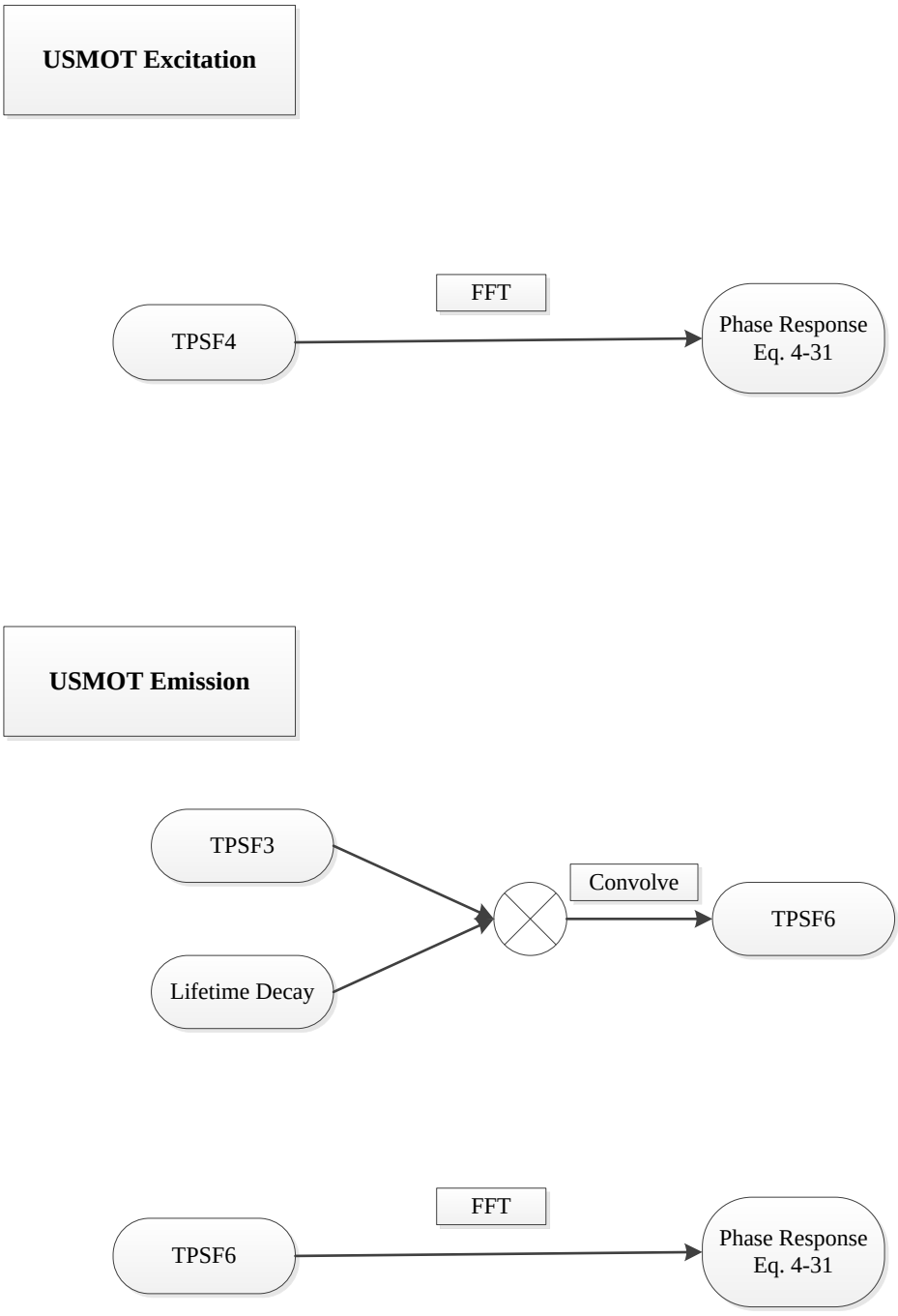

Figure 4-12 Flowchart of USMOT excitation and emission light processing

4.5 Results

The simulation results are presented in this section, lifetimes are extracted from the phase shift detected. Four cases are considered (i) the Standard geometry without using the detected excitation light as a reference, (ii) the Standard geometry using the detected excitation light as a reference, (iii) USMOT without using the detected US modulated excitation light as a reference (iv) USMOT using the detected US modulated excitation light as a reference. The use of a reference relies on the assumption that the fluorescent target is sufficiently small as to not affect the properties of the medium.

The optical properties applied in the simulation are shown in Table 4-1. In the majority of cases considered, it is assumed that a fluorophore with a 1ns lifetime is located at the mid-plane of the infinite slab.

Table 4-1 Optical properties for the simulation in 10mm thick infinite slab scattering medium [5]

μ_s of excitation	120cm^{-1}
μ_a of excitation	0.6cm^{-1}
μ_s of emission	80cm^{-1}
μ_a of emission	0.5cm^{-1}
Anisotropy g	0.9

4.5.1 Standard method (Non-USMOT) analysis

Figure 4-13 shows a standard single-exponential decay with 1ns fluorescence lifetime obtained from equation 4-32.

$$I_{Decay}(t) = I_0 e^{-t/\tau}, \quad t \geq 0 \qquad 4\text{-}32$$

where I_0 is the intensity at $t=0$, t is time and τ is the excited state lifetime.

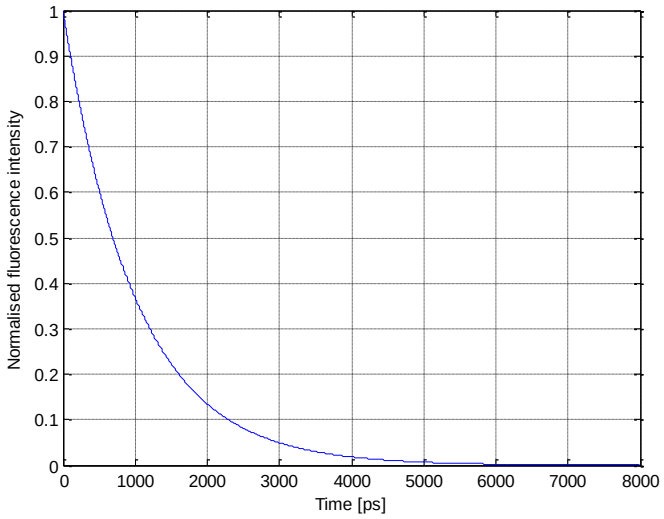

Figure 4-13 Lifetime decay at 1ns

TPSF1 (excitation light detected) and TPSF5 (convolution of light entering the fluorophore, light emitted from the fluorophore and lifetime decay as shown in Figure 4-9) are shown in Figure 4-14. This represents the excitation and emission light detected.

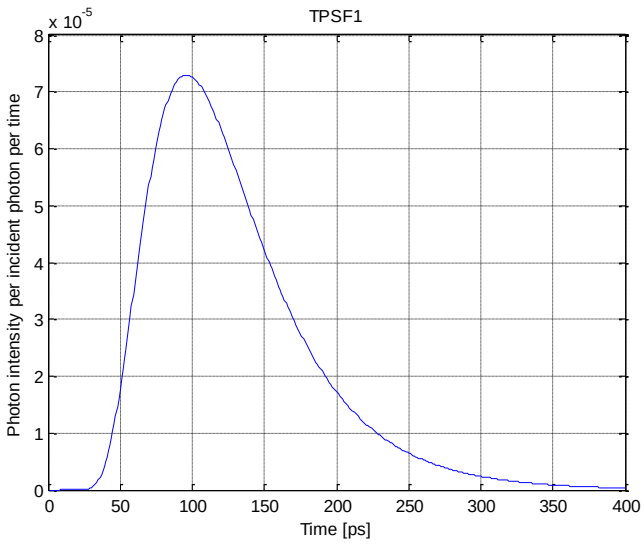

(a) TPSF of detected excitation light (TPSF1)

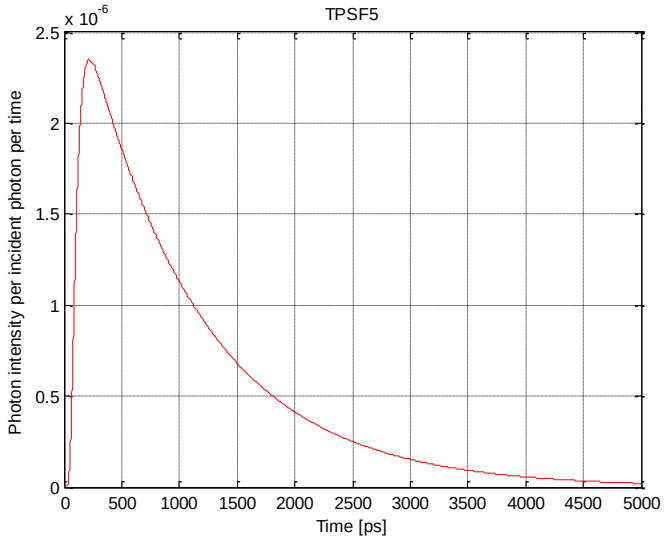

(b) TPSF of detected emission light

Figure 4-14 TPSFs of non-USMOT excitation and emission (TPSF5)

After applying the Fourier transform to TPSF1 and TPSF5, by applying Equation 4-31, the phase shift of the excitation and emission light are shown in Figure 4-15.

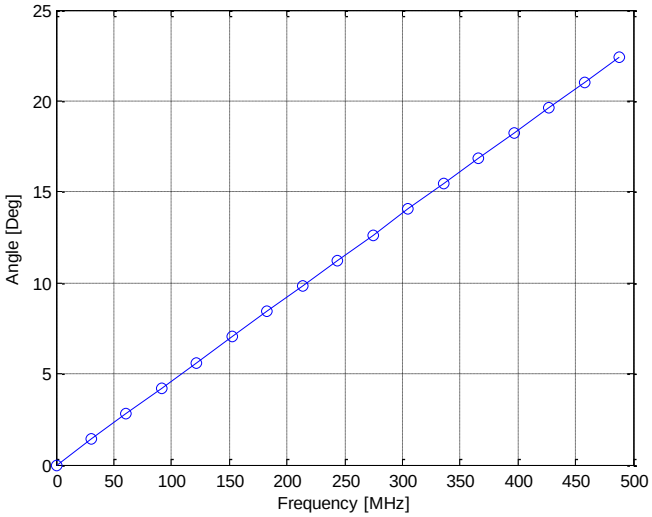

(a) Phase shift of excitation light detected, σ_r

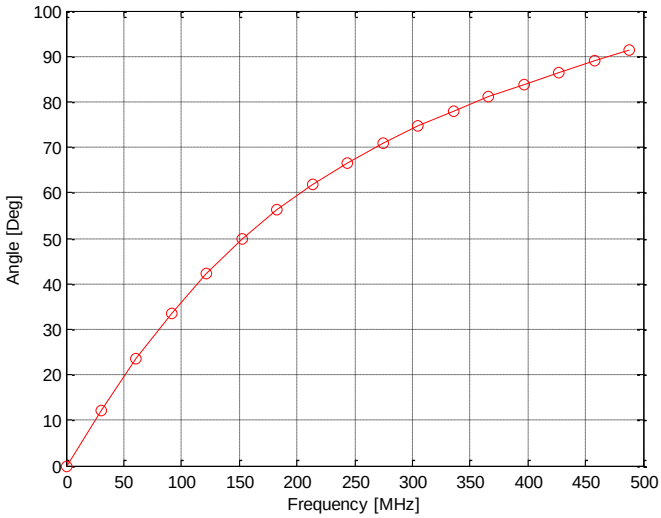

(b) Phase shift of emission light detected, σ_ω

Figure 4-15 Phase shift calculated from Standard configuration excitation and emission light

The phase shifts of the detected fluorescence emission, measured over a wide range of frequencies are shown in Figure 4-15. The phase shift of excitation light ϕ_r is mainly due to the scattering effect. As the optical length is fixed, higher input frequency leads to a relatively larger phase shift. Hence, it looks linear in Figure 4-15(a). The phase shift of emission light $\phi_\omega$contributes from both scattering and fluorescence lifetime decay. It has a steeper slope with increasing frequencies at the beginning which is shown in Figure 4-15(b).

To calculate the fluorescence lifetime of the fluorescent target without using a reference the phase of the detection fluorescence emission light ϕ_ω is

substituted into Equations 4-3. The lifetime values extracted at different wavelengths using phase are shown in Figure 4-16.

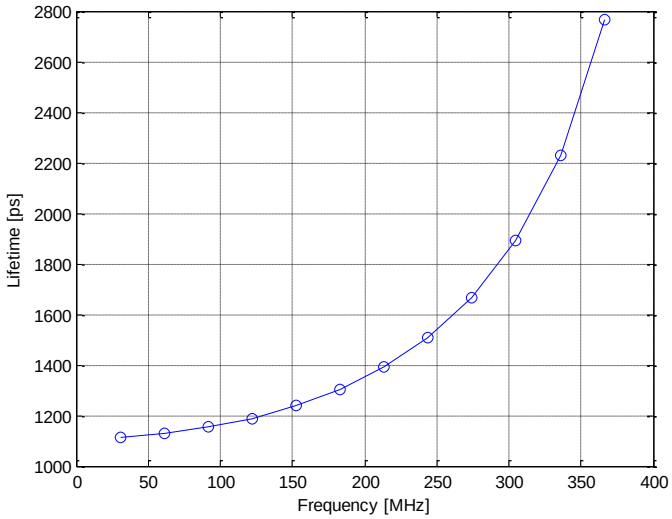

Figure 4-16 1ns lifetime extracted without using the detected excitation light as a reference

As shown in Figure 4-16 the lifetime extracted in the low frequency range is closer to the actual value. As the frequency is increased, the phase shift approaches 90 degrees which makes it more difficult to measure.

In the previous literature [82], the experiments were carried out under low scattering conditions, in which the phase shift due to scattering can be ignored. But as seen from Figure 4-16 above, the phase shift resulting from a heavily scattering medium is comparable to that of the lifetime, so an error is introduced if the phase shift calculation is made relative to the input signal.

It is therefore useful to use the detected excitation light as a reference and to apply equations 4-3 and 4-31 to obtain fluorescence lifetime. Figure 4-17 compares the case with and without this reference. It can be seen that for phase shift, the lifetime extracted with reference to the detected excitation light is more accurate especially under in the higher frequency range.

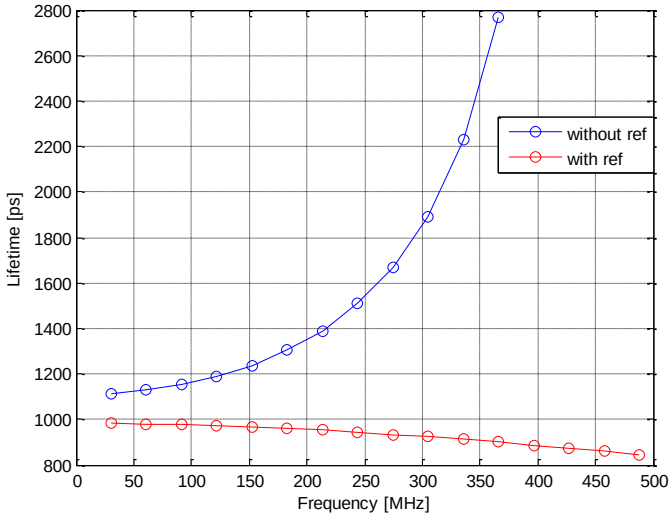

Figure 4-17 1ns lifetime extracted with and without reference

4.5.2 USMOT analysis

TPSF4 and TPSF6 are shown below which represents the ultrasound modulated excitation and emission light detected.

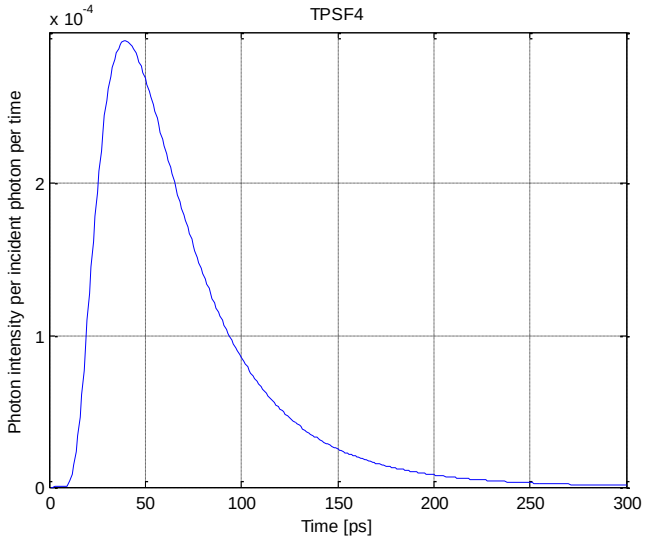

(a) TPSF output of ultrasound modulated excitation light detected (TPSF4)

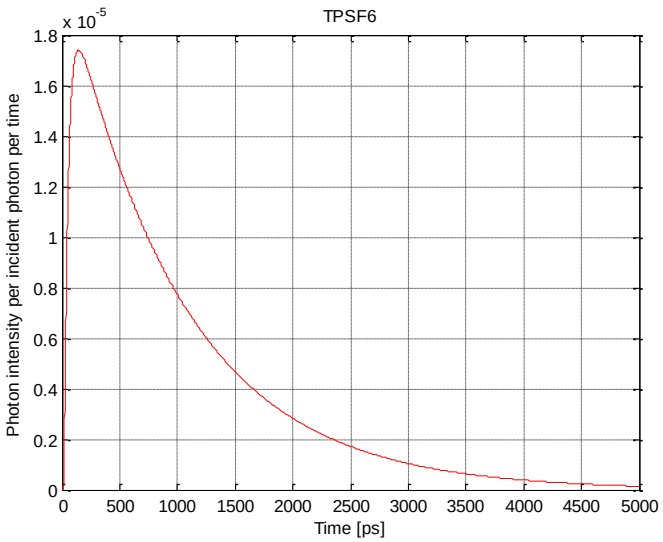

(b) TPSF output of ultrasound modulated emission light detected (TPSF6)

Figure 4-18 TPSF output of USMOT excitation and emission light detected

After a FFT is applied to the signal, the phase shift is shown in Figure 4-19. Similar to Figure 4-15, the σ_r is linearly increased with modulation frequencies and σ_ω has a steeper slope which results from the lifetime decay.

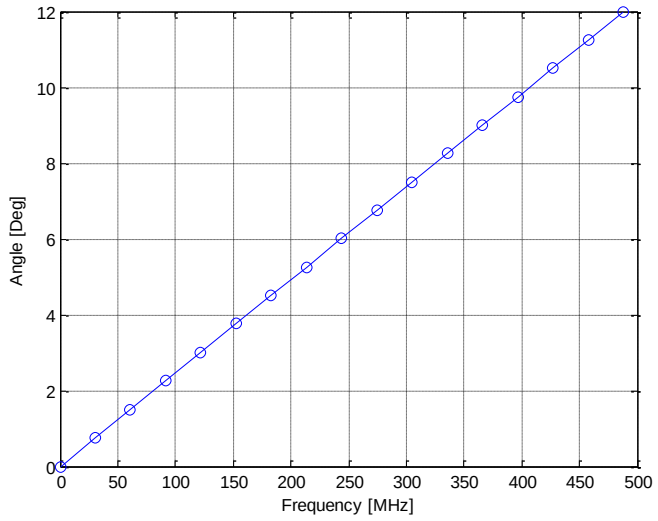

(a) Phase shift of ultrasound modulated excitation light detected, σ_r

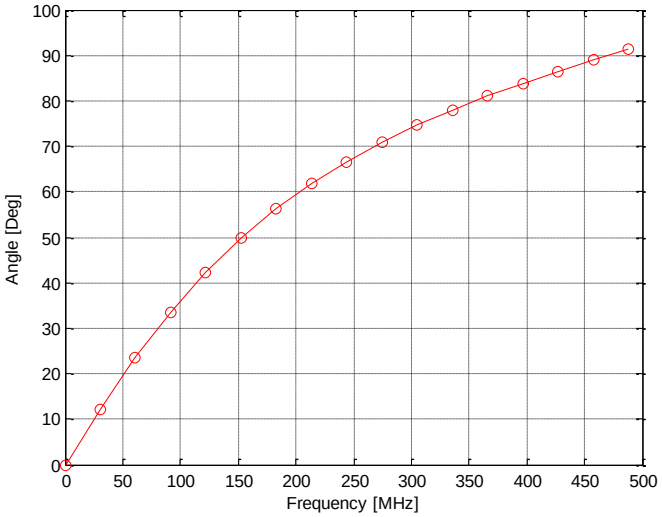

(b) Phase shift of ultrasound modulated emission light detected, σ_ω

Figure 4-19 Phase shift calculated from ultrasound modulated excitation and emission light

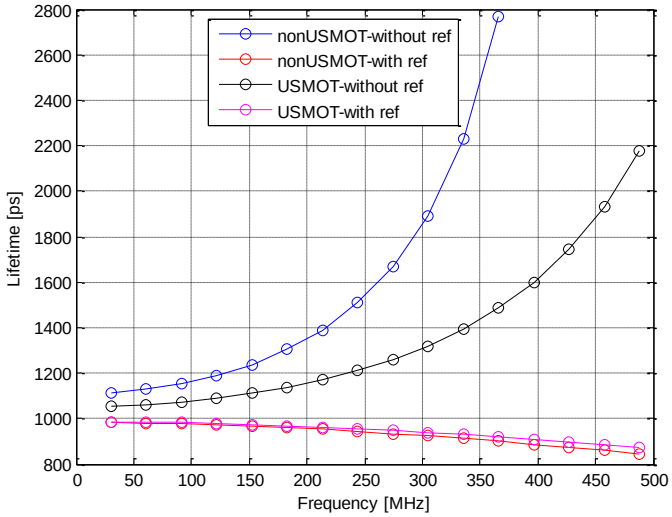

Figure 4-20 1ns lifetime extracted with and without reference & ultrasound

Figure 4-20 shows the lifetimes extracted for all four cases considered (i) the Standard geometry without using the detected excitation light as a reference, (ii) the Standard geometry using the detected excitation light as a reference, (iii) USMOT without using the detected US modulated excitation light as a

reference (iv) USMOT using the detected US modulated excitation light as a reference. The USMOT case with a reference provides the most accurate estimation of fluorescence lifetime.

4.5.3 Optical parameters variation

In this section, a series of simulations are run to investigate the effect that varying the optical properties has on the calculated fluorescence lifetimes. In all cases a 10mm thick infinite slab geometry is considered.

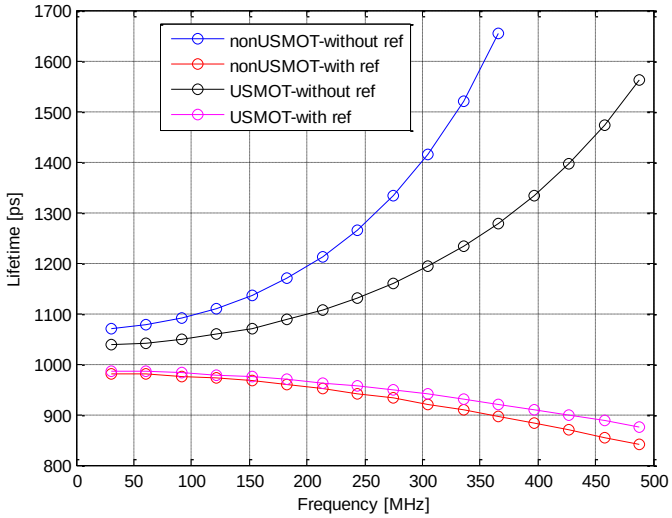

(a) 1ns Lifetime extracted by phase shift with and without reference & ultrasound with $\mu_{sex} = 60cm^{-1}$, $\mu_{aex} = 0.3cm^{-1}$, $\mu_{sem} = 40cm^{-1}$ and $\mu_{aem} = 0.25cm^{-1}$

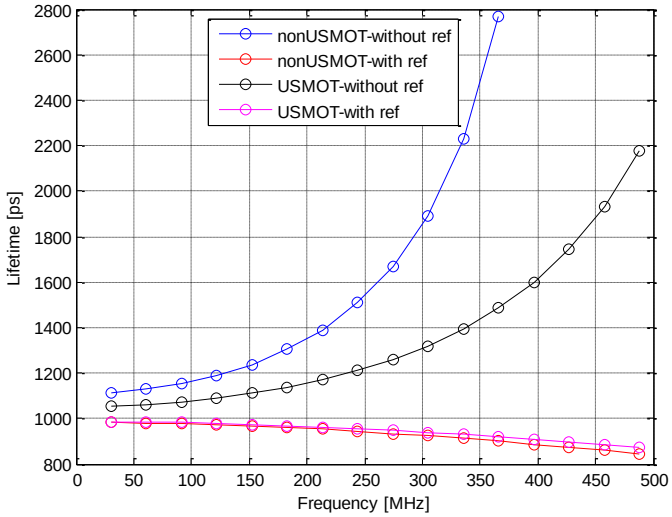

(b) 1ns Lifetime extracted by phase shift with and without reference & ultrasound with $\mu_{sex} = 120cm^{-1}$, $\mu_{aex} = 0.6cm^{-1}$, $\mu_{sem} = 80cm^{-1}$ and $\mu_{aem} = 0.5cm^{-1}$

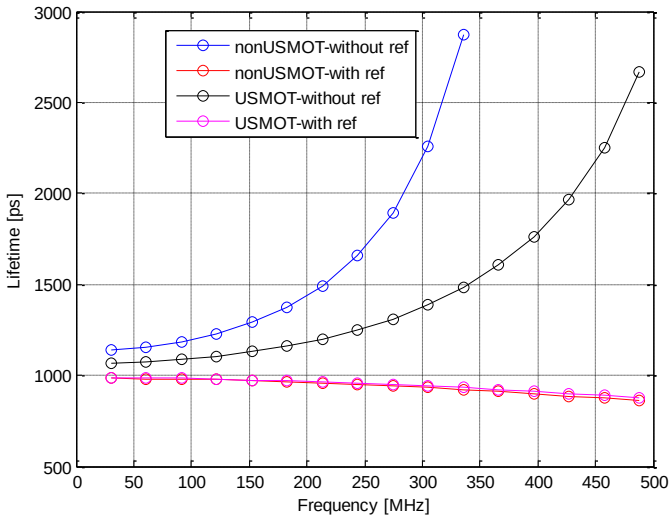

(c) 1ns Lifetime extracted by phase shift with and without reference & ultrasound with $\mu_{sex} = 180cm^{-1}$, $\mu_{aex} = 0.9cm^{-1}$, $\mu_{sem} = 120cm^{-1}$ and $\mu_{aem} = 0.75cm^{-1}$

Figure 4-21 Fluorescence lifetime for different optical properties

Based on Figure 4-21, a number of observations can be made,

a) The lifetime extracted with reference to the detected excitation light is beneficial when trying to obtain fluorescence lifetime in a heavily scattering medium.
b) More accurate results are obtained at relatively low frequency.
c) The lifetime cannot be extracted by phase shift at high frequency (≥ 100MHz) in a heavily scattering medium.

4.5.4 Applicability for different fluorophores

In this section a series of fluorophores with different lifetimes are investigated. The range of lifetime is selected from 0.3ns to 25.1ns as shown in Table 4-2, which covers most of the known fluorophore lifetimes.

Table 4-2 Typical fluorophores with lifetime

Fluorophore	Lifetime[ns]
Alexa Fluor 647	1.0
CY3	0.3
Rhodamine 110	4.0
SeTau-404-NHS	9.3
Ethidium Bromide + ssDNA	25.1

Figure 4-22 shows the lifetimes extracted from different fluorophores. The extraction accuracy gets worse as the frequency of ultrasound increases, especially for the fluorophores with long lifetime (>5ns).

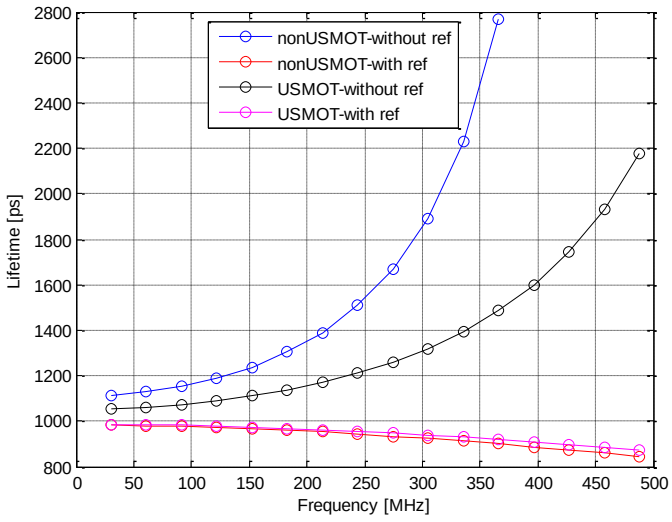

(a) 1ns Lifetime extracted by phase shift with and without reference & ultrasound with $\mu_{sex} = 120cm^{-1}$, $\mu_{aex} = 0.6cm^{-1}$, $\mu_{sem} = 80cm^{-1}$ and $\mu_{aem} = 0.5cm^{-1}$

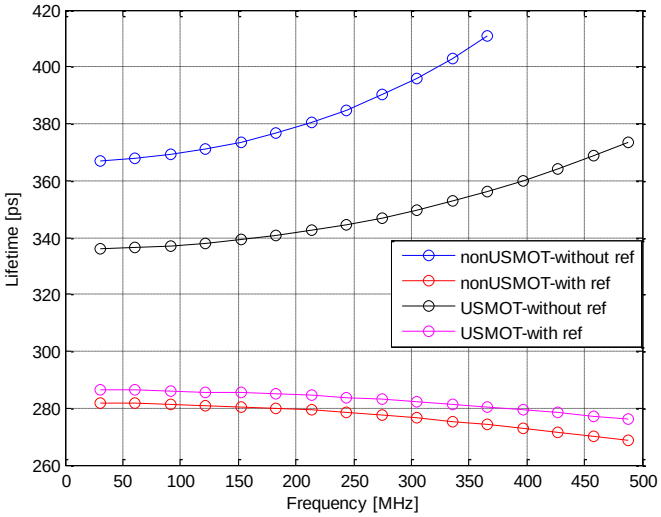

(b) 0.3ns Lifetime extracted by phase shift with and without reference & ultrasound with $\mu_{sex} = 120cm^{-1}$, $\mu_{aex} = 0.6cm^{-1}$, $\mu_{sem} = 80cm^{-1}$ and $\mu_{aem} = 0.5cm^{-1}$

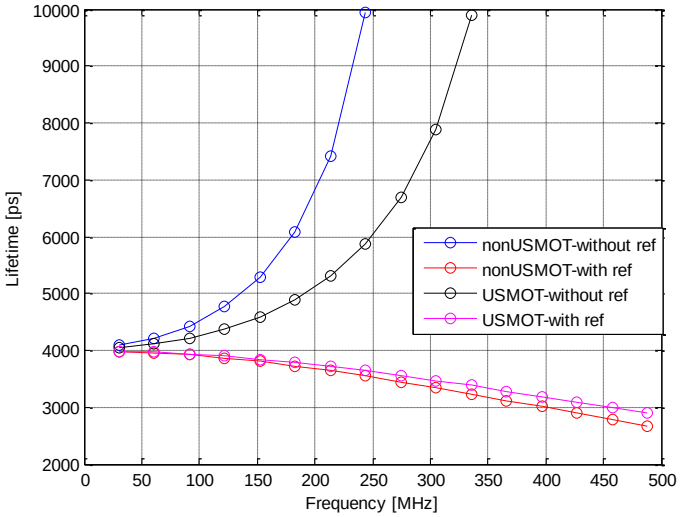

(c) 4ns Lifetime extracted by phase shift with and without reference & ultrasound with $\mu_{sex} = 120cm^{-1}$, $\mu_{aex} = 0.6cm^{-1}$, $\mu_{sem} = 80cm^{-1}$ and $\mu_{aem} = 0.5cm^{-1}$

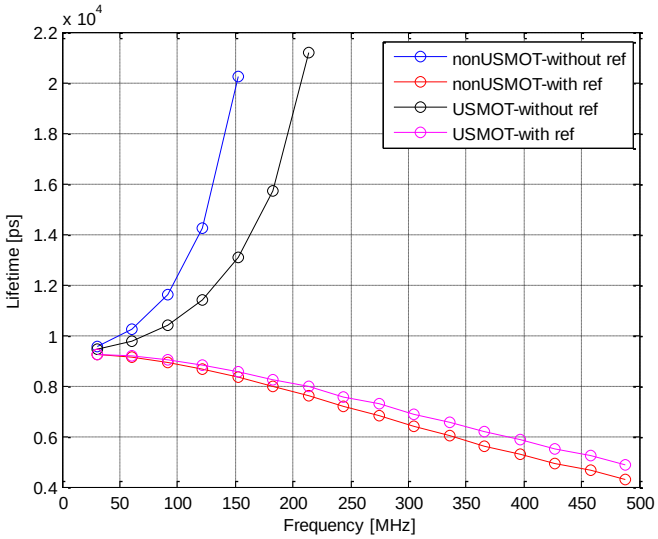

(d) 9.3ns Lifetime extracted by phase shift with and without reference & ultrasound with $\mu_{sex} = 120cm^{-1}$, $\mu_{aex} = 0.6cm^{-1}$, $\mu_{sem} = 80cm^{-1}$ and $\mu_{aem} = 0.5cm^{-1}$

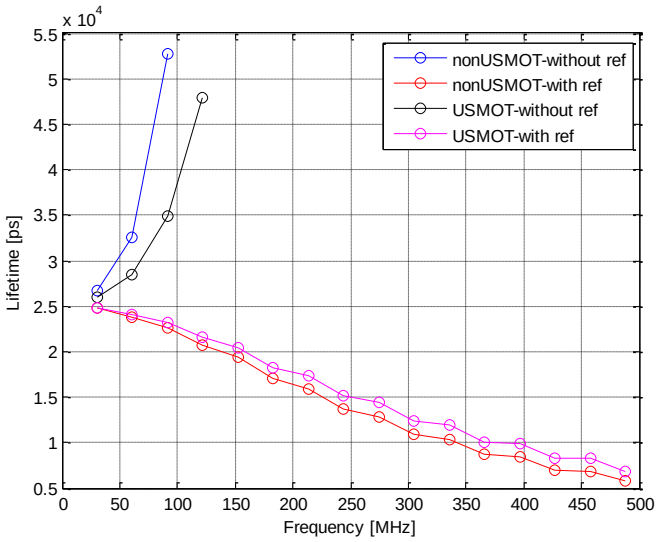

(e) 25.1ns Lifetime extracted by phase shift with and without reference & ultrasound with $\mu_{sex} = 120cm^{-1}$, $\mu_{aex} = 0.6cm^{-1}$, $\mu_{sem} = 80cm^{-1}$ and $\mu_{aem} = 0.5cm^{-1}$

Figure 4-22 Fluorescence lifetime for different fluorophores

Table 4-3 Lifetimes extracted at different frequencies

Lifetime[ns]	Lifetime Extracted [ns]		
	100MHz	200MHz	300MHz
1.0	0.982	0.962	0.938
0.3	0.286	0.284	0.282
4.0	3.914	3.624	3.310
9.3	8.909	7.549	6.268
25.1	22.548	15.559	10.537

As seen from Table 4-3, the extraction accuracy is around 95% (4ns lifetime) with 100MHz ultrasound frequency which is achievable with practical instrumentation. The accuracy reduces to 90% when the frequency increases to 200MHz. For long lifetime fluorophores, the extraction accuracy drop quickly with increasing modulation frequencies.

4.6 Discussion

Figure 4-15 shows the frequency response of the excitation and emission wavelengths. Even without a fluorescence target, phase shifts exist due to the light scattering, which result in an inaccuracy when using these parameters to extract fluorescence lifetime.

If the detected excitation light is used as a reference, as shown in Figure 4-17, it can help to reduce the effect of scattering and error in the measurement of the fluorescence lifetime decay in a heavily scattering medium. For ultrasound modulated fluorescence, the ultrasound focus can be understood as a modulated light source situated at the US focus in the middle of the slab. Compared to the Standard configurations, the shorter propagation distance to the detector leads to an increase in the lifetime extraction accuracy.

While varying the optical properties as shown in Figure 4-21, the lifetime extracted deviated from the true value more strongly with increasing scattering coefficients.

Fluorophores with different lifetimes are investigated as well. As seen in Figure 4-22, the extraction accuracy gets worse as the frequency of ultrasound increases. The phase shift goes quickly beyond 90 degrees especially for the lifetimes above 5ns. This does not occur when the lifetime is short (Figure 4-22(b)), but in this case the phase shift caused by the scattering is comparable to that from the lifetime, which degrades the accuracy of extraction. However, this can be improved by taking the excitation output as a reference as discussed previously.

A lower modulation frequency offers a better accuracy (Table 4-3). The extraction accuracy is around 95% (4ns lifetime) with 100MHz ultrasound frequency which is achievable with practical instrumentation. The accuracy reduces to 90% when the frequency increases to 200MHz.

Therefore, the optimized condition for this approach would be a fluorophore with moderate lifetime ($\leq$ 4ns) being modulated by ultrasound with low frequency ($\leq$ 100MHz).

4.7 Conclusion

The primary aim of this chapter is to introduce a novel lifetime extraction technique and investigate its performance in comparison to conventional frequency domain fluorometry. It has been shown that at low scatterer concentrations, the lifetime decay dominates and extraction is accurate whereas at high scatterer concentrations, demodulation and phase shift caused by the light scattering is comparable to that due to the lifetime, which results in errors.

This chapter shows a simulation of lifetime measurements in heavily scattering media. Taking the detected excitation light as a reference improves the accuracy. However, this approach is difficult to achieve in practice as the fluorophores can never be removed from tissue. It therefore relies on the fluorophore not affecting the optical properties of the medium.

Ultrasound modulated fluorescence improves the lifetime extraction accuracy. This approach can be considered to introduce an intensity modulated light source at the US focus that illuminates isotropically within the medium. This shortens the source detector distance compared to the original configuration and therefore the effect of scattering is reduced.

This approach has been tested under single fluorophore condition. For a single fluorophore, the extraction accuracy is improved by 5% as seen from Figure 4-20 (b) with 200MHz ultrasound frequency and with $\mu_{sex} = 120cm^{-1}$, $\mu_{aex} = 0.6cm^{-1}$, $\mu_{sem} = 80cm^{-1}$ and $\mu_{aem} = 0.5cm^{-1}$. This ratio goes up to 25% when the optical properties increased to $\mu_{sex} = 180cm^{-1}$, $\mu_{aex} = 0.9cm^{-1}$, $\mu_{sem} = 120cm^{-1}$ and $\mu_{aem} = 0.75cm^{-1}$ (Figure 4-21 (c)) in a heavily scattering medium.

Chapter 5

5 Optimising fluorescence imaging of deep tissue

5.1 Introduction

Fluorescence imaging, considered as a technique to achieve non-invasive quantitation and visualization of molecular processes is an important research direction. As discussed in section 2.4.1, several infrared and far-red fluorescent dyes have been reported during last decade with high-brightness, far-red emission spectra, excellent pH resistance and photostability [56-62]. Many researchers focus on this near-infrared fluorescence imaging driven by its deep penetration, low autofluorescence and reduced scattering and absorption, which further leads to a higher detected SNR. However, spatial resolution is another crucial element within imaging techniques. This chapter aims to find out the optimized selection of fluorophores and corresponding excitation light source based on an investigation of both the SNR and spatial resolution observed for different optical properties. These are then related to visible and near infrared wavelengths.

The excitation methods of fluorescence imaging system can be classified generally into two categories – full field imaging[147] and scanning [148]. As shown in Figure 5-1(a), most of the current commercial imaging systems use a laser with lens or a Xenon lamps to supply a full field excitation and capture images with a CCD or high speed CMOS camera (ImHD camera by PTi). This type of imaging system has been widely used especially in fluorescence imaging for its deep penetration depth (～5cm).

However, a scanning system called the moving-head scanner has been developed recently for its great improvement of minimizing spatial distortion (FMT series by Perkin Elmer). As shown in Figure 5-1(b), the light from the laser passes a mirror before hitting the sample. The sample is illuminated across its width as the scan head moves along the scan head rail. The entire sample is illuminated by the scan head, laser and mirror tracking the length of the sample. It uses an optical mechanism that is equidistant from the sample. This means that the angle and path length of the excitation beam is identical at any point on the sample. This eliminates variations in power density and spatial distortion common with full field systems but with longer scanning times. Two types of fluorescence imaging systems (full field illumination and

scanning) are modelled and compared in this chapter for their ability to resolve two fluorescence targets and the SNR.

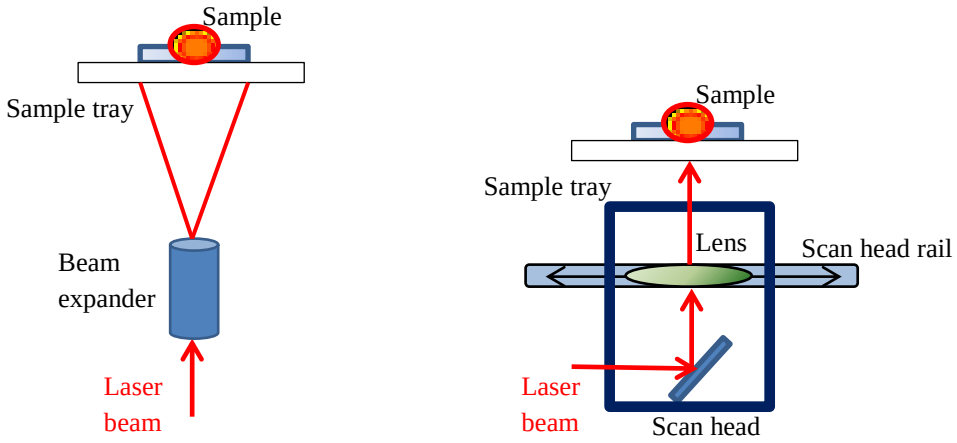

(a) Full-field system (b) Scanning system

Figure 5-1 The configurations of Full-field and illumination systems

The theoretical basis of parameters selection is discussed in section 5.2. The Monte Carlo model of full field illumination (FI) system and scanning input (SI) system are presented in section 5.3 for its flexible geometry and ability to generate 2D images, and the diffusion models are applied in section 5.4 to investigate a broad range of μ_s and μ_a. A comparison between two imaging systems are presented in section 5.5 while the optimized wavelength selection is discussed in section 5.6 with the conclusion in section 5.7

5.2 Optical windows within visible and infrared spectra

Generally, the absorbance of tissue is the sum of contributions from all absorbing components present. In living, non-pigmented tissue, the major NIR absorbers are water, lipids, oxy-haemoglobin and deoxy-haemoglobin, with the absolute value of μ_a depending on the molar concentration of each component and their respective absorption coefficients.

Previous literature reports the measurement of absorption coefficients of *in vivo* tissue. Wilson extracted the properties by using light spatial and temporal distributions [149 , 150]. Yablon *et al.* applied a technique called interferometric photothermal spectroscopy (IPTS) to measure absorption

coefficients [151], in which an interferometer is applied to measure surface displacement resulting from thermal expansion induced by a laser pulse. However this technique requires a non-scattering medium. Much research has been carried out within this area mainly based on fibre optic techniques [152, 153, 154]. Wang *et al.* reported the absorption coefficients of chicken breast within the visible spectra (400-800nm) [155], while Fantini *et al.* has measured the μ_a of human forearms in the wavelength range 633-841 nm [156]. Tuchin [5] and Cheong *et al.* [157] have tabulated the optical properties of a wide range of tissues in the wavelength range mainly from 600nm to 1500nm. For the near infrared range, Tsai reports the optical spectra from 900nm to 1350nm [158]. However, the results vary from 0.12cm^{-1} to 1.45cm^{-1} due to the type of tissue, blood concentration and experimental tolerance. As Oxy- and Deoxy-haemoglobin are considered to be the major absorbers within the tissue, the equation derived by Claridge *et al.* [159] can be applied to calculate the wavelength dependent absorption coefficient.

$$\mu_a(\lambda) = \ln 10\, V_{Hb} C_{Hb} \left(\alpha \varepsilon_{HbO_2}(\lambda) + (1-\alpha)\varepsilon_{Hb}(\lambda)\right) \qquad 5\text{-}1$$

where V_{Hb} is the volume fraction of the blood in tissue, C_{Hb} is the concentration of haemoglobin per litre of blood, α is the haemoglobin saturation, and ε_{HbO_2} and ε_{Hb} are the wavelength dependant molar extinction of oxy-haemoglobin and haemoglobin.

Characteristics from 200nm to 1000nm illustrated in Figure 5-2 were compiled by Prahl [157, 160] using the data from Gratzer and Kollias [161].

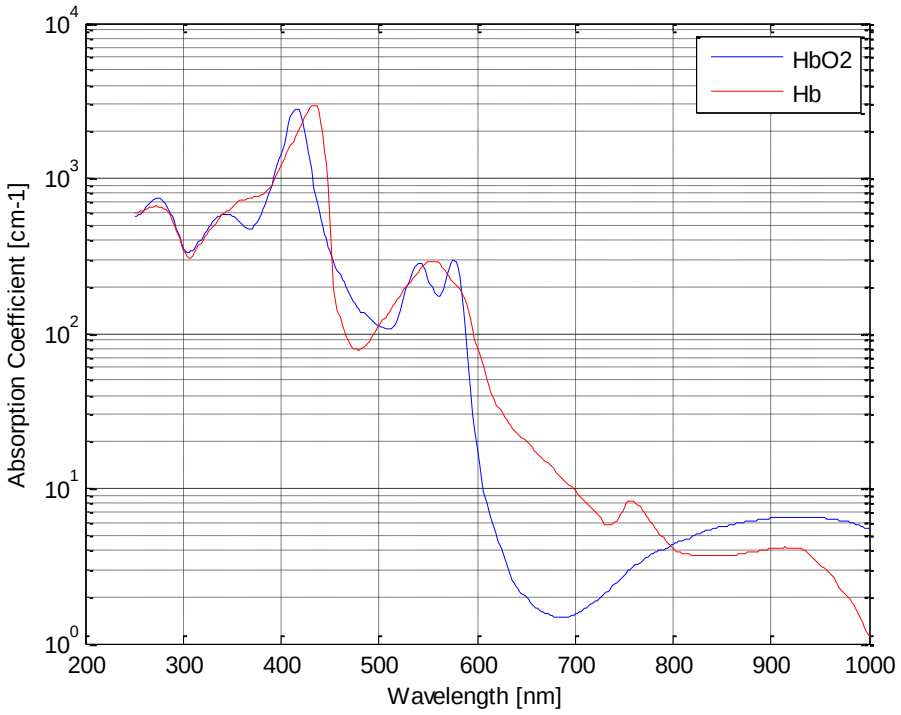

Figure 5-2 Optical characteristics of human haemoglobin. Using data from Gratzer and Kollias [161].

For the measurement of μ_s, Wang *et al.* has reported the reduced scattering coefficients μ_s' of chicken breast within 400-800nm [155]. Matcher *et al.* made measurements in the near infrared range of μ_s' for adult human forearm, calf and head between 760nm and 900nm [162]. Mourant *et al.* cover a broad range from near UV to the near IR on tissue phantoms [163]. Unlike μ_a, the results are quite consistent for all the literature with μ_s falling as the wavelength increases.

Referring to the results from previous literature, the scattering and absorption coefficients of *in vivo* tissue properties in visible wavelength are in the range of 80cm^{-1} to 140cm^{-1} and 0.2cm^{-1} to 0.8cm^{-1} respectively. And they are in the range of 20cm^{-1} to 80cm^{-1} and 0 to 0.6cm^{-1} within the infrared wavelength range. Parameters in these ranges are applied in following simulations.

5.3 Monte Carlo simulation setup

In this section, two illumination systems are presented and compared based on the spatial resolution and SNR. The signal here is defined as the photon fluence. Assuming shot noise limited detection, the noise is proportional to the square root of the photon fluence. SNR is defined as

$$SNR = \frac{F}{\sqrt{F}} \qquad 5\text{-}2$$

where F is the total photon fluence.

5.3.1 Full field illumination (FI) system

As discussed in section 2.4.3, Welch *et al.* have presented a model with uniformly distributed fluorescence in a semi-infinite medium and assumed that an excitation photon can be either scattered to another position or be absorbed and gets a chance to regenerate a photon at the emission wavelength. The probability depends on the QY of the fluorophore [109, 110].

Wang's model [21] is popular and commonly applied for its computational efficiency. The model itself does not reflect the propagation of photons in a scattering medium as a photon cannot be split into fractions. In Wang's model, a photon loss fraction of weight at each moves and will never disappear. Hence the roulette technique is applied when the weight of the photon is too small. Welch's model [109] better represents photon propagation in a scattering medium but needs longer computational time. However, this model can be easily adapted when fluorescence is introduced.

Following the concept from Welch *et al.,* a Monte Carlo model with slab geometry and localized fluorescence targets is designed. The fluorescence targets in the simulation are assumed to be two spherical objects (radius 0.2cm), which allows investigation of the trend of resolution and SNR changes when the optical parameters vary. A three dimensional Monte Carlo simulation is applied to illustrate the practical situation. The simulation configuration is shown below in Figure 5-3.

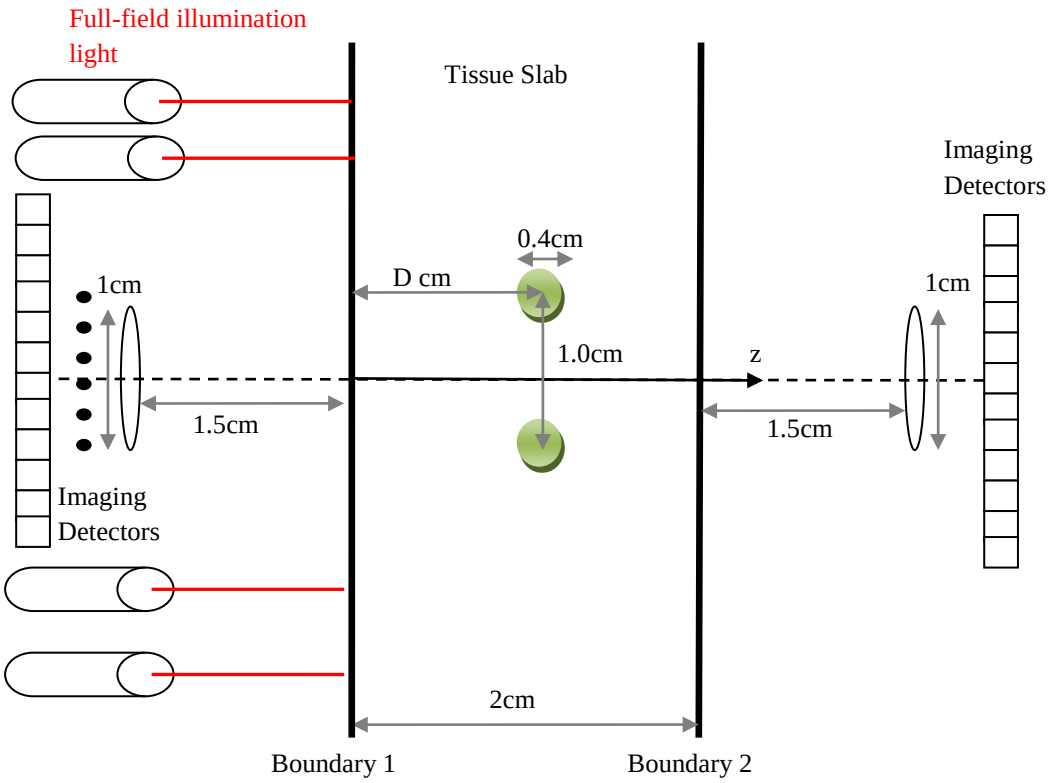

Figure 5-3 Simulation configuration of FI system

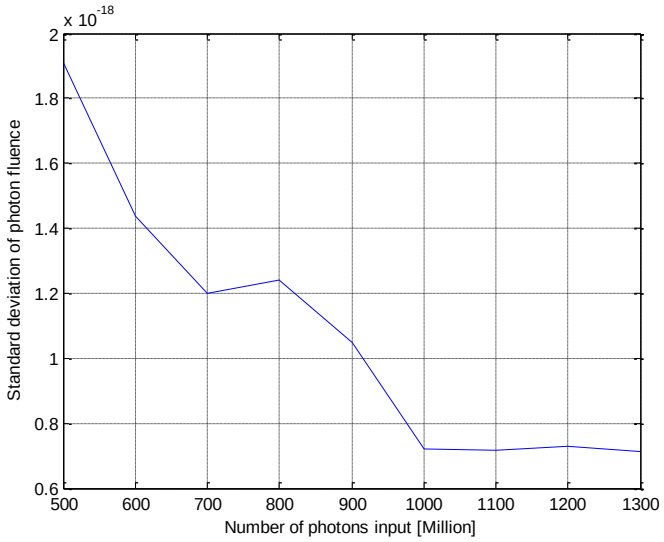

Figure 5-4 Standard deviation via number of photons input (FI system)

A fixed separation between the fluorescent targets is maintained at 1.0cm. The quantum yield (QY) is set to 40% which is consistent with the one used in Chapter 4. The thickness of the tissue slab is 2cm. Based on the standard deviation curve (Figure 5-4), one billion photons uniformly illuminate on a circular area which is 1.5cm in radius. Depending on the emergence angle and

position, photons are filtered to ensure that only photons collected by the imaging lens are retained. For these retained photons a one to one mapping of spatial position on the boundary of the tissue slab to the image plane is assumed. Optical parameters and embedded object depth, *D*, vary while the emission light images are produced in both reflection and transmission. In this model, as μ_a of excitation and emission light are different, the absorption is taken into account during the light propagation. Before a photon hits the fluorescent target, the photon can be fully absorbed or scattered to another position with full weight.

Once a photon hits fluorescent target, the probability of the three choices are determined by the QY and the ratio of μ_a and μ_s.

When excitation light enters the fluorescent targets:

$$\begin{cases} Re-emission & 0 < \xi \leq QY \\ Scattering & QY < \xi \leq QY + (1-QY) * \dfrac{\mu_{s\_ex}}{\mu_{s\_ex} + \mu_{a\_ex}} \\ Absorption & QY + (1-QY) * \dfrac{\mu_{s\_ex}}{\mu_{s\_ex} + \mu_{a\_ex}} < \xi < 1 \end{cases} \quad 5\text{-}3$$

where ξ is a random number in the range of (0 , 1).

A fraction of a photon is absorbed during this process and the remainder will continue propagating as discussed in section 3.2.4.

5.3.1.1 Results

Figure 5-5 to Figure 5-7 show the map of photon fluence detected under full field illumination with two fluorescence targets embedded inside the tissue slab.

Figure 5-5 shows images of the medium with μ_s and μ_a of excitation equal to 100cm^{-1} and 0.6cm^{-1} respectively with anisotropy g = 0.9. The values chosen are close to the optical properties of human muscle at 660nm [5]. Fluorescent targets are embedded at 0.6cm depth.

(a) Reflectance with emission optical properties μ_s = 20cm^{-1} and μ_a = 0.1cm^{-1}
(b) Transmittance with emission optical properties μ_s = 20cm^{-1} and μ_a = 0.1cm^{-1}
(c) Reflectance with emission optical properties μ_s = 20cm^{-1} and μ_a = 0.3cm^{-1}
(d) Transmittance with emission optical properties μ_s = 20cm^{-1} and μ_a = 0.3cm^{-1}
(e) Reflectance with emission optical properties μ_s = 60cm^{-1} and μ_a = 0.3cm^{-1}
(f) Transmittance with emission optical properties μ_s = 60cm^{-1} and μ_a = 0.3cm^{-1}

The same optical parameters are applied in Figure 5-6 and Figure 5-7, but with embedded object depths of 1cm and 1.4cm respectively.

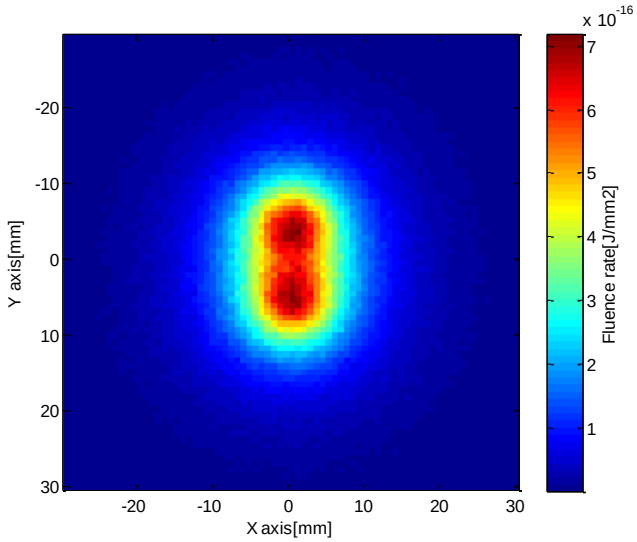

(a) Reflected image with μ_{s_em} = 20cm^{-1} & μ_{a_em} = 0.1cm^{-1}

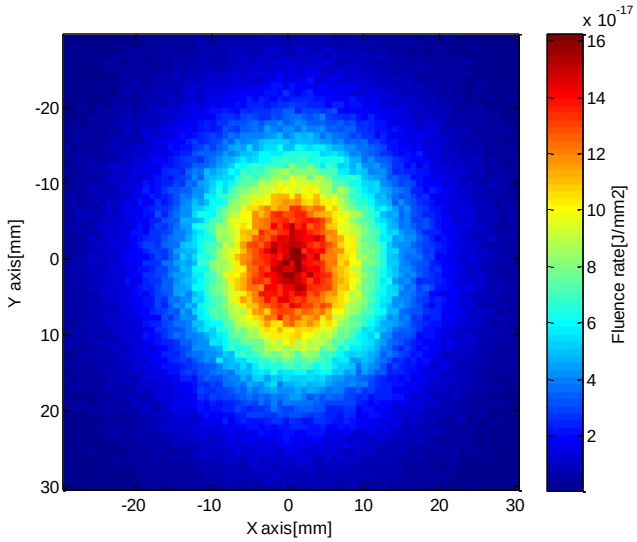

(b) Transmitted image with μ_{s_em} = 20cm^{-1} & μ_{a_em} = 0.1cm^{-1}

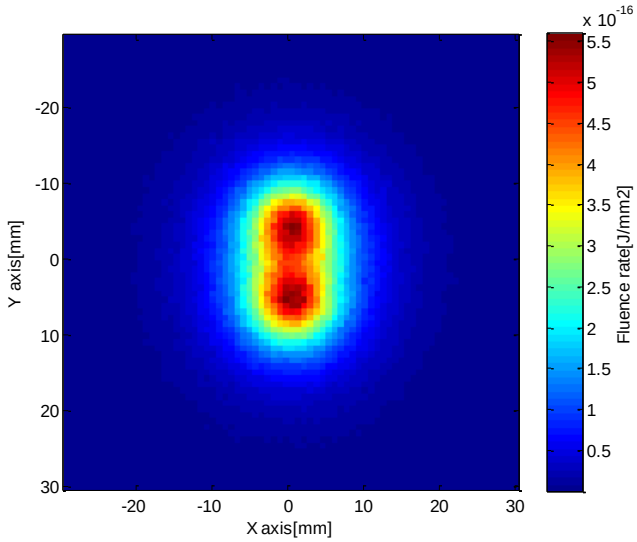

(c) Reflected image with μ_{s_em} = 20cm^{-1} & μ_{a_em} = 0.3cm^{-1}

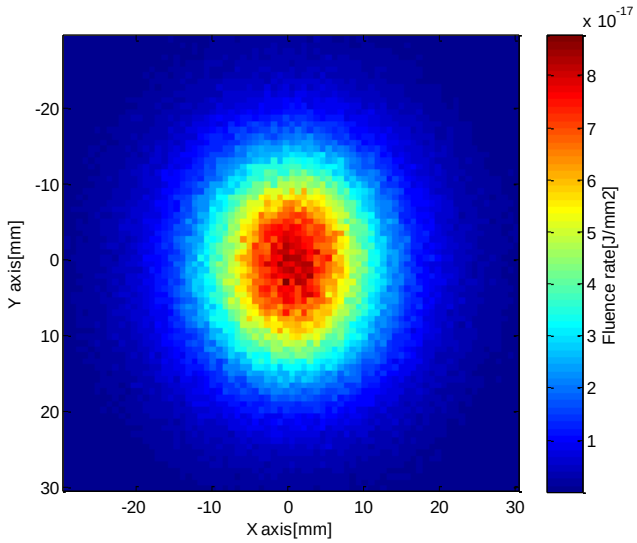

(d) Transmitted image with μ_{s_em} = 20cm^{-1} & μ_{a_em} = 0.3cm^{-1}

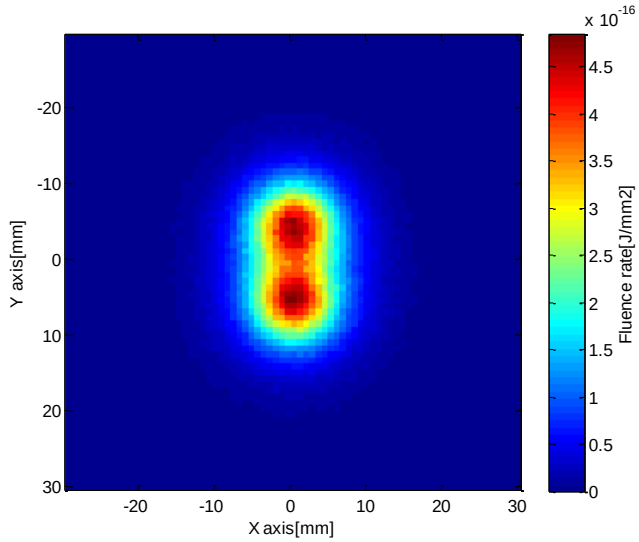

(e) Reflected image with μ_{s_em} = 60cm^{-1} & μ_{a_em} = 0.3cm^{-1}

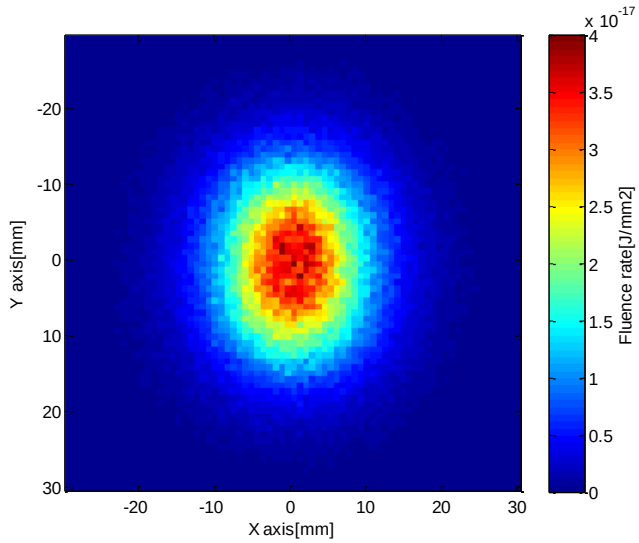

(f) Transmitted image with μ_{s_em} = 60cm^{-1} & μ_{a_em} = 0.3cm^{-1}

Figure 5-5 Photon fluence with full field illumination μ_{s_ex} = 100cm^{-1}, μ_{a_ex} = 0.6cm^{-1} and g = 0.9 at 6mm embedded depth and 20mm slab thickness.

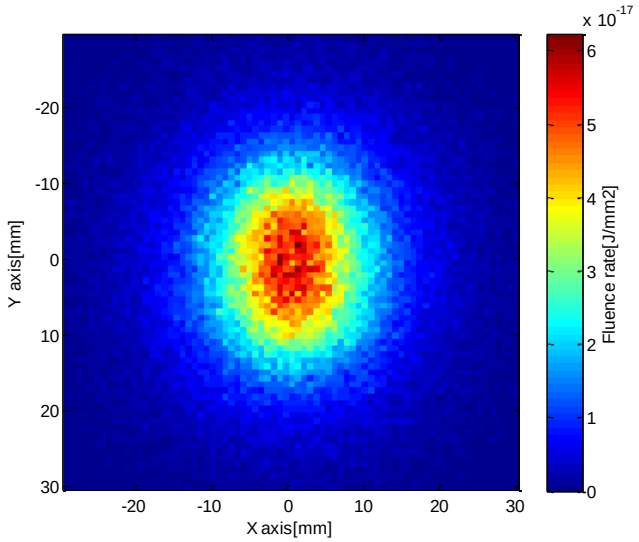

(a) Reflected image with μ_{s_em} = 20cm^{-1} & μ_{a_em} = 0.1cm^{-1}

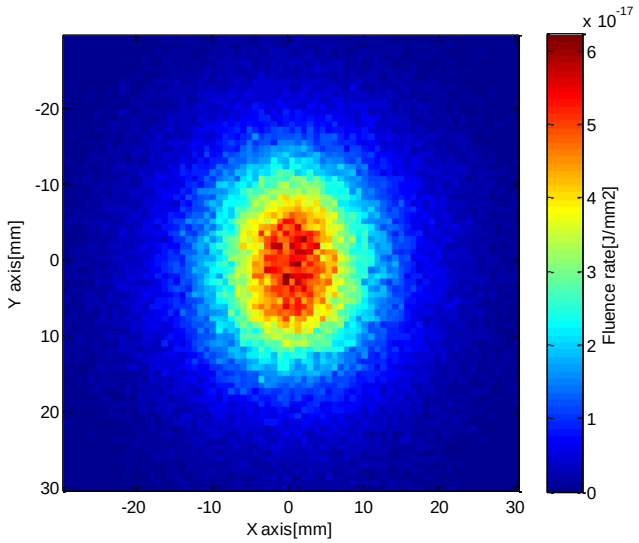

(b) Transmitted image with μ_{s_em} = 20cm^{-1} & μ_{a_em} = 0.1cm^{-1}

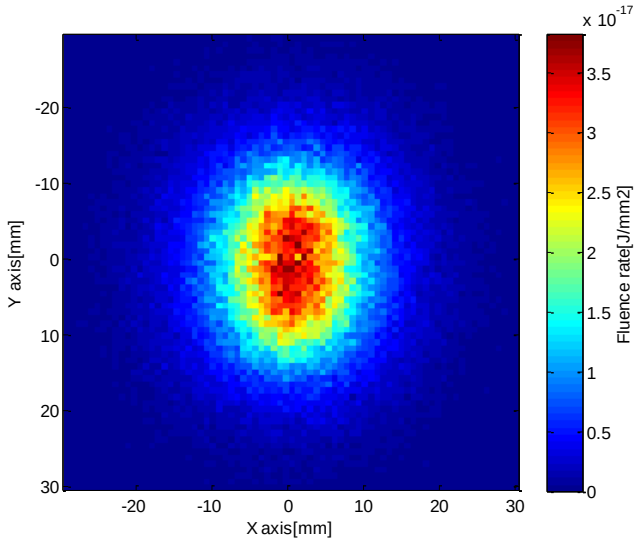

(c) Reflected image with μ_{s_em} = 20cm^{-1} & μ_{a_em} = 0.3cm^{-1}

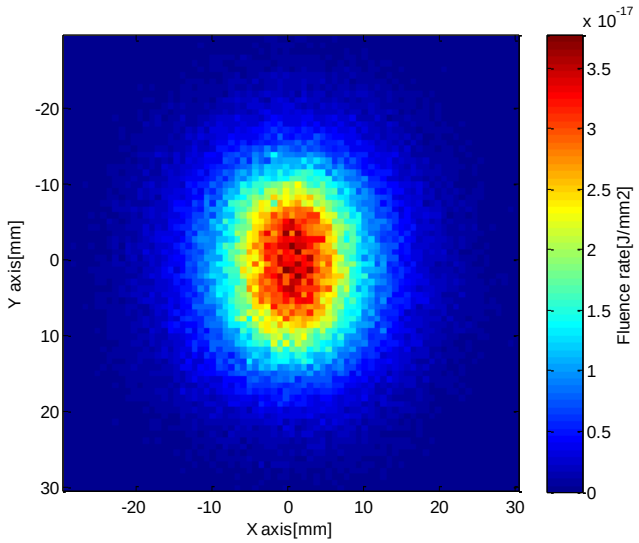

(d) Transmitted image with μ_{s_em} = 20cm^{-1} & μ_{a_em} = 0.3cm^{-1}

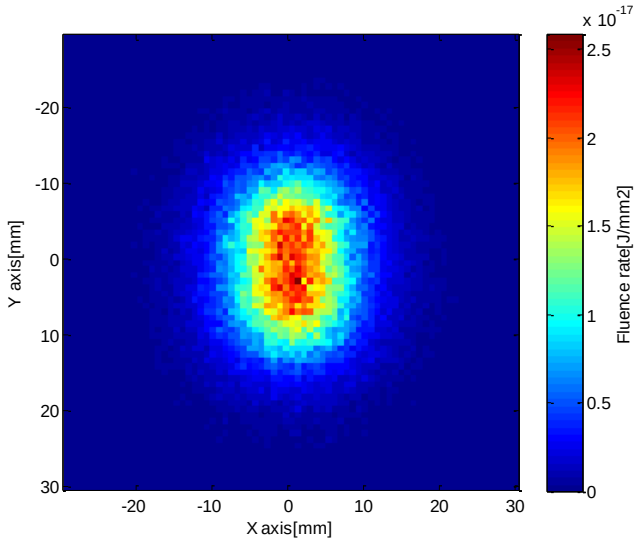

(e) Reflected image with μ_{s_em} = 60cm^{-1} & μ_{a_em} = 0.3cm^{-1}

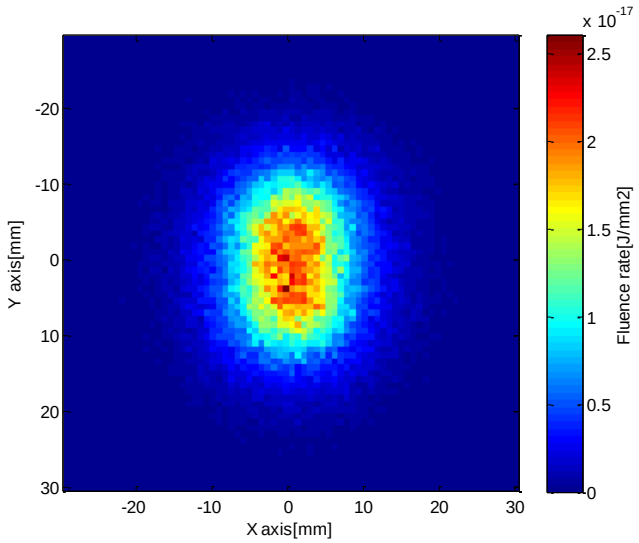

(f) Transmitted image with μ_{s_em} = 60cm^{-1} & μ_{a_em} = 0.3cm^{-1}

Figure 5-6 Photon fluence with full field illumination μ_{s_ex} = 100cm^{-1}, μ_{a_ex} = 0.6cm^{-1} and g = 0.9 at 10mm embedded depth and 20mm slab thickness.

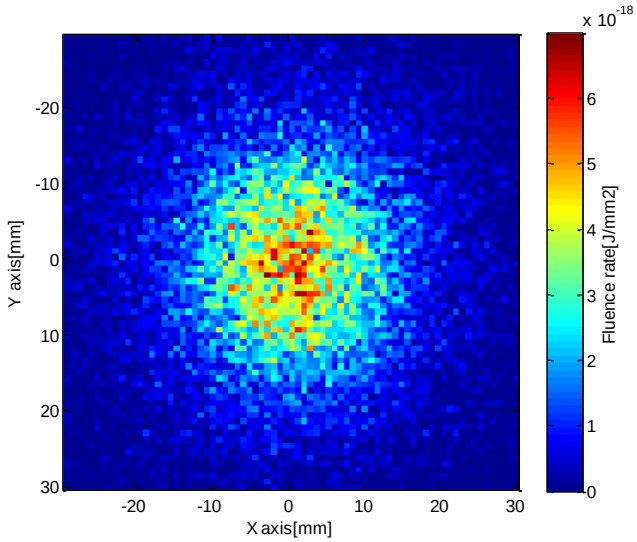

(a) Reflected image with μ_{s_em} = 20cm^{-1} & μ_{a_em} = 0.1cm^{-1}

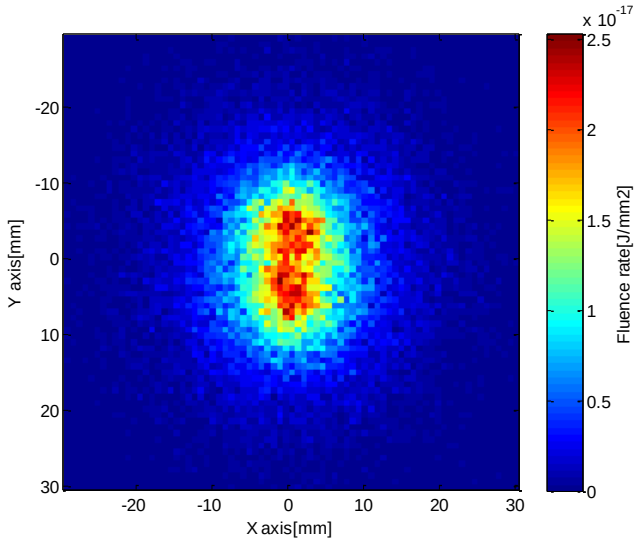

(b) Transmitted image with μ_{s_em} = 20cm^{-1} & μ_{a_em} = 0.1cm^{-1}

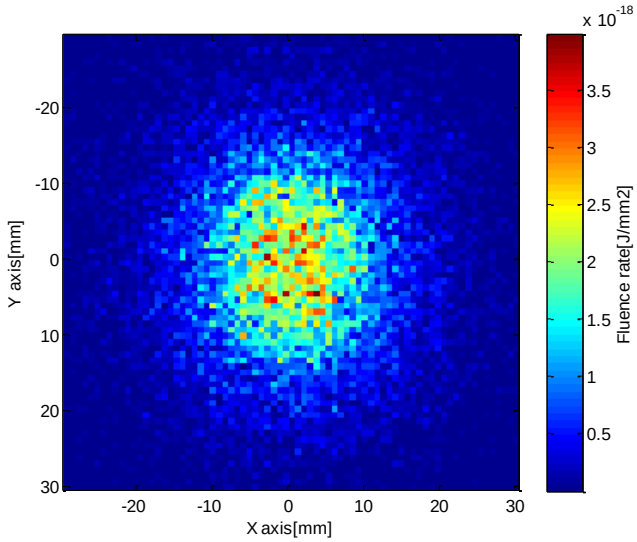

(c) Reflected image with μ_{s_em} = 20cm^{-1} & μ_{a_em} = 0.3cm^{-1}

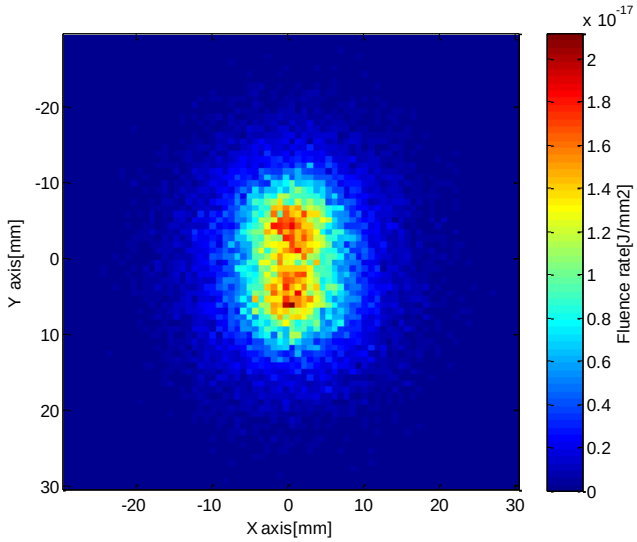

(d) Transmitted image with μ_{s_em} = 20cm^{-1} & μ_{a_em} = 0.3cm^{-1}

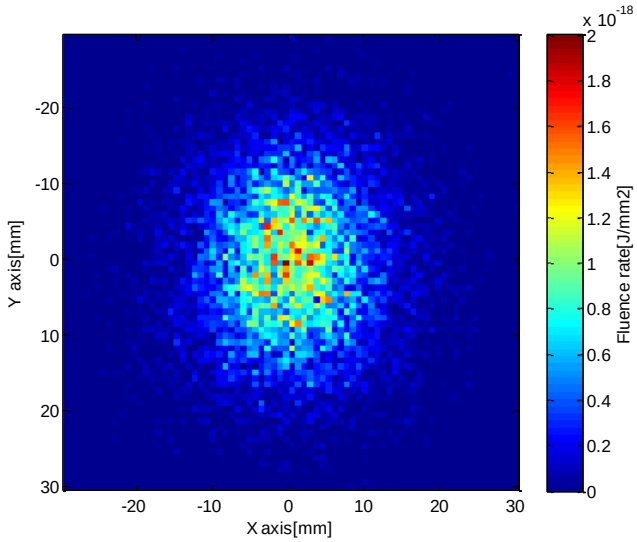

(e) Reflected image with μ_{s_em} = 60cm^{-1} & μ_{a_em} = 0.3cm^{-1}

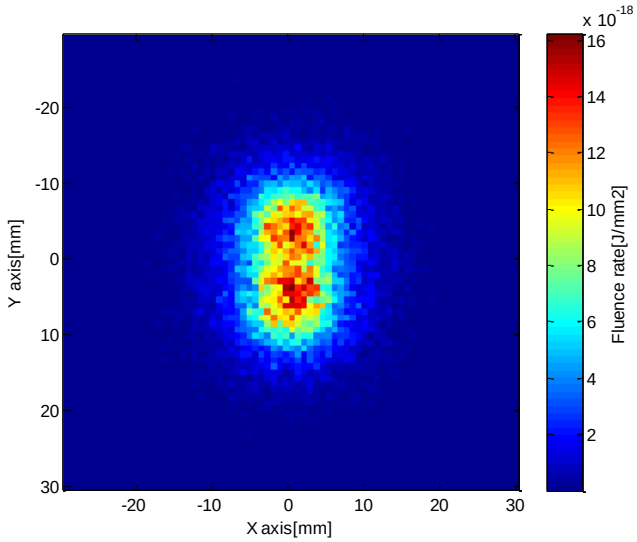

(f) Transmitted image with μ_{s_em} = 60cm^{-1} & μ_{a_em} = 0.3cm^{-1}

Figure 5-7 Photon fluence detected with full field illumination μ_{s_ex} = 100cm^{-1}, μ_{a_ex} = 0.6cm^{-1} and g = 0.9 at 14mm embedded depth and 20mm slab thickness.

Table 5-1 SNR at different target depth and emission optical properties

Depth	Emission Optical Properties	Reflection			Transmission		
		Sig. (10^{-15}J/cm^2)	Noi. (10^{-8} J/cm^2)	SNR (dB)	Sig. (10^{-15}J/cm^2)	Noi. (10^{-8} J/cm^2)	SNR (dB)
6mm	μ_{s_em} = 20cm^{-1} & μ_{a_em} = 0.1cm^{-1}	422.10	64.97	-123.75	178.96	42.30	-127.47
	μ_{s_em} = 20cm^{-1} & μ_{a_em} = 0.3cm^{-1}	264.65	51.44	-125.77	76.82	27.72	-131.15
	μ_{s_em} = 60cm^{-1} & μ_{a_em} = 0.3cm^{-1}	179.88	42.41	-127.45	24.79	15.75	-136.06
10mm	μ_{s_em} = 20cm^{-1} & μ_{a_em} = 0.1cm^{-1}	50.09	22.38	-133.00	49.70	22.29	-133.04
	μ_{s_em} = 20cm^{-1} & μ_{a_em} = 0.3cm^{-1}	25.41	15.94	-135.95	25.39	15.94	-135.95
	μ_{s_em} = 60cm^{-1} & μ_{a_em} = 0.3cm^{-1}	11.89	10.90	-139.25	11.76	10.85	-139.30
14mm	μ_{s_em} = 20cm^{-1} & μ_{a_em} = 0.1cm^{-1}	5.61	7.49	-142.51	12.90	11.36	-138.90
	μ_{s_em} = 20cm^{-1} & μ_{a_em} = 0.3cm^{-1}	2.36	4.86	-146.28	8.12	9.01	-140.91
	μ_{s_em} = 60cm^{-1} & μ_{a_em} = 0.3cm^{-1}	0.76	2.76	-151.17	5.42	7.36	-142.66

5.3.1.2 Discussion

The results from Monte Carlo simulations show the map of the photon fluence detected and the corresponding SNR. There is no quantitative comparison made of the spatial resolution through the images. However, some observations can be made from Figure 5-5 to Figure 5-7. When the objects separation is fixed at 1.2cm, the spatial resolution gets worse in reflection mode as the depth increases (Figure 5-5 (e) and Figure 5-7 (e)) but the resolution in transmission mode gets better on the other hand (Figure 5-5 (f) and Figure 5-7 (f)). The worst resolution obtained while the objects are buried in the middle of tissue slab (Figure 5-6). It can similarly be understood as the

‘banana shape’ of light propagation. As the targets move closer to the source or detector, the resolution gets better.

The effect of varying the optical parameters may be mostly clearly seen with reference to Figure 5-5. An increased μ_s leads to an increase of total photon path length, whilst a higher μ_a increases the loss during each single move. The Monte Carlo simulation results show that increasing either of them will reduce the photon fluence detected in both reflection and transmission. In terms of the spatial resolution, comparing Figure 5-5 (a) with Figure 5-5 (c), the increase of μ_a results in a better resolution which can be understood as μ_a stops the photons with long trajectory reaching the boundary.

Comparing the Figure 5-5 with Figure 5-7, the depth of the targets is the most crucial element in terms of the photon fluence detected. As the depth gets deeper, light propagates over a large volume and fewer photons enter the fluorescence target, which results in a fewer photons detected in both reflection and transmission. However, good spatial resolution is obtained in the transmission image, as the fluorescence target is near the other side of the boundary.

From the results in Table 5-1, the increased target depth leads to a lower SNR in both reflection and transmission, as the probability is higher for a photon to be absorbed in the medium with longer path length. Generally, either increased μ_s or μ_a results in a lower SNR, but this effect is not that obvious when the target is located near boundaries (-123.75dB to -127.45dB in reflection and -138.9dB to -142.66dB in transmission). The embedded depth change has greater influence on reflection than that in transmission which can be understood because of the higher photon density near the incident boundary.

5.3.2 Scanning input (SI) system

The SI system setup is shown in Figure 5-8. The size of the detector is 1cm in radius, all the light that reaches the detector will be integrated and represents the intensity corresponding to the input position. Light illuminates from a single point normally to the tissue slab, and will scan over a twenty by twenty point grid to form an image. 350K photons are launched into the tissue slab from one single point according to Figure 5-9.

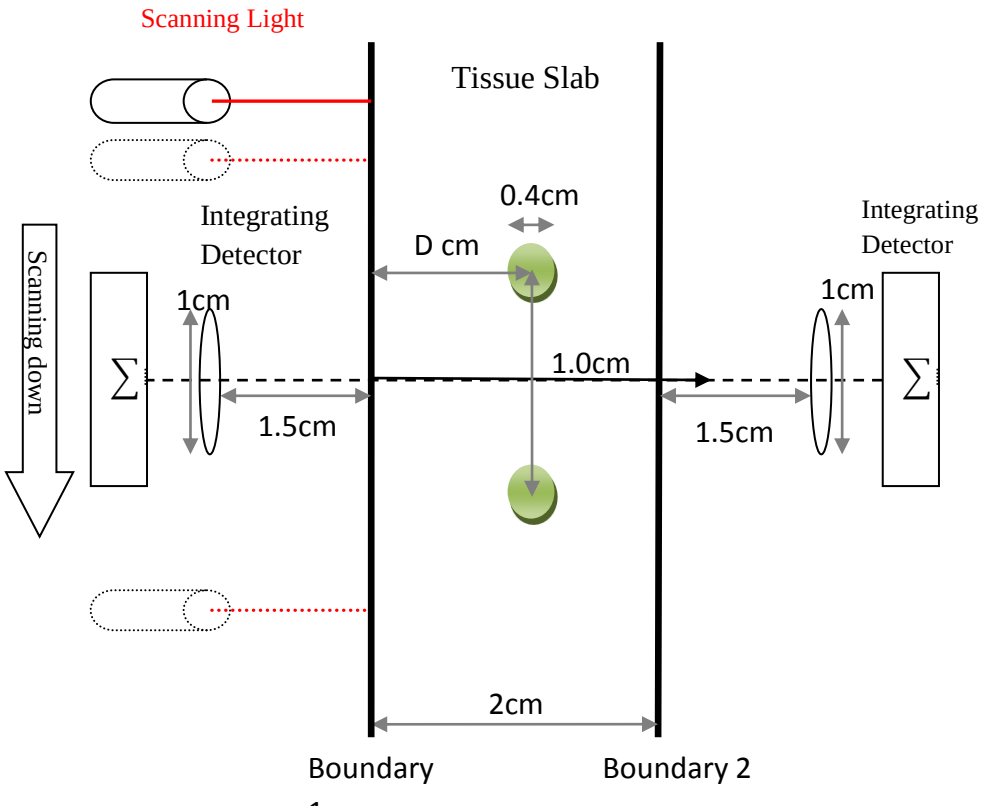

Figure 5-8 Simulation configuration of scanning input system

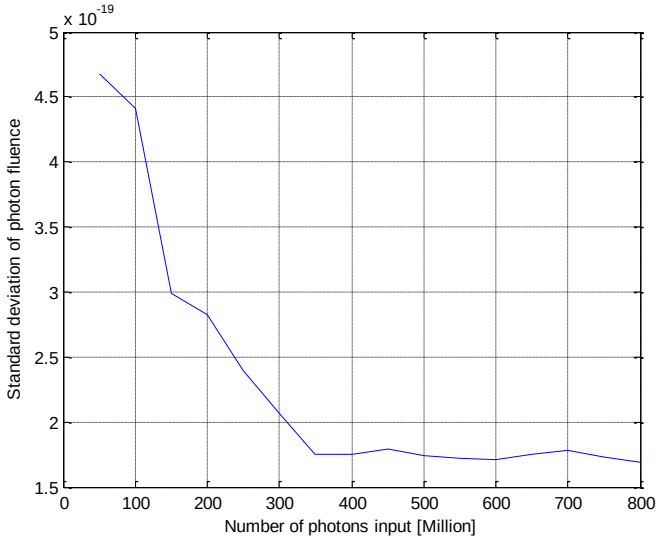

Figure 5-9 Standard deviation via number of photons input (SI system)

The geometry of the setup is the same as the FI system. The size of the fluorescence target is assumed 0.4cm in diameter, a fixed separation between the fluorescence targets is maintained at 1.0cm. The quantum yield (QY) is set to 40%. The thickness of the tissue slab is 2cm. Optical parameters and embedded depth varies while the emission light images are produced in both reflection and transmission.

Figure 5-10 to Figure 5-12 show images of the medium obtained with the SI system using the same optical properties applied in FI system. μ_s and μ_a for the excitation light are 100cm^{-1} and 0.6cm^{-1} respectively and g = 0.9.

5.3.2.1 Results

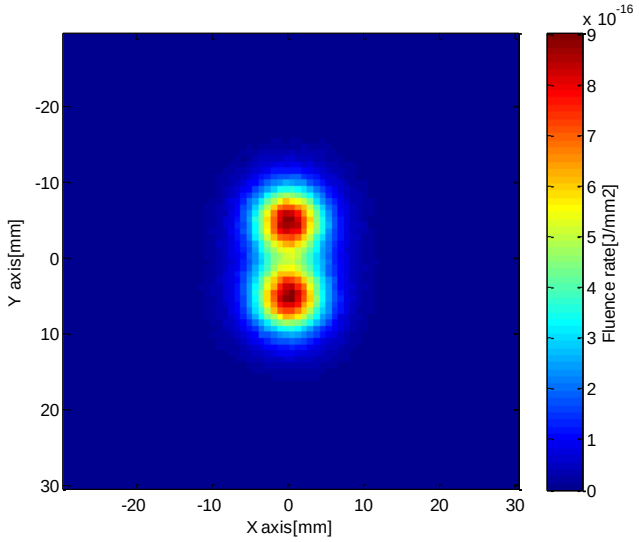

(a) Reflected image with μ_{s_em} = 20cm^{-1} & μ_{a_em} = 0.1cm^{-1}

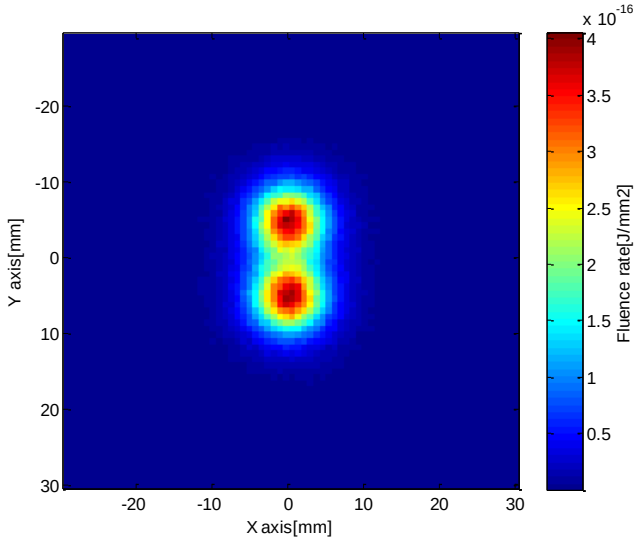

(b) Transmitted image with μ_{s_em} = 20cm^{-1} & μ_{a_em} = 0.1cm^{-1}

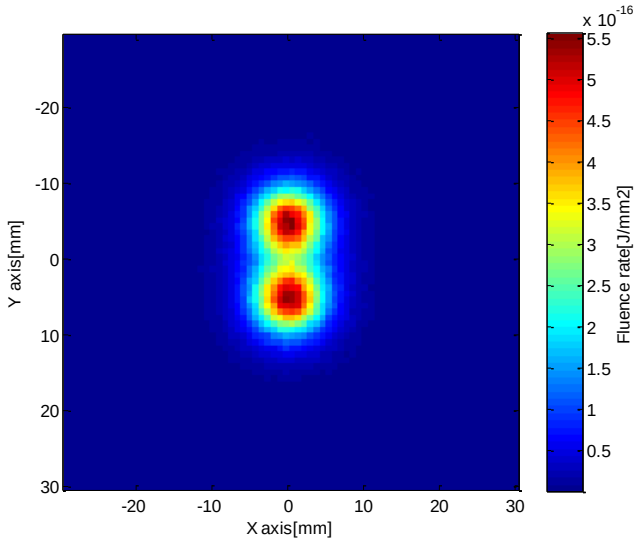

(c) Reflected image with μ_{s_em} = 20cm^{-1} & μ_{a_em} = 0.3cm^{-1}

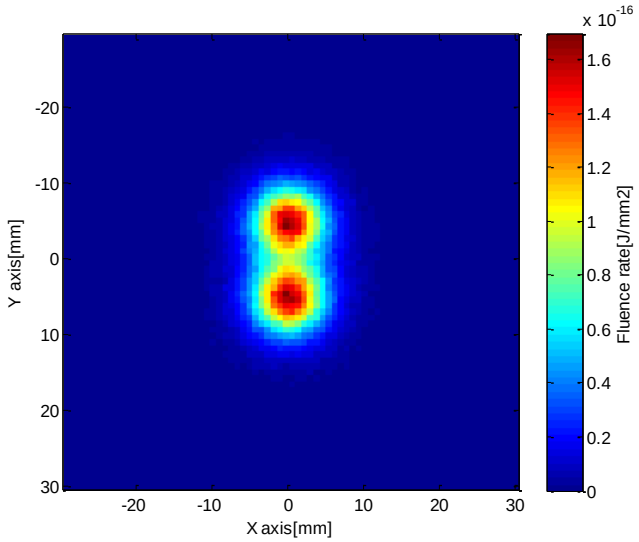

(d) Transmitted image with μ_{s_em} = 20cm^{-1} & μ_{a_em} = 0.3cm^{-1}

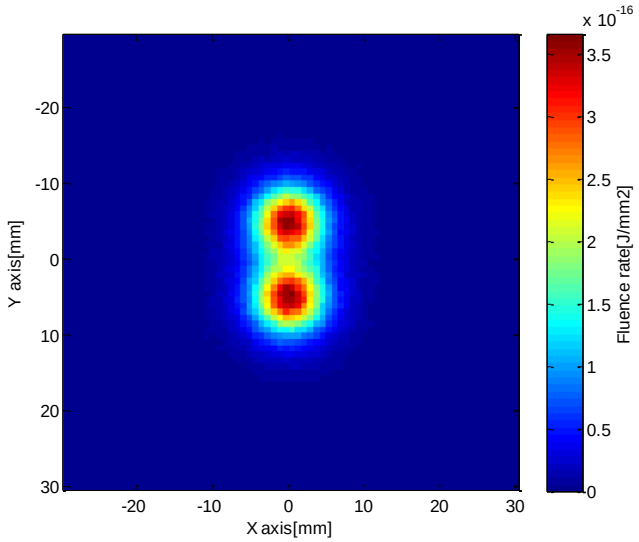

(e) Reflected image with μ_{s_em} = 60cm^{-1} & μ_{a_em} = 0.3cm^{-1}

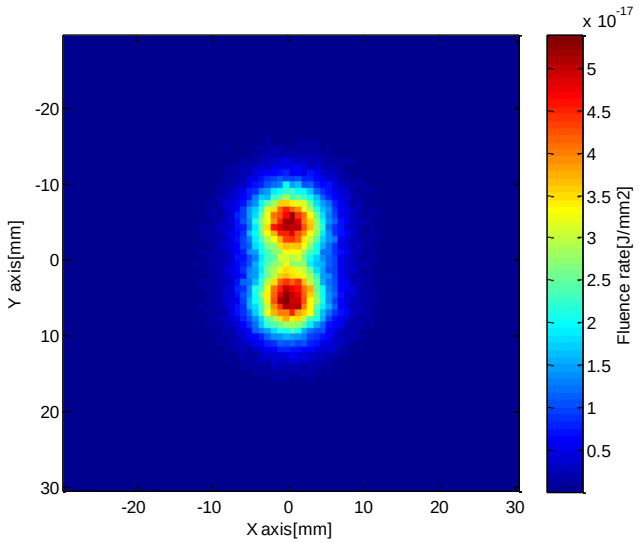

(f) Transmitted image with μ_{s_em} = 60cm^{-1} & μ_{a_em} = 0.3cm^{-1}

Figure 5-10 Photon fluence with scanning input μ_{s_ex} = 100cm^{-1}, μ_{a_ex} = 0.6cm^{-1} and g = 0.9 at 6mm embedded depth and 20mm slab thickness.

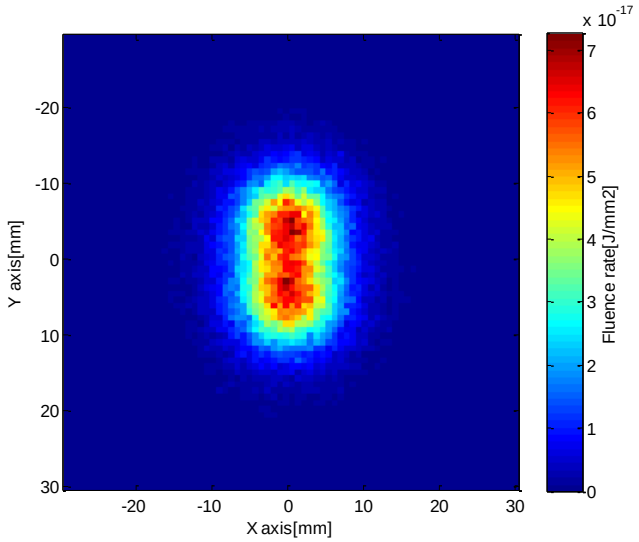

(a) Reflected image with μ_{s_em} = 20cm^{-1} & μ_{a_em} = 0.1cm^{-1}

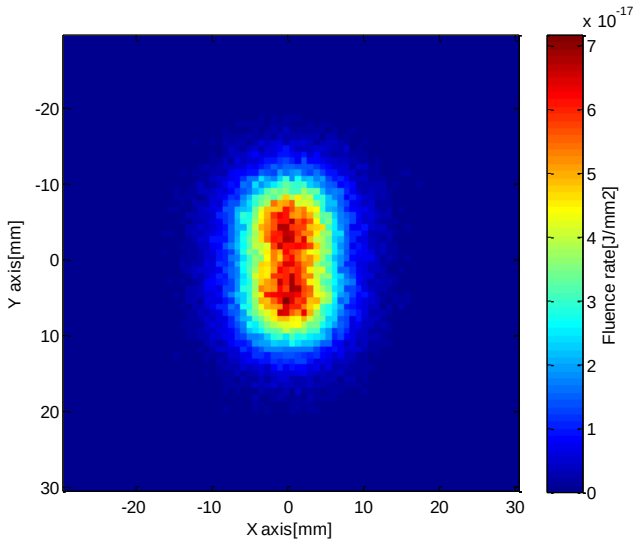

(b) Transmitted image with μ_{s_em} = 20cm^{-1} & μ_{a_em} = 0.1cm^{-1}

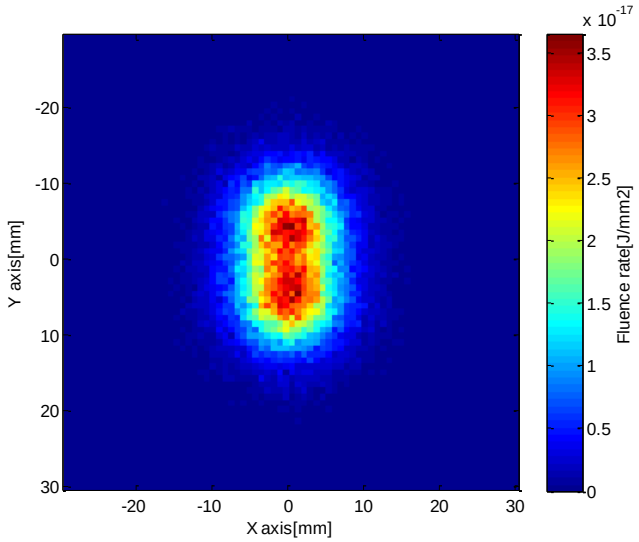

(c) Reflected image with μ_{s_em} = 20cm^{-1} & μ_{a_em} = 0.3cm^{-1}

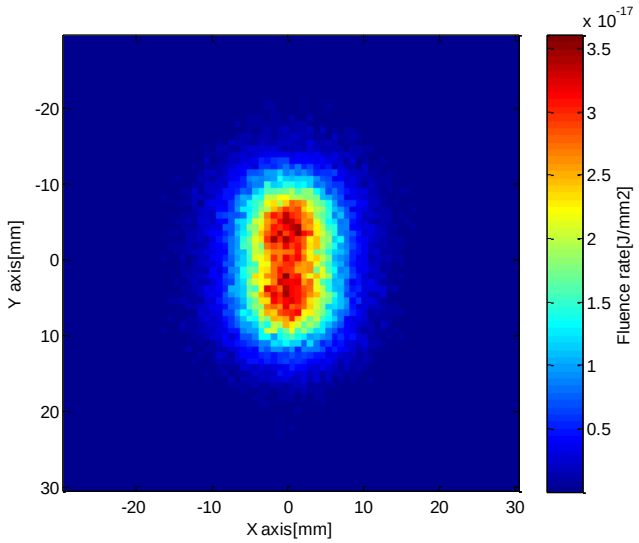

(d) Transmitted image with μ_{s_em} = 20cm^{-1} & μ_{a_em} = 0.3cm^{-1}

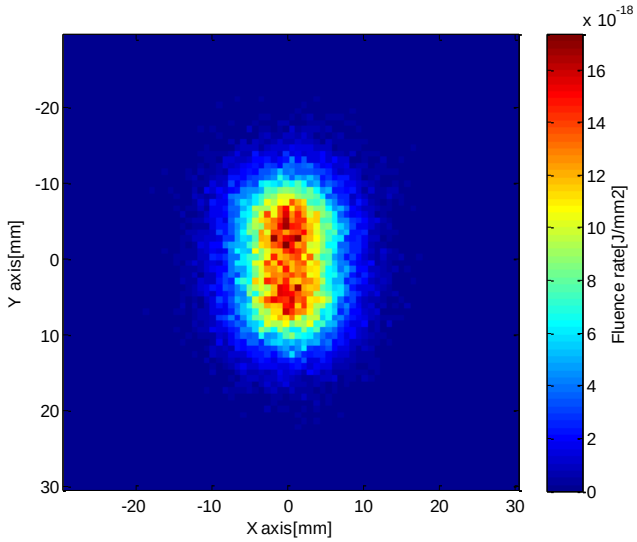

(e) Reflected image with μ_{s_em} = 60cm^{-1} & μ_{a_em} = 0.3cm^{-1}

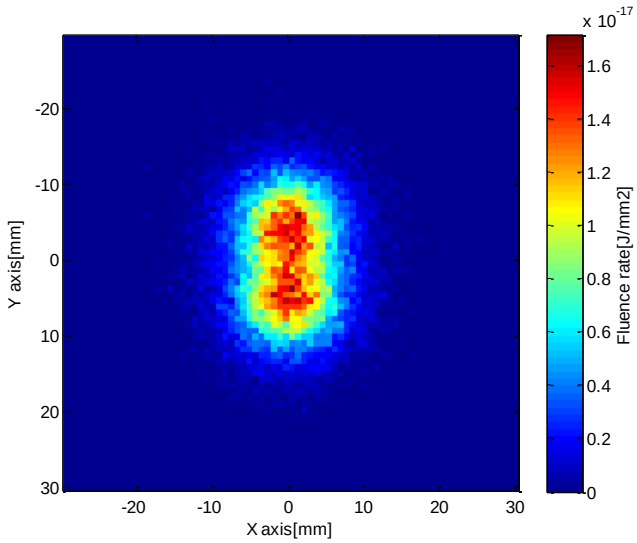

(f) Transmitted image with μ_{s_em} = 60cm^{-1} & μ_{a_em} = 0.3cm^{-1}

Figure 5-11 Photon fluence with scanning input μ_{s_ex} = 100cm^{-1}, μ_{a_ex} = 0.6cm^{-1} and g = 0.9 at 10mm embedded depth and 20mm slab thickness.

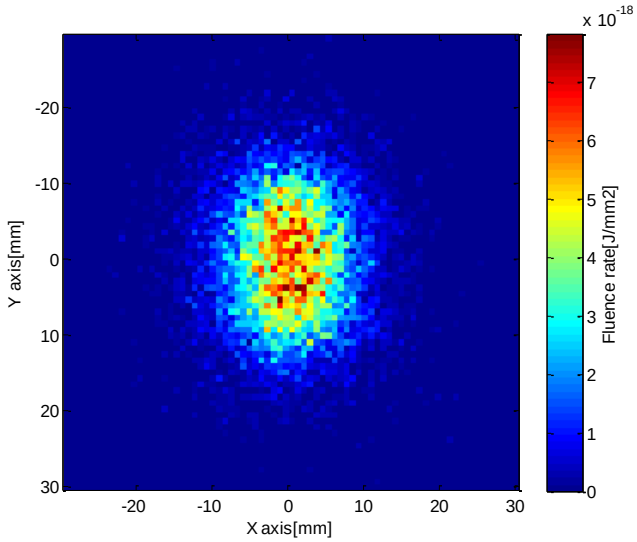

(a) Reflected image with μ_{s_em} = 20cm^{-1} & μ_{a_em} = 0.1cm^{-1}

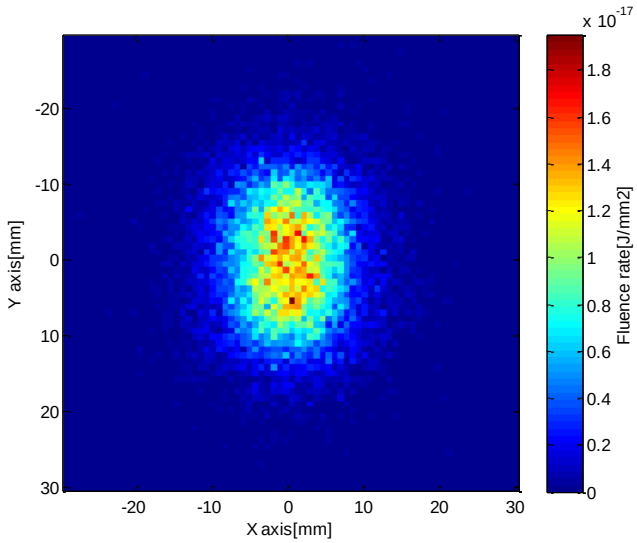

(b) Transmitted image with μ_{s_em} = 20cm^{-1} & μ_{a_em} = 0.1cm^{-1}

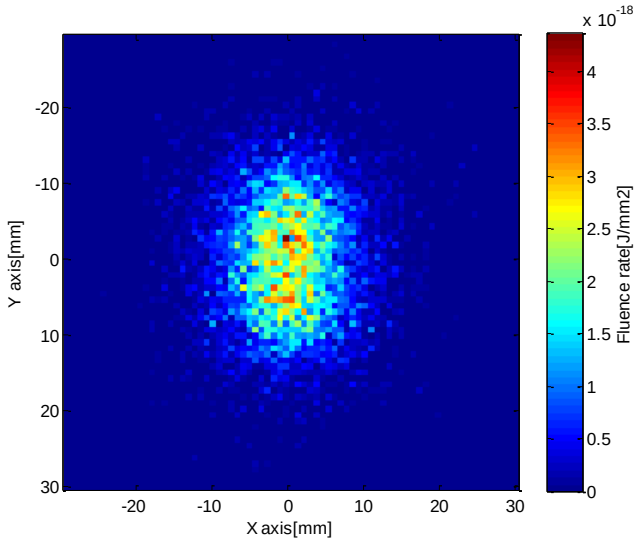

(c) Reflected image with μ_{s_em} = 20cm^{-1} & μ_{a_em} = 0.3cm^{-1}

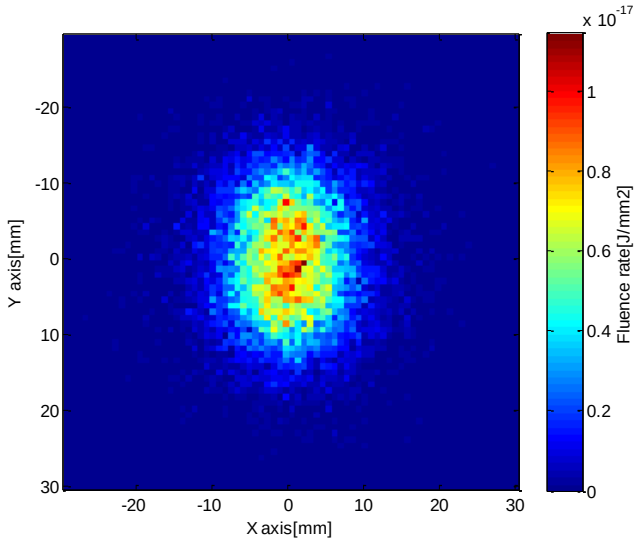

(d) Transmitted image with μ_{s_em} = 20cm^{-1} & μ_{a_em} = 0.3cm^{-1}

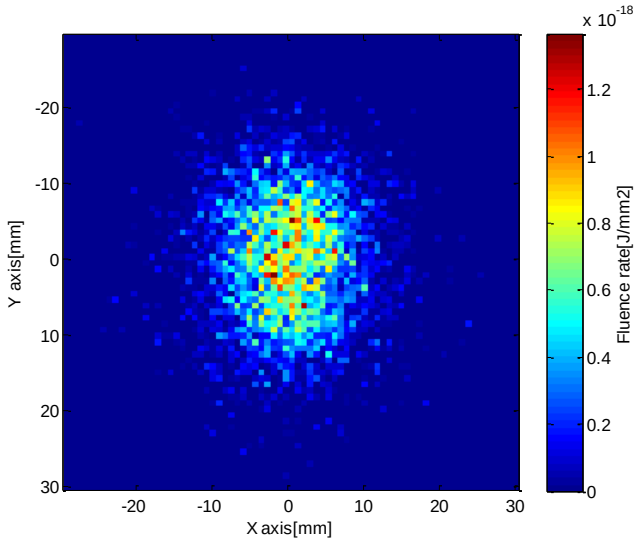

(e) Reflected image with μ_{s_em} = 60cm^{-1} & μ_{a_em} = 0.3cm^{-1}

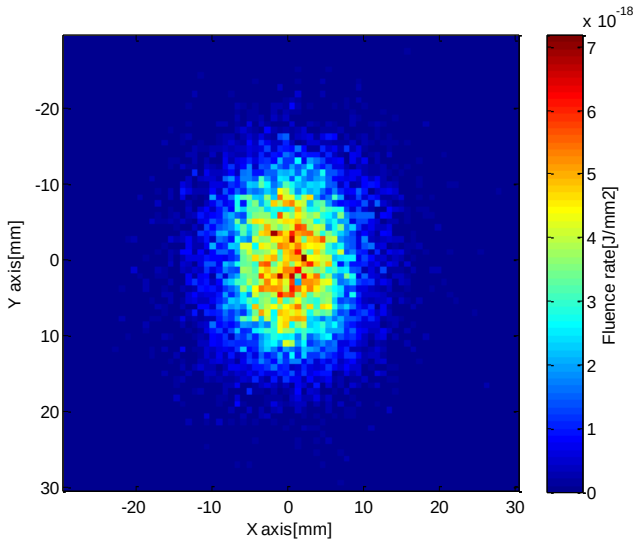

(f) Transmitted image with μ_{s_em} = 60cm^{-1} & μ_{a_em} = 0.3cm^{-1}

Figure 5-12 Photon fluence with scanning input μ_{s_ex} = 100cm^{-1}, μ_{a_ex} = 0.6cm^{-1} and g = 0.9 at 14mm embedded depth and 20mm slab thickness.

Table 5-2 SNR at different target depth and excitation optical properties

Depth	Excitation Optical Properties	Reflection			Transmission		
		Sig. (10^{-15}J/cm^2)	Noi. (10^{-8} J/cm^2)	SNR (dB)	Sig. (10^{-15}J/cm^2)	Noi. (10^{-8} J/cm^2)	SNR (dB)
6mm	μ_{s_em} = 20cm^{-1} & μ_{a_em} = 0.1cm^{-1}	206.65	45.46	-126.85	87.67	29.61	-130.57
	μ_{s_em} = 20cm^{-1} & μ_{a_em} = 0.3cm^{-1}	129.49	35.99	-128.88	37.63	19.40	-134.25
	μ_{s_em} = 60cm^{-1} & μ_{a_em} = 0.3cm^{-1}	88.34	29.72	-130.54	12.15	11.02	-139.15
10mm	μ_{s_em} = 20cm^{-1} & μ_{a_em} = 0.1cm^{-1}	24.59	15.68	-136.09	24.58	15.68	-136.09
	μ_{s_em} = 20cm^{-1} & μ_{a_em} = 0.3cm^{-1}	12.58	11.22	-139.00	12.44	11.15	-139.05
	μ_{s_em} = 60cm^{-1} & μ_{a_em} = 0.3cm^{-1}	5.85	7.65	-142.33	5.77	7.60	-142.38
14mm	μ_{s_em} = 20cm^{-1} & μ_{a_em} = 0.1cm^{-1}	2.79	5.29	-145.54	6.52	8.07	-141.86
	μ_{s_em} = 20cm^{-1} & μ_{a_em} = 0.3cm^{-1}	1.20	3.46	-149.21	4.02	6.34	-143.95
	μ_{s_em} = 60cm^{-1} & μ_{a_em} = 0.3cm^{-1}	0.39	1.98	-154.05	2.68	5.18	-145.72

5.3.2.2 Discussion

Figure 5-10 to Figure 5-12 demonstrate that depth plays a more significant role here compared to the FI system. It can be understood as fewer photons are converted to the emission wavelength. Because of the integrated detector, the exit position of emission photons is not a significant effect, and the amount of excitation photons reaching the targets is more important in a SI system.

Comparing Figure 5-10 with Figure 5-5, when the fluorescence targets are near the incident boundary, the excitation photons can easily reach them which leads to an excellent spatial resolution in both reflective (Figure 5-10 (c) with Figure 5-5 (c)) and transmitted (Figure 5-10 (d) with Figure 5-5 (d)) image.

The spatial resolution degrades rapidly in both reflection and transmission as the depth increases. The excitation light is absorbed by the medium more easily than emission due to a higher μ_s and μ_a. Deeper targets lead to a longer excitation trajectory and more photons get absorbed.

Considering Table 5-2, the SNR (dB) in reflection drops approximately 10dB as the depth increases at a step of 4mm while it is generally stable in transmission which is similar to the results of FI system. Besides, the SNR drops in both reflection and transmission as the μ_{s_em} and μ_{a_em} increased from 20cm^{-1} and 0.1cm^{-1} to 60cm^{-1} and 0.3cm^{-1}, but it is the secondary effect compared to the change of depth especially when the targets locate near the boundaries, which is equivalent to the FI system.

5.4 Diffusion model Setup

The previous section shows the Monte Carlo results for a range of optical properties. In order to investigate and evaluate the SNR and spatial resolution for different wavelengths, the simulation should be run with a wide range of μ_a and μ_s. The analytical model with diffusion approximation is applied here to save time and produce smoother curves. Two model configurations are developed to simulate the fluorescence targets inside the tissue being excited and then the emitting light at another wavelength to investigate and compare the effect on SNR and spatial resolution whilst the fluorescent targets' depth and optical properties vary.

5.4.1 Model description

To investigate the spatial resolution and SNR, two fluorescence targets are buried into the tissue slab, which is parallel to the slab boundary. The depth and separation between the two fluorescence targets are varied.

The model presented in this section is a two stage diffusion model propagating a Green's function to the target plane at the excitation wavelength and then propagating from the target to the output planes using Green's functions at the emission wavelengths. To meet both boundaries at incident and detector plane, an infinite series of dipole photon sources need to be added as discussed by Eason *et al.* [164]. When a light pulse launches from one side of the scattering medium, a TPSF can be obtained at the target plane using the Equation 4-12. By summing the fluence of each time interval of the TPSF, the overall fluence at the fluorescent target plane is obtained. Similarly, the fluorescence targets can be treated as light sources, and contribute to a TPSF at each point of the boundary. As discussed in Chapter 4, as the boundary condition $\Phi = 0$ is applied, it is appropriate to calculate the flux at the detector plane. The integral of the TPSF will give detected fluorescence emission signal.

Figure 5-13 (a) below shows a diffusion model, where the excitation light pulse launches from one side of the scattering medium. And the spatial distribution of excitation light at the mid-plane is presented in Figure 5-13 (b).

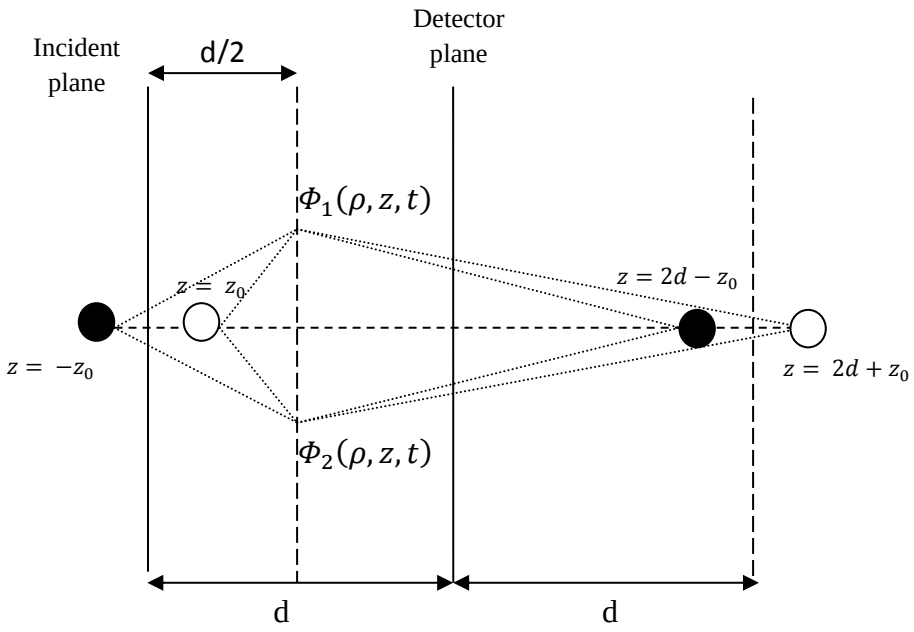

(a)

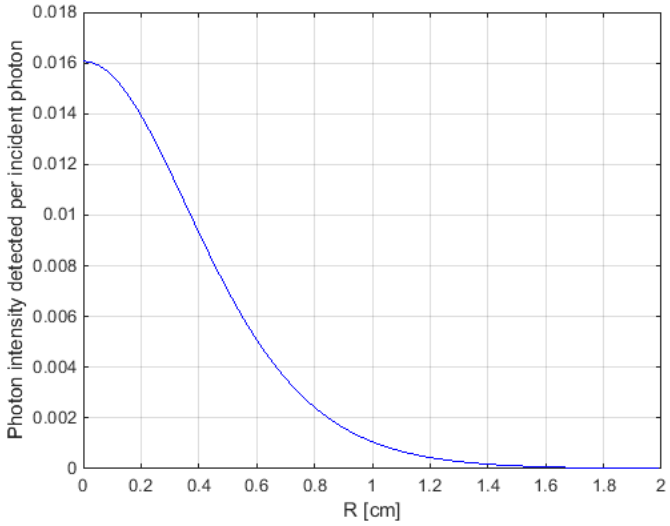

(b)

Figure 5-13 (a) Diffusion model geometry of collimated light beam illuminates a 2cm tissue slab, seven dipole sources applied, two of them are shown in the figure;. (b) Spatial distribution at the mid-plane of the slab.

Figure 5-14 (a) shows the geometry and corresponding spatial distribution at the incident boundary while two isotropic point sources which represent the two fluorescent targets are located at the mid-plane of the tissue slab. The intensity of the light source will be scaled using the excitation output at the

mid-plane. The spatial distribution represents the reflectance detected of emission wavelength and is shown in Figure 5-14 (b).

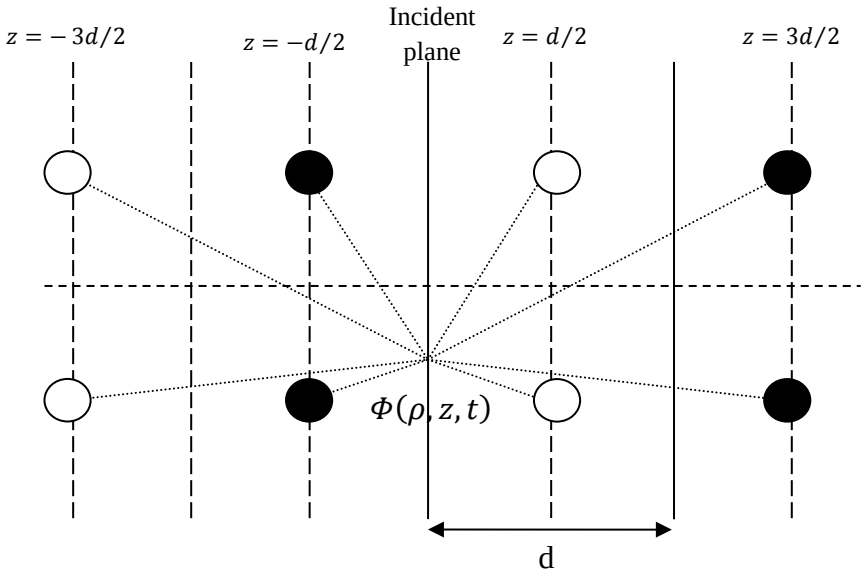

(a)

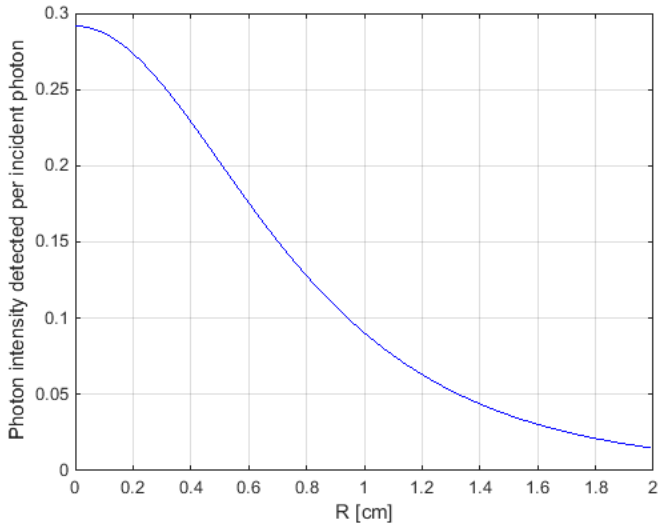

(b)

Figure 5-14 (a) Diffusion model geometry of point sources in the mid-plane illuminate isotropically, infinite dipole sources applied, two of them are shown in the figure; (b) Spatial distribution at the incident boundary.

With closer fluorescent targets separation, the light intensity within the detector plane is getting higher but with poorer spatial resolution. In contrast, better spatial resolution with poorer light intensity can be obtained by moving one target away from the other. With scanning light illumination and

integrated detectors, Figure 5-15 shows emission light distribution. The green curve below represents the sum of the detected light from the two fluorescence targets.

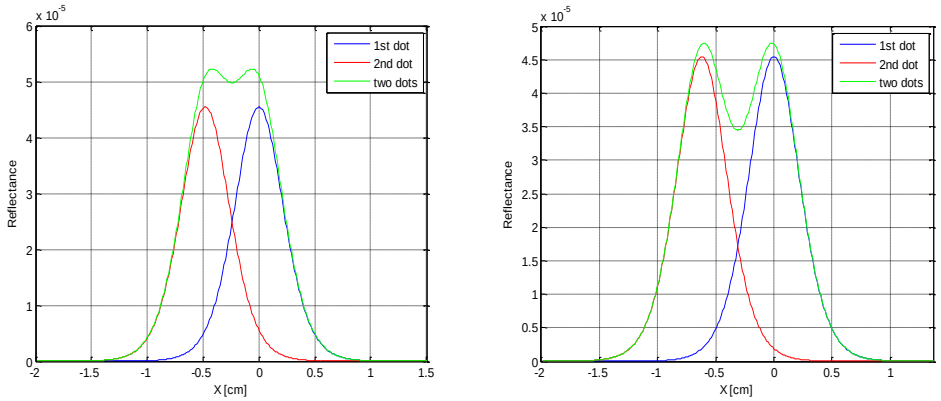

(a) (b)

Figure 5-15 Spatial light distribution of two fluorescent targets emission

In this chapter, the spatial resolution is defined as the minimum separation of two targets that can still be perceived as separate by an observer. Based on the Sparrow criterion [165], the minimum separation S_{min} achieved when the point two curves overlapped equals full-width half maximum (FWHM). The lower the value, the better the resolution. The definition of SNR here is the same as defined in section 5.3.

5.4.2 Full field illumination system

The first configuration introduced is based on the most commonly used fluorescence imaging system as shown in Figure 5-16.

The semi-infinite homogenous tissue slab is 2cm thick, with two fluorescence targets embedded at D cm in depth and L cm in separation. Multiple excitation sources are placed along the left boundary to perform full field illumination. If the separation of the light sources is small enough, the light distribution at the fluorescence plane can be assumed to be uniform. Hence the fluorescence targets become two isotropic point sources in the medium. The reflected emission light is collected by an imaging detector. The quantum yield (QY) of the fluorescent target is set to 40%, which is as same as the QY in the Monte Carlo simulation. The optical properties and depth varies over the range shown in Table 5-3.

Table 5-3 Range of parameters vary in the simulation

	Minimum	**Step**	**Maximum**
μ_s of excitation	80cm^{-1}	5cm^{-1}	140cm^{-1}
μ_a of excitation	0.2cm^{-1}	0.05cm^{-1}	0.8cm^{-1}
μ_s of emission	20cm^{-1}	5cm^{-1}	80cm^{-1}
μ_a of emission	0cm^{-1}	0.05cm^{-1}	0.6cm^{-1}
D	0.6cm	0.05cm	1.4cm

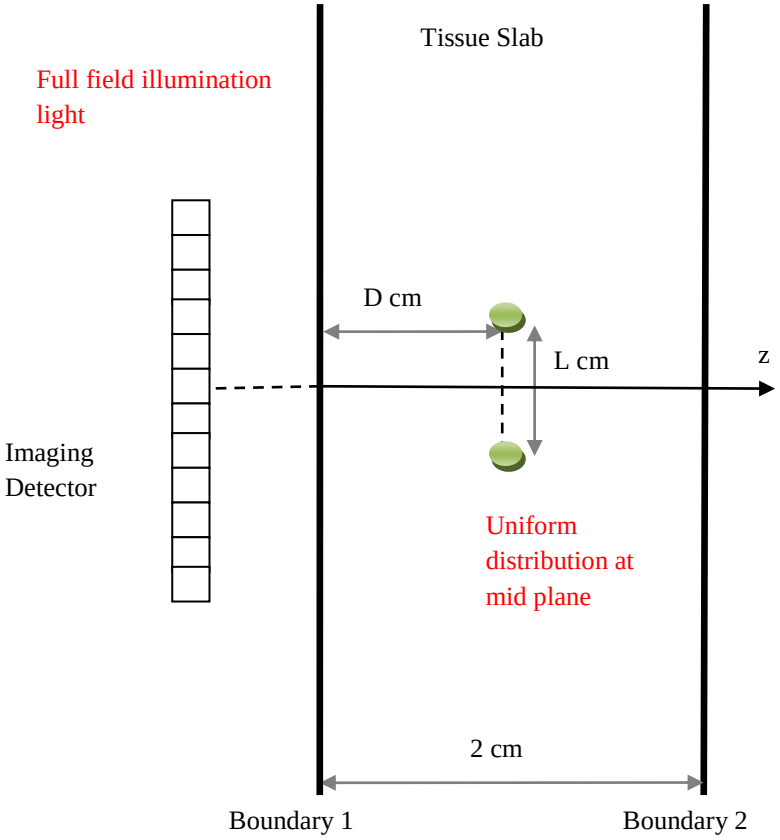

Figure 5-16 Simulation configuration of full field illumination

5.4.2.1 Results

The results compare the spatial resolution and SNR over a broad range of scattering, absorption coefficients and target depth.

Figure 5-17 (a) shows the spatial resolution against scattering and absorption coefficients of emission, with g = 0.9, μ_a and μ_s of excitation equal 0.2cm^{-1} and 80cm^{-1} respectively and D = 0.6cm.

(b) is the same as (a) but with a higher μ_a and μ_s of excitation. μ_a = 0.8 cm^{-1} and μ_s = 140cm^{-1}.

By applying the same optical parameters as (a) and (b), (c) and (d) show the spatial resolution with D = 1.0cm, while (e) and (f) show the spatial resolution with D = 1.4cm.

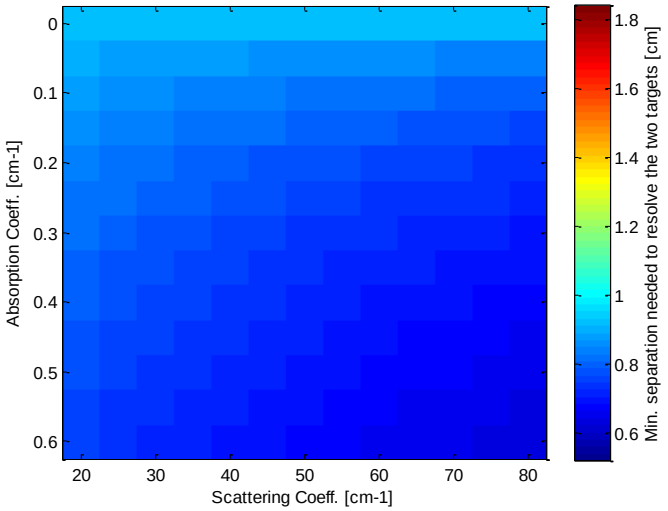

(a) μ_{a_ex} = 0.2 cm^{-1}, μ_{s_ex} = 80cm^{-1} and D = 0.6cm

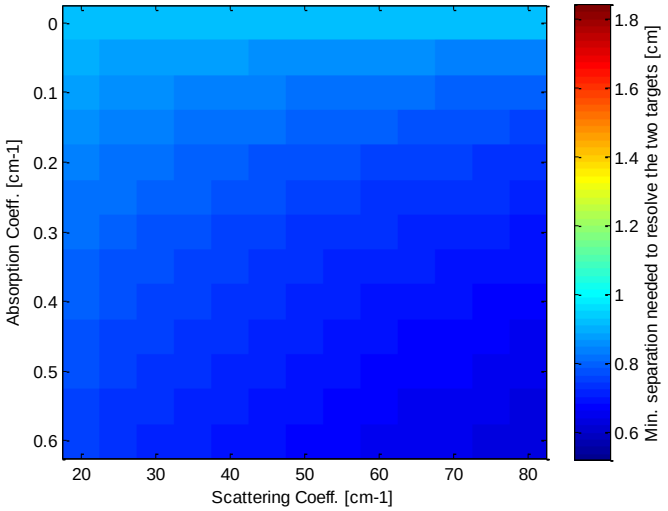

(b) μ_{a_ex} = 0.8 cm^{-1}, μ_{s_ex} = 140cm^{-1} and D = 0.6cm

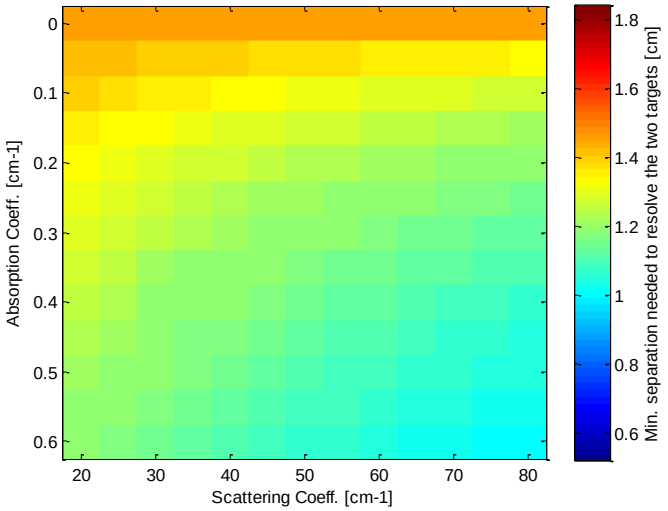

(c) μ_{a_ex} = 0.2 cm^{-1}, μ_{s_ex} = 80cm^{-1} and D = 1.0cm

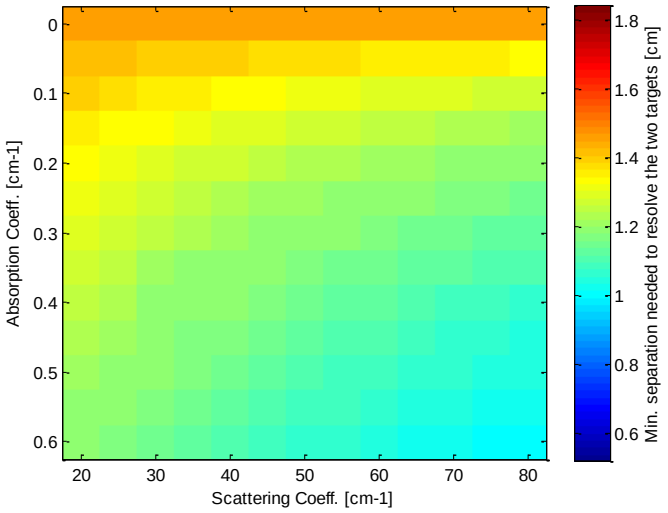

(d) μ_{a_ex} = 0.8 cm^{-1}, μ_{s_ex} = 140cm^{-1} and D = 1.0cm

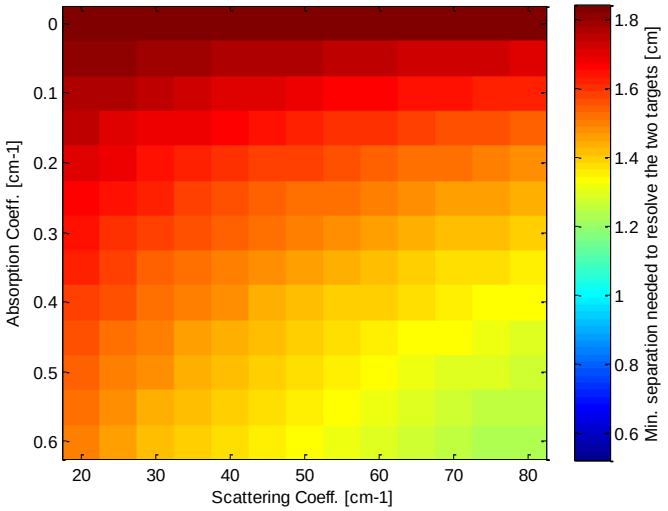

(e) μ_{a_ex} = 0.2 cm^{-1}, μ_{s_ex} = 80cm^{-1} and D = 1.4cm

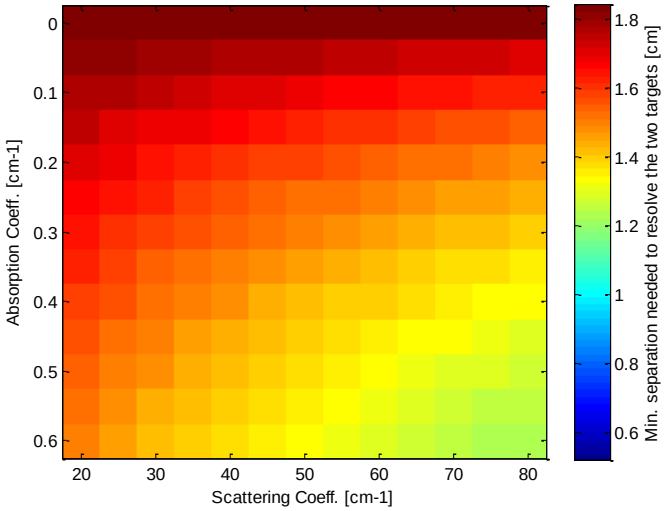

(f) μ_{a_ex} = 0.8 cm^{-1}, μ_{s_ex} = 140cm^{-1} and D = 1.4cm

Figure 5-17 Minimum separations to resolve the two objects in FI system against the optical parameters of emission wavelength.

Figure 5-18 is similar but shows the SNR detected against the optical parameters.

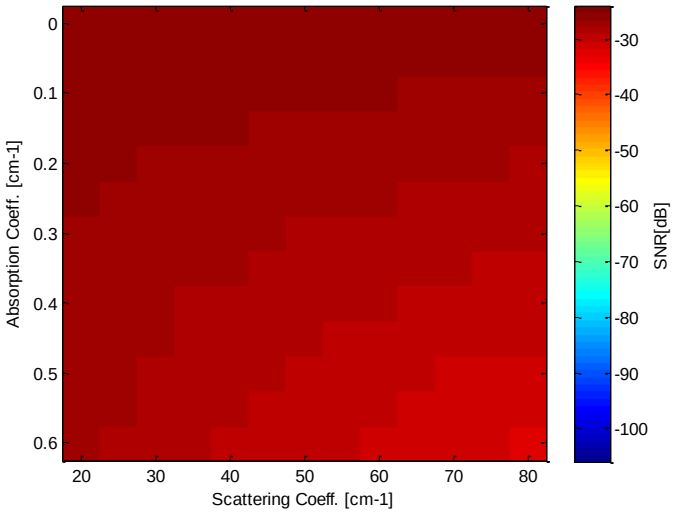

(a) μ_{a_ex} = 0.2 cm^{-1}, μ_{s_ex} = 80cm^{-1} and D = 0.6cm

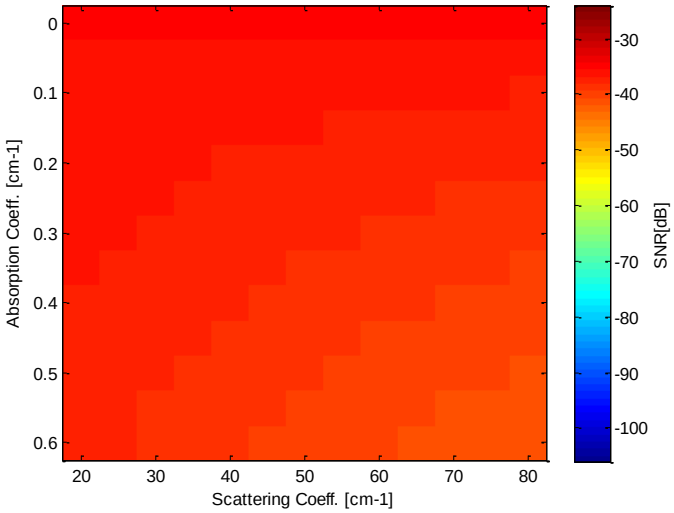

(b) μ_{a_ex} = 0.8 cm^{-1}, μ_{s_ex} = 140cm^{-1} and D = 0.6cm

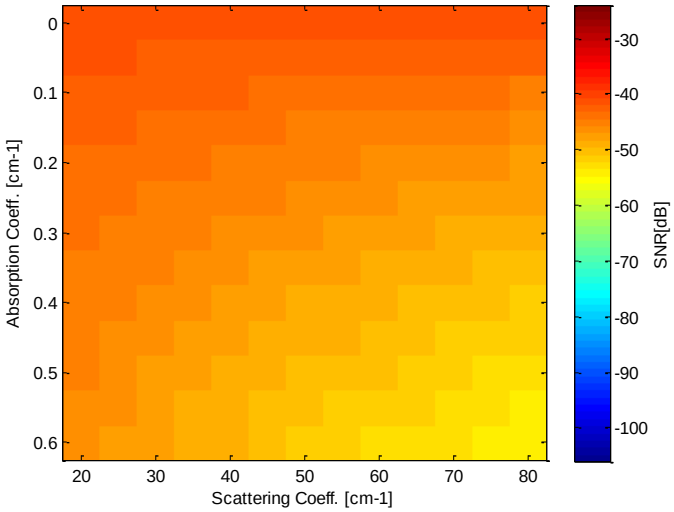

(c) μ_{a_ex} = 0.2 cm^{-1}, μ_{s_ex} = 80cm^{-1} and D = 1.0cm

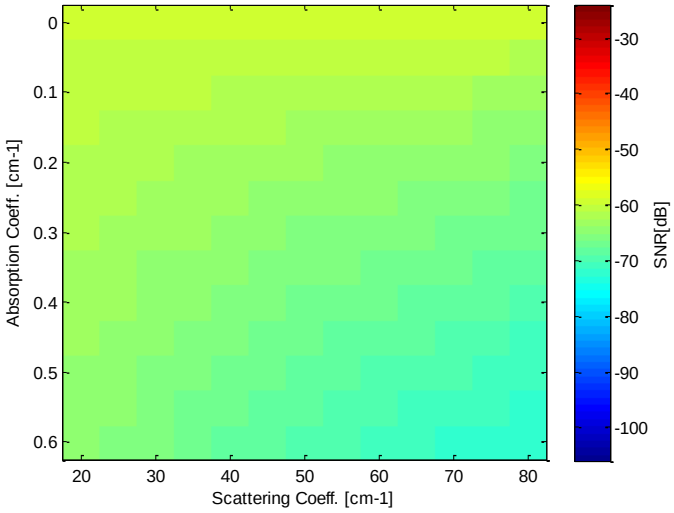

(d) μ_{a_ex} = 0.8 cm^{-1}, μ_{s_ex} = 140cm^{-1} and D = 1.0cm

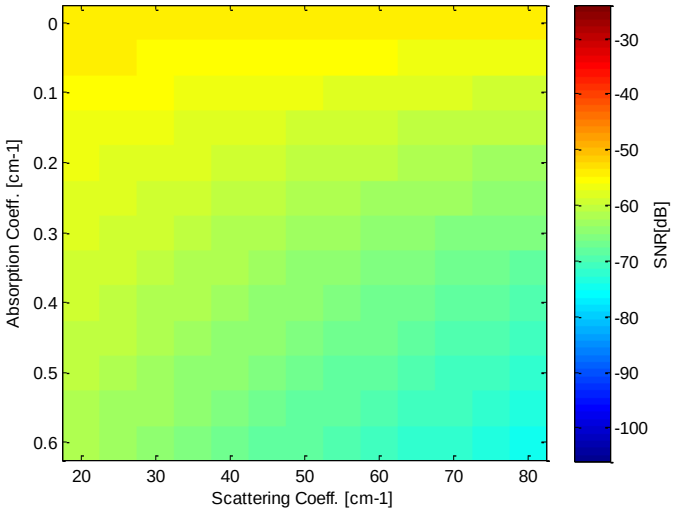

(e) μ_{a_ex} = 0.2 cm^{-1}, μ_{s_ex} = 80cm^{-1} and D = 1.4cm

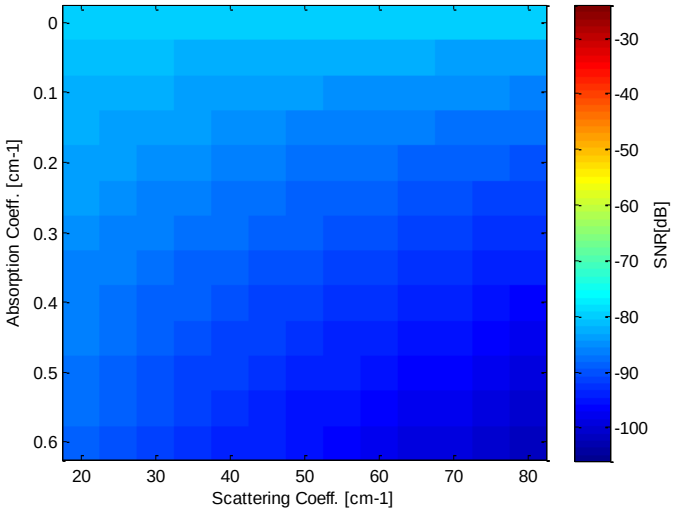

(f) μ_{a_ex} = 0.8 cm^{-1}, μ_{s_ex} = 140cm^{-1} and D = 1.4cm

Figure 5-18 SNR detected in FI system against the optical parameters of emission wavelength.

5.4.2.2 Discussion

Figure 5-17 shows how spatial resolution changes while the optical parameters and fluorophore position vary over a wide range. Comparing Figure 5-17 (a) with (b), as either μ_s or μ_a of the excitation wavelengh changes, the resolution does not change because of the uniform light distribution within the tissue slab. In practice the presence of the fluorescent targets does affect the distribution across the object plane but, due to the limitations of the model, is neglected in this case.

As the μ_a of emission increases from 0 to 0.6cm^{-1}, the FWHM of spatial light distribution at the surface gets narrower which results in the improvement of spatial resolution *e.g.* moving down along the vertical axis in Figure 5-17 (a). The resolution will get better with a relatively high μ_a, because the photons with longer trajectories will be fully absorbed within the medium and never reach the boundary. Moreover, if the μ_s of emission increases, the trend of spatial resolution will fully depend on the value of μ_a. Seen from Figure 5-17 (a), the resolution stays the same when μ_a is low (smaller than 0.1 cm^{-1}), and it improves when μ_a is relatively high, which can be understood as the increased μ_s leads to fewer photons being detected.

The three sub-figures (a), (c) and (e) shows the change of resolution with different depth of the embeded fluorophore. With fixed μ_s and μ_a, when depth increases from 0.6 to 1.4cm, the separations need to resolve the two objects have, on average, increased by 25%.

Figure 5-18 shows the SNR for the same optical parameters shown in Figure 5-17. It is demonstrated that the increases of either μ_s or μ_a of excitation leads to fewer photons entering the fluorophore (fewer photons emitted, lower intensity detected and worse SNR obtained).

The same conclusion can be drawn while μ_s or μ_a of emission increases. As either of them increases, more photons will be absorbed and the intensity of the detected light decreases which leads to a -6dB reduction in SNR. A 4mm

increase in fluorescent target depth results in a -15dB reduction in SNR as well.

5.4.3 Scanning input system

An alternative configuration is the scanning input system which has similar setup but with different illumination and detection geometries as illustrated in Figure 5-19. A narrow collimated beam is normally incident on the surface of a semi-infinite slab, and scanning is performed with a step size of 0.2mm over the range of -2cm to 2cm. Two fluorescent objects are embedded in the slab with the separation L cm. At each scan position the integrated detector collects the emitted light to form an image. The detector is fixed and radius is set to 1cm which is comparable to many photomultiplier tubes.

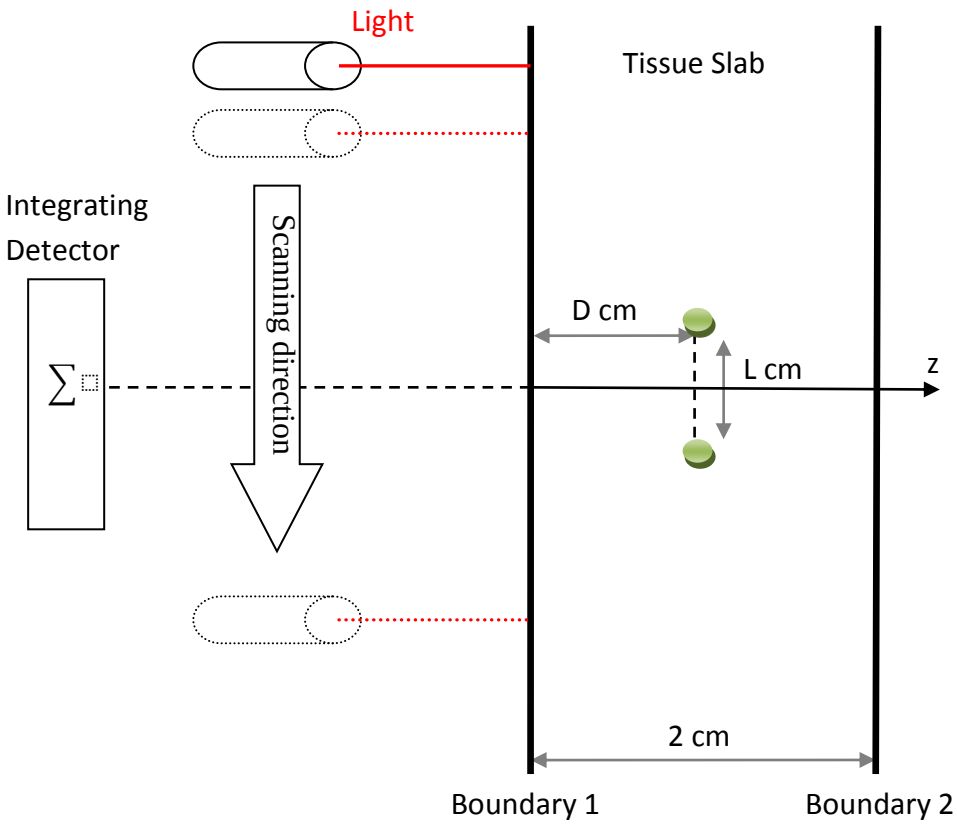

Figure 5-19 Simulation configuration of scanning input system

5.4.3.1 Results

The resolution detected using a SI system is shown in Figure 5-20. Each sub-figure demonstrates the spatial resolution against excitation parameters. Figure 5-20 (a) shows the spatial resolution against scattering and absorption coefficients of excitation, with g = 0.9, μ_a and μ_s of emission equal 0cm^{-1} and 20cm^{-1} respectively and D = 0.6cm.

(b) is the same as (a) but with a higher μ_a and μ_s of emission. μ_a = 0.6 cm^{-1} and μ_s = 80cm^{-1}.

By applying the same optical parameters as (a) and (b), (c) and (d) show the spatial resolution with D = 1.0cm, while (e) and (f) show the spatial resolution with D = 1.4cm.

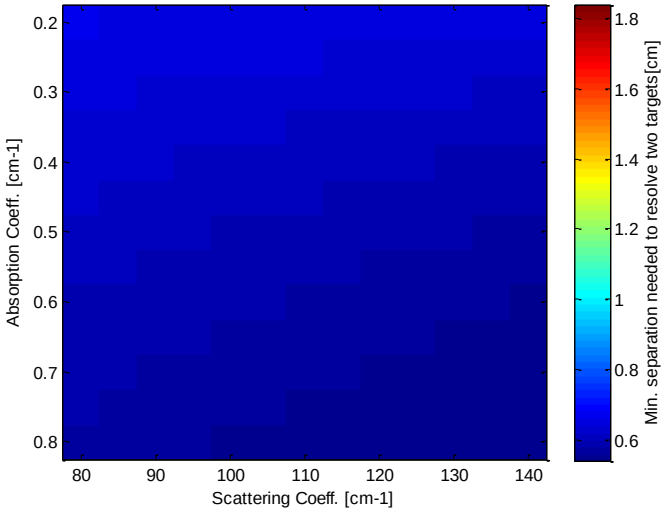

(a) μ_{a_em} = 0.1 cm^{-1}, μ_{s_em} = 20cm^{-1} and D = 0.6cm

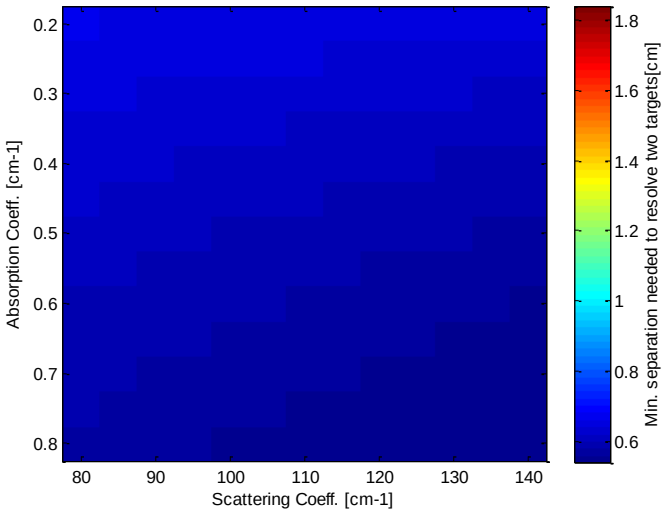

(b) μ_{a_em} = 0.6 cm^{-1}, μ_{s_em} = 80cm^{-1} and D = 0.6cm

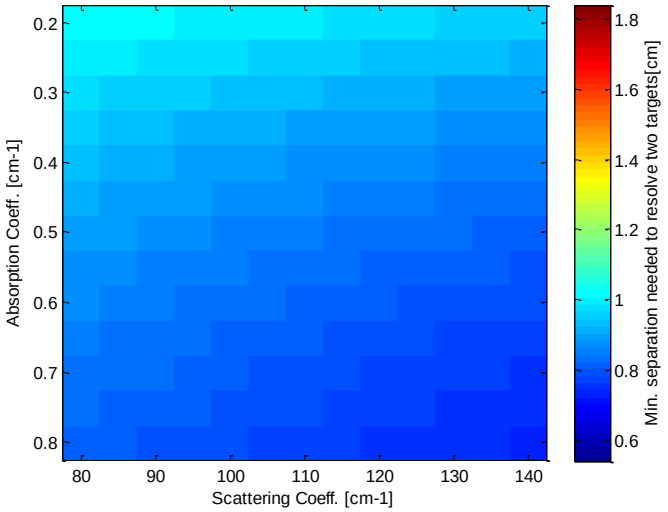

(c) μ_{a_em} = 0.1 cm^{-1}, μ_{s_em} = 20cm^{-1} and D = 1.0cm

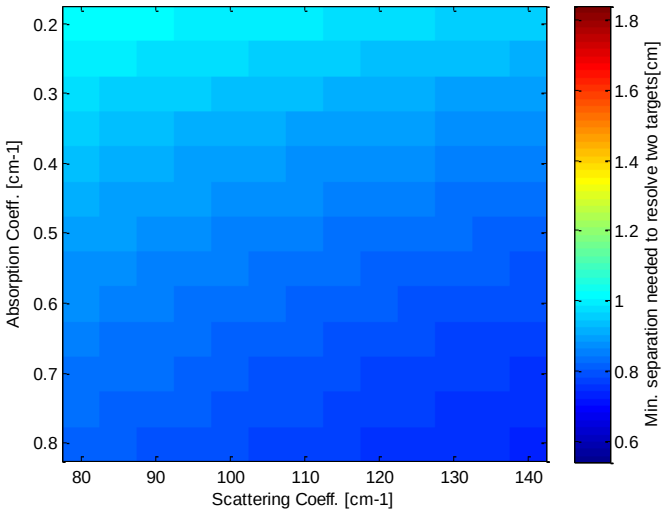

(d) μ_{a_em} = 0.6 cm^{-1}, μ_{s_em} = 80cm^{-1} and D = 1.0cm

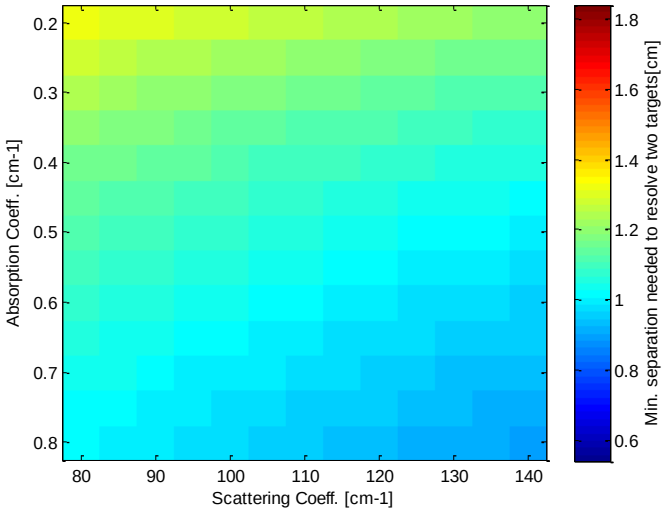

(e) μ_{a_em} = 0.1 cm^{-1}, μ_{s_em} = 20cm^{-1} and D = 1.4cm

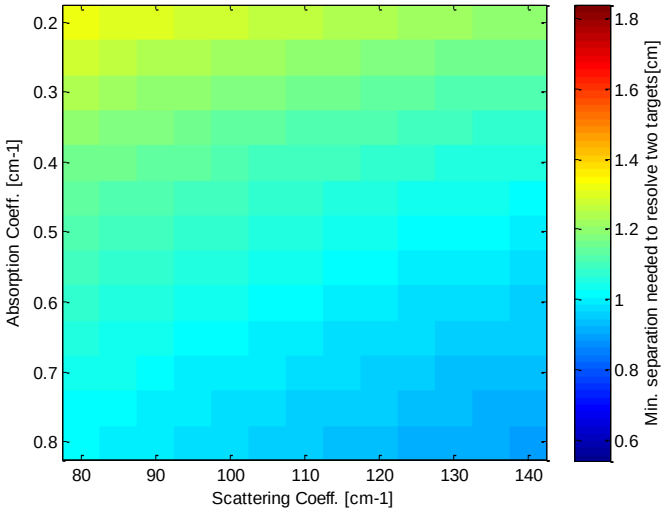

(f) μ_{a_em} = 0.6 cm^{-1}, μ_{s_em} = 80cm^{-1} and D = 1.4cm

Figure 5-20 Minimum separation to resolve the two objects in SI system against the optical parameters of emission wavelength.

Figure 5-21 is similar but shows the SNR detected against the optical parameters.

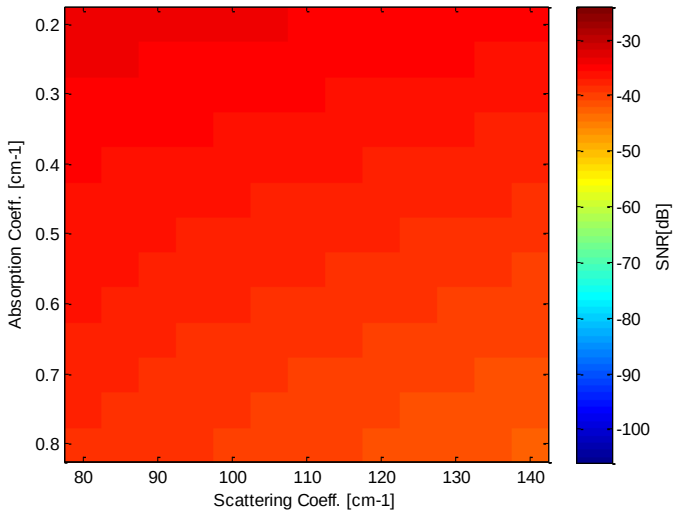

(a) μ_{a_em} = 0.1 cm^{-1}, μ_{s_em} = 20cm^{-1} and D = 0.6cm

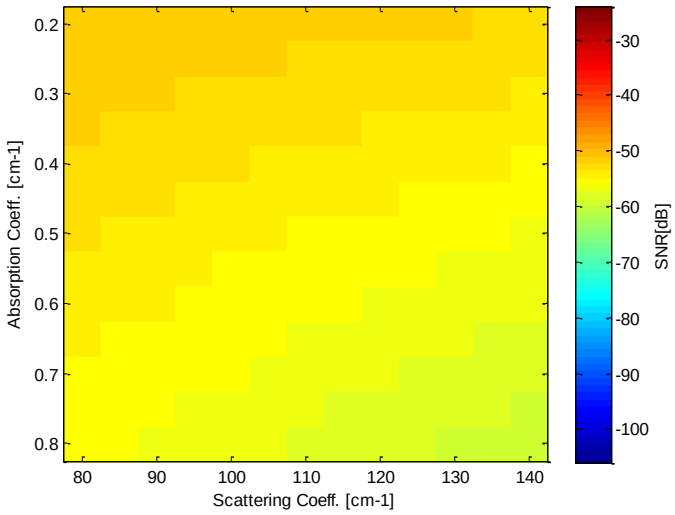

(b) μ_{a_em} = 0.6 cm^{-1}, μ_{s_em} = 80cm^{-1} and D = 0.6cm

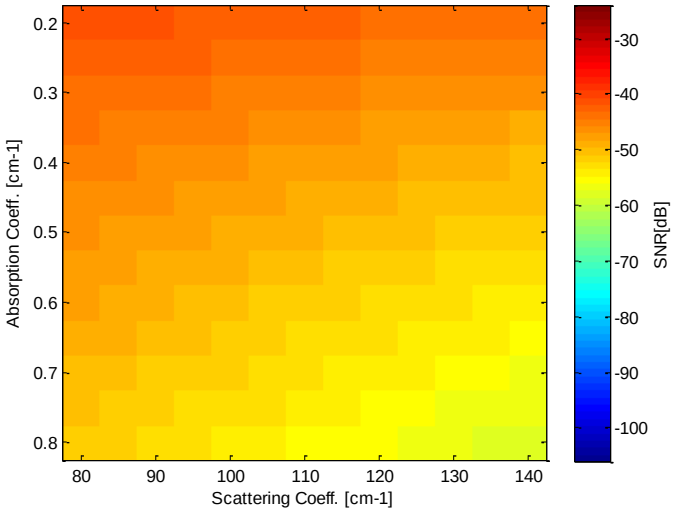

(c) μ_{a_em} = 0.1 cm^{-1}, μ_{s_em} = 20cm^{-1} and D = 1.0cm

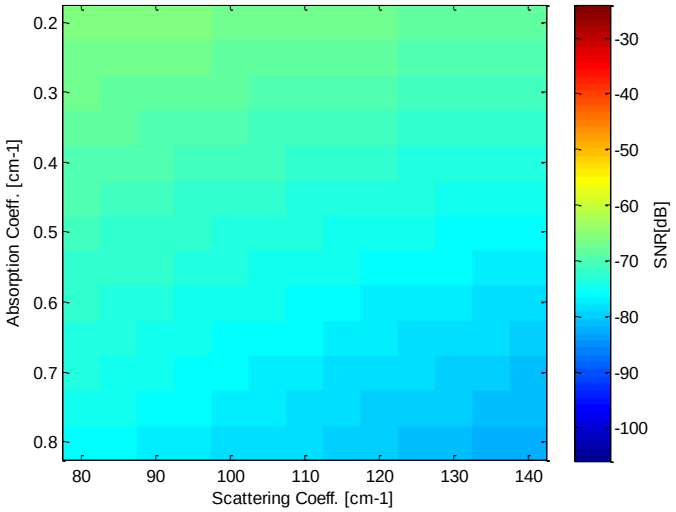

(d) μ_{a_em} = 0.6 cm^{-1}, μ_{s_em} = 80cm^{-1} and D = 1.0cm

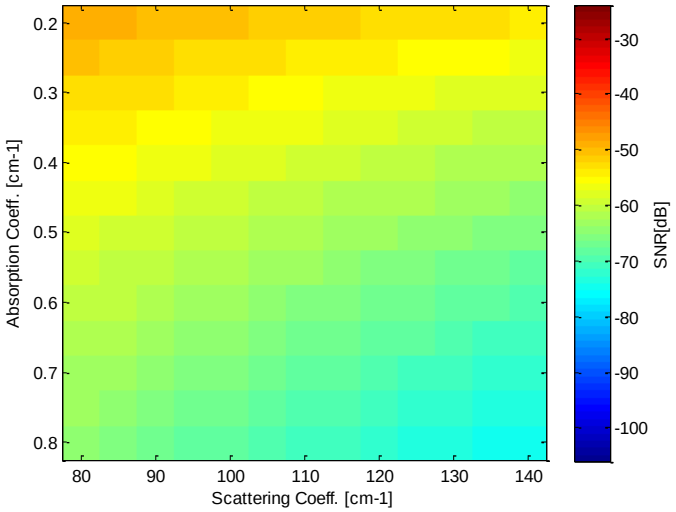

(e) μ_{a_em} = 0.1 cm^{-1}, μ_{s_em} = 20cm^{-1} and D = 1.4cm

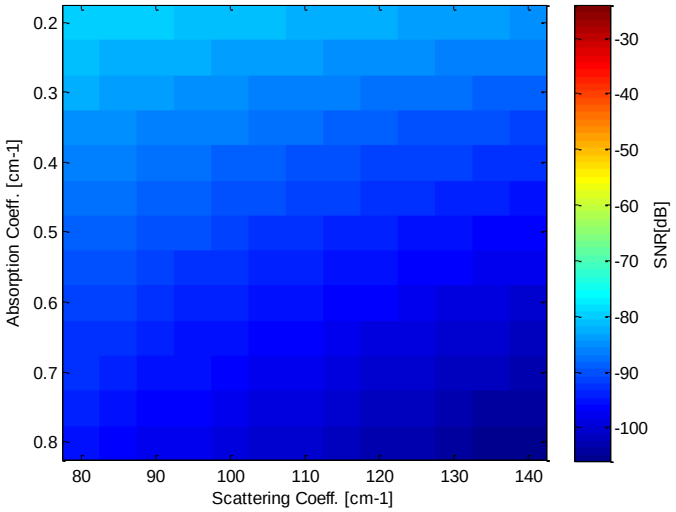

(f) μ_{a_em} = 0.6 cm^{-1}, μ_{s_em} = 80cm^{-1} and D = 1.4cm

Figure 5-21 SNR detected in SI system against the optical parameters of excitation wavelength

5.4.3.2 Discussion

As illustrated in Figure 5-20, using a SI system, the resolution stays the same while either μ_s or μ_a of emission is changed, which is the reverse for the FI illumination system which is independent of excitation wavelength. The μ_a of emission works as a scaling factor and only affects the photon fluence detected, the FWHM remains the same. The increase of μ_s leads to a much broader FWHM but due to an integrated detector (1 cm in radius) applied in this case, the results stay the same. Therefore, the resolution depends on the spatial light distribution at the object plane which depends on the optical parameters of excitation.

As the μ_a of excitation increases, the FWHM of the spatial light distribution gets narrower which results in an improvement of spatial resolution *e.g.* moving down along the vertical axis in Figure 5-20 (c). If μ_s increases, the resolution trend will be determined by the value of μ_a as discussed in section 5.4.2.2.

When light travels though the tissue slab, the increase of either μ_s or μ_a leads to an extra loss within the medium. It means for both excitation and emission, the lower that either μ_s and μ_a is, the better the SNR *e.g.* moving from bottom right to up left in Figure 5-21.

Using a diffusion model, the trade-off between spatial resolution and SNR is clearly shown. Increase of μ_s or μ_a will lead to a better spatial resolution and worse SNR. The comparison between the two systems will be discussed in the next section.

5.5 Comparison of two imaging systems

The following results are based on one important prerequisite that sufficient light propagates through the tissue, which cannot be covered all of the time experimentally. The amount of energy they can put into a tissue is limited by safety requirements to avoid tissue damage, so it will be good to compare the resolution and SNR detected of two systems when the same amount of light is put into the tissue.

Using the Monte Carlo simulation, 1 billion photons propagate through the medium for both systems. As the wavelength of the excitation light is 630nm, the total input energy is around 0.32nJ. This energy is far smaller than the power of a typical He-Ne laser (633nm, 50mW), but it is sufficient to get a convincing statistical result.

As state in section 5.1, the FI system has been widely used especially in fluorescence imaging for its fast processing and deep penetration depth. The SI system (Moving head scanner) eliminates variations in power density and spatial distortion but require longer scanning time. From the simulation results, the spatial resolution of the FI system fully depends on the optical properties of the emission light while the resolution of the SI system is affected by the optical properties of the excitation light, QY of the fluorophore and μ_a of emission light. Overall, there is a much better spatial resolution from the SI system which can be seen from both Monte Carlo and diffusion results. Figure 5-22 shows the spatial resolution against the optical parameters of the excitation wavelength under the diffusion model. On one hand, as discussed in the previous section, the μ_s and μ_a of excitation has no effect on spatial resolution for the FI system, the minimum separation needed to resolve two objects is constant with excitation optical coefficients at 0.88cm. On the other hand, as discussed in section 5.4.3.2, the spatial resolution for the SI system improves as the μ_s or μ_a increases, but even the worst case resolution is 0.68cm which is much better than that of FI system. Because the resolution here is defined as the minimum separation to resolve the two objects and the two objects are getting closer with a step size of 0.02cm, the resolution shown in Figure 5-22 is quantised.

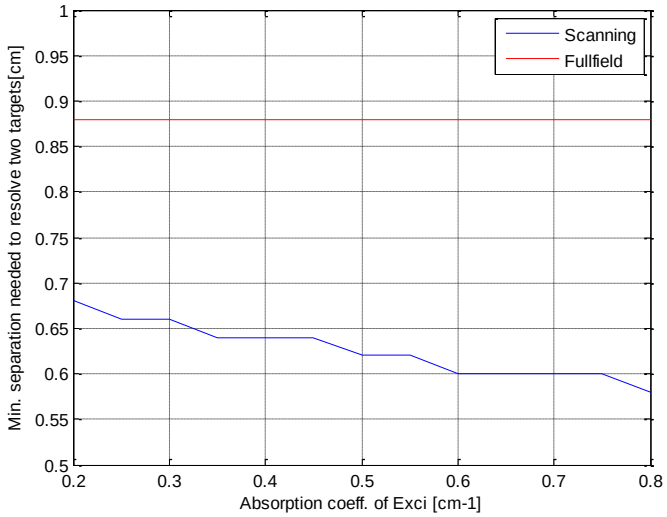

(a) Spatial resolution changes via μ_a of excitation for μ_{s_ex} = 80cm^{-1}

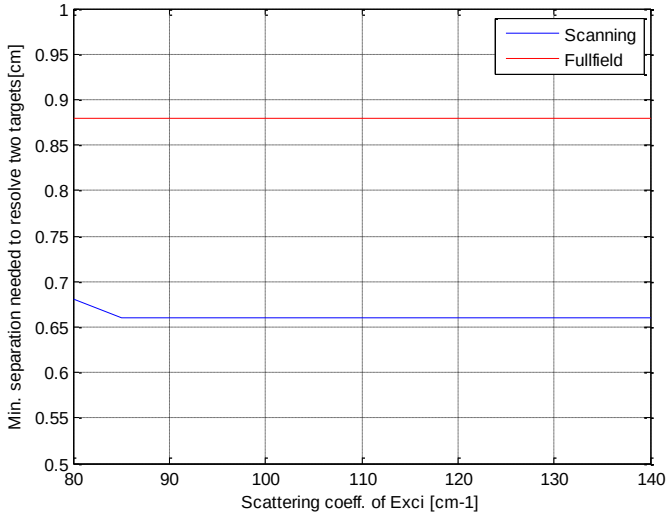

(b) Spatial resolution changes via μ_s of excitation for μ_{a_ex} = 0.2 cm^{-1}

Figure 5-22 Spatial resolution changes against optical properties of excitation wavelength for μ_{a_em} = 0.1 cm^{-1}, μ_{s_em} = 20cm^{-1} at 6mm depth

A similar conclusion can be drawn from Figure 5-23. As the μ_s or μ_a of emission increases, the resolution achieved from SI system is constant at 0.68cm and better than 0.76cm which is the best result obtained from the FI system.

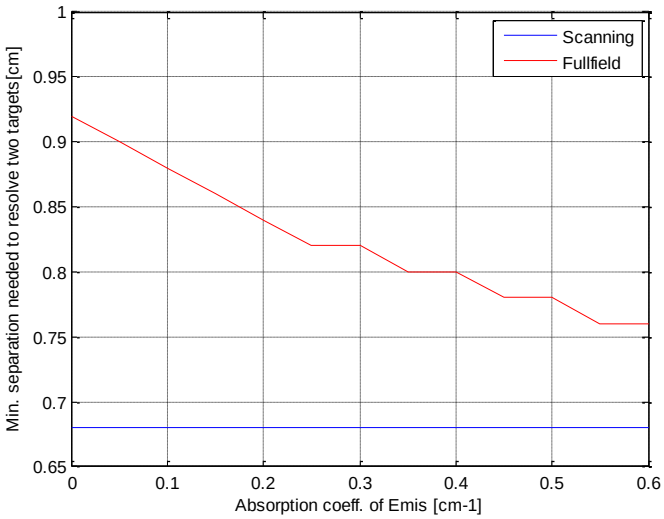

(a) Spatial resolution changes via μ_a of emission for μ_{s_em} = 20cm^{-1}.

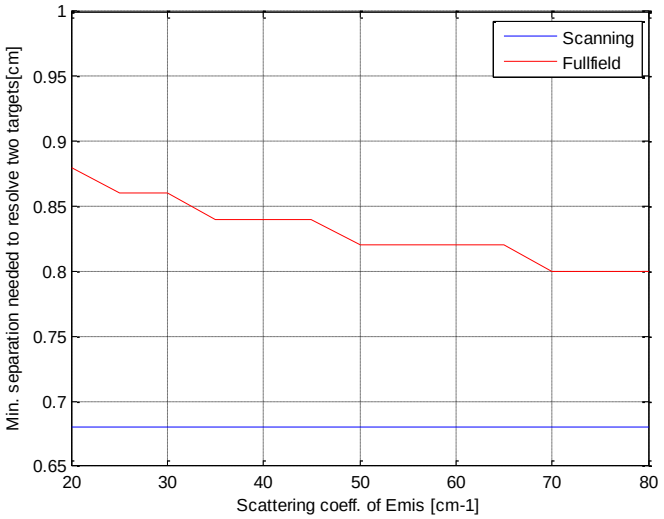

(b) Spatial resolution changes via μ_s of emission for μ_{a_em} = 0.1 cm^{-1}

Figure 5-23 Spatial resolution changes against optical properties of emission wavelength for μ_{a_ex} = 0.2 cm^{-1}, μ_{s_ex} = 80cm^{-1} at 6mm depth.

However, the comparison does not mean the scanning system should be adopted. Quantitatively comparing the Monte Carlo results Table 5-2 with Table 5-1, the SNR of the SI system is a lot worse.

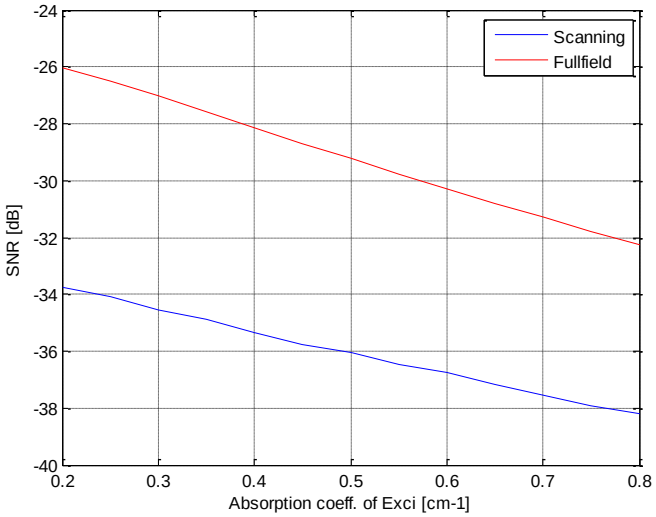

(a) SNR changes via μ_a of excitation for μ_{s_ex} = 80cm^{-1}

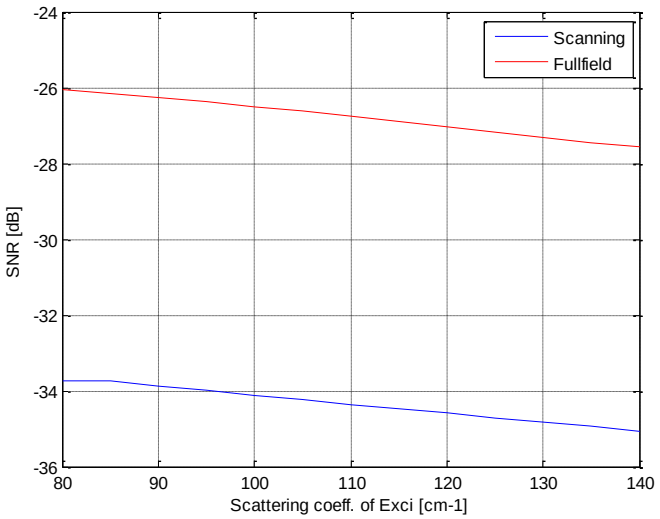

(b) SNR changes via μ_s of excitation for μ_{a_ex} = 0.2 cm^{-1}

Figure 5-24 SNR changes via μ_s or μ_a of excitation wavelength for μ_{a_em} = 0.1 cm^{-1}, μ_{s_em} = 20cm^{-1} at 6mm depth

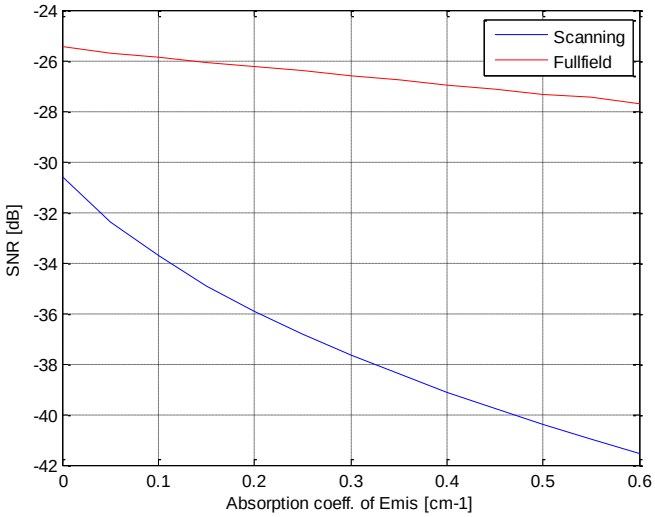

(a) SNR changes via μ_a of emission for μ_{s_em} = 20cm^{-1}.

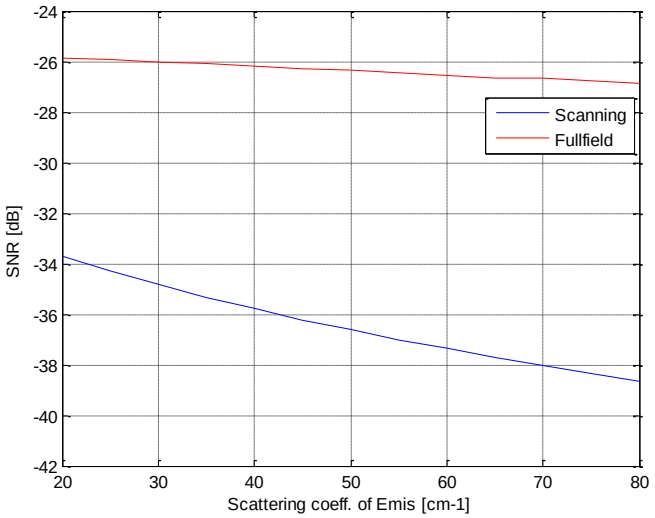

(b) SNR changes via μ_s of emission for μ_{a_em} = 0.1 cm^{-1}.

Figure 5-25 SNR changes against optical properties of emission wavelength for μ_{a_ex} = 0.2 cm^{-1}, μ_{s_ex} = 80cm^{-1} at 6mm depth.

Figure 5-24 and Figure 5-25 show the SNR change versus excitation and emission optical properties from diffusion model. The SNR obtained from FI system (∼−26dB) is much higher than that in SI system (∼-36dB).

Comparing the two imaging systems, FI system offers better SNR while SI system provides better spatial resolution. Weighing the pros and cons, when the targets are near the incident boundary, SI system should be applied for its

excellent resolution (Figure 5-10) with relatively high SNR (around -134dB from Table 5-2). In contrast, when the objects are close to the other boundary, FI system is better for its relatively high SNR (around -140dB from Table 5-1) and fair spatial resolution (Figure 5-7).

5.6 Relationship between optical properties and wavelength

5.6.1 Fluorophore selection in full field illumination system

As the spatial resolution of the FI system fully depends on the optical properties of the emission light, which has been investigated in section 5.3.1 and 5.4.2. The optical properties need to relate to wavelength in order to select appropriate fluorophore afterwards. The SNR and resolution in the NIR wavelength range are discussed in this section.

As discussed in section 5.2, the optical properties differ from tissue to tissue. There is no particular value of μ_s and μ_a, but it generally follows the same trend via wavelengths. The following discussions are based on the tissues of dermis, subdermis and muscle. (data collected from [166]).

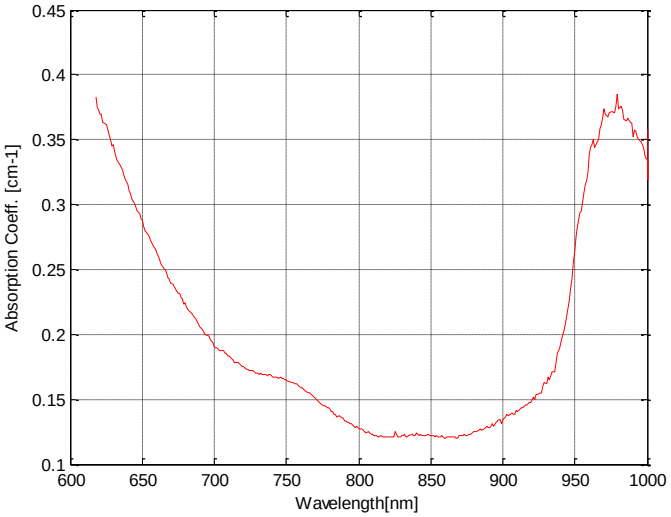

(a)

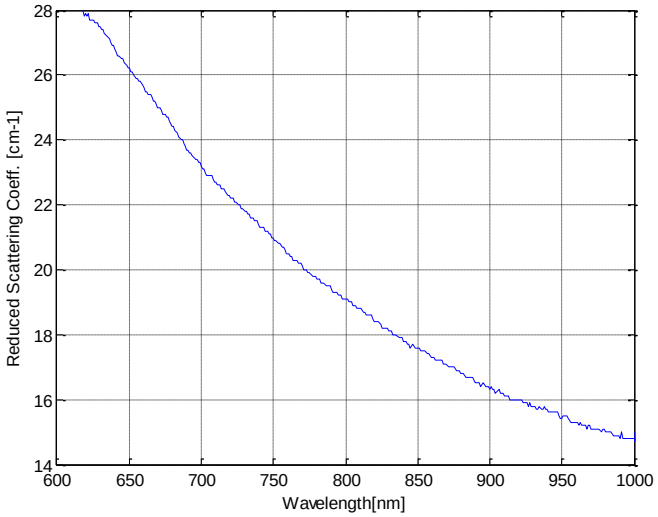

(b)

Figure 5-26 (a) Absorption coefficients of dermis spectrum; (b) reduced scattering coefficients of dermis spectrum [166]

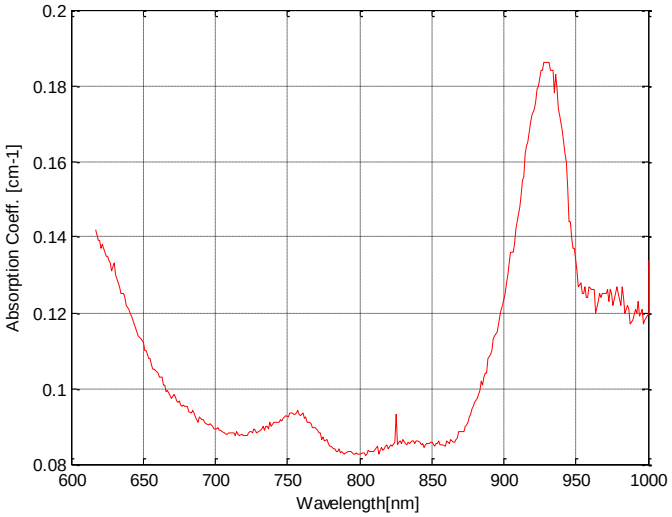

(a)

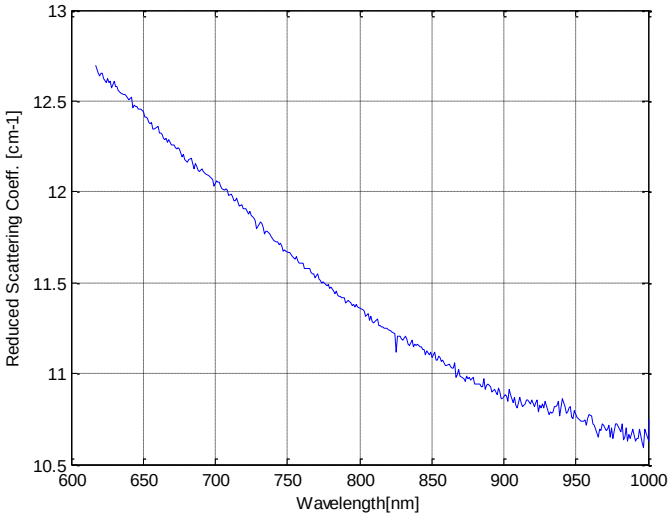

(b)

Figure 5-27 (a) Absorption coefficients of subdermis spectrum; (b) reduced scattering coefficients of subdermis spectrum [166]

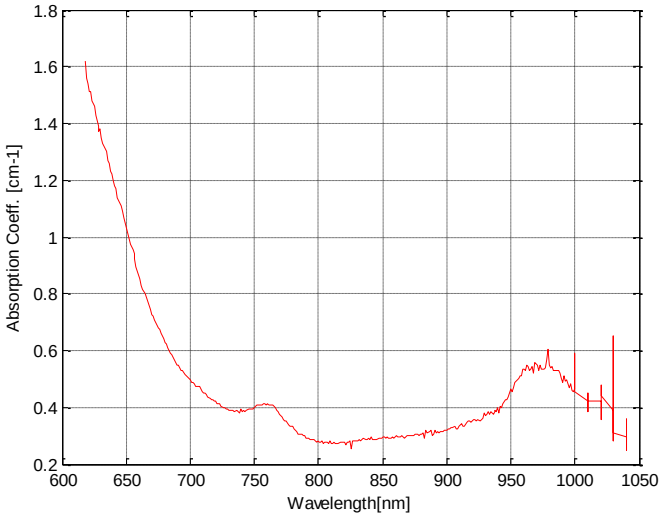

(a)

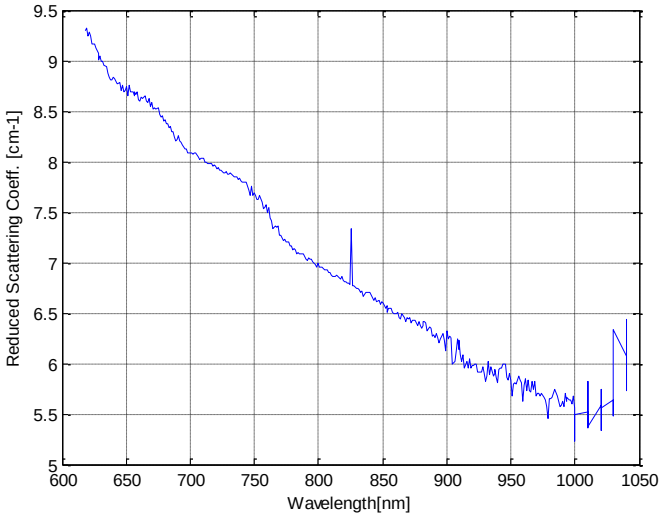

(b)

Figure 5-28 (a) Absorption coefficients of muscle spectrum; (b) reduced scattering coefficients of muscle spectrum [166]

Figure 5-26 to Figure 5-28 show the absorption and reduced scattering coefficients of dermis, subdermis and muscle. The wavelengths selected are between 600 and 1050nm, as the light above 1100nm will mostly absorbed by water.

Seen from Figure 5-26 (b) to Figure 5-28 (b), the value of reduced scattering coefficients μ_s' varies for different type of tissue, but the spectra have the same trend: increased wavelength leads to a lower μ_s'. Therefore, as discussed in section 5.4.2.2 and 5.4.3.2, decreasing μ_s' results in a higher SNR but poor spatial resolution.

The absorption spectra are more complex as shown in Figure 5-26 (a) to Figure 5-28 (a). Comparing the value of absorption coefficients μ_a, the subdermis is lower than the other two, as it is a thin layer without blood. All three spectrums have a drop at the beginning and reach the trough around 800nm, the curves then go back up until 900nm and drop again. Still from section 5.4.2.2 and 5.4.3.2 it is concluded that higher μ_a offers a better spatial resolution but poor SNR. The aim here is to find out the optimum trade-off between resolution and SNR, and then to select the optimized imaging wavelength pair (emission and excitation).

As the spatial resolution obtained from the SI system depends only slightly on the emission wavelength, the selection of fluorophore mainly focuses on the SNR. As discussed in section 5.4.3.2, the lower that either μ_s and μ_a is, the better the SNR. Refer to Figure 5-26 to Figure 5-28, it can be easily concluded that the fluorophore with the longest possible emission wavelength would be the optimum choice when using a SI system. The following discussions are mainly focused on the FI system.

Figure 5-29 to Figure 5-31 below show the change of SNR and spatial resolution via emission wavelength at a step of 20nm within different tissues. The excitation light is set to 670nm.

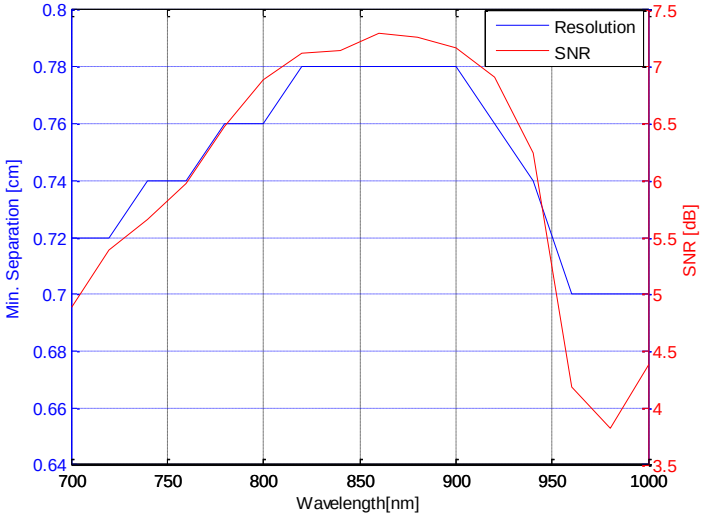

Figure 5-29 SNR and spatial resolution spectrum of Dermis

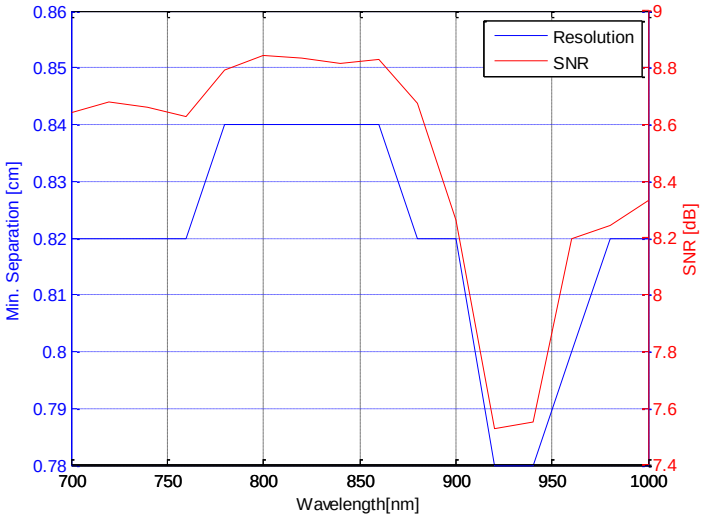

Figure 5-30 SNR and spatial resolution spectrum of Subdermis

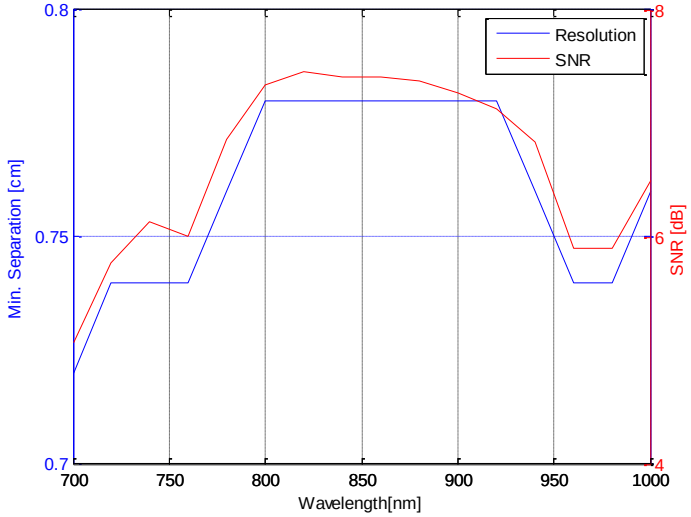

Figure 5-31 SNR and spatial resolution spectrum of Muscle

The common point of Figure 5-29 to Figure 5-31 that is the best SNR and worst resolution is achieved around 860nm. The best resolution wavelength varies for different tissues, but it generally follows the variation of absorption coefficients.

5.6.2 Auto-fluorescence (AF) in scanning input system

AF is due to endogenous fluorophores within the background medium to distinguish it from fluorescent signals obtained by adding exogenous markers at the fluorescent targets. As the selection of the excitation light wavelength has little influence on the spatial resolution in the FI system, light at longer wavelength can simply be chosen as it has low AF effect and high SNR (provided fluorophores that can be excited at longer wavelengths are available). In the SI system, the wavelength selection of emission light becomes the secondary effect, as the spatial resolution depends only on the wavelength of excitation light. The AF effect should therefore not be neglected in SI systems.

The new model is the combination of Welch's uniform fluorescence model and the model presented in section 5.3.1. Unlike the previous setup described in section 5.3.1, the photon can be fully absorbed, scattered to another position with full weight or absorbed but emitted as new photon at a longer wavelength before a photon hits the fluorescent target, which indicates the AF.

The probability of the three choices are determined by the QY_{AF} and the ratio of μ_a and μ_s.

Propagation in the background medium containing autofluorescence:

$$\begin{cases} Autofluorescence & 0 < \xi \leq QY_{AF} \\ Scattering & QY_{AF} < \xi \leq QY_{AF} + (1 - QY_{AF}) * \dfrac{\mu_{s\_ex}}{\mu_{s\_ex} + \mu_{a\_ex}} \\ Absorption & QY_{AF} + (1 - QY_{AF}) * \dfrac{\mu_{s\_ex}}{\mu_{s\_ex} + \mu_{a\_ex}} < \xi < 1 \end{cases} \quad 5\text{-}4$$

where ξ is a random number in the range of (0 , 1).

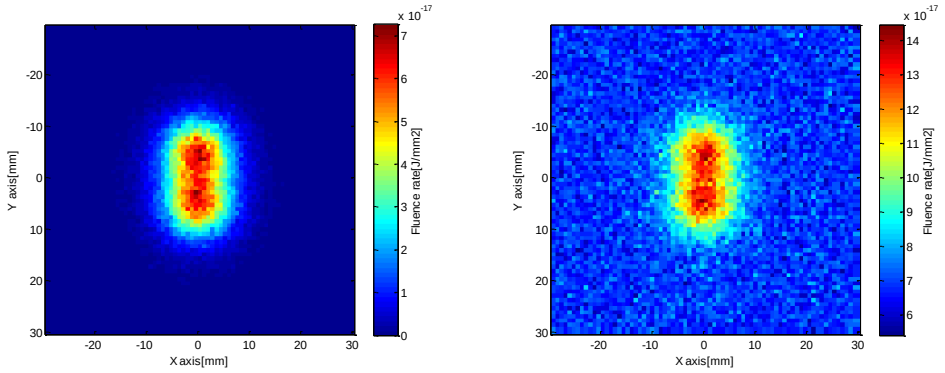

(a) Reflected images without & with AF μ_{s_em} = 20cm^{-1} & μ_{a_em} = 0.1cm^{-1}

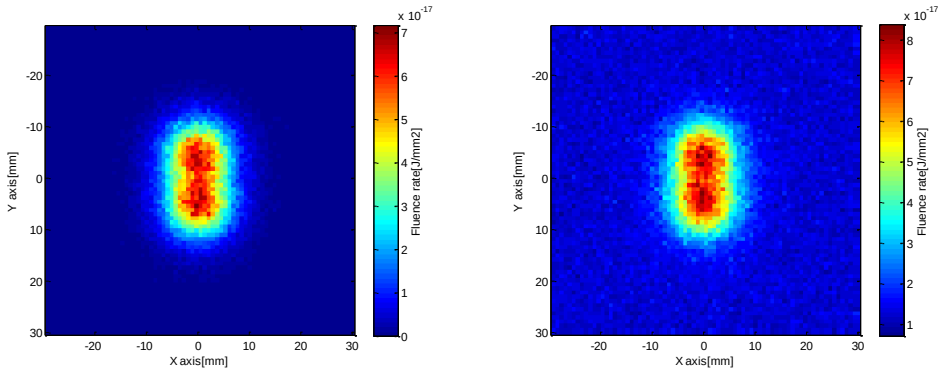

(b) Transmitted images without & with AF μ_{s_em} = 20cm^{-1} & μ_{a_em} = 0.1cm^{-1}

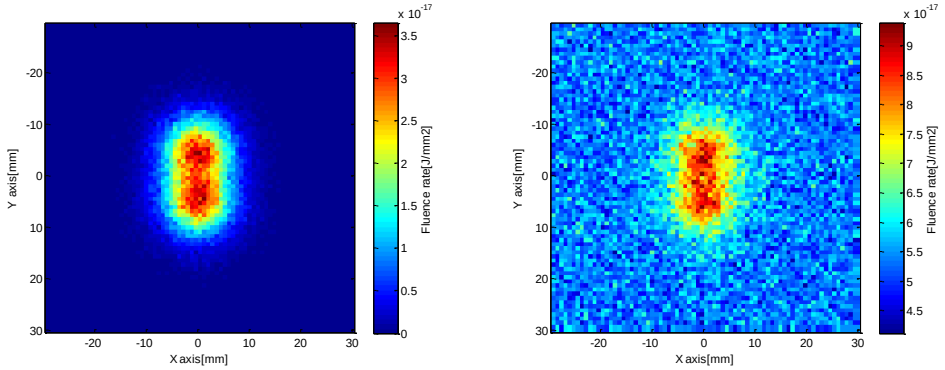

(c) Reflected images without & with AF μ_{s_em} = 20cm^{-1} & μ_{a_em} = 0.3cm^{-1}

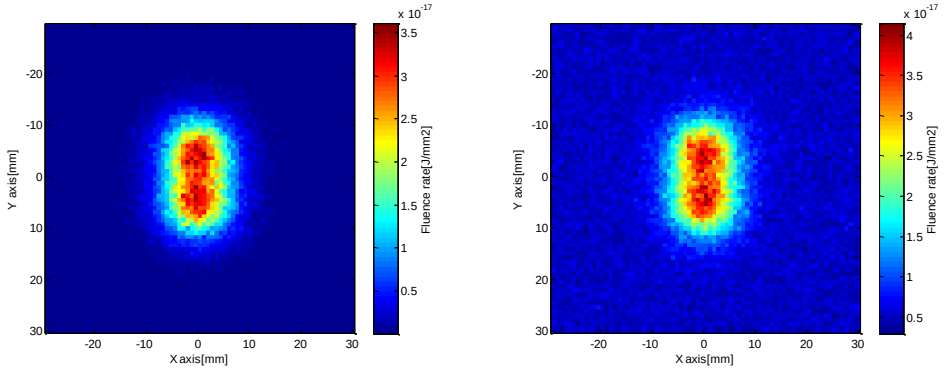

(d) Transmitted images without & with AF μ_{s_em} = 20cm^{-1} & μ_{a_em} = 0.3cm^{-1}

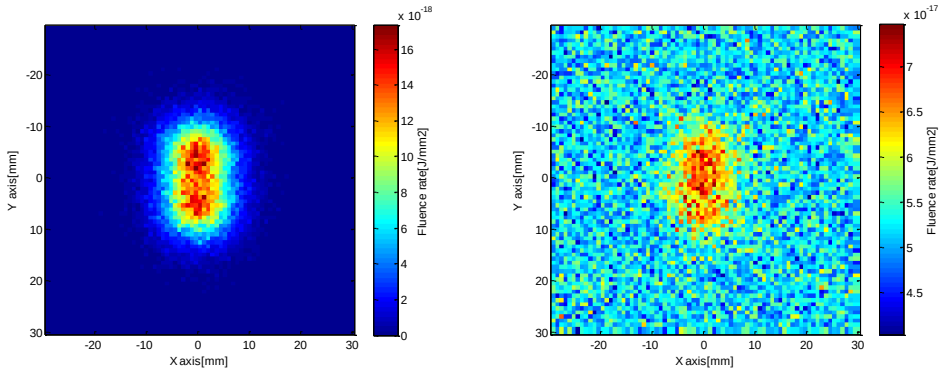

(e) Reflected images without & with AF μ_{s_em} = 60cm^{-1} & μ_{a_em} = 0.3cm^{-1}

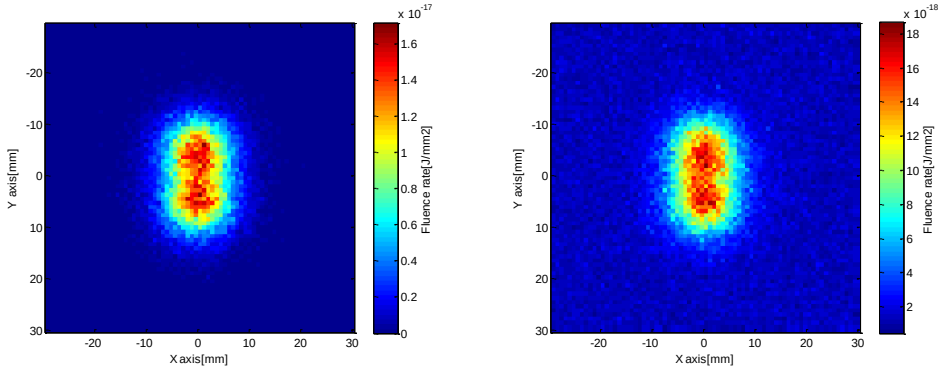

(f) Transmitted images without & with AF μ_{s_em} = 60cm^{-1} & μ_{a_em} = 0.3cm^{-1}

Figure 5-32 Photon fluence with & without AF effect at 10mm embedded depth and 20mm slab thickness.

The AF here is modelled simply as uniformly distributed fluorophores, which increase the probability for an excitation photon transfer to a longer wavelength. Hence, the images with AF effect are of higher photon fluence (Figure 5-32) but lower SNR (Table 5-4).

Table 5-4 SNR at different excitation optical properties with & without AF

Depth	Emission Optical Properties	SNR(dB) of Reflection		SNR(dB) of Transmission	
		No AF	AF	No AF	AF
10mm	μ_{s_em} = 20cm^{-1} & μ_{a_em} = 0.1cm^{-1}	-136.09	-149.90	-136.09	-144.70
	μ_{s_em} = 20cm^{-1} & μ_{a_em} = 0.3cm^{-1}	-139.00	-151.89	-139.05	-146.83
	μ_{s_em} = 60cm^{-1} & μ_{a_em} = 0.3cm^{-1}	-142.33	-160.38	-142.38	-149.02

Figure 5-33 and Table 5-6 show the photon fluence image and corresponding SNR variation with different target depths.

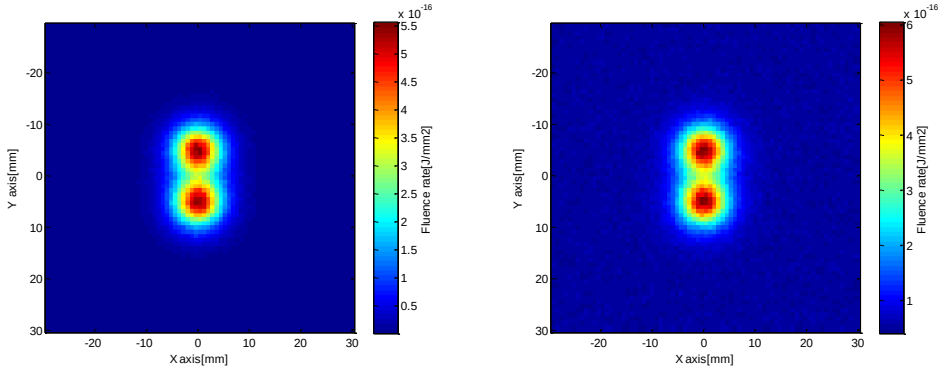

(a) Reflected images without & with AF at 6mm depth

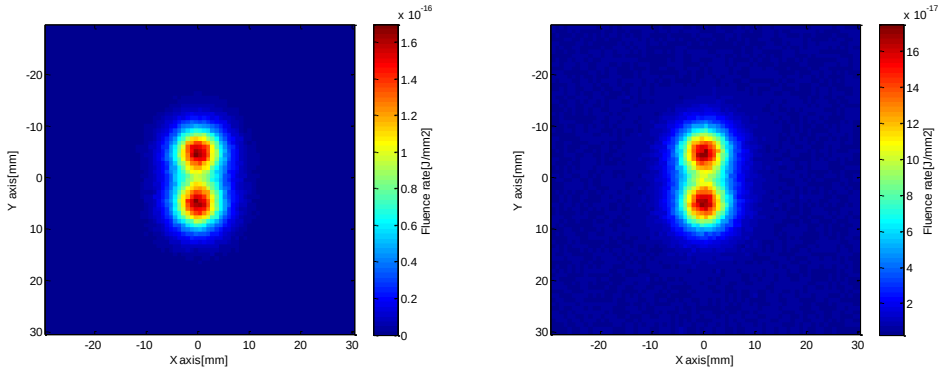

(b) Transmitted images without & with AF at 6mm depth

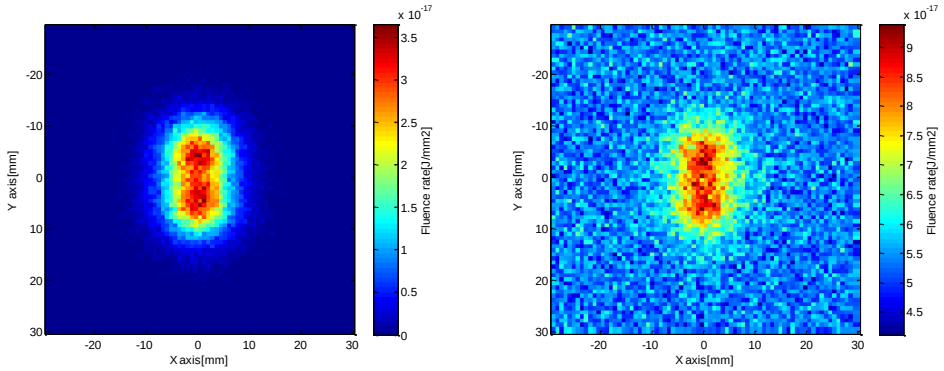

(c) Reflected images without & with AF at 10mm depth

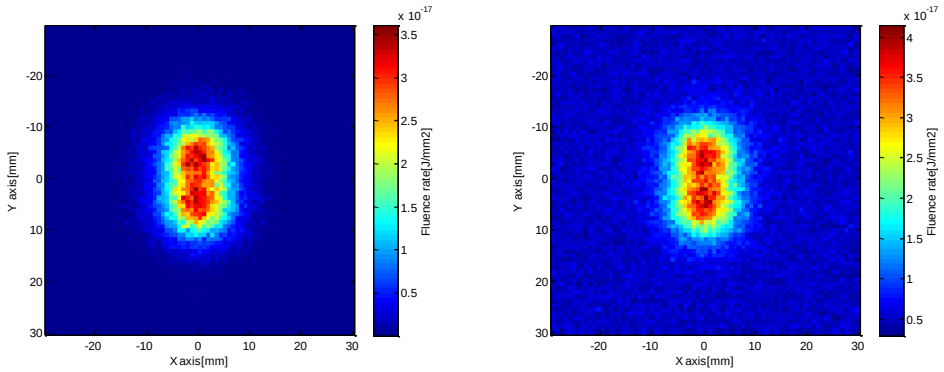

(d) Transmitted images without & with AF at 10mm depth

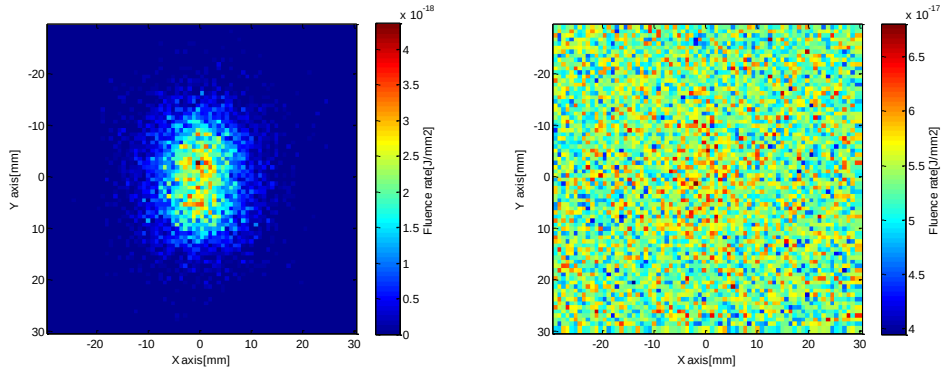

(e) Reflected images without & with AF at 14mm depth

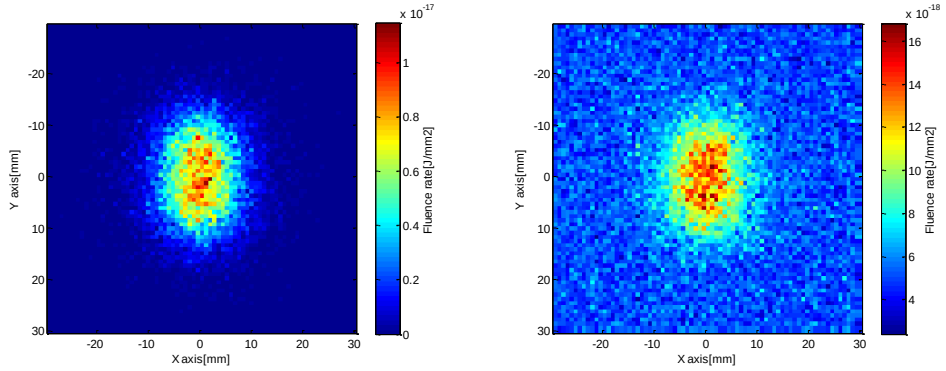

(f) Transmitted images without & with AF at 14mm depth

Figure 5-33 Photon fluence with & without AF effect at μ_{s_em} = 20cm^{-1} & μ_{a_em} = 0.3cm^{-1} and 20mm slab thickness.

Table 5-5 SNR at different embedded depth with & without AF

Emission Optical Properties	**Depth**	**SNR(dB) of Reflection**		**SNR(dB) of Transmission**	
		No AF	AF	No AF	AF
μ_{s_em} = 20cm^{-1} & μ_{a_em} = 0.3cm^{-1}	**6mm**	-128.88	-136.87	-134.25	-139.66
	10mm	-139.00	-151.89	-139.05	-146.83
	14mm	-149.21	-173.67	-143.95	-155.20

It is demonstrated in the above figures and tables that the presence of AF leads to a poorer SNR and spatial resolution.

In general, the absorbance efficiency of QDs decreases with increasing wavelength of both excitation and emission. Therefore, the greater the gap between the excitation wavelength and the peak emission wavelength, the less interference there will be from AF [167]. However, short wavelengths also mean high absorbance and scattering in tissue.

As discussed previously, shorter wavelengths offer a higher quantum yield of QDs and higher background scattering and absorbance at the same time. But the improvement of quantum yield cannot balance that degradation from heavy scattering and high absorption. In general, the selection of excitation wavelength should be as long as possible with the precondition that it is sufficient to excite the QDs.

5.7 Conclusion

This chapter investigates the spatial resolution and intensity over a broad range of optical parameters which corresponds to a broad range of excitation and emission wavelengths and aims to find out the optimized excitation and emission pairs. Table 5-6 shows the trend of Resolution and SNR with optical parameters.

Table 5-6 Trend of resolution and SNR against optical parameters

	Full field illumination system		**Scanning system**	
	Resolution	SNR	Resolution	SNR
μ_s of excitation increase	→	↓	↑	↓
μ_a of excitation increase	→	↓	↑	↓
μ_s of emission increase	↑	↓	→	↓
μ_a of emission increase	↑	↓	→	↓

As seen from Table 5-6, it is impossible to get better resolution and higher intensity simultaneously and, a trade-off always exists as discussed in section 5.4.2.2. Previous literature mainly focused on near infrared tissue spectroscopy due to its deep penetration ability. Near infrared usually means low scattering and low absorption, which will definitely lead to a stronger signal. But the near infrared image may produce even worse spatial resolution than the visible one.

For full field illumination systems, the excitation light has little effect on the spatial resolution in terms of the variation of optical properties because of the uniform light distribution within the tissue slab. The excitation wavelength selection is mainly based on the effect on fluorophore and background medium, *e.g.*, quantum yield, brightness. The emission wavelength selection refers to the cell ingredient and experiment purpose. Generally, the best SNR

is achieved around 860nm and wavelength around 950nm will be chosen if spatial resolution is the primary demand.

The wavelength selection in a scanning system is totally different. Emission spectrum is a secondary effect on fluorophore selection because the spatial resolution fully depends on the spatial light distribution of the object plane which results from the optical parameters of excitation. Other characteristics of fluorophore, *e.g.*, absorption spectrum of the fluorophore and auto-fluorescence of the medium should be considered. The excitation light selection is limited in the visible range, and longer wavelength leads to a better SNR but worse resolution. However, when the wavelength drops under 550nm μ_a is much higher and becomes the dominant factor. Most photons are absorbed which makes it difficult to form a reasonable image.

Chapter 6

6 Infrared fluorescent target imaging

6.1 Introduction

The analysis and evaluation of the SNR and spatial resolution of a fluorescence target embedded in a scattering medium were presented in chapter 5. This was based on the simulated data. This chapter aims to experimentally investigate the imaging properties of visible and NIR probes.

Of particular interest in this thesis are CdSe quantum dots (QDs) which have good photostability, long duration (two weeks) and a peak emission wavelength that can be easily controlled for the different ratio mixed with Manganese. These QDs are developed at the Schools of Chemistry and Physics at the University of Nottingham.

6.2 Experimental configuration

The experimental setup is shown in

Figure **6-1**. A 500mW red laser (Bfi Optilas PB 256-c) and a beam expander are employed to provide a full field light illumination over an area (radius = 15mm) on the samples. The samples (4mm in radius and with 2mm separation) consist of CdSe Quantum dots (200nM) and Manganese which are placed on a glass slide and covered by an agar gel with polystyrene microspheres of diameter 1.6 μm embedded within it. Red food dye is used to produce absorption. The thickness of the gel varies (up to 5mm) but with the fixed scattering and absorption coefficients μ_s = 100cm^{-1} and μ_a = 0.2cm^{-1} at 670nm. A hyper-spectral camera (The Cooke Co. Sensicam QE) combines with a C-mount lens to produce a one dimensional spectral image. A slit in front of the camera sits on a computer controlled XYZ motorized stage (Standa 8MT175-50) which scans along the Y axis to produce a two dimensional image (60mm * 86mm). Before the start of experiment, images are captured when the laser illuminates on a 99% reflectance Spectralon target for calibration. The exposure time in the experiment is then set to 20ms, as longer time will result in a saturation of the camera by the excitation light.

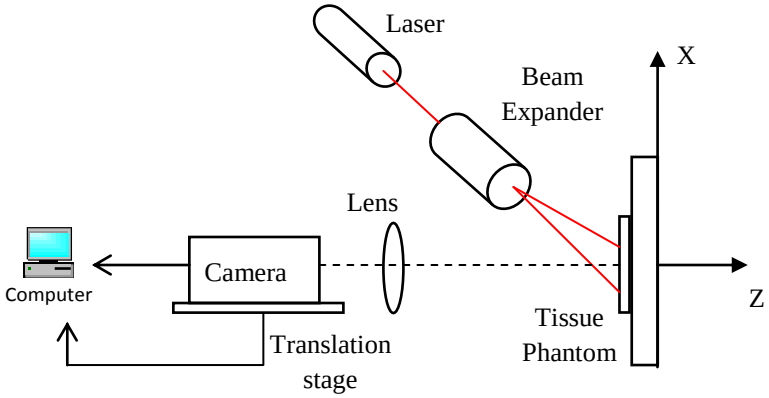

Figure 6-1 Experimental configuration

6.2.1 Sim. and Exp. results

Before the experiment starts, a new Monte Carlo model has been designed with the same configuration to estimate the fluence of fluorescence imaging. The light beam crosses the incident boundary with an angle of 45 degree to the axis of Z and minus Y in an area of 7.07 cm^2. The depth of the scattering medium and sizes of the fluorescence targets are the same as the experimental setup.

Figure 6-2 and Figure 6-3 show the simulated full field images of excitation (670nm) and emission (870nm) wavelengths with different tissue thickness.

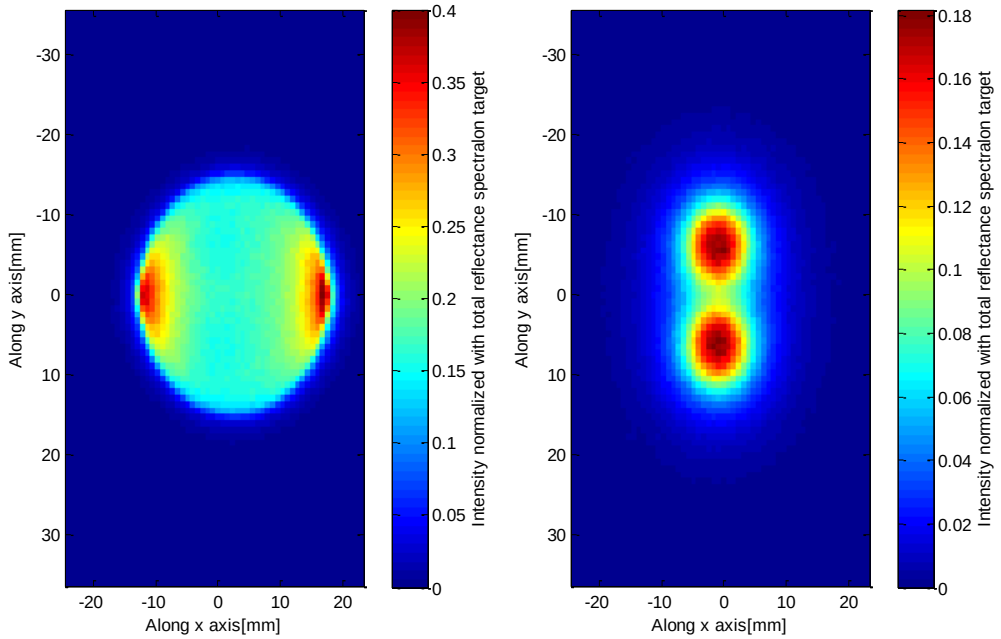

(a) Image at 670nm (b) Image at 870nm

Figure 6-2 (a) Full field images at excitation wavelength. (b) Full field images at emission wavelength. Scattering layer thickness = 3mm, μ_s = 100cm^{-1}

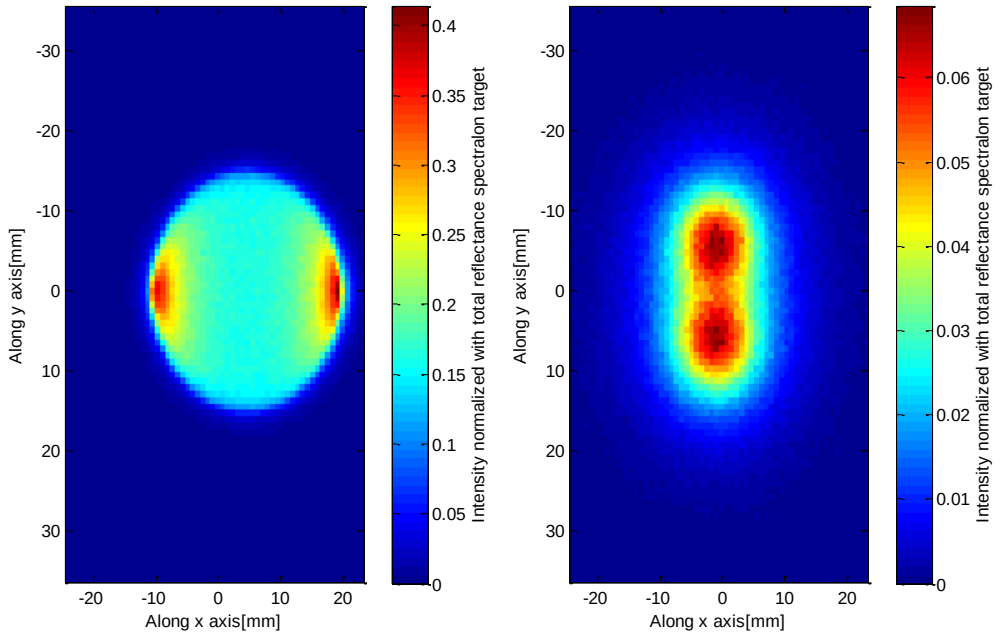

(a) Image at 670nm (b) Image at 870nm

Figure 6-3 (a) Full field images at excitation wavelength. (b) Full field images at emission wavelength. Scattering layer thickness = 5mm, μ_s = 100cm^{-1}

In the simulations, the two targets are distinguished clearly in Figure 6-2 (b), and the edge get more obscure as the slab thickness increase to 5mm as shown in Figure 6-3 (b).

Figure 6-4 (a) and (b) show the full field images of excitation (670nm) and emission (870nm) wavelengths respectively when the laser illuminates the sample. The edge, visible in both figures, is the glass slide on which the quantum dots sit. Figure 6-4 (a) shows the excitation light case, in which the fluorescent targets are visible because they absorb the excitation light but are quite obscure. On the contrary, the two fluorescent targets are clearly resolved in the emission image Figure 6-4 (b). Figure 6-4 (c) shows the intensity spectrum of the light reflected at a single pixel from the sample.

Figure 6-5 and Figure 6-6 show similar results but with the scattering gel overlaying the fluorescent targets. The thickness of the tissue phantom equals 3mm and 5mm respectively (μ_s = 100cm^{-1} and μ_a = 0.2cm^{-1} @ 670nm).

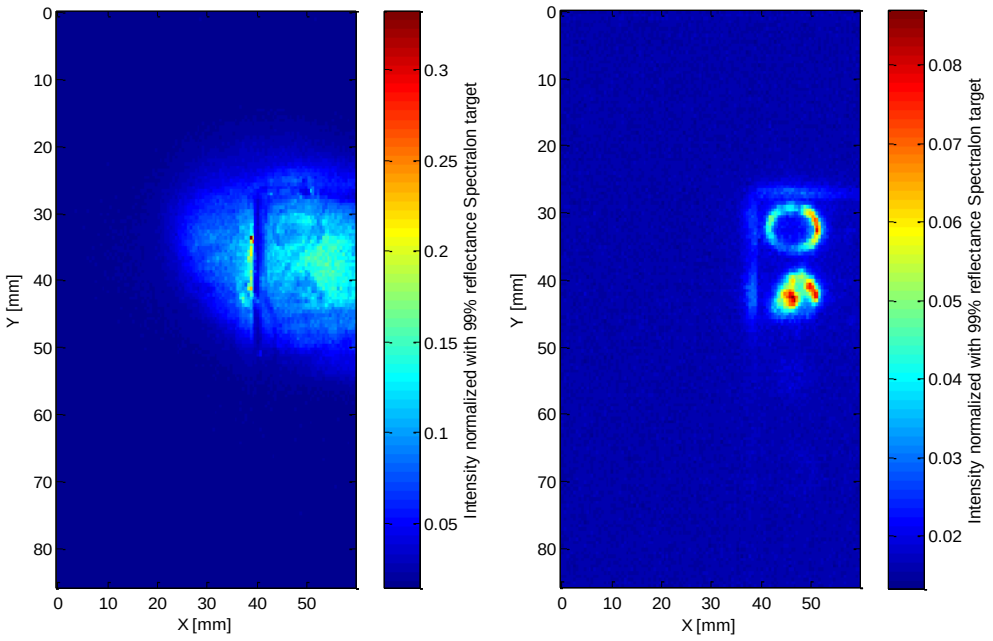

(a) Image at 670nm (b) Image at 870nm

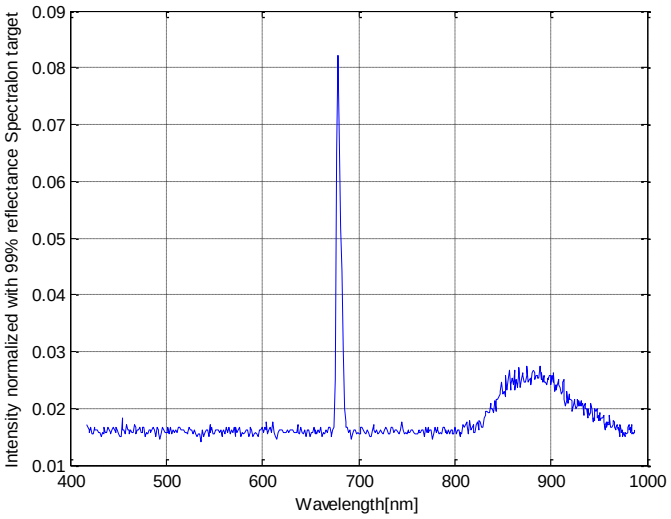

(c)

Figure 6-4 (a) Full field images at excitation wavelength. (b) Full field images at emission wavelength. (c) Intensity spectrum reflected from the sample (x=46mm, y=46mm). No scattering layer over the target.

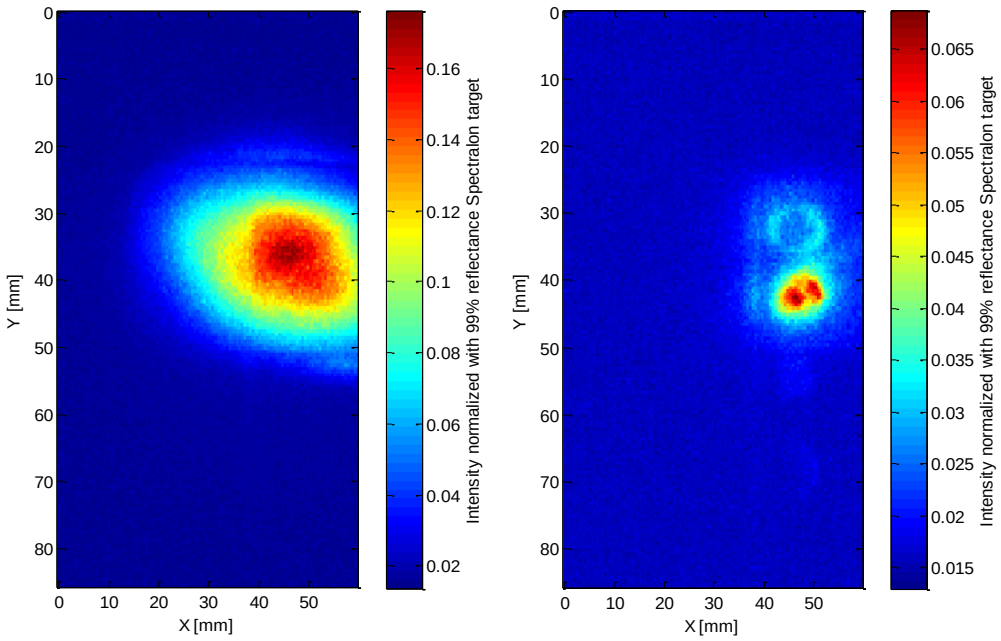

(a) Image at 670nm (b) Image at 870nm

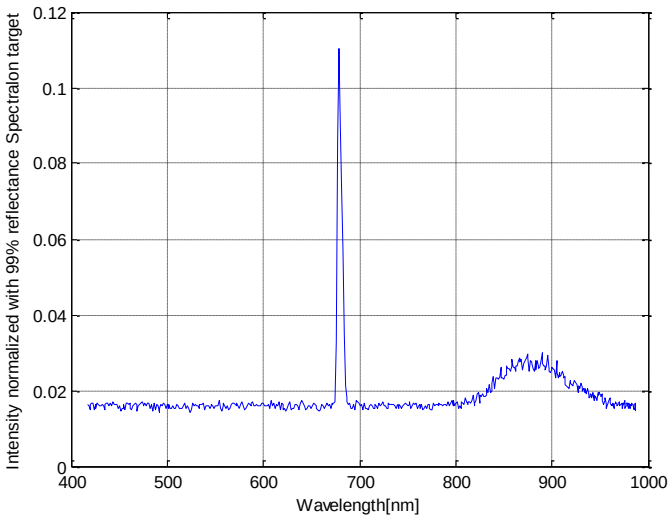

(c)

Figure 6-5 (a) Full field images at excitation wavelength. (b) Full field images at emission wavelength. (c) Intensity spectrum reflected from the sample (x=46mm, y=46mm). Scattering layer thickness = 3mm, μ_s = 100cm^{-1}

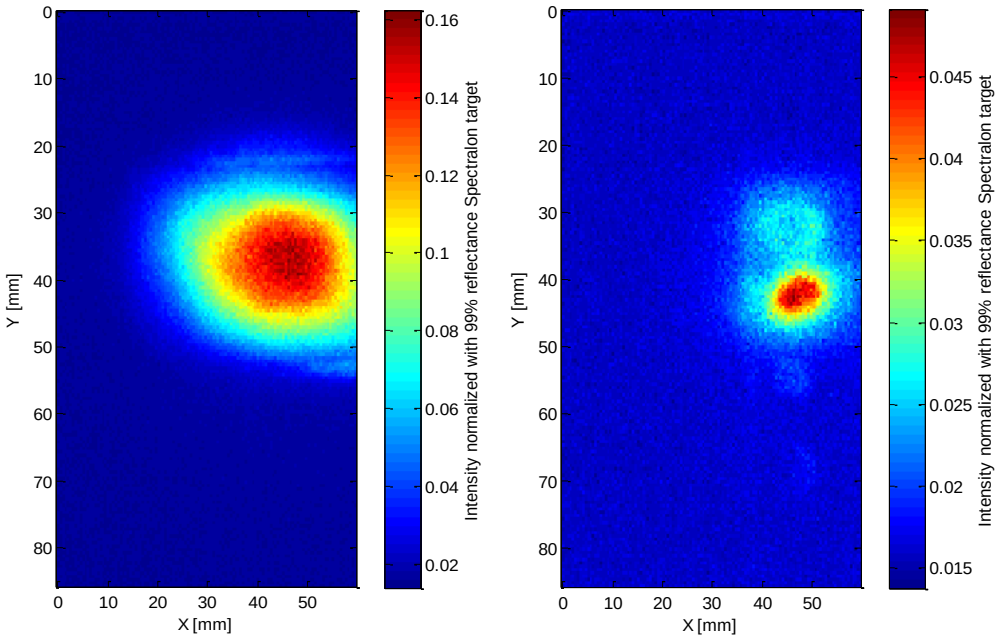

(a) Image at 670nm (b) Image at 870nm

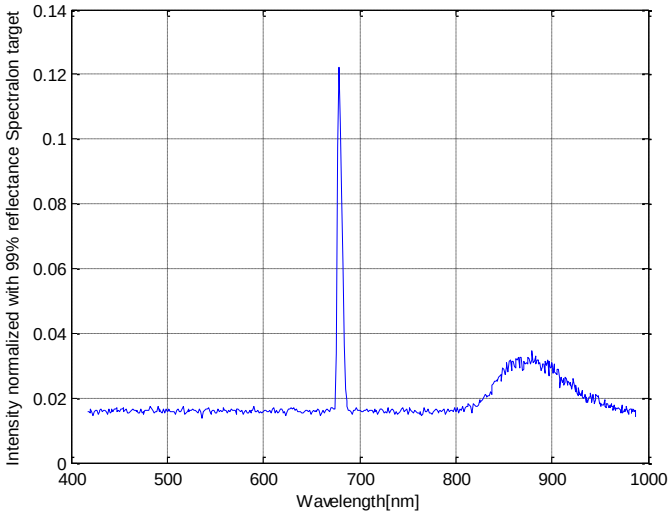

(c)

Figure 6-6 (a) Full field images at excitation wavelength. (b) Full field images at emission wavelength. (c) Intensity spectrum reflected from the sample (x=46mm, y=46mm). Scattering layer thickness = 5mm, μ_s = 100cm^{-1}

6.2.2 Discussion

Seen from experimental results, Figure 6-4 (a) and (b), both excitation and emission images are obtained with excellent spatial resolution without a tissue phantom overlaying the targets. The densities of the QDs within the fluorescent targets are not uniform, which makes the image of the upper sample look like a ring. As demonstrated in Figure 6-4 (c), the maximum peak occurs at the excitation wavelength, and the emission spectrum is over a range of 840nm to 910nm, which is narrow compared to conventional fluorophores (typically around 100 to 150nm).

When the 3mm thick tissue phantom is placed over the fluorescent target, Figure 6-5 (b) shows poorer spatial resolution compared with Figure 6-4 (b). However, the two samples can still be distinguished. With a thicker tissue phantom on top, the spatial resolution get even poorer and it is hard to distinguish due to the scattering medium as illustrated in Figure 6-6 (b) which is in agreement with the simulation results (Figure 6-2 and Figure 6-3). Both simulation and experiment use the total reflectance Spectralon target for calibration. Comparing Figure 6-5 (a) with Figure 6-2 (a), the centre of the image has the strongest reflected detection which is due to the non-uniform excitation from the beam expander.

The signals shown in Figure 6-5 (c) and Figure 6-6 (c) have higher excitation light intensity than that shown in Figure 6-4 (c). It can be understood as the reflection while the excitation light travel through the surface of scattering medium, as the distance between the object and camera is fixed.

6.3 Revised experimental configuration

As seen from the excitation spike of Figure 6-6 (c), the exposure time is limited in previous experiments to avoid the camera saturation. In order to obtain a higher SNR, the exposure time needs to be increased. An optical longpass filter (Thorlabs, FGL695) is applied to filter out the light below 700nm and therefore avoids the camera saturation. The red laser applied is replaced by a 50mW green laser (Oxxius, 532s-50-col-pp), so that even though the excitation light is of lower power, the excitation can be filtered out much more efficiently.

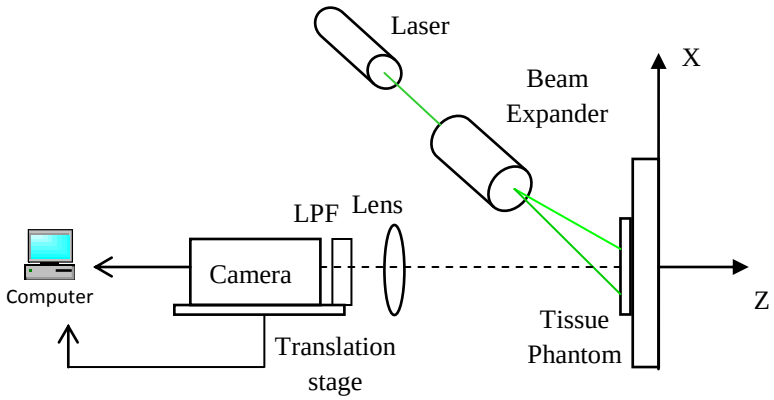

Figure 6-7 Revised experimental configuration

6.3.1 Sim. and Exp. results

Figure 6-8 and Figure 6-9 show the full field images of excitation (532nm) and emission (870nm) wavelengths with different tissue thickness from simulation result.

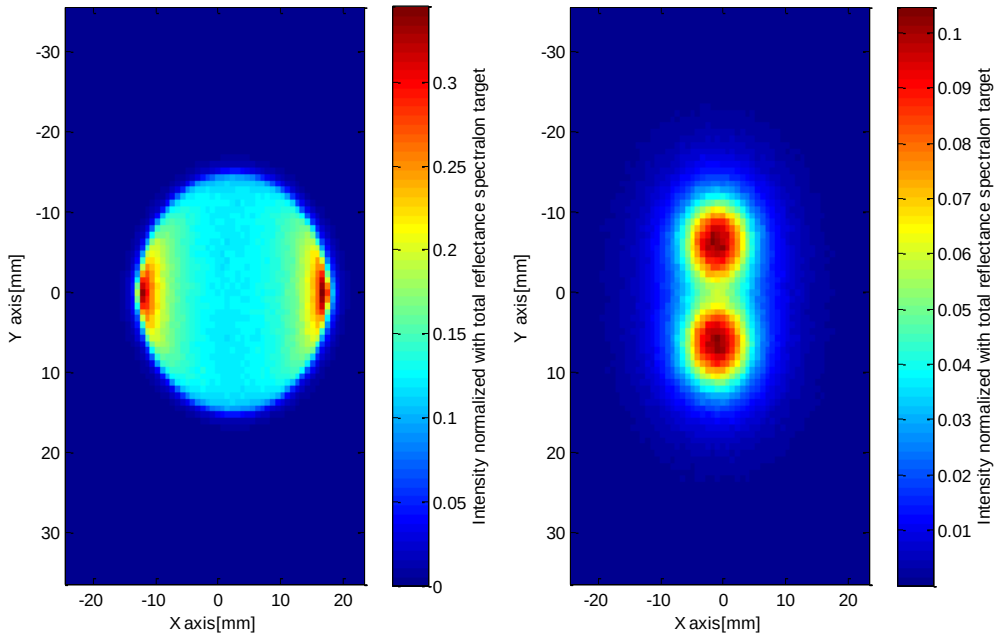

(a) Image at 532nm (b) Image at 870nm

Figure 6-8 (a) Full field images at excitation wavelength. (b) Full field images at emission wavelength. Scattering layer thickness = 3mm, μ_s = 100cm^{-1}

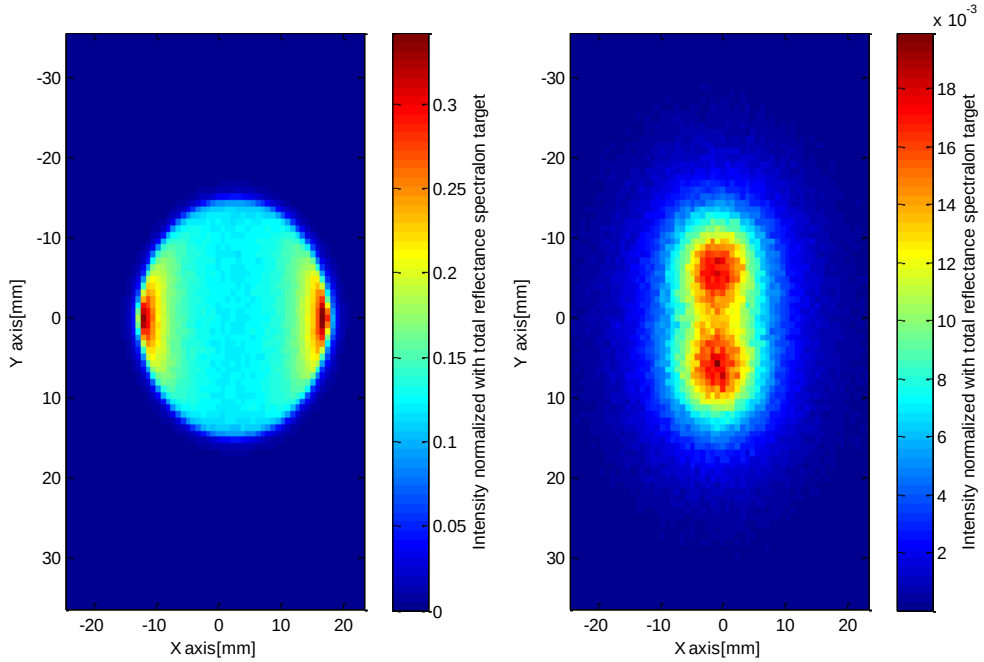

(a) Image at 532nm (b) Image at 870nm

Figure 6-9 (a) Full field images at excitation wavelength. (b) Full field images at emission wavelength. Scattering layer thickness = 3mm, μ_s = 100cm^{-1}

Figure 6-8 and Figure 6-9 are shown with the same setup but at a shorter excitation wavelength. Compared to Figure 6-3(b), the emission figure is nosier than at the same depth due to a heavier scattering effect in excitation stage.

Figure 6-10 (a) and (b) show the full field images of excitation (532nm) and emission (870nm) wavelength respectively when the laser directly illuminates on the sample. The exposure time is 150ms. Figure 6-10 (c) shows the intensity spectrum of the sample, in which the excitation light has been filtered out to a level beneath the dark noise of the camera.

Figure 6-11 and Figure 6-12 show similar results but with the scattering gel overlaying the fluorescent targets. The thickness of the tissue phantom equals 3mm and 5mm respectively (μ_s = 100cm^{-1} and μ_a = 0.2cm^{-1} @ 670nm).

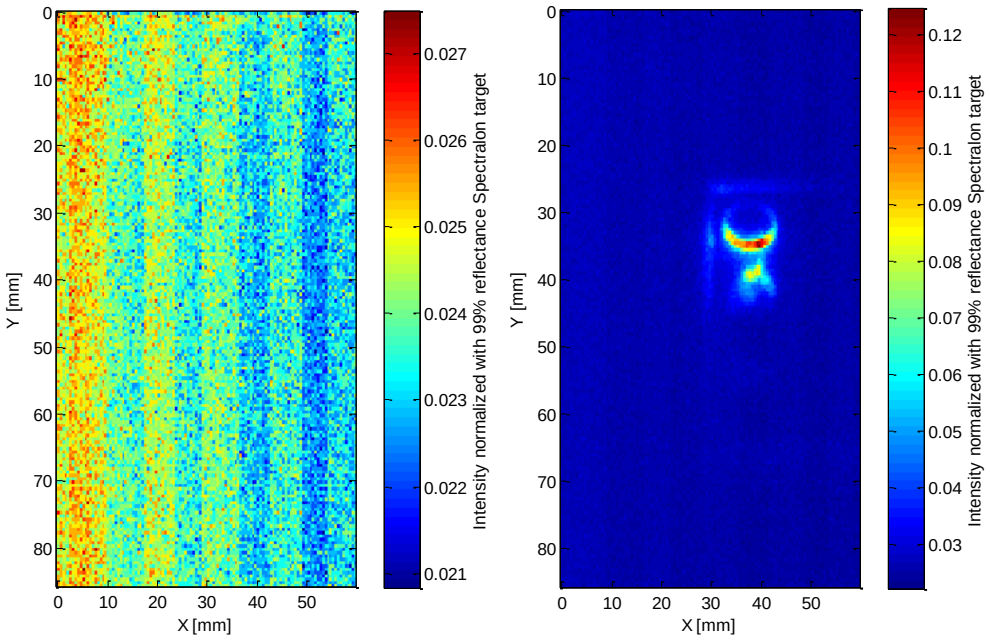

(a) Image at 530nm

(b) Image at 870nm

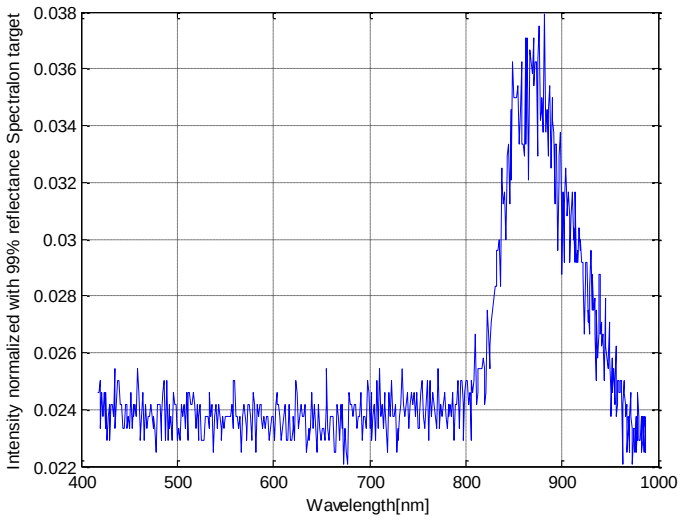

(c)

Figure 6-10 (a) Full field images at excitation wavelength. (b) Full field images at emission wavelength. (c) Intensity spectrum reflected from the sample. No scattering layer over the target.

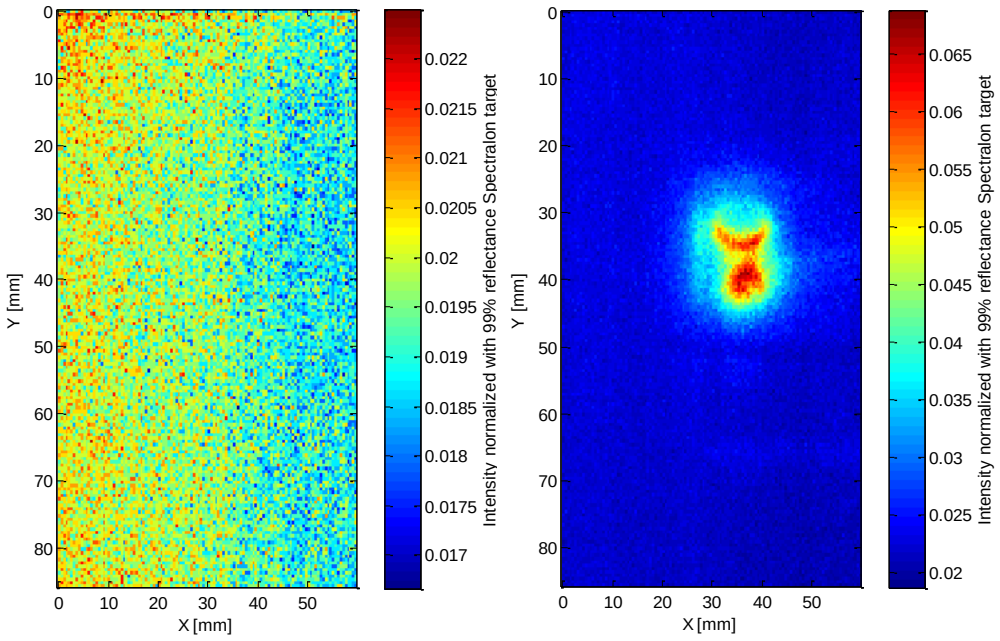

(a) Image at 530nm (b) Image at 870nm

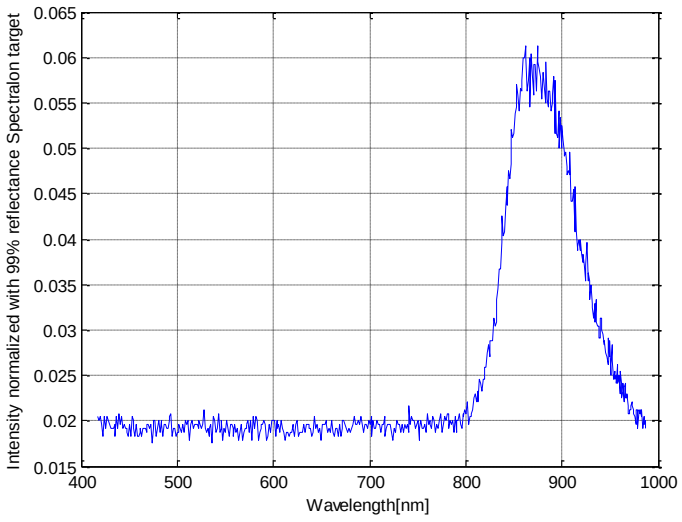

(c)

Figure 6-11 (a) Full field images at excitation wavelength. (b) Full field images at emission wavelength. (c) Intensity spectrum reflected from the sample. Scattering layer thickness = 3mm, μ_s = 100cm^{-1}

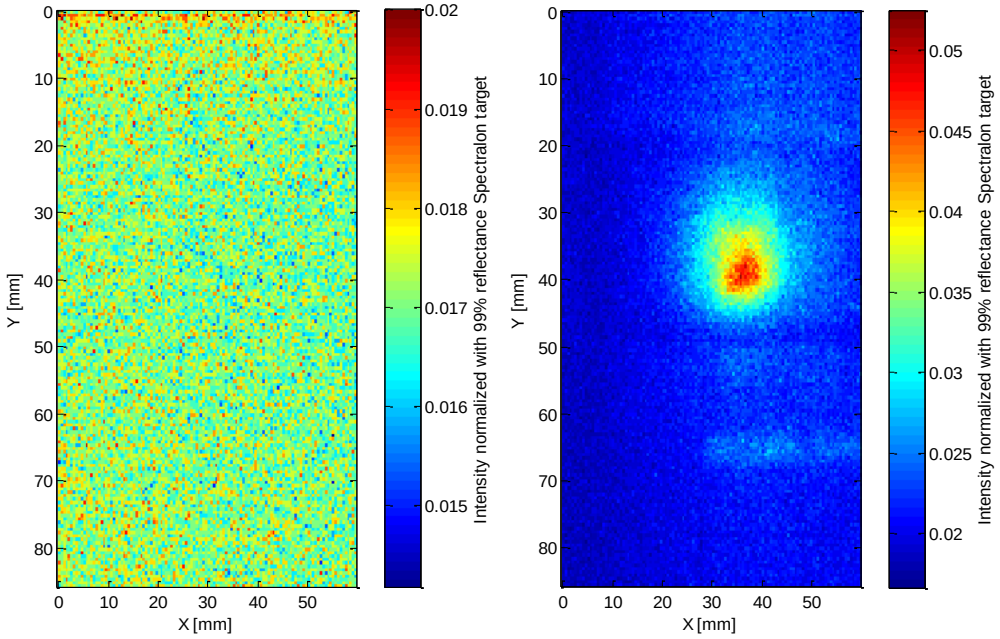

(a) Image at 530nm (b) Image at 870nm

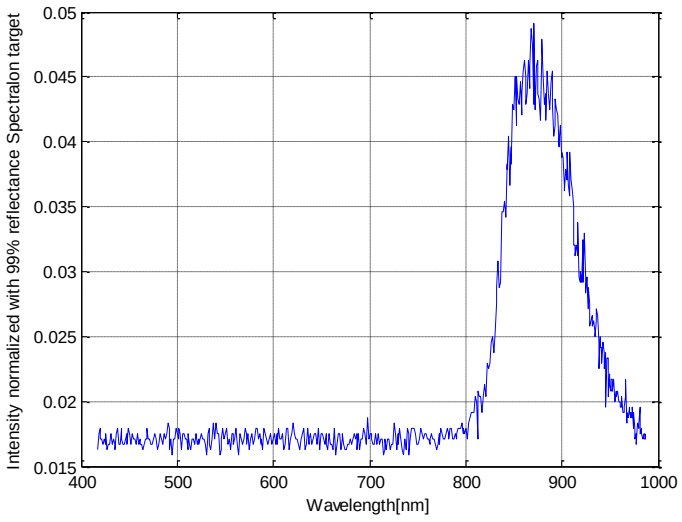

(c)

Figure 6-12 (a) Full field images at excitation wavelength. (b) Full field images at emission wavelength. (c) Intensity spectrum reflected from the sample. Scattering layer thickness = 5mm, μ_s = 100cm^{-1}

6.3.2 Discussion

As seen from the simulation results, compared Figure 6-9 with Figure 6-3, the spatial resolution of emission image excited by the green laser is worse than that excited by the red laser, because of a higher scattering and absorption coefficients.

Comparing the spatial resolutions of experimental results, the green laser yields worse result than that of red one due to heavier scattering as well. However, as illustrated in Figure 6-10 (c), by filtering out the excitation light, the emission light intensity detected is higher than that shown in Figure 6-4 (c) which is due to the longer exposure time. In the experiment, the illumination on the sample has an angle about 60 degree to the X axis (Seen in Figure 6-7) which makes the incident light profile have approximately 33% variation in the illumination across the field of view. This variation causes the uneven light emission and further influences the spatial resolution. In Figure 6-10 (b), when no scattering layer is over the samples, only the lower half of first sample and upper half of second one are excited compared to Figure 6-4 (b), which finally results in a worse resolution in Figure 6-4 (b) than that in Figure 6-10 (b).

6.4 Conclusion

This chapter aims to investigate and evaluates the SNR and spatial resolution experimentally obtained from infrared quantum dots with different excitation light, and qualitatively compares these with the simulation results.

Referred to the simulation results, all the setups are under an ideal situation which gives the conclusion that the change of excitation light in the full field system only affects the SNR. Practically, due to the time and equipment constraints, the comparison is not sufficiently made. Shorter excitation wavelengths offer a higher QDs absorption efficiency, which has advantage under non-scattering conditions. However, within the scattering medium, it leads to a higher scattering which degrades the SNR.

The practical results above are comparable to the simulations, the difference is in the excitation light which influences spatial resolution. The spatial resolution is also affected by the non-uniform light illumination and quantum dot density of samples.

Chapter 7

7 Conclusion & Future work

7.1 Introduction

The aim of this project has been to investigate a range of techniques and develop corresponding models for optical imaging through heavily scattering media. The criteria applied in this thesis to evaluate the performance of the systems are the SNR and spatial resolution.

Section 7.2 summarizes imaging techniques investigated in thesis. The overall conclusions are discussed in sections 7.3 while the possible future work is suggested in section 7.4.

7.2 Summary of the thesis

An USMOT Monte Carlo model is presented in Chapter 3 to find out the optimum experimental setup evaluated based on the SNR detected. Varying optical and acoustic parameters, *e.g.*, scattering and absorption coefficients, ultrasound frequencies and detector size are performed in the simulation.

Chapter 3 also provides a preliminary combination of incoherent USMOT with the fluorescent imaging technique in which the SNR of ultrasound modulated fluorescence signal can be optimized by changing the modulation frequency.

Based on the mechanisms proposed by Yuan *et al.* [126], another attempt of this ultrasound modulated fluorescence technique is the application of improving the accuracy of lifetime extraction in heavily scattering media which is presented in Chapter 4. Lifetime extraction is the most important step of fluorescence lifetime imaging microscopy which is considered as an advanced fluorescence imaging technique for its ability in distinguishes multiple fluorophores. In this chapter, a novel ultrasound associated technique is presented in single lifetime extraction to improve the performance of this technique in heavily scattering media.

Two fluorescence imaging systems which have been developed in both Monte Carlo and diffusion models are presented in Chapter 5. Two systems are investigated with a broad range of excitation and emission optical parameters which are then related to the wavelength of *in vivo* tissues with the aim of

obtaining the optimized imaging pairs. Performance is evaluated based on SNR and spatial resolution. The discussions are based on dermis, subdermis and muscle and take the autofluorescence effect into consideration.

The experimental results presented in Chapter 6 are a supplementary to the simulations in Chapter 5. CdSe quantum dots covered by an agar gel with polystyrene microspheres embedded within it are illuminated with light at different wavelengths.

7.3 Overall conclusion

All the models presented in this thesis aims to build up the optimum experimental setups and estimate the optimized practical results. The simple incoherent USMOT effect modeled in chapter 3 can be measured with reasonable SNR (modulation around 4% of DC level) under low frequency ultrasound modulation (smaller than 2MHz), when the ultrasonic wavelength is much longer than the optical path. Meanwhile, as the modulation depth decreases with an increase in ultrasound frequency, the incoherent effect is too weak to observe at high frequencies. Therefore, the optimum condition to model incoherent USMOT effect is suggested which includes a high power red or NIR laser, low frequency ($\leq$ 2MHz) ultrasound transducer and appropriate size of detector (5mm~10mm in radius). The coherent effects are considered as the dominant mechanisms in USMOT, but the incoherent model is still valuable as it offers a chance to model fluorescent light.

The combination of incoherent USMOT and ultrasound modulated fluorescence model aims to probe both mechanical and physiological parameters at the same time. The SNR of modulated fluorescence can be optimized by making the modulated frequency, $f = c/2d$, where d is the diameter of the target and c is the speed of the light in the medium. With 2MHz ultrasonic modulation, the SNR of the modulated fluorescent light is up to 26dB. However, the size of the target is hard to estimate with higher frequencies.

NIR fluorescence imaging is another technique expected to figure importantly among biomedical imaging field for its deep penetration depth and high SNR. The

selection of excitation light and fluorophore mainly depends on the application and imaging system, as best resolution is coupled with worst SNR. As discussed in section 5.1, the commercial imaging systems can be separated into two groups by excitation methods, full field illumination (FI) system and scanning input (SI) system. Comparing the FI and SI imaging systems, FI system offers a better SNR while the SI system provides a better imaging resolution. The selection of imaging pairs depends on the tissue type, auto-fluorescence, absorption spectrum quantum yield and brightness. In general, the longest available wavelength for both excitation and emission are the optimum choice, for their reduced μ_s and μ_a and low AF effect. For particular tissues, the optimized SNR and spatial resolution are obtained around 850nm and 950nm respectively for dermis, subdermis and muscle.

The fluorescence lifetime imaging of heavily scattering media has been introduced but not widely used today. The main challenge of this technique is the accuracy of lifetime imaging. The novel ultrasound associated lifetime extraction technique offers more accurate results than that from existing frequency domain technique and make it possible to extract lifetimes in a heavily scattering medium. By taking the excitation output as a reference and assuming the influence introduced by the fluorophore is negligible, the extraction accuracy can be further improved especially in high modulated frequency. However, as the phase shift goes quickly beyond 90 degrees, the optimized condition for this approach would be a fluorophore with moderate lifetime ($\leq$ 4ns) being modulated by ultrasound with low frequency ($\leq$ 100MHz).

7.4 Future works

7.4.1 Ultrasound techniques

A simple binary USMOT Monte Carlo grating model is presented in chapter 3, mainly focusing on the variation of optical properties. This work was carried out early in the PhD studies and helped to guide research in the remainder of this thesis. However, it is far from the actual USMOT interaction. A more practical sinusoidal model will be the future work. In addition, the change of

refractive index has not been considered, which sacrifices the accuracy to improve the computation efficiency.

7.4.2 NIR fluorescence techniques

The thesis aims to find out the optimized wavelength pairs based on SNR and spatial resolution in fluorescence imaging, which requires a large quantity of data of optical properties from visible spectrum to infrared. The current simulations are based on particular tissues (dermis, subdermis and muscle), a preliminary conclusion is given but this still needs to be validated from experimental results, which is not included in the thesis due to limitations in the time and equipment. In future work, a wide range of samples will be used with different μ_s, μ_a, thickness and QDs concentration. In addition, the experiments should be carried out with different excitation light and QDs using both FI and SI systems.

7.4.3 Combining techniques

The current ultrasound modulated fluorescence model presented is based on an incoherent USMOT model but the modulation efficiency is much lower compared with the coherent phase modulation mechanisms in USMOT as stated by Yuan *et al.* [126]. The improvement of modulation efficiency should be one of the future research fields. The use of microbubbles is one big step towards that direction [127] and coherent mechanisms of ultrasound fluorescence need to be considered as well [168].

7.5 Closing remark

To conclude, this thesis has mainly investigated USMOT, fluorescence imaging and the combination of these two techniques for optical imaging through scattering media. The techniques are evaluated with different acoustic and optical parameters based on the SNR and spatial resolution, and optimized experimental setups are proposed.

Appendix

Diffusion Equation (DA) for semi-infinite homogeneous slab

The equations presented in the thesis are based on the work from Patterson *et.al* [142]. However, no completed solution is presented in [142] except two expressions of reflectance $R(\rho, z, t)$ and transmittance $T(\rho, z, t)$with three and four dipoles respectively.

$$R(\rho, z, t) = (4\pi Dc)^{-3/2} t^{-5/2} exp(-\mu_a ct) exp\left(-\frac{\rho^2}{4Dct}\right)\left\{z_0 \exp\left(-\frac{{z_0}^2}{4Dct}\right) - (2d - z_0) exp\left[-\frac{(2d - z_0)^2}{4Dct}\right] + (2d + z_0) exp\left[-\frac{(2d + z_0)^2}{4Dct}\right]\right\} \quad \text{A-0-1}$$

$$T(\rho, z, t) = (4\pi Dc)^{-3/2} t^{-5/2} exp(-\mu_a ct) exp\left(-\frac{\rho^2}{4Dct}\right)\left\{(d - z_0) \exp\left(-\frac{(z - z_0)^2}{4Dct}\right) - (d + z_0) exp\left[-\frac{(d + z_0)^2}{4Dct}\right] + (3d - z_0) exp\left[-\frac{(3d - z_0)^2}{4Dct}\right] - (3d + z_0) exp\left[-\frac{(3d + z_0)^2}{4Dct}\right]\right\} \quad \text{A-0-2}$$

where *c* is the speed of light in the tissue, *d* is the slab thickness, *D* is the diffusion coefficient and z_0 is the depth position where incident photons are initially scattered at

$$D = \frac{1}{\mu_a + (1 - g)\mu_s} \quad \text{A-0-3}$$

$$z_0 = \frac{1}{(1 - g)\mu_s} \quad \text{A-0-4}$$

μ_a is the absorption coefficient, μ_s is the scattering coefficient, and g is the anisotropy.

From the radiative transfer equation (RTE), the following derivations are based on the diffusion theory and same assumptions are made as in the Patterson's paper [142].

$$\frac{1}{c}\frac{\partial L(\vec{r},\hat{s},t)}{\partial t} = -\hat{s}\cdot\nabla L(\vec{r},\hat{s},t) - \mu_t L(\vec{r},\hat{s},t) + \mu_s\int_{4\pi} L(\vec{r},\hat{s},t)P(\hat{s}',\hat{s})\,d\Omega' + S(\vec{r},\hat{s},t) \quad \text{A-0-5}$$

where $L(\vec{r},\hat{s},t)$ is the radiance which can be defined as energy flow per unit normal area per unit solid angle per unit time, $\mu_t = \mu_s + \mu_a$ is the extinction coefficient, $P(\hat{s}',\hat{s})$ is the phase function, representing the probability of light with propagation direction $\hat{s}'$ being scattered into $\hat{s}$ and $S(\vec{r},\hat{s},t)$ describes the light source.

The simplifying assumptions are,

1. The specific intensity of the radiance is assumed to be isotropic and can be approximated with the first two orders of the Taylor's expansion.

$$L(\vec{r},\hat{s},t) = \frac{1}{4\pi}\Phi(\vec{r},t) + \frac{3}{4\pi}\vec{J}(\vec{r},t)\cdot\hat{s} \quad \text{A-0-6}$$

   where $\Phi(\vec{r},t)$ is the fluence rate and $\vec{J}(\vec{r},t)$ is the fluence flux vector.

2. The phase function $P(\hat{s}',\hat{s})$ depends only on the angle between the scattered $\hat{s}'$ and incident $\hat{s}$ directions. By substituting equation A-0-6 for radiance, the RTE can be rewritten as

$$\frac{1}{c}\frac{\partial}{\partial t}\Phi(\rho,z,t) + \nabla\vec{J}(\vec{r},t) + \mu_a\Phi(\rho,z,t) = S(\rho,z,t) \quad \text{A-0-7}$$

3. It is assume that the diffuse photon fluence rate $\Phi(\rho,z,t)$ satisfies the diffusion equation, and the change of fluence flux $\vec{J}(\vec{r},t)$ over one transport mean free path is negligible, by applying the Fick's law,

$$\vec{J}(\rho,d,t) = -D\nabla\Phi(\rho,z,t)|_{z=d} \quad \text{A-0-8}$$

equation A-0-7 can be rewritten as

$$\frac{1}{c}\frac{\partial}{\partial t}\Phi(\rho,z,t) - D\nabla^2\Phi(\rho,z,t) + \mu_a\Phi(\rho,z,t) = S(\rho,z,t) \qquad \text{A-0-9}$$

where $S(\rho,z,t)$ is the photon source.

In the real case, the source is assumed to be a narrow collimated pulsed light beam which is normally incident upon the surface of the scattering slab. However, it is a good approximation to model it as a pulsed point source from the position the light starts scattering isotropiclly $\delta(\rho,z-z_0,t)$.

In this situation, the solution of A-0-9 in a homogeneous infinite medium is [164],

$$\Phi(\rho,z,t) = c(4\pi Dct)^{-3/2}exp\left(-\frac{\rho^2+z^2}{4Dct} - \mu_a ct\right) \qquad \text{A-0-10}$$

To find the solution in a homogeneous slab, the boundary condition is applied which is achieved by adding infinite number of dipoles having the same optical property and representing pairs of positive and negative sources. The sources are placed at

$$\begin{cases} z_+ = 2md + z_0 \\ z_- = 2md - z_0 \end{cases} m = (0, \pm1, \pm2, \dots\dots) \qquad \text{A-0-11}$$

The fluence rate can be represented by the sum of the contribution of each source,

$$\Phi(\rho,z,t) = \Phi_+(\rho,z,t) + \Phi_-(\rho,z,t) \qquad \text{A-0-12}$$

with

$$\begin{aligned} &\Phi_+(\rho,z,t) \\ &= c(4\pi Dct)^{-3/2}exp\left(-\mu_a ct \right. \\ &\left. -\frac{\rho^2}{4Dct}\right)exp\left(\sum_{m=-\infty}^{m=+\infty} exp\left[-\frac{(z-2md-z_0)^2}{4Dct}\right]\right) \end{aligned} \qquad \text{A-0-13}$$

$$\Phi_{-}(\rho,z,t) = -c(4\pi Dct)^{-3/2} exp\left(-\mu_a ct - \frac{\rho^2}{4Dct}\right) exp\left(\sum_{m=-\infty}^{m=+\infty} exp\left[-\frac{(z-2md+z_0)^2}{4Dct}\right]\right) \quad \text{A-0-14}$$

The final expression for the fluence rate at distance ρ and depth z is

$$\Phi(\rho,z,t) = c(4\pi Dct)^{-3/2} exp\left(-\mu_a ct - \frac{\rho^2}{4Dct}\right)\left\{\sum_{m=-\infty}^{m=+\infty} exp\left[-\frac{(z-2md-z_0)^2}{4Dct}\right] - \sum_{m=-\infty}^{m=+\infty} exp\left[-\frac{(z-2md+z_0)^2}{4Dct}\right]\right\} \quad \text{A-0-15}$$

References

[1] L. Wang, "Ultrasound-mediated biophotonic imaging: A review of acousto-optical tomography and photo-acoustic tomography", Disease Markers, **19,** 123–138 (2004).

[2] G.D. Michailidis, P. Papageorgiou and D.L. Economides, "Assessment of fetal anatomy in the first trimester using two- and three-dimensional ultrasound", The British journal of radiology, **75**, 215–219 (2002).

[3] D. Krakow, J. Williams III, M. Poehl, D.L. Rimoin and L.D. Platt, "Use of three-dimensional ultrasound imaging in the diagnosis of prenatal-onset skeletal dysplasias". Ultrasound in Obstetrics and Gynecology, **21**, 467–472 (2003).

[4] American National Standards Institute and Laser Institute of America. *2007* Safe use of laser, ANSI Z136.1, Washington, DC: ANSI.

[5] V. Tuchin, Tissue Optics (SPIE, Bellingham, WA, USA, 2000).

[6] D.S. Elson, R. Li, C. Dunsby, R. Eckersley and M. Tang, "Ultrasound-mediated optical tomography: a review of current methods", Interface Focus., **1**, 632-648 (2011).

[7] H. Dehghani, S. Srinivasan, B.W. Pogue and A. Gibson, "Numerical modelling and image reconstruction in diffuse optical tomography", Phil. Trans. R. Soc. A**, 367**, 3073-3093 (2009).

[8] D.A. Boas, D.H. Brooks, E.L. Miller, C.A. DiMarzio, M. Kilmer, R.J. Gaudette and Q. Zhang, “Imaging the body with diffuse optical tomography”, Signal Processing Magazine, IEEE, **18**, 57-75 (2001).

[9] D. Huang, E.A. Swanson, C.P. Lin, J.S. Schuman, W.G. Stinson, W. Chang, M.R. Hee, T. Flotire, K. Gregory, C.A. Puliafito and J.G. Fujimoto, “Optical coherence tomography”, Science, **254**, 1178–1181 (1991).

[10] C. Mason, J.F. Markusen, M.A. Town, P. Dunnill and R.K. Wang, “The potential of optical coherence tomography in the engineering of living tissue”, Phys. Med. Biol., **49**, 1097-1115 (2004).

[11] S.G. Resink, W. Steenbergen, and A.C. Boccara, “State-of-the art of acoust-optic sensing and imaging of turbid media”, J. of Biomed. Opt., **17**, 040901 (2012).

[12] L. Wang, “Multiscale photoacoustic microscopy and computed tomography”, Nat. photonics., **3**, 503-509 (2009).

[13] L. Wang, “Mechanisms of ultrasonic modulation of multiply scattered coherent light: a Monte Carlo model”, Opt. Lett., **26**, 1191-1193 (2001).

[14] W. Leutz and G. Maret, “Ultrasoic modulation of multiply scattered light”, Physica B., **204**, 14-19 (1995).

[15] M. Kempe, M. Larionov, D. Zaslavsky, and A.Z. Genack, “Acousto-optic tomography with multiply scattered light”, J. Opt. Soc. Am. A, **14**, 1151-1158 (1997).

[16] L. Wang and X. Zhao, “Ultrasound-modulated optical tomography of absorbing objects buried in dense tissue-simulating turbid media”, Applied Optics, **36**, 7277-7282 (1997).

[17] D. Contini, F. Martelli, and G.Zaccanti, “Photon migration through a turbid slab described by a model based on diffusion theory”, Applied Optics, **36**, 4587-4599 (1997).

[18] R.C. Haskell, L.O. Svaasand, T.T. Tsay, T.C. Feng, M.S. McAdams and B.J. Tromberg, "Boundary conditions for the diffusion equation in radiative transfer", Journal of the Optical Society of America A, **11**, 2727–2741 (1994).

[19] N. Metropolis and S. Ulam, “The Monte Carlo Method”, Journal of the American Statistical Association, **44**, 335–341 (1949).

[20] H.T. MacGillivray and R.J. Dodd, “Monte-Carlo simulations of galaxy systems”, Astrophysics and Space Science, **86**, 437-452 (1982).

[21] L. Wang, S.L. Jacques, “Monte Carlo Modeling of Light Transport in Multi-layered Tissues in Standard C”, PhD Thesis.

[22] S.A. Prahl, M. Keijzer, S.L. Jacques, and A.J. Welch, “A Monte Carlo Model of Light Propagation in Tissue”, Dosimetry of Laser Radiation in Medicine and Biology, SPIE Institute Series, IS **5**, 102-111 (1989).

[23] L.G. Henyey and J.L. Greenstein, “Diffuse Radiation in the Galaxy”, Astrophysics Journal, **93**, 70-83 (1941).

[24] S.A.Prahl, M.Keijer, "A Monte Carlo Model of Light Propagation in Tissue", SPIE Institute Series, **IS 5**, (1989).

[25] H.C. van de Hulst, Light Scattering by Small Particles, (Dover Publications Inc., New York, NY, USA, 1981).

[26] L. Wang, "Mechanisms of ultrasonic modulation of multiply scattered coherent light: an analytic model," Phys. Rev. Lett., **87**, 043903 (2001).

[27] S. Sakadzic and L. Wang, "Ultrasonic modulation of multiply scattered coherent light: an analytical model for anisotropically scattering media", Phys. Rev. E, **66**, 026603 (2002).

[28] S. Sakadzic and L. Wang, "Modulation of multiply scattered coherent light by ultrasonic pulses: an analytical model", Phys. Rev. E, **72**, 036620 (2005).

[29] G.D. Mahan, W.E. Engler, J.J. Tiemann and E. Uzgiris, "Ultrasonic tagging of light theory", Applied Physical Sciences, **95,** 14015-14019 (1998).

[30] A. Nieva and C.A. Dimarzio, and "Monte Carlo simulations in acousto-photonic imaging", Optical Society of America, **Biomed Topical Meeting**, 1-3 (2002).

[31] S. Sakadzic and L. Wang, "Correlation transfer equation for ultrasound-modulated multiply scattered light", Phys. Rev., **74**, 036618 (2006).

[32] S. Sakadzic and L. Wang, “Correlation transfer equation for multiply scattered light modulated by an ultrasonic pulse”, J.Opt.Soc.Am.A, **24**, 2797–2806 (2007).

[33] Q. Liu, S. Norton and T. V-Dinh, “Modeling of nonphase mechanisms in ultrasonic modulation of light propagation”, Applied Optics, **47**, (2008).

[34] T.S. Leung and S. Powell, “Fast Monte Carlo simulations of ultrasound modulatelight using a graphics processing unit”, *J. Biomed. Opt*., 15, 055007 (2010).

[35] S. Powell and T.S. Leung, “Highly parallel Monte-Carlo simulations of the acousto-optic effect in heterogeneous turbid media”, J. of Bio. Opt., **17**, 045002 (2012).

[36] F.A. Marks, H.W. Tomlinson and G.W. Brooksby, “Comprehensive approach to breast cancer detection using light: photon localization by ultrasound modulation and tissue characterization by spectral discrimination”, *in Photon Migration and Imaging in Random Media and Tissue*, B. Chance and R. R. Alfano, eds., Proc. SPIE **1888**, 500-510 (1993).

[37] M. Kempe, M. Larionov, D. Zaslavsky and A.Z. Genack, “Acousto-optic tomography with multiple scattered light”, J. Opt. Soc. Am., **14**, 1151-1158 (1997).

[38] Y.Z. Li, H.L. Zhang, C.H. Kim, K.H. Wagner, P. Hemmer and L.V. Wang, “Pulsed ultrasound modulated optical tomography using spectral-hole burning as a narrowband spectral filter”, Appl. Phys. Lett., **93**, 011111 (2008).

[39] M. Hisaka, and Y. Sasakura, “Light scattering characteristics of biological tissues in coaxial ultrasound-modulated optical tomography”, Japanese J. of Appl. Phys., **48**, 067002 (2009).

[40] S. Leveque, A.C. Boccara, M. Lebec, and H. Saint-Jalmes, “Ultrasonic tagging of photon paths in scattering media: parallel speckle modulation processing”, Opt. Lett., **24**, 181–183 (1999).

[41] S. Leveque-Fort, “Three-dimensional acousto-optic imaging in biological tissues with parallel signal processing”, Appl. Opt., **40**, 1029-1036 (2000).

[42] G. Yao, and L. Wang, “Theoretical and experimental studies of ultrasound-modulated optical tomography in biological tissue”, Appl. Opt., **39**, 659-664 (2000).

[43] S. Kothapalli and L. Wang, “*Ex vivo* blood vessel imaging using ultrasound-modulated optical microscopy”, J. of Biomed. Opt., **14**, 014015 (2009).

[44] A. Lev and B. Sfez, “*In vivo* demonstration of the ultrasound-modulated light technique”, J. Opt. Soc. Am., **20**, 2347-2354 (2003).

[45] A. Lev, E. Rubanov, B. Sfez, S. Shany, and A.J. Foldes, “Ultrasound-modulated light tomography assessment of osteoporosis”, Opt. Lett., **30**, 1692-1694 (2005).

[46] M. Gross, P. Goy, B.C. Forget, M. Atlan, R. Ramaz, A.C. Boccara and A.K. Dunn, "Heterodyne detection of multiply scattered monochromatic light with a multipixel detector", Opt. Lett., **30**, 1357-1359 (2005).

[47] A.G. Bell, "On the production and reproduction of sound by light", Am. J. Sci., **20**, 305-324 (1880).

[48] C.G. Hoelen, F.F. de Mul, R. Pongers and A. Dekker, "Three-dimensional photoacoustic imaging of blood vessels in tissue", Optics letters, **23**, 648-650 (1998).

[49] M. Tang, D.S. Elson, R. Li, C. Dunsby and R.J. Eckersley, "Photoacoustics, thermoacoustics, and acousto-optics for biomedical imaging," Proc. IMechE., **224**, 291-306 (2010).

[50] N.T. Huynh, B.R. Hayes-Gill, F. Zhang and S.P. Morgan, "Ultrasound modulated imaging of luminescence generated within a scattering medium", J. Biomed. Opt., **18**, 020505 (2013).

[51] S. Luo, E. Zhang, Y. Su, T. Cheng and C. Shi, "A review of NIR dyes in cancer targeting and imaging", Biomaterials, **32**, 7127-7138 (2011).

[52] F. Leblond, S.C. Davis, P.A. Valdes and B.W. Pogue, "Pre-clinical whole-body fluorescence imaging: Review of instruments, methods and applications", J. Photochem. & Photobio. B: Biology, **98**, 77-94 (2010).

[53] J. Rao, A. Dragulescu-Andrasi and H. Yao, "Fluorescence imaging *in vivo*: recent advances", Current Opinion in Biotechnology, **18**, 17–25 (2007).

[54] J.V. Frangioni, "*In vivo* near-infrared fluorescence imaging", Curr. Opin. Chem. Biol., **7**, 626-634 (2003).

[55] B. Ballou, L.A. Ernst and A.S. Waggoner, "Fluorescence imaging of tumors *in vivo*", Curr. Med. Chem., **12**, 795-805 (2005).

[56] C.H. Tung, Y. Lin, W.K. Moon, and R. Weissleder, "A receptor-targeted near-infrared fluorescence probe for *in vivo* tumor imaging", Chembiochem, **3,** 784–786 (2002).

[57] J.R. Johnson, N. Fu, E. Arunkumar, W.M. Leevy, S.T. Gammon, D. Piwnica-Worms, B.D. Smith, "Squaraine rotaxanes: superior substitutes for Cy-5 in molecular probes for near-infrared fluorescence cell imaging", Angew Chem Int Ed, **46**, 5528–5531 (2007).

[58] N.G. Gurskaya, A.F. Fradkov, A. Terskikh, M.V. Matz, Y.A. Labas, V.I. Martynov, Y.G. Yanushevich, K.A. Lukyanov and S.A. Lukyanov, "gfp-like chromoproteins as a source of far-red fluorescent proteins", FEBS Lett., **507**, 16-20 (2001).

[59] L. Wang, W.C. Jackson, P.A. Steinbach and R.Y. Tsien, "evolution of new nonantibody proteins via iterative somatic hypermutation", Proc. Natl. Acad. Sci. USA, **101**, 16745-16749 (2004).

[60] M.A. Shkrob, Y.G. Yanushevich, D.M. Chudakov, N.G. Gurskaya, Y.A. Labas, S.Y. Poponov, N.N. Mudrik, S.A. Lukyanov and K.A. Lukyanov, "Far-red fluorescent protein evolved from a blue chromoprotein from Actinia equina", J. Biochem., **392**, 649-654 (2005).

[61] D. Shcherbo, E.M. Merzlyak, T.V. Chepurnykh, A.F. Fradkov, G.V. Ermakova, E.A. Solovieva, K.A. Lukyanov, E.A. Bogdanova, A.G. Zaraisky, S. Luyanov, and D.M. Chudakov, "Bright far-red fluorescent protein for whole-body imaging", Nat. Methods, **4**, 741-746 (2007).

[62] D. Shcherbo, C.S. Murphy, G.V. Ermakova, E.A. Solovieva, T.V. Chepurnykh, A.S. Shcheglov, V.V. Verkhusha, V.Z. Pletnev, K.L. Hazelwood, P.M. Roche, S. Lukyanov, A.G. Zaraisky, M.W. Davidson, and D.M. Chudakov, "Far-red fluorescent tags for protein imaging in living tissues", Biochem. J., **418**, 567-574 (2009).

[63] Y. Wang and L. Chen, "Quantum dots, lighting up the research and development of nanomedicine." Nanomed. Nanotech. Biol. Med., **7**, 385-402 (2011)

[64] D.J. Bharali and S.A. Mousa, "Emerging nanomedicines for early cancer detection and improved treatment: current perspective and future promise.", Pharmacol. & Ther., **128**, 324-335 (2010).

[65] M. Nurunnabi, K.J. Cho, J.S. Choi, K.M. Huh and Y.K. Lee. "Targeted near-IR QDs-loaded micelles for cancer therapy and imaging." Biomaterials, **31**, 5436-5444 (2010).

[66] H. Wang, T.B. Huff, D.A. Zweifel, W. He, P.S. Low, A. Wei, *et al.* "*In vitro* and *in vivo* two-photon luminescence imaging of single gold nanorods.", P. Natl. Acad. Sci. USA., **102**, 15752-15756 (2005).

[67] S.M. Janib, A.S. Moses and J.A. MacKay, “Imaging and drug delivery using theranostic nanoparticles.” Adv. Drug Deliver, **62**, 1052-1063 (2010).

[68] X. He, K. Wang and Z. Cheng, “*In vivo* near-infrared fluorescence imaging of cancer with nanoparticle-based probes.” Wiley Interdiscip Rev Nanomed Nanobiotechnol, **2**, 349-366 (2010).

[69] A.P. Alivisatos, “Semiconductor clusters, nanocrystals, and quantum dots”, Science, **271**, 933-937 (1996).

[70] X. Michalet, F.F. Pinaud, L.A. Bentolila, J.M. Tsay, S. Doose, J. Li, G. Sundaresan, A. Wu, S.S. Gambhir and S. Weiss, “Quantum dots for live cells, *in vivo* imaging, and diagnostics”, Science, **307**, 538-544 (2005).

[71] R.G. Aswathy, Y. Yoshida, T. Maekawa and D.S. Kumar, “Near-infrared quantum dots for deep tissue imaging”, Ana.l Bioanal. Chem., **397**, 1417-1435 (2010).

[72] T.D. Lacoste, X. Michalet, F. Pinaud, D.S. Chemla, A.P. Alivisatos and S.Weiss, “Ultrahigh-resolution multicolor colocalization of single fluorescent probes”, Proc. Natl. Acad. Sci. U.S.A., **97**, 9461-9466 (2000).

[73] X. Michalet, F. Pinaud, T.D. Lacoste, M. Dahan, M.P. Bruchez, A.P. Alivisatos and S. Weiss, “Properties of Fluorescent Semiconductor Nanocrystals and their Application to Biological Labeling”, Single Mol., **2**, 261-276 (2001).

[74] M. Dahan, S. Levi, C. Luccardini, P. Rostaing, B. Riveau and A. Triller, "Diffusion Dynamics of Glycine Receptors Revealed by Single–Quantum Dot Tracking", Science, **302**, 442-445 (2003).

[75] S. Hohng and T. Ha, "Near-complete suppression of quantum dot blinking in ambient conditions", J. Am. Chem. Soc., **126**, 1324-1325 (2004).

[76] B. Ballou, L.A. Ernst and A.S. Waggoner, "Fluorescence imaging of tumors *in vivo*", Curr. Med. Chem., **12**, 795-805 (2005).

[77] I.L. Medintz, H.T. Uyeda, E.R. Goldman and H. Mattoussi, "Quantum dot bioconjugates for imaging, labeling and sensing", Nat. Mater, **4**, 435-446 (2005).

[78] D.R. Larson, W.R. Zipfel, R.M. Williams, S.W. Clark, M.P. Bruchez, F.W. Wise and W.W. Webb, "Water-soluble quantum dots for multiphoton fluorescence imaging *in vivo*", Science, **30**, 1434-1436 (2003).

[79] L. Kelmanson, "Enhanced red and far-red red fluorescent proteins for in vivo imaging", *Nature Methods*, **6**, (2009).

[80] J. Lecoq and M.J. Schnitzer, "An infrared fluorescent protein for deeper imaging", Nat. Biotechnol., **29**, (2011).

[81] G.S. Filonov, K.D. Piatkevich, Li-Min Ting, Jinghang Zhang, K. Kim, V.V. Verkhusha, "Bright and stable near-infrared fluorescent protein for *in vivo* imaging", Nat. Biotechnol., **29**, 757-761 (2011).

[82] J.R. Lakowicz, “Principles of Fluorescence Spectroscopy” 1Plenum, New York (1985).

[83] J.R. Lakowicz, “Topics in Fluorescence Spectroscopy” 1Plenum, New York (2002).

[84] J.P. Robinson, “Emerging Tools For Single-Cell Analysis”, Wiley-Liss, New York (2000).

[85] J.W. Lichtman and J.A. Conchello, Fluorescence microscopy, Nat. Methods, **2**, 910-919 (2005).

[86] X.D. Li, M.A. O’Leary, D.A. Boas, B. Chance and A.G. Yodh “Fluorescent diffuse photon density waves in homogeneous and heterogeneous turbid media: analytic solutions and applications”, Appl. Opt., **35**, 3746-3758 (1996).

[87] A.E. Cerussi, J.S. Maier, S. Fantini, M.A. Franceschini, W.W. Mantulin and E. Gratton “Experimental verification of a theory for the time-resolved fluorescence spectroscopy of thick tissues”, Appl. Opt., **36**, 116-124 (1997).

[88] F. Dushinsky, Z.phys., **81**, 7 (1933).

[89] E.A. Bailey and G.K. Rollefson, “The determination of the fluorescence lifetimes of dissolved substances by a phase shift method”, J. Chem. Phys., **21**, 1315–1326 (1953).

[90] A.M. Bonch-Breuvich, I.M. Kazarin, V.A. Molchanov and I.V. Shirokov, "An experimental model of a phase fluoremeter", Instrum. Exp. Tech., **2**, 231–236 (1959).

[91] J.B. Birks and D.J. Dyson, "Phase and modulation fluorometer", J. Sci. Instrum., **38**, 282–285 (1961).

[92] R.D. Spencer and G. Weber, "Measurement of sub-nanosecond fluorescence lifetimes with a cross-correlation phase fluorometer", Ann. N.Y. Acad. Sci., **158**, 361–376 (1969).

[93] A. Grinvald and I.Z. Stelnberg, "On the analysis of fluorescence decay kinetics by the method of least-squares", Anal. Biochem., **59**, 583-598 (1974).

[94] J.H. Easter, R.P. DeToma, and L. Brand, "Nanosecond time-resolved emission spectroscopy of a fluorescence probe adsorbed to l-a-egg lecithin vesicles", Biophys. J., **16**, 571-583 (1976).

[95] Z. Bay, "Calculation of Decay Times from Coincidence Experiments", Phys. Rev., **77**, 419–419 (1950)

[96] S.S. Brody, "Instrument to Measure Fluorescence Lifetimes in the Millimicrosecond Region", Rev. Sci. Instrum., **28**, 1021-1026 (1957).

[97] D.V. O'Connor, W.R. Ware, J.C. Andre, "Deconvolution of fluorescence decay curves, a critical comparison of techniques", J. Phys. Chem., **83**, 1333-1343 (1979).

[98] E.Gratton and M. Limkeman, “A continuously variable frequency cross-correlation phase fluorometer with picosecond resolution”, Biophys. J., 44, 315-324 (1983).

[99] J.R. Lakowicz and B.P. Maliwal, “Construction and performance of a variable-frequency phase-modulation fluorometer”, Biophys. Chem., 21, 61-78 (1985).

[100] Theodorus, W.J. Gadella, Jr., T.M. Jovin and R.M. Clegg, “Fluorescence lifetime imaging microscopy (FLIM) Spatial resolution of microstructures on the nanosecond time scale”, Biophysical Chemistry, **48**, 221-239 (1993).

[101] M.Hassan, J.Riley et al, “Fluorescence lifetime imaging system for *in vivo* studies”, Mol. Imaging, **6**, 229-236 (2007).

[102] C.L. Hutchinson, J.R. Lakowicz, and E.M. Sevick-Muraca, “Fluorescence lifetime based sensing in tissues: a computational study”, Biophys. J., **68**, 1574–1582 (1995).

[103] C.L. Hutchinson, T.L. Troy and E.M. Sevick-Muraca, “Fluorescence-lifetime determination in tissues or other scattering media from measurement of excitation and emission kinetics”, Appl.Opt., **35**, 2325-2332 (1996).

[104] J. Wu, M.S. Feld and R.P. Rava, ‘‘Analytical model for extracting intrinsic fluorescence in turbid media’’, Appl. Opt., **32**, 3585–3595 (1993).

[105] H.J. Sterenborg, A.E. Saarnak, R. Frank and M. Motamedi, "Evaluation of spectral correction techniques for fluorescence measurements on pigmented lesions *in vivo*", J. Photochem. Photobiol., **B35**, 159–165 (1996).

[106] C.M. Gardner, S.L. Jacques and A.J. Welch, "Fluorescence spectroscopy of tissue: recovery of intrinsic fluorescence from measured fluorescence", Appl. Opt., **35**, 1780–1792 (1996).

[107] M.S. Patterson and B.W. Pogue, "Mathematical model for time-resolved and frequency-domain fluorescence spectroscopy in biological tissues", Appl. Opt., **33**, 1963–1974 (1994).

[108] D.Y. Paithankar, A.U. Chen, B.W. Pogue, M.S. Patterson and E.M. Sevick-Muraca, "Imaging of fluorescent yield and lifetime from multiply scattered light reemitted from random media", Appl. Opt., **36**, 2260–2272 (1997).

[109] A.J. Welch and R. Richards-Kortum, ''Monte Carlo simulation of the propagation of fluorescent light'', in Laserinduced Interstitial Thermotherapy, G. Mu ̈ller and A. Roggan, eds. (Society of Photo-Optical Instrumentation Engineers, Bellingham, Wash.), 174–189 (1995).

[110] A.J. Welch, C.M. Gardner, R. Richards-Kortum, E. Chan, G. Criswell, J. Pfefer and S. Warren, "Propagation of fluorescence light", Lasers Surg. Med., **21**, 166–178 (1997).

[111] J. Swartling, A. Pifferi, A. Enejder and S. Andersson-Engels, "Accelerated Monte Carlo models to simulate fluorescence spectra from layered tissues", J. Opt. Soc. Am. A, **20**, 714-727 (2003).

[112] A. Kienle and M.S. Patterson, "Determination of the optical properties of turbid media from a single Monte Carlo simulation", Phys. Med. Biol., **41**, 2221–2227 (1996).

[113] A. Pifferi, R. Berg, P. Taroni and S. Andersson-Engels, "Fitting of time-resolved reflectance curves with a Monte Carlo model", in Advances in Optical Imaging and Photon Migration, R. R. Alfano and J. G. Fujimoto, eds., Vol. 2 of OSA Trends in Optics and Photonics Series (Optical Society of America, Washington, D.C.), 311–314 (1996).

[114] S.L. Jacques, "Monte Carlo simulations of fluorescence in turbid media", Ch. 6 in *Handbook of Biomedical Fluorescence*, M.A. Mycek, B.W. Pogue, publ. Marcel-Dekker, New York, NY (2003).

[115] V. Ntziachristos, C.H. Tung, C. Bremer and R. Weissleder, "Fluorescence molecular tomography resolves protease activity *in vivo*", Nat. Med., **8**, 757–760 (2002).

[116] C.M. McCann, P. Waterman, J.L. Figueiredo, E.Aikawa, R. Weissleder and J.W. Chen, "Combined magnetic resonance and fluorescence imaging of the living mouse brain reveals glioma response to chemotherapy", Neuroimage, **45**, 360–369 (2009).

[117] S.L. Gibbs-Strauss, J.A. O'Hara, P.J. Hoopes, T. Hasan and B.W. Pogue, "Noninvasive measurement of aminolevulinic acidinduced protoporphyrin IX fluorescence allowing detection of murine glioma *in vivo*", J. Biomed. Opt., **14**, 014007 (2009).

[118] J. Chen, C.H. Tung, U. Mahmood, V. Ntziachristos, R. Gyurko, M.C. Fishman, P.L. Huang and R. Weissleder, "*In vivo* imaging of proteolytic activity in atherosclerosis", Circulation, **105**, 2766–2771 (2002).

[119] X. Montet, J.L. Figueiredo, H. Alencar, V. Ntziachristos, U. Mahmood and R. Weissleder, "Tomographic fluorescence imaging of tumor vascular volume in mice", Radiology, **242**, 751–758 (2007).

[120] J. von Burstin, S. Eser, B. Seidler, A. Meining, M. Bajbouj, J. Mages, R. Lang, A.J. Kind, A.E. Schnieke, R.M. Schmid, G. Schneider and D. Saur, "Highly sensitive detection of early-stage pancreatic cancer by multimodal near-infrared molecular imaging in living mice", Int. J. Cancer, **123**, 2138–2147 (2008).

[121] A. Koenig et al., "*In vivo* mice lung tumor follow-up with fluorescence diffuse optical tomography", J. Biomed. Opt., **13**, 011008 (2008).

[122] K.M. Kozloff, R. Weissleder and U. Mahmood, "Noninvasive Optical Detection of Bone Mineral", J. Bone Miner. Res., **22**, 1208–1216 (2007).

[123] A. Zaheer, R.E. Lenkinski, A. Mahmood, A.G. Jones, L.C. Cantley and J.V. Frangioni, "*In vivo* near-infrared fluorescence imaging of osteoblastic activity", Nat. Biotechnol., **19**, 1148–1154 (2001).

[124] M. Kobayashi, T. Mizumoto, Y. Shibuya and M. Enomoto, “Fluorescence tomography in turbid media based on acousto-optic modulation imaging”, Appl. Phys. Lett., **89**, 181102 (2006).

[125] M. Kobayashi, T. Mizumoto, T.Q. Duc and M. Takeda, Proc. SPIE, “Fluorescence tomography of biological tissue based on ultrasound tagging technique”, **6633**, 663306 (2007).

[126] B. Yuan, J. Gamelin and Q. Zhu, “Mechanisms of the ultrasonic modulation of fluorescence in turbid media”, J. Appl. Phys., **104**, 103102 (2008).

[127] B. Yuan, Y. Liu, P.M. Mehl and J. Vignola, “Microbubble-enhanced ultrasound-modulated fluorescence in a turbid medium”, Appl. Phys. Lett., **95**, 181113 (2009).

[128] M. Born and E. Wolf, "Principles of Optics: Electromagnetic Theory of Propagation, Interference and Diffraction of Light," Sixth corrected Ed., Pergamon Press (1986).

[129] E. Hecht, "Optics," Second Ed., Addison-Wesley Publishing Company, Inc. (1987).

[130] S.A. Prahl, M. Keijzer, S. L. Jacques, and A. J. Welch, “A Monte Carlo model of light propagation in tissue”, Proc. SPIE, **5**, 102–111 (1989).

[131] E. Alerstam, S. Andersson-Engels and T. Svensson, “White Monte Carlo for time-resolved photon migration”, J. of Biomed. Opt., **13**, 041304 (2008).

[132] L.G. Henyey and J.L. Greenstein, "Diffuse Radiation in the Galaxy," Astrophys. J., **93**, 70-83 (1941).

[133] L. Wang and G. Ku, “Frequency-swept ultrasound-modulated optical tomography of scattering media”, Optical Letters, **23**, 975-977 (1998).

[134] J. Li and L. Wang, “Ultrasound-modulated optical computed tomography of biological tissues”, Appl. Phys. Lett., **84**, 1597-1599 (2004).

[135] M. Hisaka, T. Sugiura, and S. Kawata, “Optical cross-sectional imaging with pulse ultrasound wave assistance”, J. Opt. Soc. Am. A - Opt. Image Sci. Vis., **18**, 1531-1534 (2001).

[136] A. Lev and B. G. Sfez, “Pulsed ultrasound-modulated light tomography”, OPTICS LETTERS, **28**, 1549-1551 (2003).

[137] L. Wang, S.L. Jacques and X. Zhao, “Contibuous-wave ultrasonic modulation of scattered laser light to image objects in turbid media”, OPTICS LETTERS, **20**, 629-631 (1995).

[138] N.T. Huynh, H. Ruan, D. He, B.R. Hayes-Gill and S.P. Morgan, “Effect of Object Size and Acoustic Wavelength on Pulsed Ultrasound Modulated Fluorescence Signals”, J. of Biomed. Opt., **17**, 076008 (2012).

[139] R.H. Mayer, J.S. Reynolds and E.M. Sevick-Muraca, “Measurement of the fluorescence lifetime in scattering media by frequency-domain photon migration”, Appl.Opt., **38**, 4930-4938 (1999).

[140] N.T. Huynh, D. He, B.R. Hayes-Gill, J.A. Crowe, J.G. Walker, M.L. Mather, F.R. Rose, S.P. Morgan, N.G. Parker and M.J. Povey, “Application of amaximum likelihood algorithm to ultrasound modulated optical tomography”, J. of Biomed. Opt., **17**, 026014 (2012).

[141] Tim Freegard, *Introduction to the physics of waves*, Cambridge University Press (2012).

[142] M.S. Patterson, B. Chance, and B.C. Wilson, "Time resolved reflectance and transmittance for the non-invasive measurement of tissue optical properties," Appl. Opt. **28**, 2331-2336 (1989).

[143] G. Ma, J.F. Delorme, P. Gallant and D.A. Boas, “Comparison of simplified Monte Carlo simulation and diffusion approximation for the fluorescence signal from phantoms with typical mouse tissue optical properties”, Appl. Opt. **46**, 1686-1692 (2007).

[144] C. Grunwald, K. Schulze, G. Giannone, L. Cognet, B. Lounis, D. Choquet and R. Tampé, “Quantum yield optimized fluorophores for site-specific labeling and super-resolution imaging”, J. Am. Chem. Soc., **133**, 8090–8093 (2011).

[145] S.H. Han, S. Farshchi-Heydari and D.J. Hall, “Analysis of the fluorescence temporal point-spread function in a turbid medium and its application to optical imaging”, J.Biomed.Opt., **13** (2008).

[146]K.H. Shim and B.G. Kim, "Simple Frequency-Domain Fluorescence-Lifetime Measurement System Using Violet Laser Diode", Journal of the Korean Physical Society, **49**, 647-651 (2006).

[147] V.Venugopal, J. Chen, F. Lesage and X. Intes, "Full-field time-resolved fluorescence tomography of small animals", Optics Letters, **35**, 3189-3191 (2010).

[148] "fluorescence imaging principles and methods handbook", Amersham Biosciences, 63-0035-28 Rev. AB, (2002).

[149] T.J. Farrell, M.S. Patterson and B.C. Wilson, "A diffusion theory model of spatially resolved, steady-state reflectance for the noninvasive determination of tissue optical properties *in vivo*", Med. Phys., **19**, 879–888, (1992).

[150] A. Kienle, L. Lilge, M.S. Patterson, R. Hibst, R. Steiner and B.C. Wilson, "Spatially resolved absolute diffuse reflectance measurementsfor noninvasive determination of the optical scattering and absorptioncoefficients of biological tissue", Appl. Opt., **35**, 2304–2314, (1996).

[151] A.D. Yablon, N.S. Nishioka, B.B. Mikic´ and Vasan Venugopalan, "Measurement of tissue absorption coefficients by use of interferometric photothermal spectroscopy", Applied Optics, **38**, 1259-1272 (1999).

[152] T.P. Moffitt and S.A. Prahl, "In vivo sized-fiber spectroscopy," in SPIE Proc. Optical Biopsy III, **3917**, R.R. Alfano, Ed., 2000, 225–231 (2000).

[153] T.P. Moffitt and S.A. Prahl, "Sized-fiber reflectometry for measuring local optical properties," IEEE J. Quantum Electronics, **7**, 952-958 (2001).

[154] Hanli Liu, "Determination of reduced scattering coefficient of biological tissue from a needle-like probe", Optical Express, **13**, No.13, 4828-4892 (2005).

[155] Guillermo Marquez, Lihong V. Wang, Shao-Pow Lin, J.A. Schwartz, and S.L. Thomsen, "Anisotropy in the absorption and scattering spectra of chicken breast tissue", Applied Optics, **37**, No. 4, 798-804 (1998).

[156] M.A. Franceschini, E. Gratton, D. Hueber, and S. Fantini, "Near-Infrared Absorption and Scattering Spectra of Tissues in Vivo", the International Soc. For Opt. Engineering, **3597**, 526-531 (1999).

[157] W.F. Cheong, S.A. Prahl, and A.J. Welch, "A Review of the Optical Properties of Biological Tissues," IEEE J. Quantum Electronics, **26**, 2166-2185 (1990).

[158] C.L. Tsai, J.C. Chen and W.J. Wang, "Near-infrared Absorption Property of Biological Soft Tissue Constituents", J. Med. Biol. Eng., **21**, No.1, 7-13 (2001).

[159] E. Claridge, D. Hidović-Rowe, P. Taniere and T. Ismail, "Quantifying mucosal blood volume fraction from multispectral images of the colon", Medical Imaging 2007: Physiology, Function, and Structure from Medical Images, **6511**, .709559 (2007).

[160] S.A. Prahl, “Tabulated molar extinction coefficient for hemoglobin in water,” http://omlc.ogi.edu/spectra/hemoglobin/summary.html (1998).

[161] Gratzer and Kollias, data is web based at
http://omlc.ogi.edu/spectra/hemoglobin/index.html

[162] S.J. Matcher, M. Cope and D.T. Delpy, “*In vivo* measurements of the wavelength dependence of tissue-scattering coefficients between 760 and 900 nm measured with time-resolved spectroscopy”, Applied Optics, **36**, 386-396 (1997)

[163] J.R. Mourant, Tamika Fuselier, James Boyer, T.M. Johnson, and I.J. Bigio, “Predictions and measurements of scattering and absorption over broad wavelength ranges in tissue phantoms”, Applied Optics, **36**, No.4, 949-957 (1997).

[164] G. Eason, A. Veitch, R. Nisbet and F. Turnbull, “The theory of the Backscattering of light by blood”, J. Phys., **11**, 1463-1479 (1978).

[165] R. Barakat, “Application of Apodization to Increase Two-Point Resolution by the Sparrow Criterion. I. Coherent Illumination”, J. of The Opt. Soc. of America, **52**, 276-283 (1962).

[166] J. Laufer, R. Simpsony, M. Kohly, M. Essenpreis and M. Cope, “Effect of temperature on the optical properties of *ex vivo* human dermis and subdermis”, Phys. Med. Biol., **43**, 2479–2489 (1998).

[167] M. Monici, “Cell and tissue autofluorescence research and diagnostic applications”, Biotechnol Annu. Rev., **11**, 227–256 (2005).

[168] B. Yuan and Y. Liu, “Ultrasound-modulated fluorescence from rhodamine B aqueous solution”, J. of Biomed. Opt., **15**, 021321 (2009).